Reservoir quality analysis of the Triassic sandstones in the Nederweert and Naaldwijk areas.

A post-mortem study

Zeenat Maniar

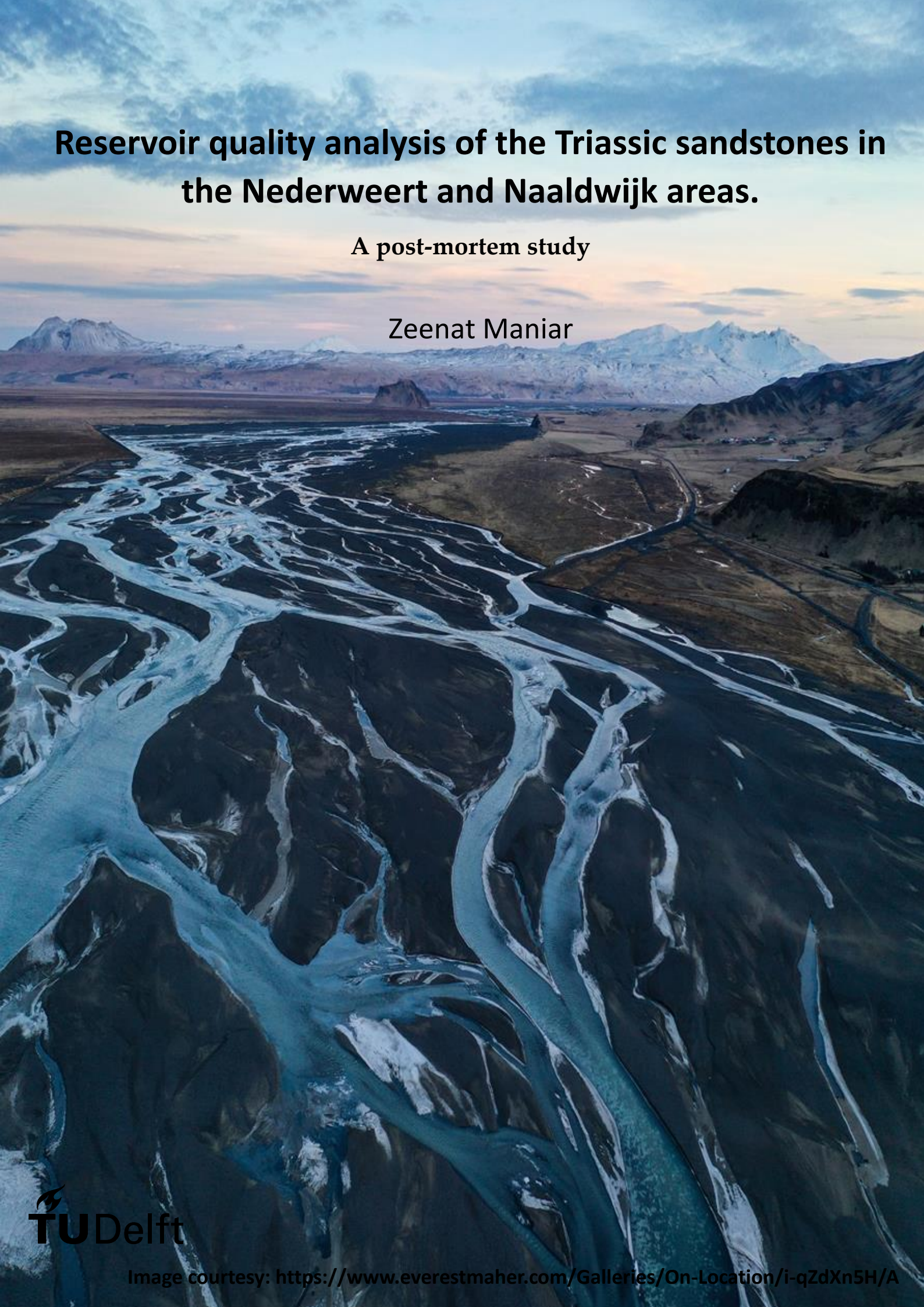

TU Delft

Image courtesy: https://www.everestmaher.com/Galleries/On-Location/i-qZdXn5H/A

`

Reservoir quality analysis of the Triassic sandstones in the Nederweert and Naaldwijk areas.

A post-mortem study

By

Zeenat Maniar

Student number:4755189

in partial fulfilment of the requirements for the degree of

Master of Science

in Applied Geology

at the Delft University of Technology,

to be defended publicly on Monday September 16, 2019 at 10:00 am.

`

This thesis has been approved by the

University Supervisor: Dr. Marinus Eric Donselaar, Delft University of Technology.

Company Supervisor: Charlotte de Wijkerslooth, HVC Group.

Thesis committee:

Dr. Marinus Eric Donselaar, Delft University of Technology

Charlotte de Wijkerslooth, HVC Group.

Dr. Allard Martinius, Delft University of Technology

Dr. Auke Barnhoorn, Delft University of Technology

Dr. Joep Storms, Delft University of Technology

An electronic version of this dissertation is available at http://repository.tudelft.nl/.

16th September 2019.

`

Acknowledgements

Firstly, I would like to extend my gratitude to my thesis supervisor Dr. Rick Donselaar for his constructive guidance throughout the thesis. Thank you for imparting your knowledge in the field of reservoir sedimentology and the positive criticism that has led to better results.

I would also like to thank Charlotte de Wijkerslooth (HVC) for always making sure I had everything that was needed to progress further in my study and always being very approachable. I am also thankful to Tarek Hopman (HVC) for the insightful discussions in the course of this research.

I am grateful to Dr. Marita Felder from Panterra Geoconsultants for sharing her expertise in the field of diagenesis and making valuable suggestions.

I would also like to thank Andre Slupik from TNO who was extremely helpful during the core study conducted in Zeist.

Lastly, I am thankful to my parents and all my friends for their constant support.

Contents

List of Figures

List of Tables

Executive Summary:

With increase in the demand for heat energy, and the growing conscience of the world to reduce CO_2 emissions, transition to cleaner energy alternatives has gained momentum. In the Netherlands, the potential for cost-effective geothermal heat extraction from sedimentary aquifers has led to the exploration of siliciclastic Triassic reservoirs in the West Netherlands Basin and Roer Valley Graben for their suitability.

In 2017, Westland geothermal exploration well NLW-GT-01 was drilled tapping depths of over 4000 meters and encountering temperatures of about 100°C. In contradiction to the pre-drill expectations of having appreciable porosity and permeability values between 10-500mD, the Upper Volpriehausen sandstones exhibited porosity and permeabilities ranging between 1.4% to 3.9% and $\leq$0.02mD respectively. The sandstones were highly compacted and severely cemented by dolomite and quartz. These cements blocked all the macropores leaving no visible porosity in the thin sections. Although, the cored interval was extensively fractured the measured permeability values were negligible.

This thesis presents the results of an assessment of the factors leading to the deterioration of intrinsic porosity and permeability of Triassic aquifers lying in the Westland and Nederweert regions. In this project, grain-size analysis using core plugs, thin-section study, petrophysical data analysis, and FMI log interpretation were conducted to understand the depositional environment of the Lower Germanic Trias Group precisely the cored sections of the Nederweert Sandstone Member in NDW-01 well and the Volpriehausen sandstones in NLW-GT-01 borehole. Due to the complex tectonic history coupled with locally different paleoenvironments, the current depths of the Triassic deposits in the investigated area did not correlate with the reservoir quality of the adjacent shallower wells. In addition to the local depositional conditions in the basin, the variable precipitation in the source area, and the distance of sediment transport have defined the rock characteristics. The primary grain-textures, such as roundness, sorting, packing, as well as the detrital framework and authigenic minerals, were found to influence the sandstone porosity. The tightness of the reservoir was due to significant mechanical compaction and cementation described by a diagenetic reconstruction explaining the evolution of porosity with depth with negligible generation of secondary porosity. The deterioration of the reservoir quality is correlatable to the burial history and its resulting consequences, namely mechanical and chemical compaction endured by the rock during periods of basin subsidence and uplift. These analyses have put the deviation of pre-drill results from those that were obtained through post-drill evaluations into perspective.

1. Background

1.1. Introduction

To achieve the ambitious goal of combating climate change by restraining the rise of global temperatures, the Dutch Government is striving for a Climate Neutral Energy Supply in 2050 which means having an energy regime free of CO_2 emissions (EBN, 2018).To this end, an accelerated energy transition is needed to reduce the dependency on fossil fuels and limit CO_2 emissions. The research and application of concepts such as CO_2 sequestration, hydrogen storage, geothermal energy extraction, and other sustainable alternatives to conventional fossil fuels are on the rise.

The extensively mapped Dutch subsurface that harbours underexplored potential geothermal targets has a major role to play in this energy transition, as shown in (Fig:1; Kramers, et al. (2012)).

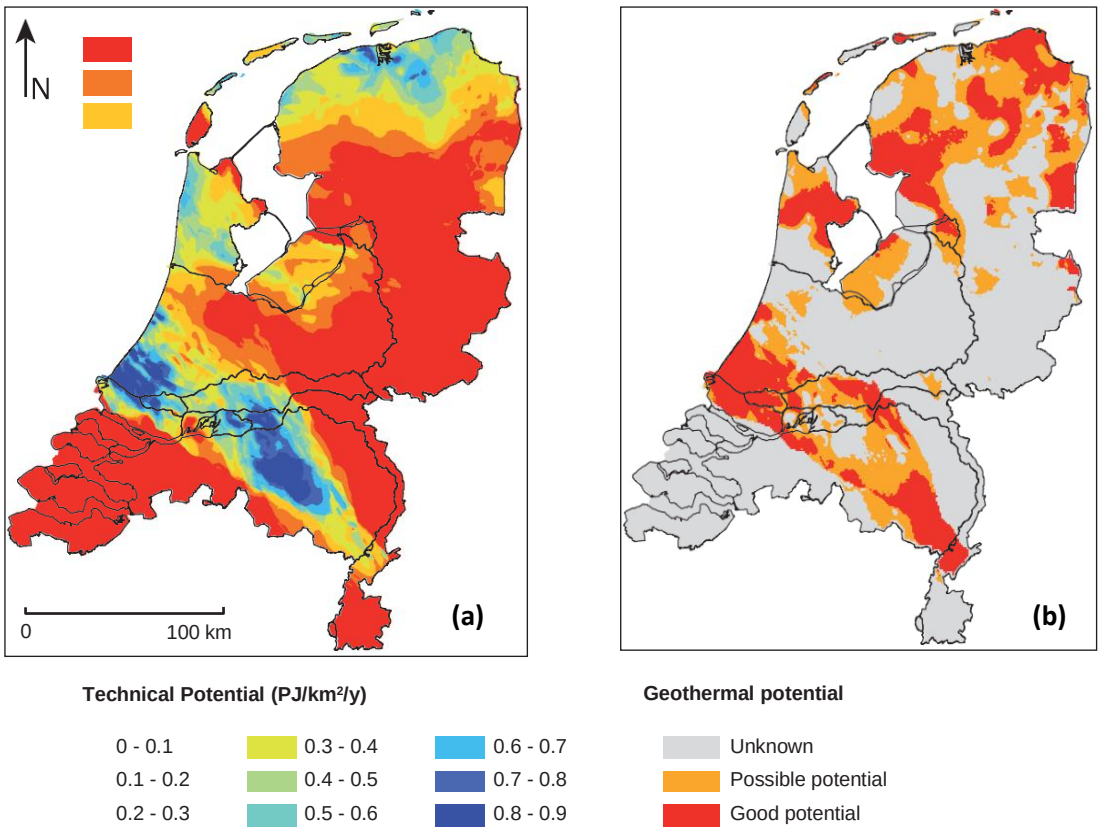

Figure 1: Distribution of the (a)Technical Potential in PJ/km²/y and (b)Geothermal Potential for all the mapped aquifers in the Netherlands (Kramers, et al., 2012).

In the Netherlands, the strata potentially suitable for geothermal exploration include shallow Cenozoic sandstone aquifers (less than 1000m deep), aquifers in the Lower Cretaceous (predominantly found in the West Netherlands Basin) and Jurassic (Delft Sandstone Member), Triassic aquifers in the Roer Valley Graben and the West Netherlands Basin and finally the Late Permian aquifer-Slochteren Formation towards the north of the Netherlands (see Fig. 2; Kramers, et al., 2012).

An average geothermal gradient of 31°C/km makes the subsurface of the Netherlands, a low enthalpy geothermal source (Pluymaekers, et al., 2012). A subsurface temperature of around 30-40°C at 1000 meters of depth is not high enough for direct use, and so heat pumps are used to raise the temperatures to an optimal level. With the increase in depth, higher temperatures are encountered. Studies are being carried out to find potential ultra-deep reservoirs at depths of over 4000 metres where the temperature is higher than 130°C (T&A Survey, 2018; Stichting Platform Geothermie, DAGO, Stichting Warmtenetwerk, EBN,Ministry of Economic Affairs and Climate and the Ministry of the Interior and Kingdom Relations, 2018) in order to meet the increasing energy demand sustainably.

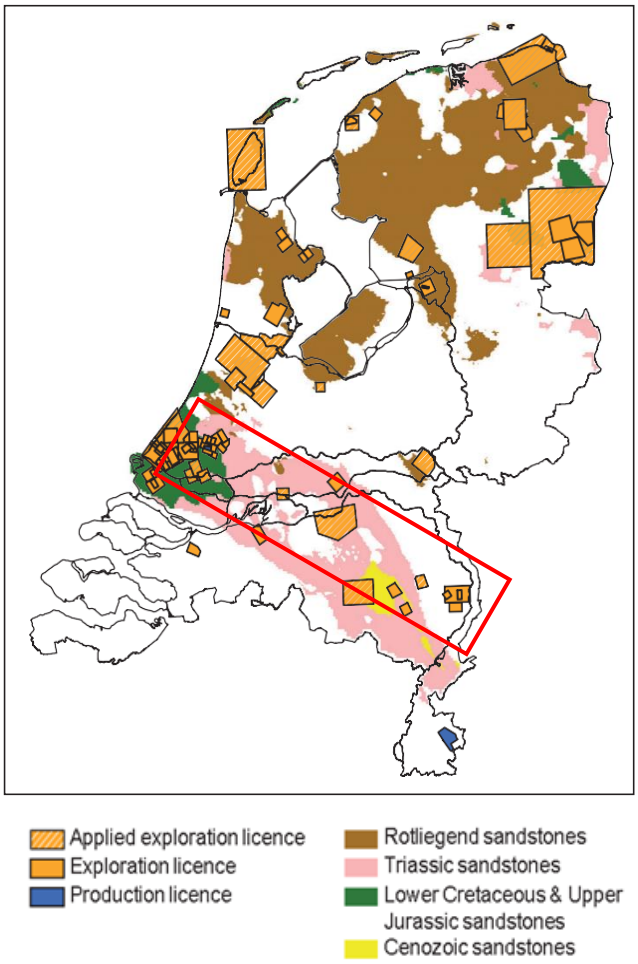

Figure 2: Distribution of the geothermally targeted aquifers along with based on ThermoGIS. (Kramers, et al., 2012)

As per Stichting Platform Geothermie (2018), the major difference between geothermal and ultra-deep geothermal is the extensive amount of subsurface data and drilling experience at depths lesser than 4000m as a result of hydrocarbon exploration (more than 3000 onshore boreholes). In the case of ultra-deep drilling, the subsurface knowledge is limited to seven boreholes tapping depths greater than 4000m.SDE+ government subsidy and Green Deal subsidy schemes provided for geothermal heat exploration projects make it a competitive alternative in the sustainable energy mix. This has paved way for more research to understand the deep subsurface better if the goal of a Climate Neutral Energy Supply is to be achieved by 2050.

This MSc thesis is a comprehensive reservoir quality assessment of the Lower Germanic Trias sandstones, namely the Nederweert Sandstone Member (Lower Buntsandstein) and the Volpriehausen Sandstone Member (Main Buntsandstein). This research is formulated by the integration of all the available and analysed subsurface data needed to build a predictive reservoir quality model.

Hydreco Geomec and Energiefonds Brabant ventured on the Green Deal Geothermal Brabant project with the objective of exploration and realization of a minimum of five geothermal projects in the Brabant. For this project, the 292 meters thick Nederweert Sandstone Member lying at shallow depths of 2280-2572m in NDW-01 well is an attractive candidate. However, since this bore was drilled in 1964-65, the available information about the reservoir quality is scarce. Existence of suitable rock parameters in this massive sandstone package would open up new possibilities of green energy extraction in the Brabant and take a step towards sustainability.

The Naaldwijk well was drilled as a part of the Trias Westland geothermal project in 2017-18. This project was a joint effort of companies such as Flora Holland, HVC, Westland Infra, and the Municipality of the Westland who wanted to extract heat energy for providing to the greenhouse horticulture in the Westland region. It was a dual play project with Triassic sandstones as the primary target and the Lower Cretaceous sandstones as a back-up option. The reservoir property evaluations carried out by T&A Survey in 2008 had indicated that the 182m thick Triassic aquifer had the potential to provide for 80% of the heat demand in Westland as the water temperature in this Trias layer was expected to be in the range of 130-150°C with P50 geothermal output of about 40MW. However, TNO had a different opinion and stated that the permeabilities would not be high enough to achieve a considerable geothermal output. Due to the misinterpretation of the Röt Formation in the logging while drilling (LWD) gamma-ray log, the core was acquired from the Lower Detfurth-Upper Volpriehausen sandstones rather than the previously planned Hardegsen sandstones. The cored sandstones turned out to be extremely tight with negligible permeability between 0.00 and 0.02mD despite the abundant fractures. Water could not be pumped upwards due to the tightness of the Trias layer- Volpriehausen. The gas intervals between 4150-4210 meters made the production test more complex (T&A Survey, 2018).NLW-GT-01 proved to be an unsuitable bore for geothermal heat extraction under standard conditions. However, the second well which penetrated a depth of 2.7 kilometres in the Cretaceous succeeded to become an ideal geothermal target with optimal flow and a bottom-hole temperature of 87°C (T&A Survey, 2018).

1.2. Research Objective

This study aimed at a detailed analysis of the sample material supportive in understanding the nature and cause of tightness of the Triassic reservoir encountered in the Naaldwijk. Core description and determination of lithofacies, analysis of the wireline log responses, FMI analysis and interpretation, diagenetic history modelling coupled with porosity evolution, were undertaken as a part of this research project.

Post-mortem analysis carried out on permeability deterioration and the spatial distribution of low-permeability intervals added to the existing knowledge about the influence of early-diagenetic (upon burial) and late-diagenetic (during maximum burial) development of the Volpriehausen sandstone. Also, the sedimentological analysis performed on the Nederweert NDW-01 core helped in gaining a better understanding of the depositional environment in the south-eastern part of the Roer Valley Graben during the Triassic.

The objective of this report is to provide insight into the aquifer quality of the Triassic sandstones, particularly the Nederweert Sandstone Member and the Volpriehausen Formation for their suitability for geothermal heat extraction. Since NLW-GT-01 core is obtained from a relatively deeper interval as compared to most wells in the Netherlands, the results obtained from this study can be applied to analogous siliciclastic aquifers which are deeply buried and have experienced a similar tectonic evolution.

Therefore, the analysis carried out on all the samples and documents available for NLW-GT-01 and NDW-01 was aimed at explaining the following:

1. Assessment of primary textural parameters of the grains and their influence on the evolution of porosity and permeability.
2. Influence of the mineralogical composition of the rock on mechanical and chemical diagenetic processes.
3. Reasons for deterioration of the porosity and permeability with depth.
4. Depositional setting of the Naaldwijk and Nederweert areas.
5. Failure to meet the pre-drill expectations.
6. Generalized formulations to be considered during future exploration of similar deeply buried clastic aquifers.

The report is envisaged to contain the post-drill evaluations. With the availability of new information, new development strategies need to be formulated to harness the remaining potential.

1.3. Report Structure

This report comprises of a total of 7 Chapters. Chapter 1 provides the background for this research project and the research questions dealt with in the course of this study. Chapter 2 gives information about the structural and stratigraphic setting of the investigated areas. In Chapter 3, a summary of all the available datasets is provided. Chapter 4 discusses the workflow procedure. Chapter 5 describes the results obtained from core study, petrophysical logs, grain-size analysis, porosity and permeability models. It also explains the diagenetic evolution of the Naaldwijk area, FMI interpretation results along with the paleogeography and depositional model of the Triassic sandstones in the studied areas. A comparative reservoir quality study between NLW-GT-01 and its neighbouring wells along with the wells in Drechtsteden area is also presented in this chapter. The conclusions and recommendations for future work are listed in Chapters 6 and 7 respectively.

2. Regional Geology

The investigated wells NLW-GT-01 and NDW-01 lie within prominent extensional and transtensional Dutch rift basins: The West Netherlands Basin (WNB) and the Roer Valley Graben (RVG) respectively as indicated in (Fig. 3; Kombrink, et al. (2012)).

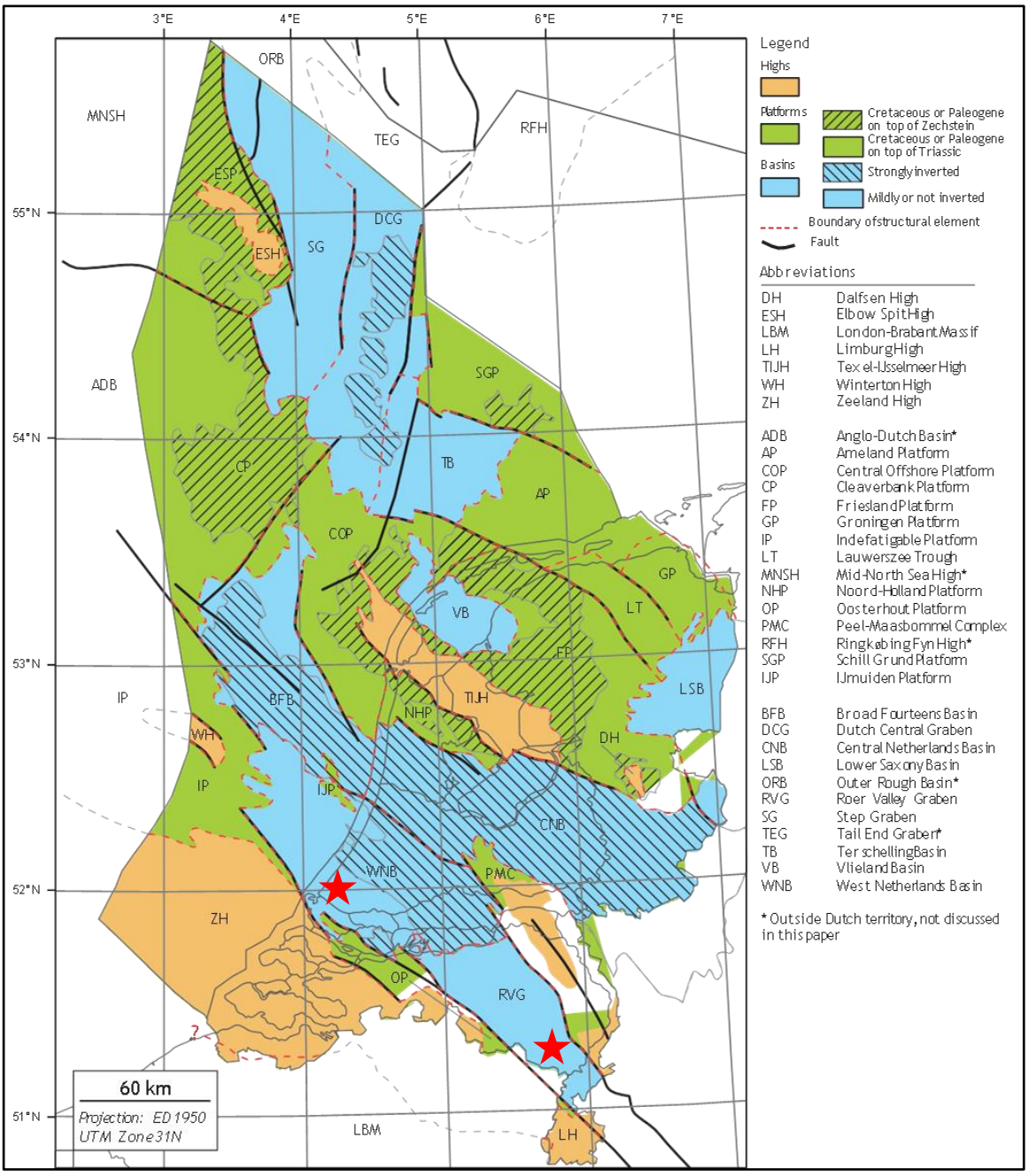

Figure 3: Late Jurassic -Early Cretaceous structural elements of the Netherlands (Kombrink, et al., 2012). The wells of the present study lie in the mildly inverted regions of the West Netherlands Basin (WNB) and the Roer Valley Graben (RVG) and are indicated with a red star.

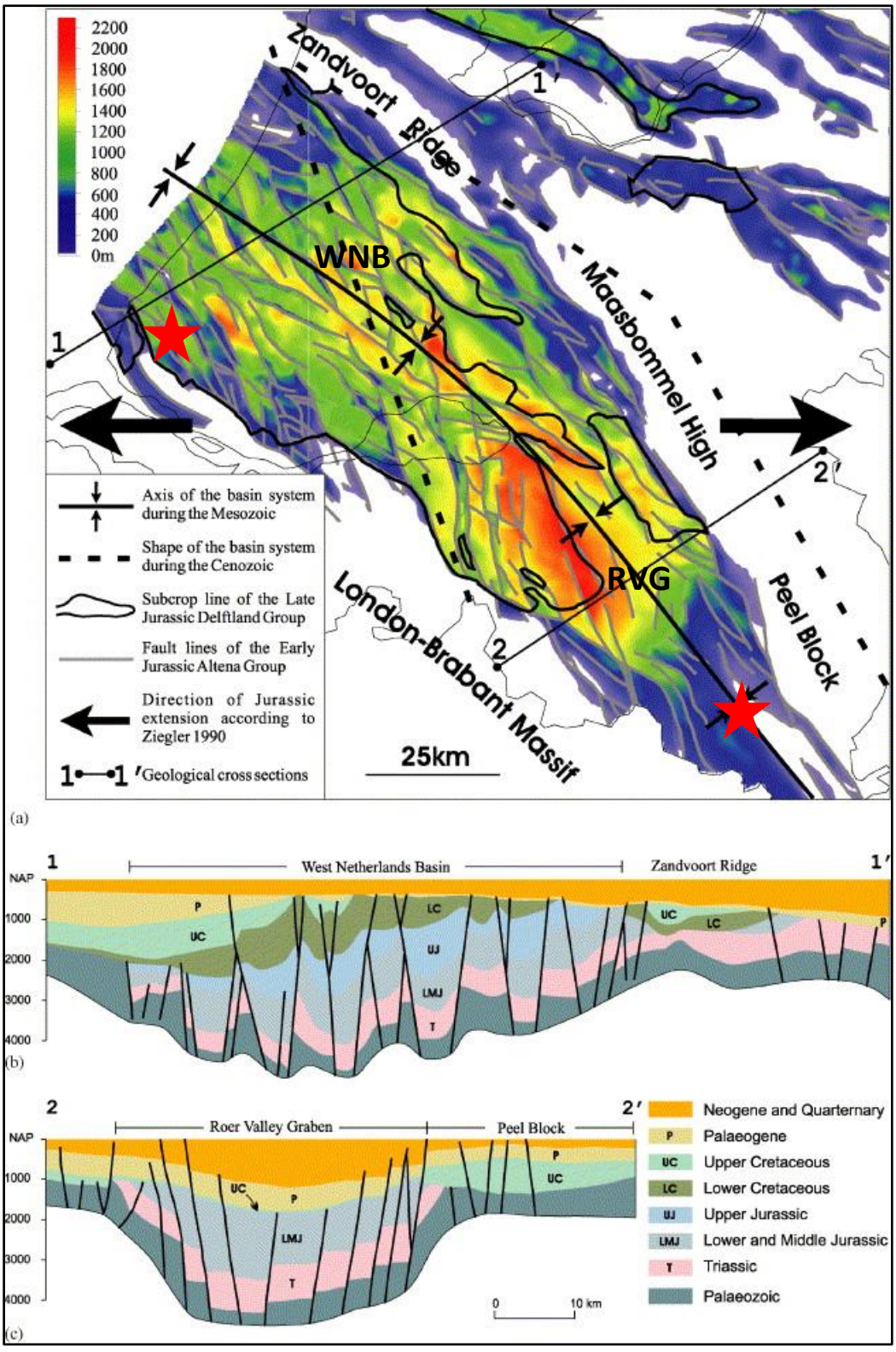

Figure 4: (a) Thickness distribution map of the Altena Group deposited during the Lower-Middle Jurassic along with structural elements adjacent to the WNB and the RVG and the stress directions during the Mesozoic (b) Geological cross-section along SW-NE across the WNB and the Zandvoort Ridge and (c) across the RVG and the Peel Block (Worum, et al., 2005).The red stars indicate the well locations.

The NW-SE trending WNB is a Jurassic Basin extending from the offshore Netherlands onto the onshore. Towards the south, it is separated from the London Brabant Massif by a distinct fault-zone while towards the north-east, the Zandvoort Ridge separates it from the Central Netherlands and the Broad Fourteen Basins. The fault-bounded Roer Valley Graben (RVG) is the south-eastern transition of the WNB. There is no distinct separation between these two basins. This NNW-SSE trending RVG consists of numerous half-graben structures. The Peel Boundary fault limits the north-eastern extent of the RVG while a series of antithetic faults bound its south-western margin (Geluk, et al., 1994). A complex faulting mechanism (Fig. 4; Worum, et al. (2005)) comprising of reverse and normal fault reactivations characterizes the tectonic history of these basins.

2.1. Structural Evolution:

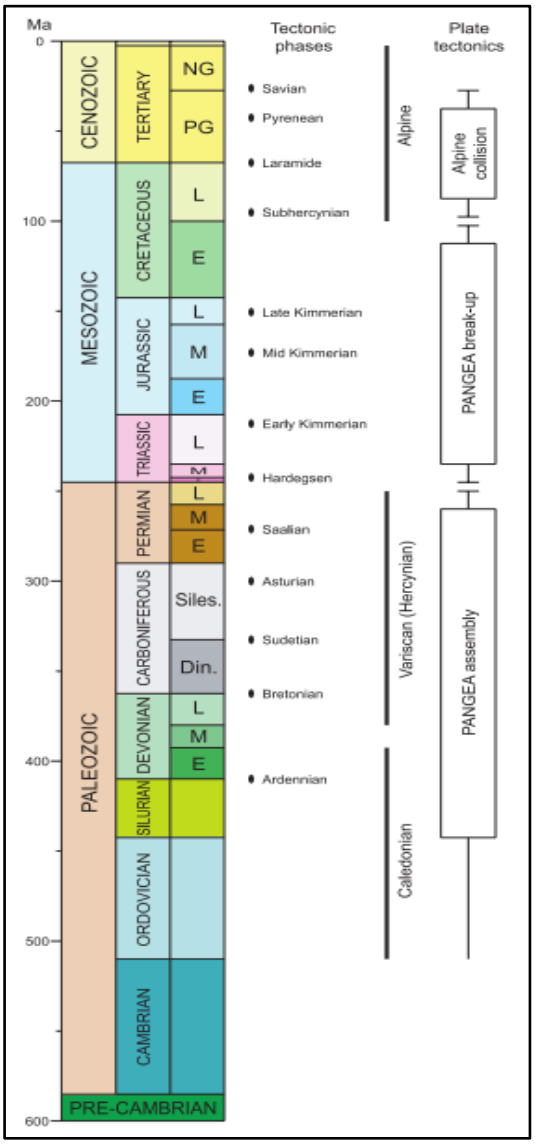

Figure 5: Lithospheric plate movements and their relationship with the tectonic events in the Netherlands (De Jager, 2007).

The WNB and RVG developed from the suturing and fragmentation of the intra-cratonic South Permian Basin (Pharaoh, et al., 2010). These basins formed in response to the following tectonic phases: i) Late Palaeozoic collapse, ii) the Mesozoic rifting iii) the Late Mesozoic-Cenozoic tectonic events (De Jager, 2007; Pharaoh, et al., 2010) refer (Fig. 5; De Jager,(2007)) which are explained as below:

i) The Late Palaeozoic collapse

The NW-SE trend of the Caledonian orogeny resulted from the collision of the continental masses of North America, Greenland, and north-western Europe with the Caledonian fold belt crossing the northern North Sea (Ziegler, 1975). The supercontinent Pangea formed due to the amalgamation of Laurussia and Gondwana as a consequence of the Variscan orogeny during the Late Carboniferous. As a result of the wrench-induced collapse and widespread magmatic activity due to the final suturing phases of Pangea in the Early Permian, the South Permian Basin situated in the foreland of the Variscan orogen was destabilized (Pharaoh, et al., 2010). In the Late

Permian following the thermal doming and severe erosion, the North and South Permian Basins began to subside (Pharaoh, et al., 2010).

ii) The Mesozoic rifting

According to Pharaoh, et al. (2010), until the Mid-Triassic, thermal subsidence controlled the development of the North and South Permian basins. However, the broad saucer-shaped subsidence pattern of the South Permian Basin was interrupted by the development of the northerly trending Central, Horn and Glückstadt grabens that were initiated at that time. The stress field in north-west Europe was re-oriented due to the Mid-Jurassic crustal separation and the opening of the Alpine Tethys Ocean (Pharaoh, et al., 2010). Also, during the Mid-Jurassic, the northern South Permian Basin was uplifted and eroded while sediments continued to deposit in the southern part (De Jager, 2007; Pharaoh, et al., 2010). The crustal extension of the North Sea rift system during the Late Jurassic and Early Cretaceous resulted in NW trending transtensional basins along the southern margin of the South Permian Basin (Pharaoh, et al., 2010).

The main structural elements of the Dutch sub-surface developed during the Late Jurassic and Early Cretaceous. The transtensional reactivation of the pre-existing basement structures resulted in the development of the NW-SE trending basins such as the Sole Pit, West Netherlands, Central Netherlands, Roer Valley and Vlieland basins (Pharaoh, et al., 2010). These basin-controlling faults accommodated the east-west extension evident in the Central Graben (Pharaoh, et al., 2010). The Hardegsen unconformity which distinguishes the Upper and Lower Germanic Trias Group is associated with the Kimmerian rifting phase (Van Hulten, 2008). The Mid-Kimmerian tectonic in early Middle Jurassic caused the upliftment of the Central North Sea Dome (Ziegler, 1990; Underhill & Partington, 1993; Pharaoh, et al., 2010). Most parts of the Netherlands underwent regional uplift and erosion due to the Late Jurassic inversion pulses. During the Early Cretaceous, the Broad Fourteens, West and Central Netherlands Basins along with the Roer Valley Graben started rupturing (Van Hulten, 2008). Marine clastics were deposited in the Central Netherlands basin while continental sedimentation occurred in the Roer Valley Graben during the Lower Cretaceous. The West and Central Netherlands Basins separated by the wrench-induced Zandvoort Ridge were filled up 2500m thick sequences of sands and clays of the Upper Jurassic to Lower Cretaceous (Pharaoh, et al., 2010). The surrounding platforms were uplifted and strongly eroded, giving rise to the Late Kimmerian Unconformity. Upper Jurassic and Lower Cretaceous clastics and associated basalts filled the extension generated half grabens in the West Netherlands Basin (Pharaoh, et al., 2010).

iii) The Late Mesozoic-Cenozoic tectonic events

Early-Late Cretaceous subsidence of the South Permian Basin was accompanied by minor extensional faulting. It was followed by the build-up of intraplate compressional stresses as indicated by the inversion of Mesozoic tensional basins and upthrusting of basement blocks which began in the Late Turonian and became more intense during the Campanian and Palaeocene (Ziegler, 1990) as indicated by (Fig. 6; De Jager, (2007)).

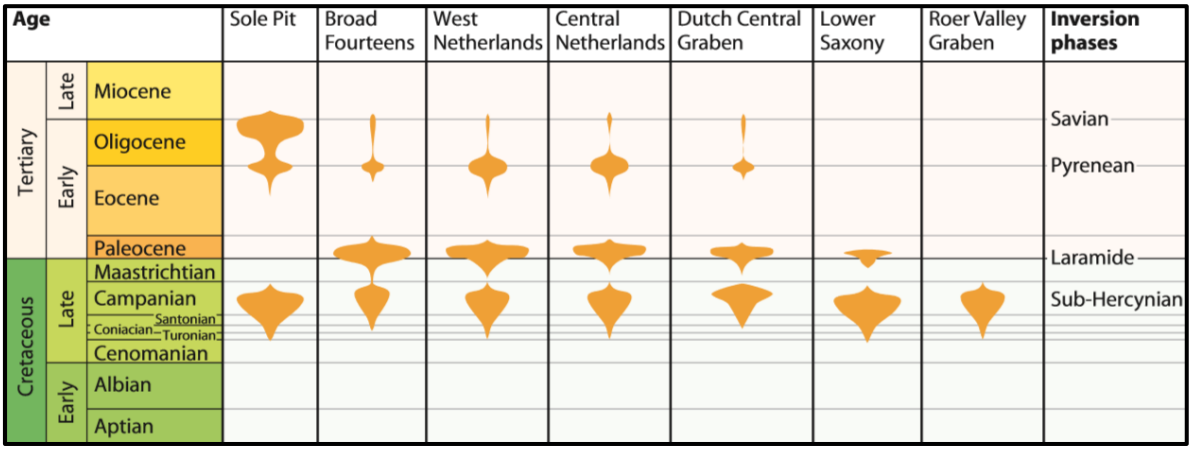

Figure 6: Age of occurrence and the relative magnitude of the pulses generated during the Alpine Orogeny on the Sole Pit and Dutch Basins (De Jager, 2007).

In the West Netherlands Basin and to a lesser extent in the Roer Valley Graben, the **Sub-Hercynian (Campanian)** and **Laramide (Maastrichtian-Palaeocene)** inversion pulses caused the reverse reactivation of the pre-existing faults. This gave rise to a series of prominent WNW and NNW trending flower structures as a result of the transpressional movements (Van Hulten, 2008; Pharaoh, et al., 2010). The Roer Valley Graben was impacted more strongly by the Sub-Hercynian inversion phase than the Laramide phase (Luijendijk, et al., 2011) (see Fig. 6; De Jager, (2007). During the Laramide inversion phase, the West and Central Netherlands Basins were uplifted and severely eroded, locally down to the Triassic, while the stable highs subsided and were filled with thick Chalk sequences (Van Hulten, 2008).

The **Pyrenean (end-Eocene)** compressional pulse caused broad uplift without any reactivation of the Mesozoic West and Central Netherlands basins, the amplitude of which decreases into the Broad Fourteens Basin (Pharaoh, et al., 2010). Relaxation of the stress regime resulted in localized normal reactivation of faults at the end of the Pyrenean inversion movement (Pharaoh, et al., 2010). The reactivated faults during the Pyrenean phase had a strike-slip component as the main stress orientation was at an oblique angle to the pre-existing grain structure (Van Hulten, 2008).

The final **Savian (end-Oligocene / Early Miocene)** pulse led to a further significant uplift in the West Netherlands Basin (De Jager, 2007) of the order of 200 to 300m (Van Wijhe, 1987a; Pharaoh, et al., 2010) while the Roer Valley Graben was subjected to strong subsidence which

continues to the present day (Geluk, et al., 1994; Michon, et al., 2003; Kombrink, et al., 2012). According to Kombrink, et al. (2012), the Paleogene uplift of the West Netherlands Basin was more severe than in the Roer Valley Graben, and as a result, the post-inversion chalk which is wholly eroded in West Netherlands Basin is preserved in the Roer Valley Graben (Michon, et al., 2003).

2.2. Stratigraphy

In the Netherlands, Triassic stratigraphy is divided into two groups. The first group is the Lower Germanic Trias Group comprising of fine-grained sandstones with numerous oolite beds of the Lower Buntsandstein. This group also consists of the coarser-grained sheet sandstones of the Main Buntsandstein alternating with oolitic claystones. The more marine-influenced (Geluk, 2005) second group- the Upper Germanic Trias Group consists of evaporites and claystones (Geluk & Rohling, 1997) as depicted in (Fig. 7; Dinoloket). The Triassic aquifers mainly comprise of clastic rocks where sequences of fluvial and aeolian sandstones make up the Lower Triassic sequences, and fluvio-deltaic sandstones constitute the Upper Triassic (De Jager, 2007). The Main Buntsandstein Subgroup occurs as a thick massive reservoir package in the south but breaks-up northwards into numerous thinner sandstone units (De Jager, 2007). These units comprise of the Volpriehausen, Detfurth and the Hardegsen formations separated by siltstone and claystone beds (Ames & Farfan, 1996; Geluk & Rohling, 1999; Pharaoh, et al., 2010).

The sedimentology and depositional environment of the Lower Germanic Trias Group- particularly the Volpriehausen Formation and the Nederweert Sandstone Member will be studied in further detail in Chapter 5 (5.1 and 5.8).

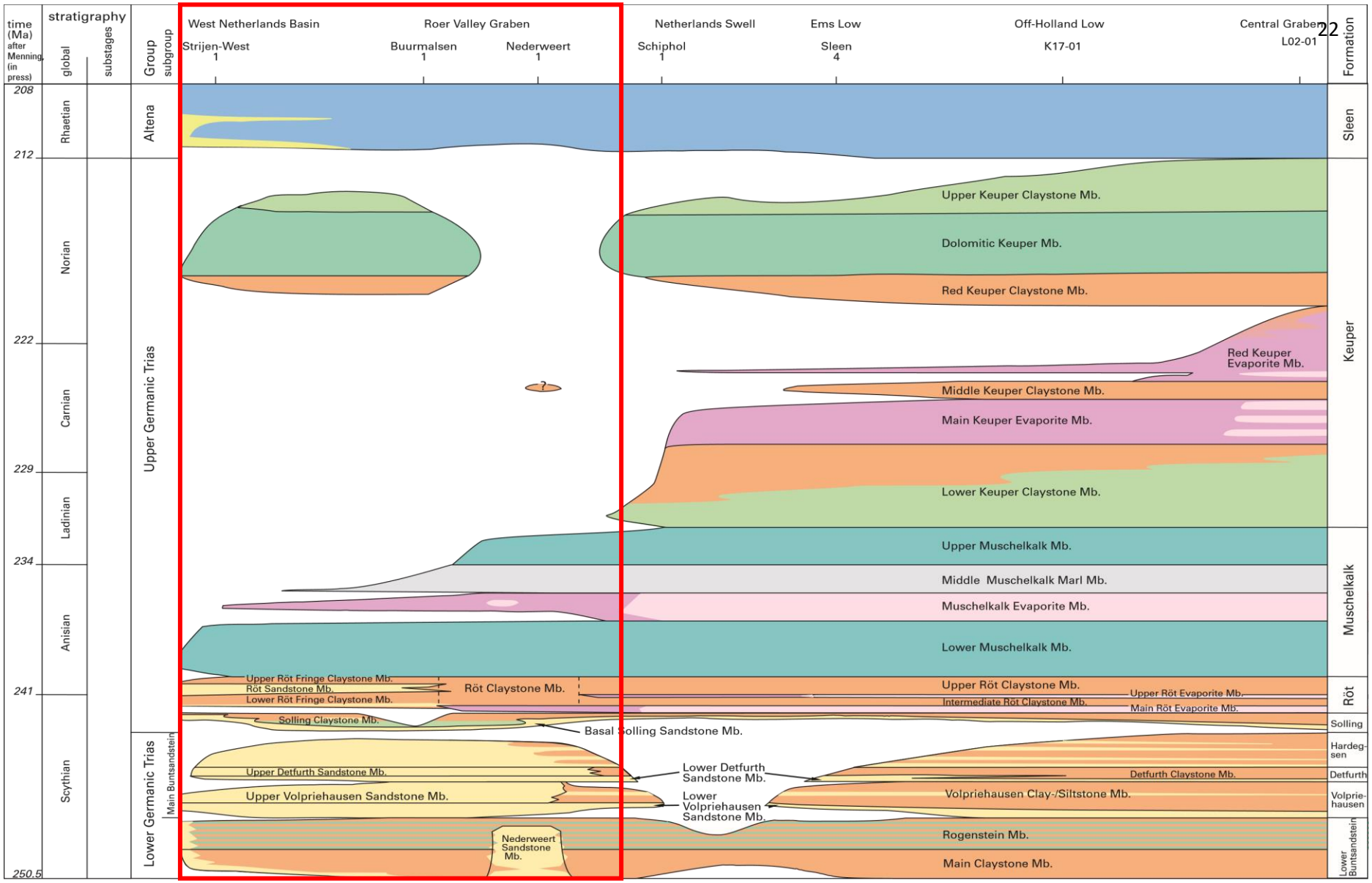

Figure 7: Triassic Chronostratigraphy of the Dutch basins (Dinoloket). Note: The investigated area is highlighted by a red box.

Lower Germanic Trias Group

The Lower Germanic Trias Group consists of the Lower and Main Buntsandstein successions.

Lower Buntsandstein Formation (Late Permian-Induan)

About 300-350m thick sequence of silt and claystones with 20-25 well-expressed fining upward cycles (Geluk & Rohling, 1997) makes up the Lower Buntsandstein Formation (Geluk, 2005). It is constituted by the Main Claystone and Rogenstein Members. These members comprise of cyclic alternations (Geluk, 2005) of fine-grained sandstones, claystones, siltstones deposited in a brackish to saline lacustrine environment. The thickness of these clastic sediments is so uniform that the internal fining-upward sequences can be correlated over vast distances (Boxem, 2015). Due to their fine-grained nature, these deposits are not considered as potential geothermal targets. However, in the south-eastern part of the Roer Valley Graben in the Netherlands, the Nederweert Sandstone Member belonging to the Lower Germanic consists of up to 292m thick sandstone unit with some conglomerate and siltstone intercalations. This massive sandstone unit grades into Main Claystone and Rogenstein Members towards the north. The core analysis of this Nederweert sandstone incorporated in this thesis will help in determining its potential for geothermal exploration.

Main Buntsandstein Subgroup (Olenekian)

The Volpriehausen, Detfurth and Hardegsen Formations constitute the Main Buntsandstein Subgroup. This subgroup consists of cyclic alternations of (sub)-arkosic sandstones and clayey siltstones. Each of the formations consist of large-scale fining upward sequence onto which smaller fining upwards and coarsening upward sequences are superimposed.

Volpriehausen Formation

The Volpriehausen is the lowermost formation of the Main Buntsandstein Sub-group with a maximum thickness up to 150m in the RVG. It is considered to be a potential reservoir.

The *Lower Volpriehausen Sandstone Member* consists of (sub)-arkosic sandstones strongly cemented by a high amount of calcite and dolomite in the lowermost part (Boxem, 2015). In the northern offshore Netherlands (Geluk & Rohling, 1997), the facies are dominantly aeolian. However, they become more fluvial southwards.

The *Upper Volpriehausen Sandstone Member* consists of reddish-green silty sandstone with oolite intercalations cemented by dolomite, anhydrite and ankerite minerals. These sandstones are more fine-grained than the Lower Volpriehausen Sandstone Member. Its thickness has been significantly reduced by uplift and erosion (Detfurth and Solling unconformities) (Geluk, 2005; Boxem, 2015).

The Upper Volpriehausen Sandstone transitions gradually into a more shaly *Volpriehausen Clay-Siltstone Member* towards the Netherlands Swell (Geluk, 2005; Boxem, 2015).

Detfurth Formation

The basal fluvial sandstone of the Detfurth Formation is the *Lower Detfurth Sandstone* Member. It occurs in the Early Triassic lows (Geluk, 2005) and shales out towards the north. It has a thickness of about 20-40meters in the West Netherlands Basin, where it consists entirely of sandstone loosely cemented by quartz while halite cementation is more common in the northern offshore deposits.

The *Detfurth Claystone Member* follows the thickness trend of the Lower Detfurth Sandstone Member (Boxem, 2015). It consists of anhydritic claystone successions with thin intercalations of siltstone, gradually grading into sandstones in the southern offshore and onshore.

The *Upper Detfurth Sandstone Member* is the sand-rich equivalent of the Detfurth Claystone Member present at the basin-margins.

Hardegsen Formation

The *Hardegsen Formation* consists of an alternation of red claystones and sandstones. It forms the upper part of the Detfurth-Hardegsen Megasequence rather than being an independent sequence (Geluk & Rohling, 1997; Geluk, 2005).

Due to pre-Solling erosion, its occurrence is limited to lows – only erosional remains. The Hardegsen siliciclastics have a thickness of about 70 meters in the West Netherlands Basin and occur as massive sandstone units in the basin fringe areas.

The better sorted aeolian deposits of the Hardegsen are known to have a superior reservoir quality than the other formations of the Main Buntsandstein Subgroup.

Upper Germanic Trias Group

The Upper Germanic Trias Group comprises of the *Solling, Röt, Muschelkalk* and *Keuper Formations*. With the exception of the Solling Formation, which contains a lower Basal Solling Sandstone Member, the sediments of the Upper Germanic Trias mainly comprise of fine-grained deposits of siltstones and claystones (Solling), evaporites(characteristic), claystones and siltstones (Röt), limestones, dolomites and marls and evaporites (Muschelkalk) and anhydrite, halite and claystones (Keuper) (Boxem, 2015). The fine grain-size and heterogeneous lithology make the Upper Germanic Trias Group an unattractive prospect for geothermal energy extraction.

3. Available Dataset

In order to build a depositional model for the Triassic sandstones in the Naaldwijk (NLW-GT-01) and the Nederweert areas (NDW-01)(Fig. 8; nlog), an integration of the available subsurface data such as the sedimentological logs , wireline log responses, thin sections and rock property data obtained from the core plugs is required. This compilation of data provides insight to the depositional mechanism and the paleoclimate at the time of deposition.

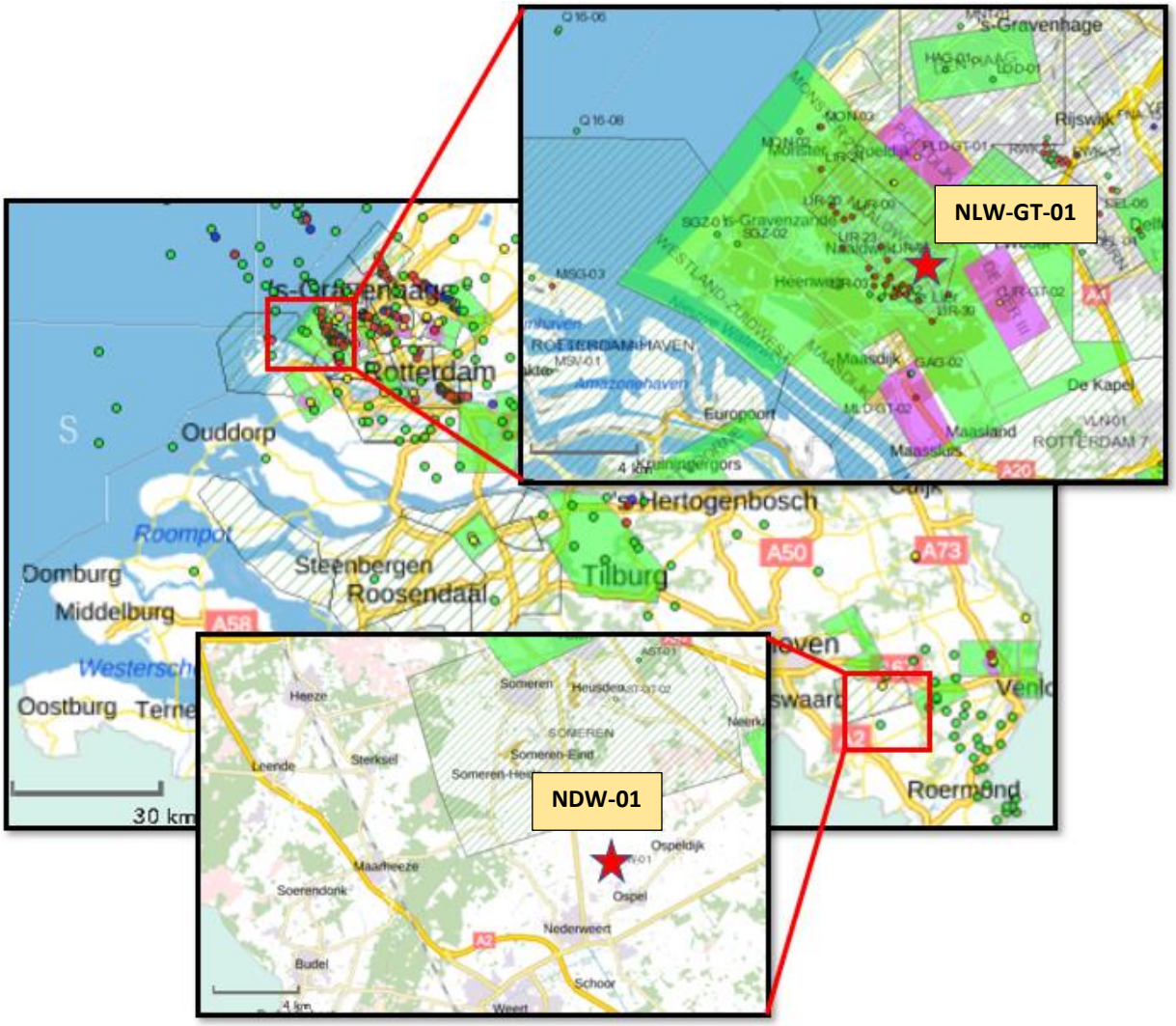

Figure 8: Location of the wells NLW-GT-01 and NDW-01 in the South Holland and Limburg province respectively (nlog). The red stars indicate the well positions.

The available dataset comprises of the following: Refer (Table 1; Fig. 9)

Table 1: Dataset available for research.

	Core	Core Plugs	Thin Section	Wireline Logs						
				Gamma Ray	Caliper	Neutron	Density	Sonic	Resistivity	FMI Log
NDW-01	✓	✓	×	✓	×	✓	×	✓	×	×
NLW-GT-01	✓	✓	✓	✓	✓	✓	✓	✓	✓	✓

3.1. Wireline logs

The gamma-ray, neutron and sonic logs for NDW-01 were acquired through the publicly available nlog site. As this well was drilled in 1964, the availability of digital data was relatively scarce.

The raw dataset for this project mainly comprised of wireline logs constituting gamma-ray, neutron-porosity, density, calliper, resistivity, and sonic logs. These petrophysical logs and the FullBore MicroImager (FMI) logs for NLW-GT-01 were provided by Schlumberger. The logging tool was FMI-8 (FMI-HD) with 8 pads. Each pad has 24 mounted button electrodes making a total of 192 sensors. The sampling rate of the tool is 0.254cm with a borehole coverage of about 80% in the 8.5-inch section. The FMI-HD tool has a horizontal and vertical resolution of 0.51cm with a calliper accuracy of ±0.51cm, deviation and azimuthal accuracy of ±0.2°. The high spatial resolution of 510µm makes it easier to image fractures with an aperture of less than 10µm.

3.2. Core and Core Plugs

NDW-01 and NLW-GT-01 cores were laid down by TNO at Zeist for their sedimentological interpretation. NDW-01 core was 10.02m in length and covered depths between 2368.50-2377.37m MD while the NLW-GT-01 well had a 29.7m long unslabbed cylindrical core covering depths between 4250-4279.7m MD. The former was also unslabbed, however, it was cut into quarter cylinders, two of which were put together forming a half. This half cylindrical core was then described and the sedimentological logs were made.

39 core plug samples of NDW-01 (core plug length varied between 2 and 5 cm with a diameter of about one inch) and 11 core plug samples of NLW-GT-01 (about 4 cm in length and 1 inch in diameter) were photographed. Photographs of the trimmed ends of the core plugs were taken by Leica Camera AG software (see Appendix). These photographs were used to perform grain-size analysis by measuring the grain-diameter using ImageJ software. It is to be noted that the plugs belonging to the NDW-01 are not the same as mentioned on the nlog website but are new samples taken from the core by PanTerra Geoconsultants.

3.3. Thin sections

Three thin sections (HS1, HS2 and HS11) of NLW-GT-01 were also provided by TNO. In addition to this, X-ray diffraction (XRD) data was supplied by PanTerra Geoconsultants.

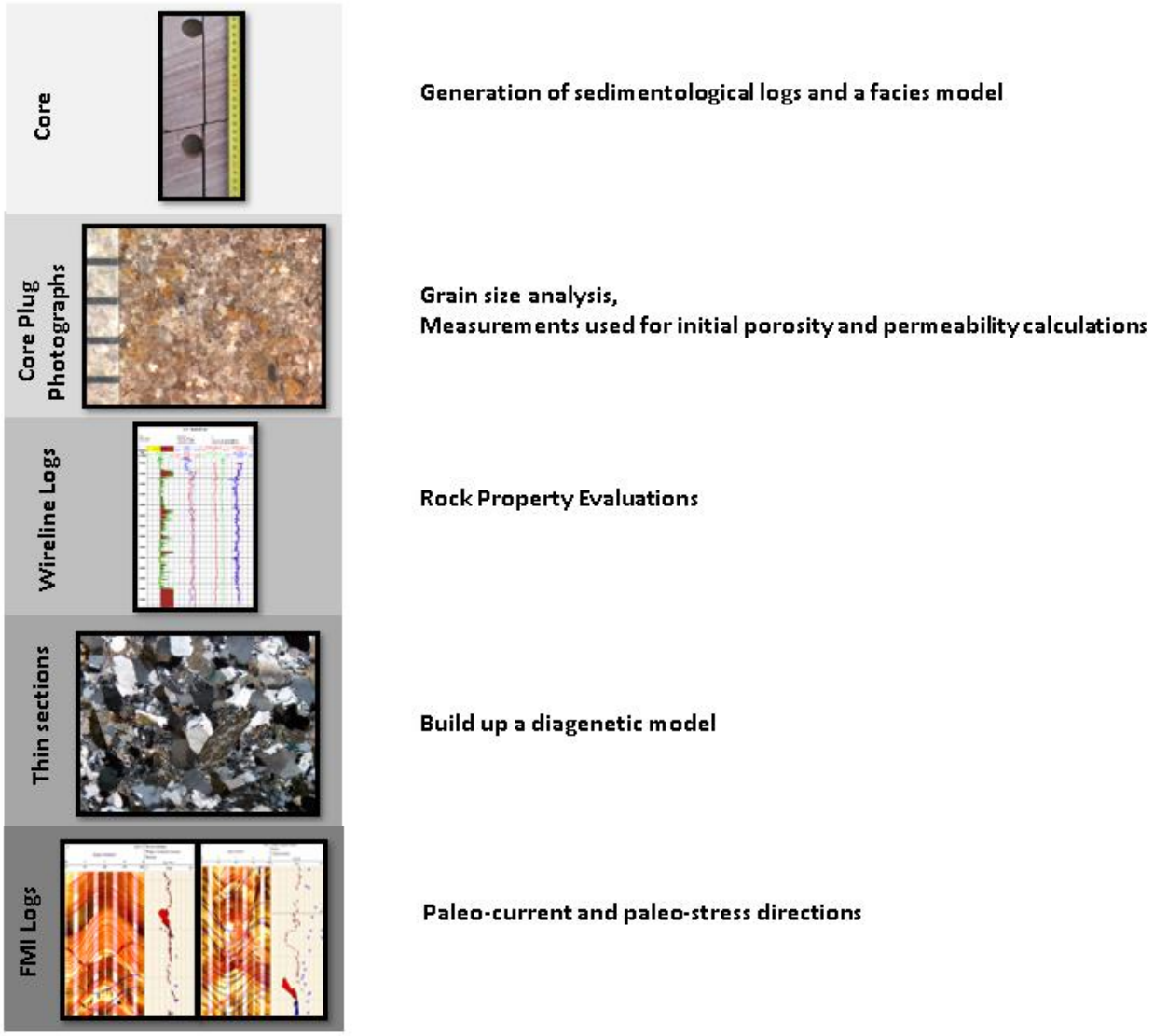

Figure 9: Summary of data analysis and interpretation.

4. Methodology:

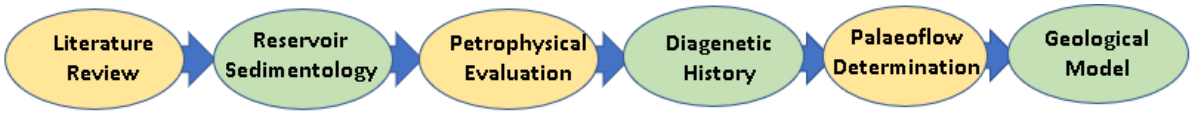

Figure 10: Overview of the workflow followed in this study.

The proposed workflow for this project consisted of the following steps:

i. **Literature Review**: The archived publications suitable for application in the research area were studied. It was a key step as it formed the basis for building up a regional stratigraphic and structural understanding of the study area. The important findings and empirical relations stated by numerous authors were sometimes effectively applied in case of similarities occurring between the two aspects that are being compared. It thus helped in building up a correlation.

ii. **Reservoir Sedimentology:** Core description for both the wells was performed. The generated sedimentological logs depicted various lithofacies which were correlated with the rock properties obtained from the petrophysical logs. The photographs of the trimmed-ends of the core plug samples were used to analyse the grain-size distribution. Mean grain-diameter, sorting and skewness values obtained from this analysis helped in estimating the transport energy and the distance of transport. Initial porosity and permeability at the time of deposition was then obtained by applying empirical relations and the porosity loss was calculated. This porosity loss was better explained by coupling it with the diagenetic and burial history of the Naaldwijk field.

iii. **Petrophysical Evaluation**: Gamma-ray, neutron porosity, density, and sonic logs were used to find out the reservoir thickness, porosity, permeability and water saturation. Several mineralogical cross plots were generated for the identification of lithologies.

iv. **Palaeoflow Direction Determination:** The borehole images played a crucial role in reservoir characterisation. The individual pad images were stitched together to form a continuous borehole image log along the depth interval of 4129.43- 4393.29m MD. A thorough manual dip picking was performed in order to obtain accurate orientations and robust statistical data for further analysis. A total of 1217 dips were interpreted on the FMI image along the interval 4250-4280m MD (30m) and assigned to 3 dip sets namely the cross-beds, conductive fractures and major conductive fractures. Dip trace performed on these features helped in defining the orientation of the cross-beds and fractures,

thereby indicating a dominant paleo-flow direction for the cross-beds and the paleo-stress directions for the fractures.

v. **Diagenetic Model**: A detailed thin-section analysis was conducted on the three samples obtained from NLW-GT-01, namely HS1, HS2, and HS11 from the lower parts of Detfurth Formation and the upper parts of the Volpriehausen Formation. The thin-sections were analysed under a microscope and photographed in 4X and 10X magnifications. The diagenetic events were arranged in ascending order of occurrence and correlated with the loss in porosity after every event.

vi. **Reservoir Architectural Model:** The integration of all the previously obtained results led to the generation of a reservoir architectural model. This model is based on depositional settings, paleo-climate, and paleo-flow direction.

5. Results

5.1. Core Analysis

A core not only provides a complete stratigraphic section of the subsurface that can be viewed and described in great detail but also helps in correlating the petrophysical log responses with the facies present in the core.

A core description study for both the wells NDW-01 and NLW-GT-01 was carried out at the Central Core Sample Storage of TNO in Zeist. These cores were described on sedimentary log sheets at a scale of 1:50 by graphic drawings. They were also photographed for later use. The core study aimed at identifying the lithofacies, which could be further correlated with the petrophysical log responses and other measured reservoir properties.

The following cored intervals have been analysed:

Table 2: Overview of the cored stratigraphic intervals.

Core	Top	Bottom	Total Thickness	Stratigraphic Interval
	(m) MD	(m) MD	(m)	
NDW-01	2368.50	2377.37	10.02	Nederweert Sandstone Member
NLW-GT-01	4250.00	4279.70	29.70	Detfurth - Upper Volpriehausen Sandstone Member

5.1.1. Core Description

NDW-01

The cored sandstones are pinkish-red. The colour fades to whitish pink in cemented areas. The grain-size ranges from very fine to medium-grained. The sandstones are characterized as moderately sorted, although in well-laminated samples sorting within individual lamina is better. The core depicts a more constant depositional environment with stacked cross-sets of approximately 50cm in height. The net-to-gross ratio is about 0.95.

Unlike NLW-GT-01, NDW-01 is a vertical well, and hence the well deviation was not considered while measuring the dip angles of the beds on the core. The bed orientation depends on the direction in which the core was cut. The cylindrical quarters of the core helped in the differentiation of horizontal beds from inclined ones through 3D visualization of the beds.

Box 1 Top: 2368.50m Bottom: 2369.43m

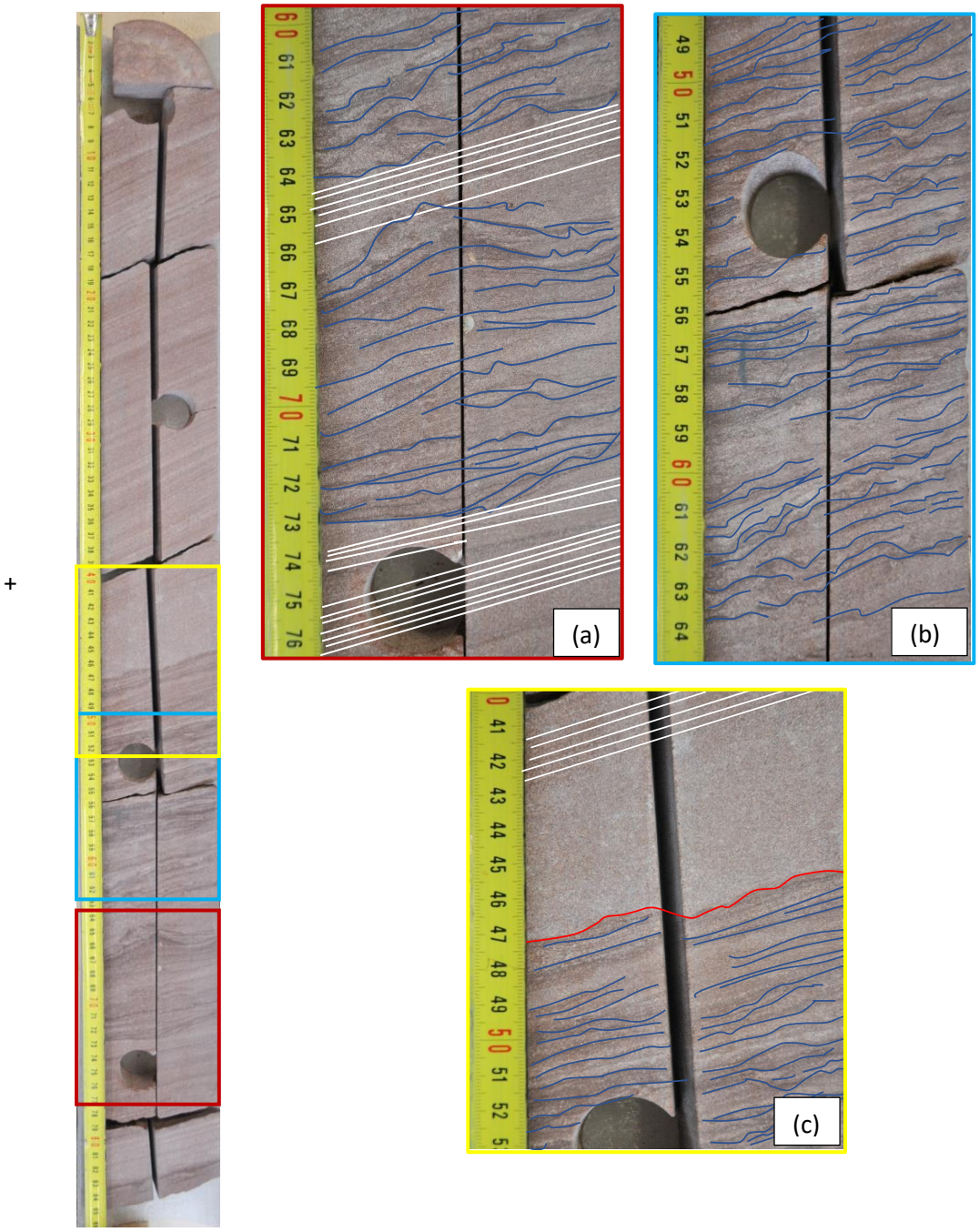

Figure 11: (a) Wavy and deformed laminations(blue)on the foreset. (b) Dark deformed bottomset laminations. (c)Bed Boundary(red) between the dark mineral enriched bottomsets and cleaner sand-rich steeper foresets.

The cored section in Fig. 11 comprises of cross-stratified, fine to medium-grained sandstone. Cross laminations show an upward increase in the dip angle (10° to 25°) which in terms of sedimentary features indicates a transition from low-angle bottomsets to high-angle foresets. The bottomsets comprise of wavy and deformed laminations accentuated by dark minerals which might be clay or heavy mineral deposits (see Fig. 11).

Box 3 Top: 2370.21m Bottom: 2371.37m

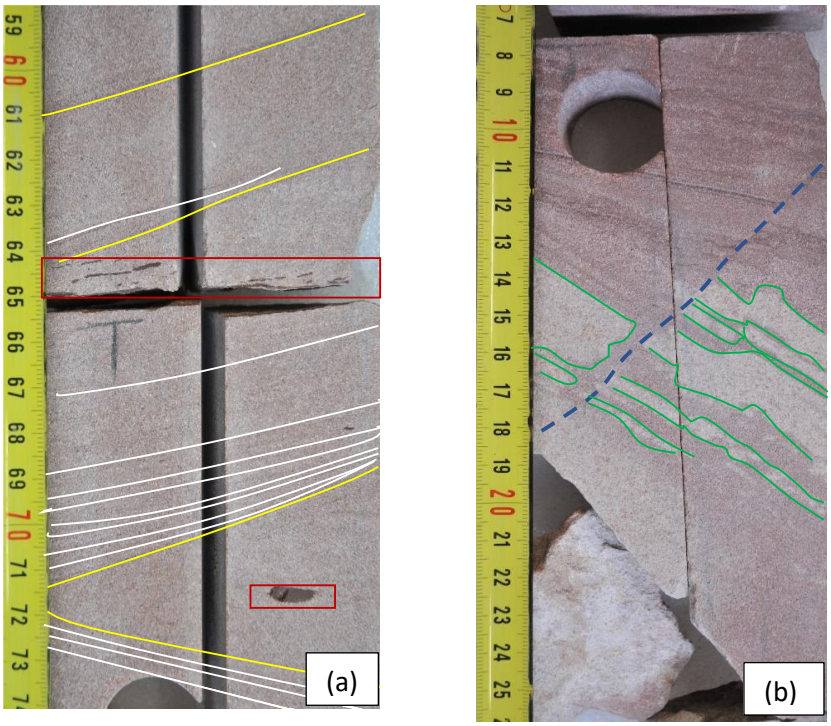

Figure 12: (a)Flattened clay flakes (red box) and set boundary (yellow) (b) A fracture with displacement of cemented(green) beds.

Box 4 Top: 2371.37m Bottom: 2372.27m Box 5 Top: 2372.27m Bottom: 2373.15m

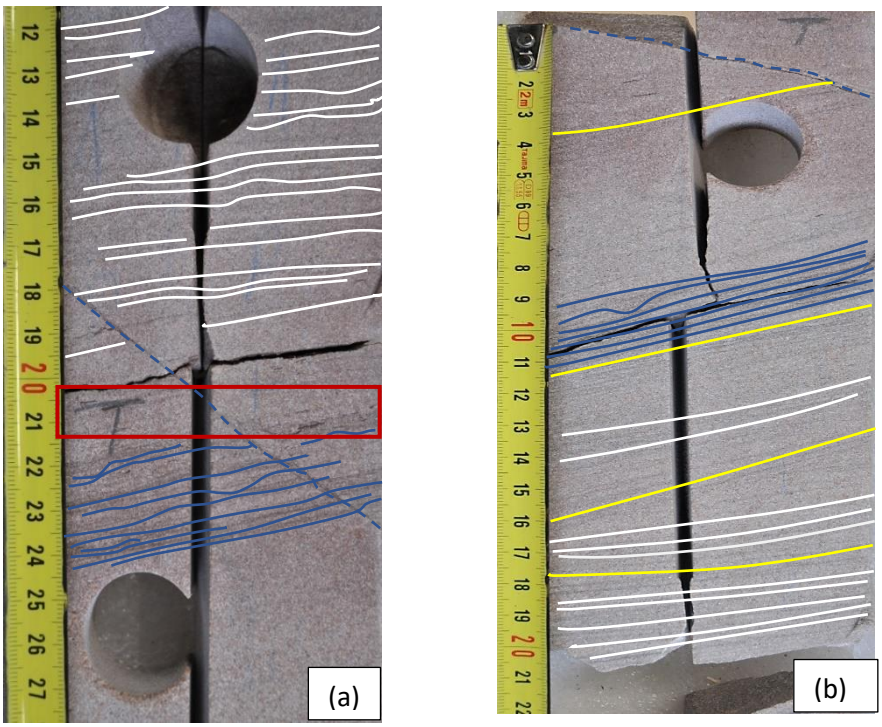

Figure 13: (a) A fracture (dashed blue) cross cutting the dark laminae (solid blue), (b) colour variation of the sand deposits and set boundaries (yellow).

Reddish-brown flattened clay clasts are aligned on the foresets. The opposite dipping truncation surfaces imply the presence of trough cross-bedding (see Fig. 12a).

In Fig. 12(b), the whitish cemented beds are displaced by a fracture cutting across the foresets. Fractures can also be seen in Fig. 13(a, b).

The light-coloured interval seen in Fig. 13(b) is due to the precipitation of patchy cement while the reddish colour of the sandstone is probably due to oxidation.

Box 5 Top: 2372.27m Bottom: 2373.15m **Box 8 Top: 2374.85m Bottom: 2375.65m**

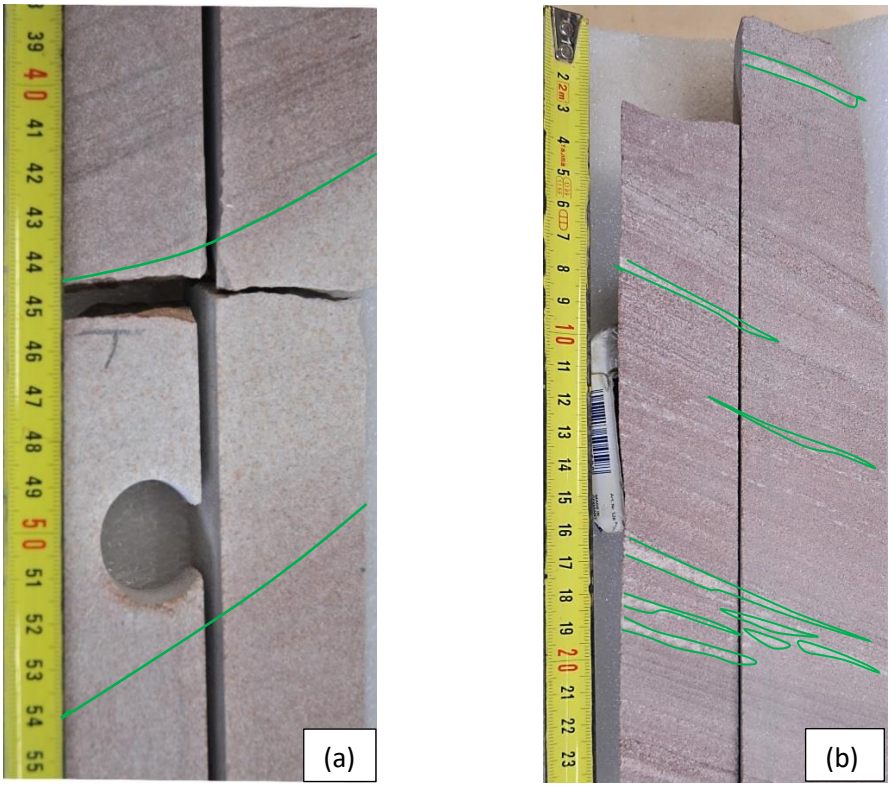

Figure 14: Types of cement deposition in the core: (a) Patchy-cement deposits (green); (b) Precipitation of cement(green)along the foresets.

In Fig. 14(a) the white precipitate can be seen cementing the medium-grained sands (coarser than the oxidized sands). Minor patchy white leached areas (cement) that approximately conform to the cross- laminations can be seen in Fig. 14(b).

The cementation in Fig. 14(a) may have occurred because the medium-grained sands being more porous allowed the cement-rich waters to percolate in easily. After precipitation, these cements blocked the pore spaces and reduced the rock porosity. Coarser sediments thus became more lithified. The porosity may have also reduced to values less than those seen in the finer-grained red sands.

NLW-GT-01

The NLW-GT-01 core is not slabbed yet, and hence the entire core cylinder was laid down for analysis. The first five metres from the top belong to the Detfurth Formation (4250-4255m), and the rest (4255-4279.7m) consist of the Upper Volpriehausen Sandstone Member.

The grain-size ranges from very fine to medium-grained sandstones with an occasional increase to coarse-grained sands at specific intervals. A preferential vertical succession of lithofacies is not apparent. The colour of the sandstone ranges from prominently grey to buff. The net-to-gross ratio is about 0.8. The entire core length is mostly cross-bedded with four visually distinct fractures occurring at the depths of 4258.30m,4259.28m,4273.70m, and 4273.75m. These fractures dip in the opposite direction to the cross-beds. However, much cannot be said about the dip direction of these sedimentary and structural features yet as there was no indication of proper directional orientation of the core when it was described.

Box 25 Top: 4272.90m Bottom: 4273.90m

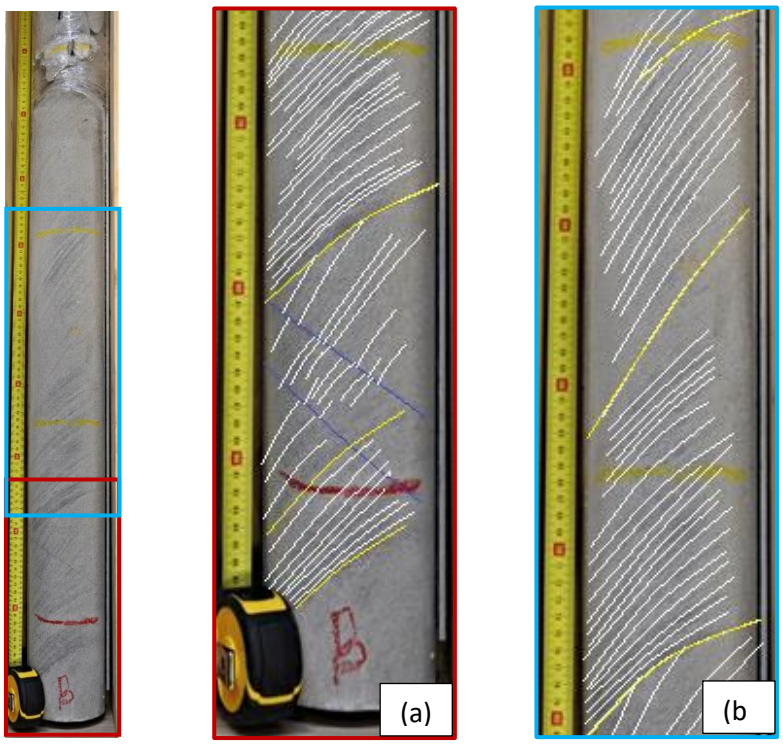

Figure 15: (a) Two fractures at the bottom with the displacement of less than 1cm. and (b) trough cross-beds accentuated by the deposition of heavy minerals/clay with clearly defined set boundaries White: Foreset; Yellow: Set Boundary; Blue: Fracture

Box 24 Top: 4271.80m Bottom: 4272.50m

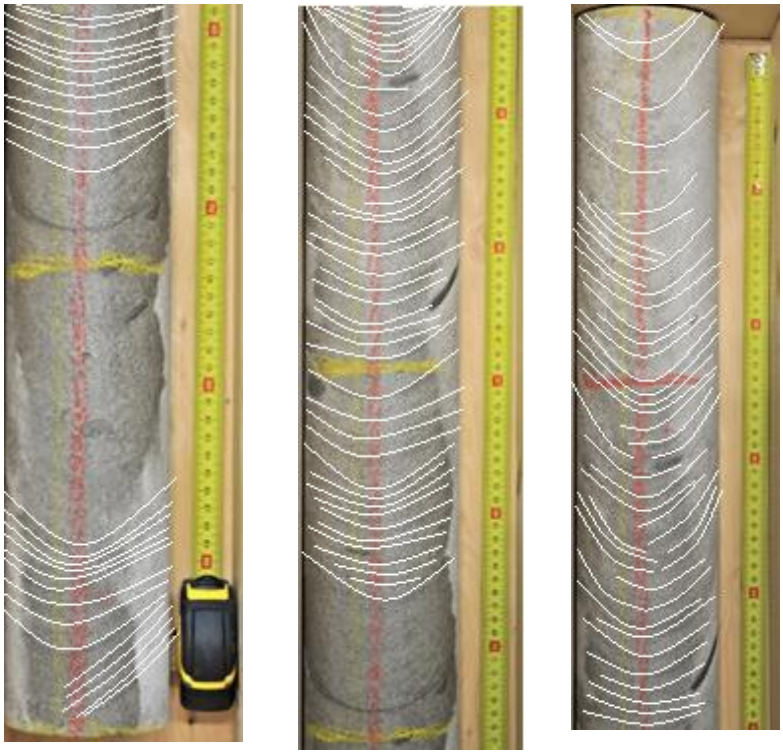

Figure 16: Cross-beds without a distinct set boundary.

The cross beddings, as seen in Fig. 15 and 16 above are well-preserved. The set height ranges from 5cm to about 20cm with well-defined foresets. An apparent upward increase in the dip angle of the foresets from 10° to 20° and then a gradual decrease towards the top is observed in Fig. 15. Two fractures occur at the bottom of the core. In Fig. 15(a) one of the fractures occurs at a depth of 4273.75m with a displacement of about 0.80cm while the other fracture at 4273.70m shows a smaller displacement of 0.25cm.

The dip angle variations in Fig. 16, although not very distinct, appear to decrease towards the top of the core. The elongated clay pebbles in Fig. 16 are aligned along the beds, demonstrating a phase of extension after deposition. Bed boundaries are not visible. This can be explained by the abundance of cross-beds throughout the core.

The changes in the dip angles reflect that the trough cross-stratification were deposited in the form of sigmoidal cross-beds comprising of a tangential base and an upward increase in the dip angle that gradually flattens out at the top.

Box 22 Top: 4269.80m Bottom: 4270.80m

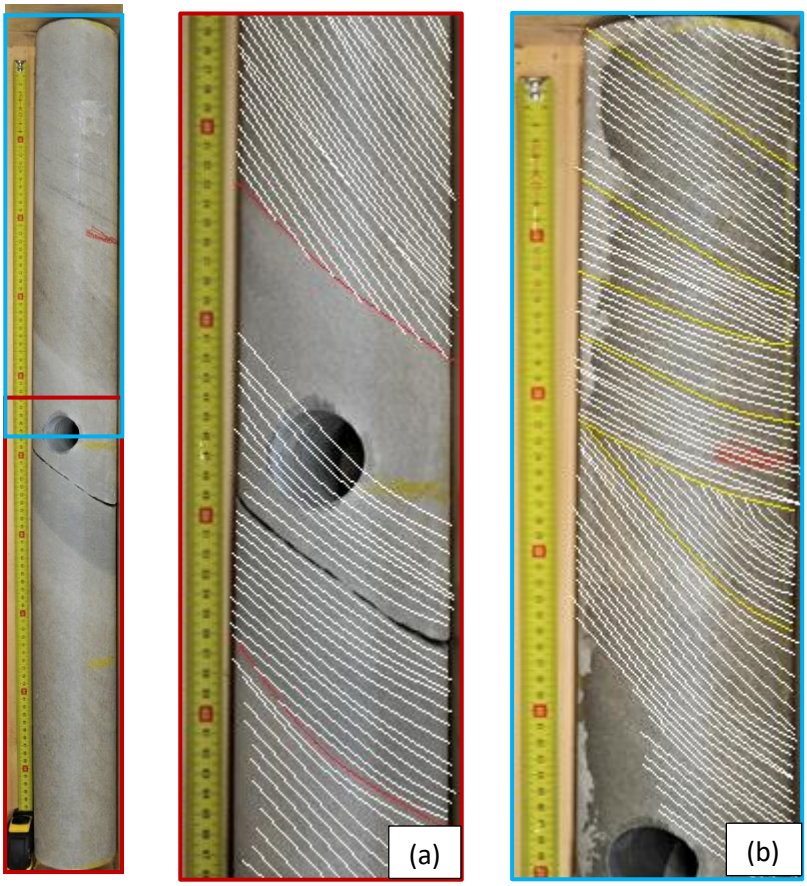

Figure 17: Red: Set boundaries marked by a change in the colour of the sediment deposited; Yellow: Set boundaries marked by a change in the dip angle of the foresets.

The set boundaries are distinguished by a change in the colour of the beds from light grey to darker grey (see Fig.17). The dip angles range from about 2° at the bottom/top of the set to about 25° on the steeply dipping foresets when the well deviation (39°) is taken into account.

Box 12 Top: 4260.60m Bottom:4261.60m

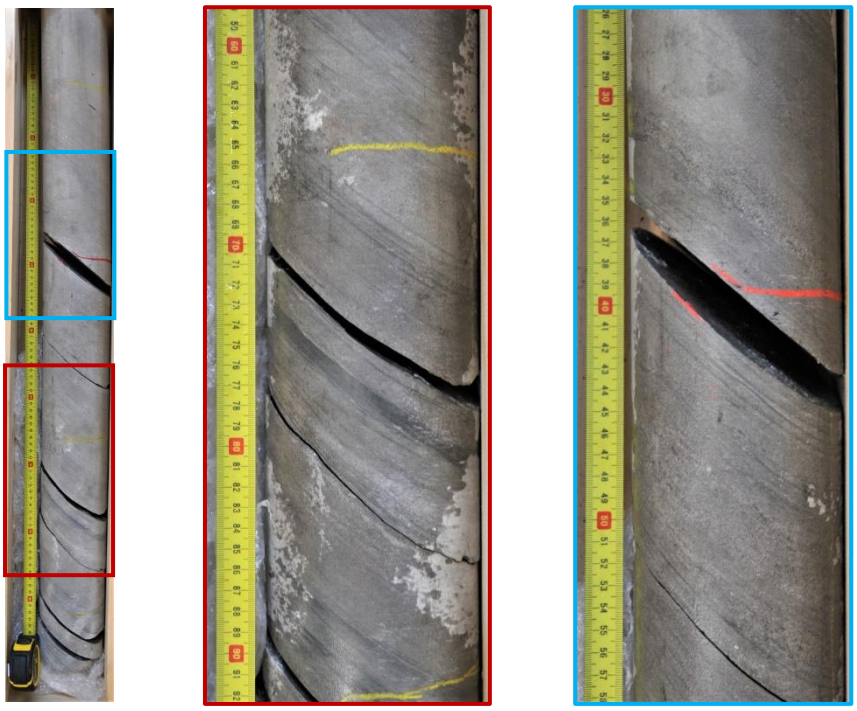

Figure 18: Alternation of thin(cm-scale) fine sands and silt. (alteration of light grey and dark grey).

Box 10 Top: 4258.50m Bottom: 4259.50m

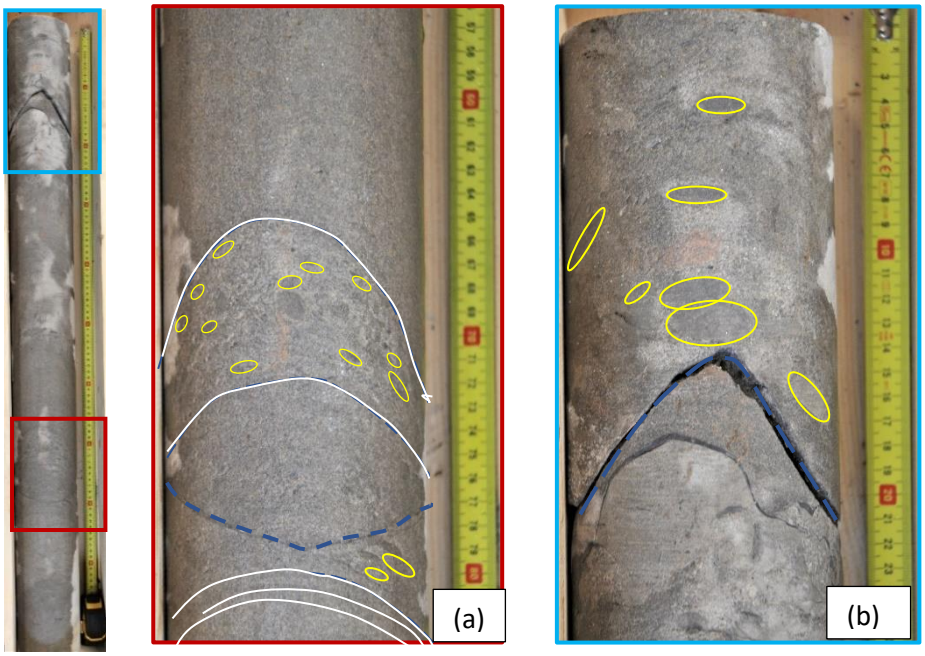

Figure 19: Fractures(blue) seen dipping 180 degrees opposite to the dip of the cross-beds. Flattened pebbles(yellow).

An alternation of fine-sandstone-siltstone-claystone layers can be seen in Fig. 18. There is a probability of the occurrence of coal in this interval; however, as the core is not slabbed yet, it is not possible to state the presence of coal with utmost certainty.

Sandstone pebbles with a diameter <3cm are embedded in a finer-grained matrix can be seen at a depth of about 30cm from the bottom in Fig. 19(a).

5.1.2. Description of Lithofacies

In this section, the lithofacies association of wells NDW-01 and NLW-GT-01 are defined and subsequently interpreted in terms of depositional processes. The lithofacies encountered in the studied cores are briefly described below:

Lithofacies SMs and SMn (Well-Stratified Muddy Sandstone)

Lithofacies SMs are defined by sub-horizontally bedded and typically heterolithic alternation of very fine-grained sandstone, siltstone and/or claystone. Lithofacies SMs occurs in the NLW-GT-01 core. Lithofacies SMn consists of homogenised siltstone and occurs in both the cores but is less common.

Lithofacies SWf/m (Wavy Stratified Fine to Medium-grained Sandstone)

Lithofacies Group SW is defined as wavy and irregularly stratified sandstone with less than 30% clay admixed or interbedded as mm-scale laminae/drapes. Stratification may have been deformed by fluidization. Lithofacies group SW is predominantly fine-grained. However, it is sometimes characterized in the NDW-01 core by an alternation of fine-grained and medium-grained laminae.

Lithofacies SNf (Non-Stratified Fine-grained sandstone)

Lithofacies SNf consists of homogenised very fine to fine-grained sandstone with less than 20% clay. This facies occurs as small intervals (cm- rarely dm) in both NDW-01 and NLW-GT-01 well.

Lithofacies SSf/m (Well Stratified Fine to Medium Grained Sandstone)

Lithofacies SSf consists of very fine to fine-grained sandstone while SSm consists of medium-grained sandstone with less than 20% clay. Stratification types include horizontal or sub-horizontal stratification on a mm to cm-scale, low-angle cross-stratification and high-angle cross-stratification on a cm or dm scale. Mm/cm-sized flakes may even occur in both the horizontally and trough cross-bedded units.

Lithofacies SXf/m (Cross-bedded Fine to Medium Grained Sandstone)

Lithofacies SXf predominantly consists of trough cross-bedded very fine to fine-grained sandstone while SXm consists of medium-grained sandstone with less than 20% clay-sized

fraction. Dm-scale cross-stratification with festoon-shaped sets. Clay flakes occur both at the set boundaries and upon foresets.

Lithofacies PS (Pebbly Sandstone)

Lithofacies PS is defined as a sandstone with a significant pebble content; pebbles are matrix-supported. Pebbles in well NLW-GT-01 comprise mm/cm-sized intraclasts. These are mainly composed of silt and clay. Sandstone matrix is very fine or fine-grained. Bedding is generally not apparent.

5.1.3. Description of Lithofacies Association

Lithofacies tend to be organised into relatively well-defined larger units termed as lithofacies associations. Lithofacies association can then be correlated to the probable depositional environments. Within the investigated cored intervals of wells NDW-01 and NLW-GT-01, two dominant association sequences can be distinguished, which are as follows:

Mudstone Dominated Sequences:

Lithofacies Association Ms

Lithofacies Association Ms consists of mm to cm-scale, horizontally to sub-horizontally bedded claystone or siltstone and very fine-grained sandstone, alternating with minor dm-scale, fine-grained parallel bedded sandstone. Thin argillaceous bands are locally present. Generally, a preferential vertical succession of lithofacies is not apparent. This lithofacies association is observed only in the cored section of the well NLW-GT-01.

SMs and SMn are the dominant lithofacies with SNf, SSf/m, SXf present in minor amounts.

Interpretation: The depositional environment could be that of a desert lake but near a clastic source such as an alluvial fan.

Sandstone Dominated Sequences:

Three sandstone dominated lithofacies assemblages have been distinguished: S1, S2, and S3.

Lithofacies Association S1 Description

Lithofacies Association S1 is dominated by wavy or sub-horizontally laminated very fine to medium-grained sandstones. These sandstones locally incorporate claystone clasts alternating with homogeneous fine-grained sandstones. Minor fine-grained moderately high-angle cross-stratified sandstones are also interbedded. This association occurs in both the wells.

The main Lithofacies include SSf, SW, SNf with a minor amount of SXf and PS.

Interpretation: Sedimentary structures (cross-bedding, rip-up clasts) indicate deposition by flowing water rather than the wind. The combination of rip-up clasts and horizontal/low-angle bedding suggests that upper flow regime conditions prevailed. Sand transport took place in unconfined sheetfloods rather than channelized streams. High angle cross-bedding probably formed during the waning stages of floods.

Lithofacies Association S2 Description

Lithofacies Association S2 is characterized by the presence of cross-bedded very fine to medium-grained sand. Irregular truncation surfaces suggest the presence of trough-cross bedding. Generally, the set heights are about 10-25cm but may occasionally exceed 0.5m. Clay flakes are sometimes concentrated on foresets.

SXf, SSf are the dominant lithofacies while SWf, PS and SNf are present in a smaller proportion.

Interpretation: The occurrence of cross-bedding and intraclasts indicates deposition by flowing water. As opposed to S1, the flow was probably confined to channels. The lack of grain-size trends and the scale of cross-bed sets (cm-dm) suggest that these channels were shallow and braided. Under semi-arid conditions which prevailed during the deposition of the studied deposits, runoff is episodical. This implies that the fluvial channels are wadis instead of permanent rivers.

Lithofacies Association S3 Description

Lithofacies Association S3 contains cm to dm-scale matrix to clast supported intraformational conglomerate beds. Intraclasts generally consist of claystone and siltstones. This facies association is only present in well NLW-GT-01.

PS and SSf are the main lithofacies while SNf occurs in smaller amounts.

Interpretation: The presence of intraclasts lags may have been caused by rapid lateral shifting of the braided channels and incorporation of fine-grained off-channel sediments. The individual cycles within this association display an erosional base followed by conglomeratic basal part and an upper sandy part showing sedimentary structures.

Legend:

<table>
<tr><td></td><td>Ms</td><td>Desert Lake</td></tr>
<tr><td></td><td>S1</td><td rowspan="3">Stacked low sinuous river and sheetflood deposits.</td></tr>
<tr><td></td><td>S2</td></tr>
<tr><td></td><td>S3</td></tr>
</table>

NDW-01

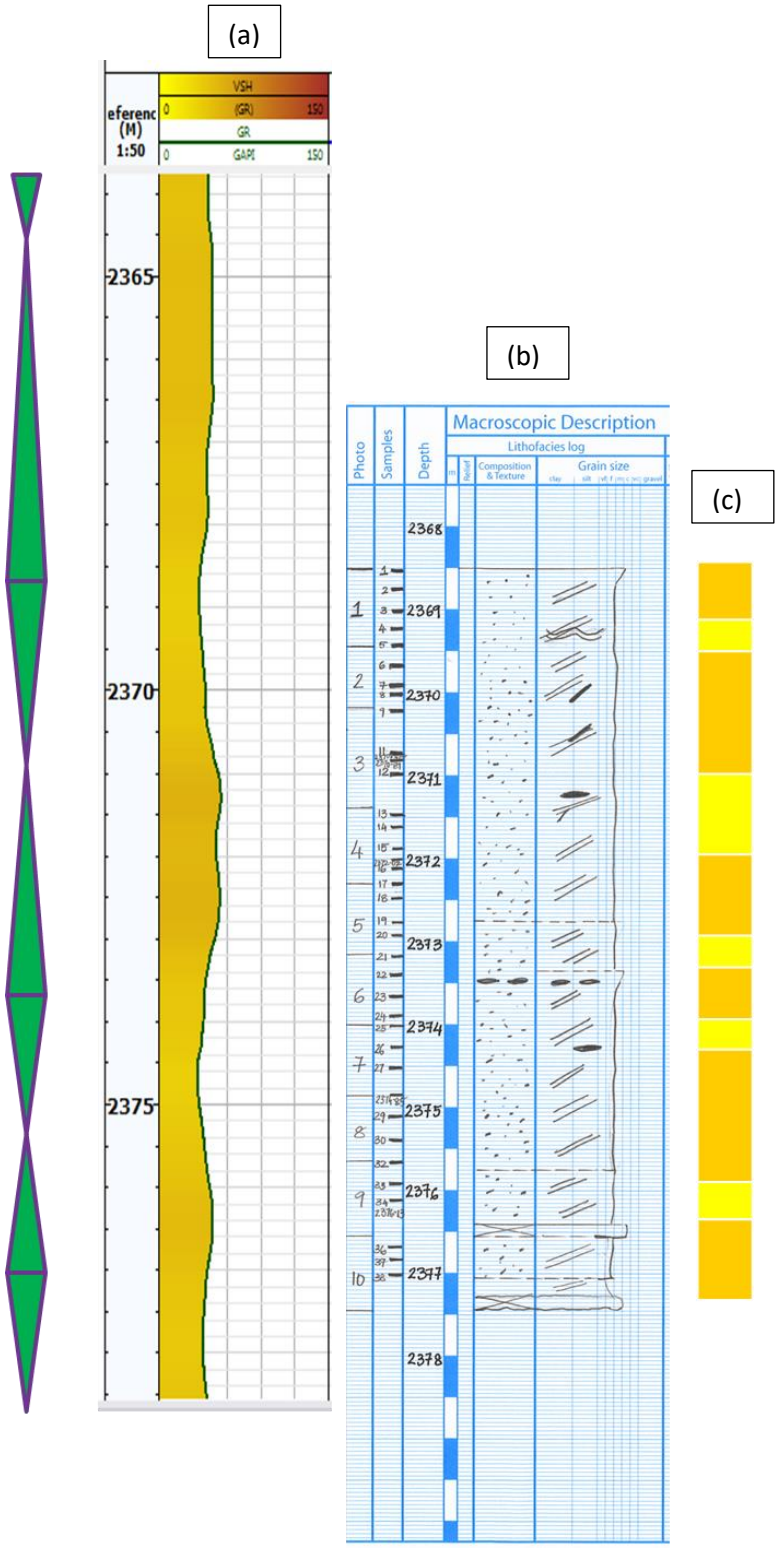

Figure 20: Core analysis of NDW-01. (a) Gamma-ray response (b) Sedimentological Log (c) Interpreted Lithofacies. The green triangles reflect the A/S ratio where the upward pointing triangle represents a higher A/S ratio and vice versa.

NLW-GT-01

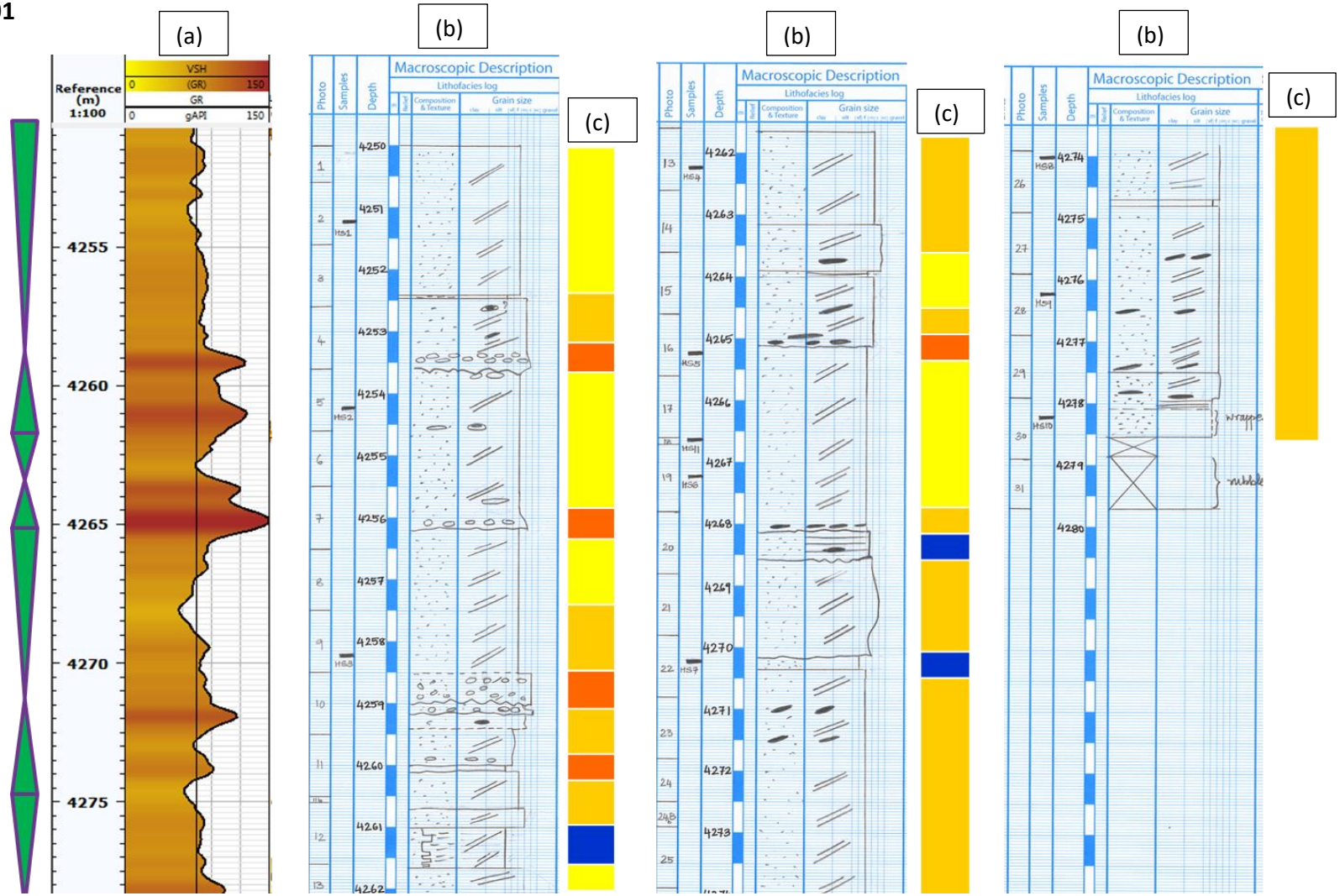

Figure 21: Core analysis of NLW-GT-01. (a) Gamma-ray response (b) Sedimentological Log (c) Interpreted Lithofacies. The green triangles reflect the A/S ratio where the upward pointing triangle represents a higher A/S ratio and vice versa.

A downward-pointing triangle represents a low A/S ratio characterized by sand-rich facies while a high A/S ratio reflected by the higher gamma-ray response of shale-rich facies is represented by an upward-pointing arrow.

In NDW-01 core, sedimentary structures related to mid-channel/ bank attached bars are also absent. Floodplain deposits are also missing. The lack of argillaceous beds indicates that deposition took place in a subaerial setting (see Fig.20). The occurrence of wavy laminae with the thinly bedded nature of the bottomsets suggests that the paleo-water table was at times, close to the sediment surface. The presence of cross-bedding indicates deposition by flowing water in confined channels. The depositional setting could be that of a shallow ephemeral fluvial system.

In the NLW-GT-01 core, the multi-storey sand-bodies are considered to reflect repeated channel cutting often marked by a basal channel conglomerate followed by the in-channel migration of sandy channel bedforms. High-angle cross-bedded units are interpreted to be deposited by channelled streams, while horizontally/ sub-horizontally bedded units may have been deposited by more unconfined flows, such as sheetfloods. Lithofacies association S1 and S2 with Ms (see Fig. 21) indicates periods of sand deposition were alternating with periods of restricted sand influx, during which the lacustrine conditions prevailed. Distinctly cross-stratified sandstones containing claystones are ascribed to deposition from moderate to high-energy fluvial currents in ephemeral channels. These are braided as suggested by the random vertical arrangement of lithofacies.

5.2. Petrophysics

The main aim of the petrophysical evaluation was to determine the lithologies, thicknesses of the stratigraphic intervals, porosity, permeability and water saturation. In order to ensure the reliability of the log readings, the porosity and permeability readings need to be compared with the laboratory measurements of the core plugs.

NDW-01

The Nederweert Sandstone Member is a thick package (292m) of sandstone present in the well NDW-01, (see Fig. 22). Since it is one of the ancient wells to be drilled, only gamma-ray, sonic and neutron logs are available.

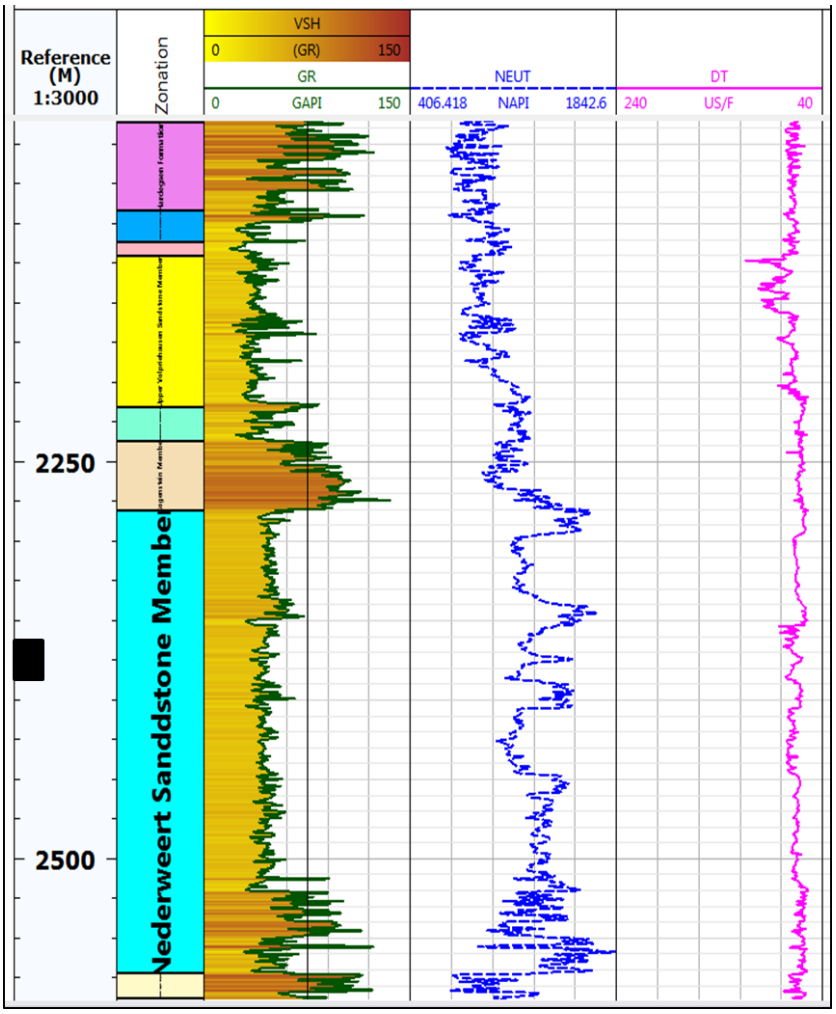

Figure 22: Petrophysical logs of NDW-01. The black box indicates the cored interval.

The base of the Nederweert Sandstone Member consists of claystone beds that can be identified by high gamma-ray readings. The rest of the sandstone appears to be clean with a consistent sonic measurement.

NLW-GT-01

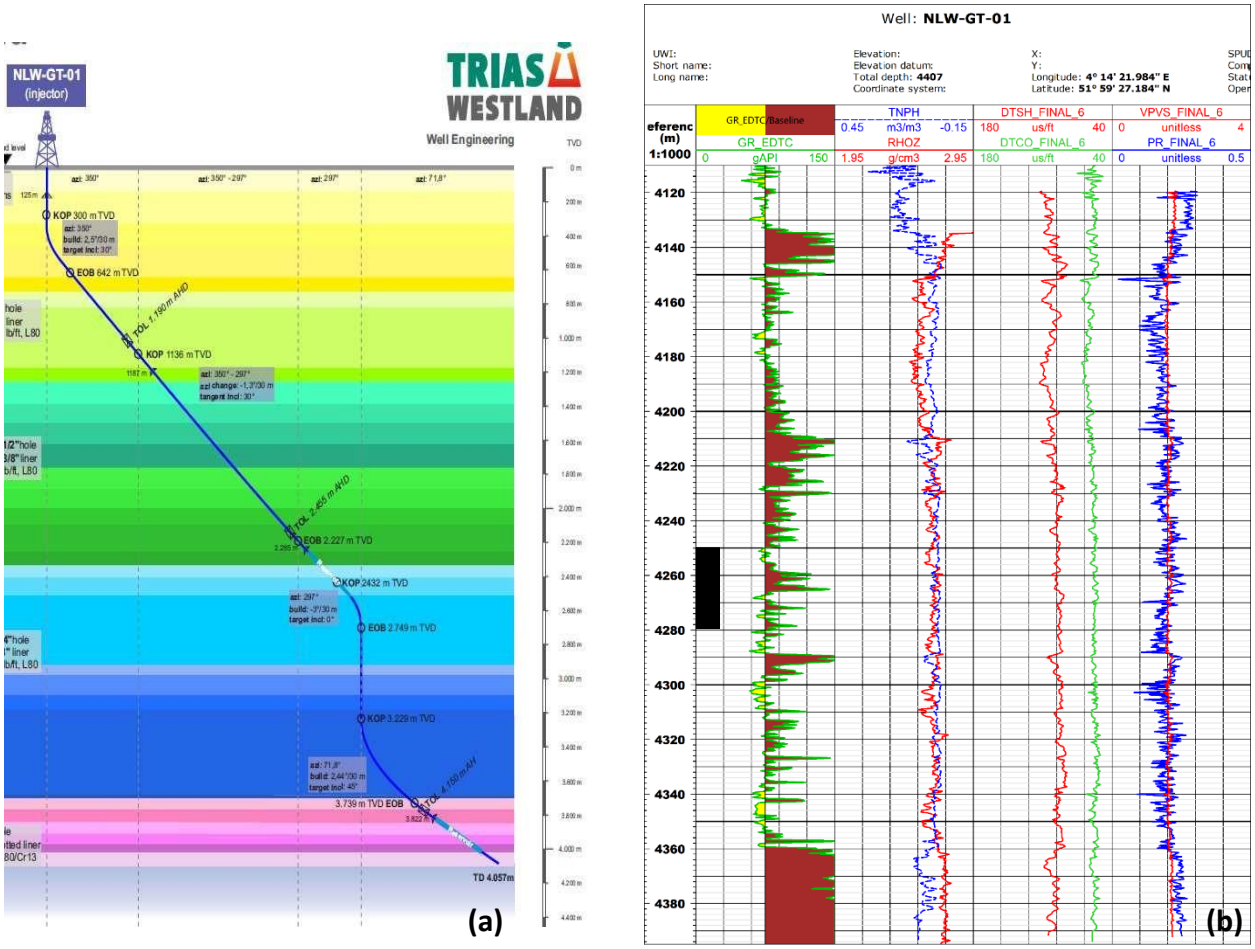

Figure 23 :(a) Well path of NLW-GT-01 (Trias Westland, 2018) (b) Wireline logs. The black box indicates the cored interval.

The drill-path of NLW-GT-01 is depicted in Fig 23(a). The reservoir (yellow) and non-reservoir(brown) units are differentiated by setting the V_{sh} cut-off to 50%, see Fig. 23(b).

Several reservoir parameters were calculated using Techlog and Excel.

5.2.1. Lithology classification

Due to the availability of several petrophysical logs such as neutron (NPHI), bulk density (RHOZ), sonic (VPVS) and photoelectric (PEFZ), cross plots were generated. Cross plots help in the classification of the lithologies by plotting petrophysical parameters against each other.

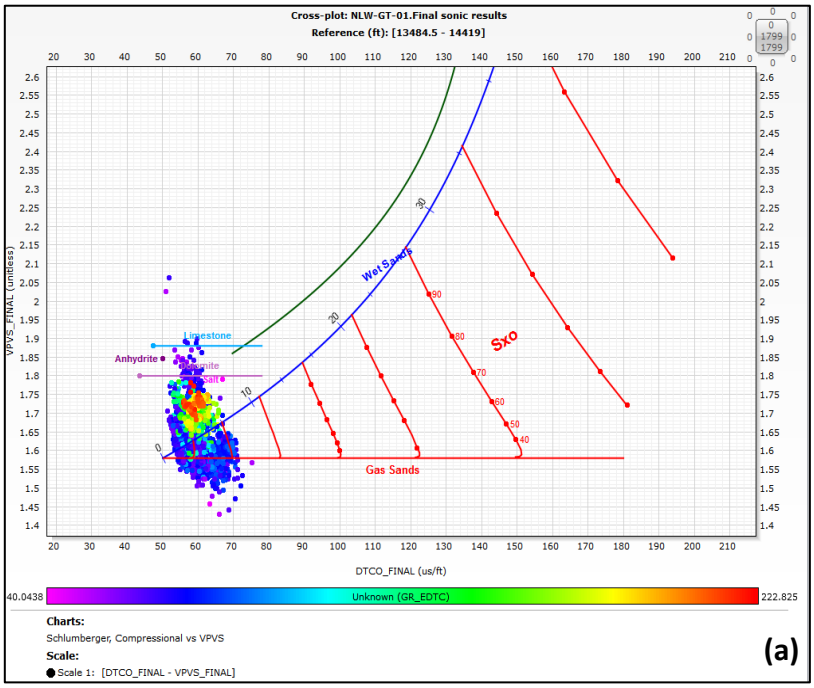
Cross-plot: NLW-GT-01.Final sonic results
Reference (ft): [13484.5 - 14419]
VPVS_FINAL (unitless)
DTCO_FINAL (us/ft)
Wet Sands
Sxo
Gas Sands
Limestone
Anhydrite
Dolomite
Salt
Unknown (GR_EDTC)
40.0438
222.825
Charts:
Schlumberger, Compressional vs VPVS
Scale:
Scale 1: [DTCO_FINAL - VPVS_FINAL]
(a)

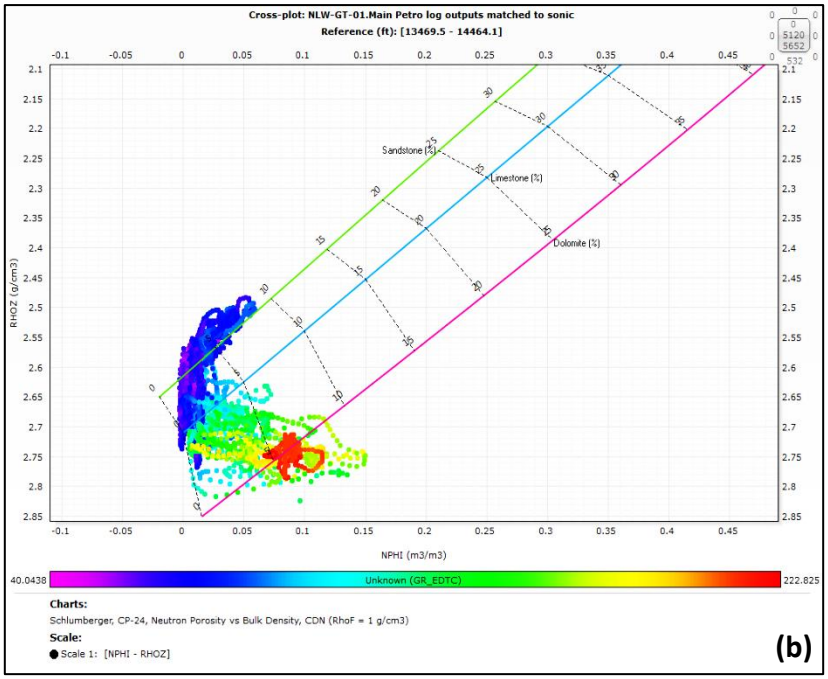
Cross-plot: NLW-GT-01.Main Petro log outputs matched to sonic
Reference (ft): [13469.5 - 14464.1]
RHOZ (g/cm3)
NPHI (m3/m3)
Sandstone (%)
Limestone (%)
Dolomite (%)
Unknown (GR_EDTC)
40.0438
222.825
Charts:
Schlumberger, CP-24, Neutron Porosity vs Bulk Density, CDN (RhoF = 1 g/cm3)
Scale:
Scale 1: [NPHI - RHOZ]
(b)

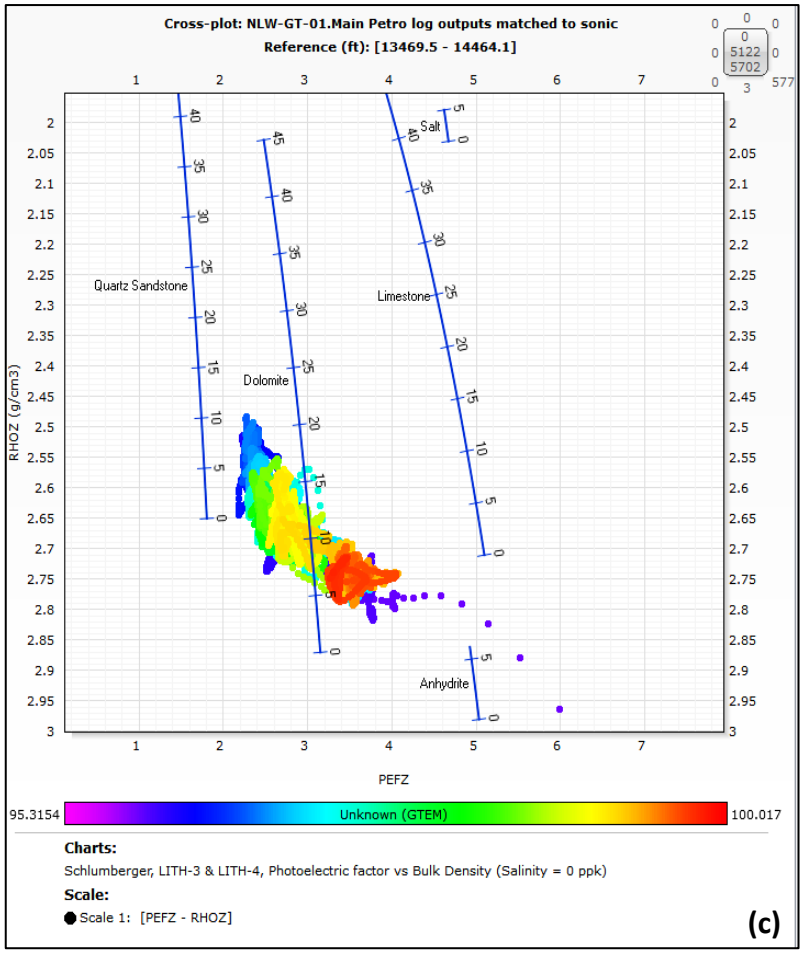

Figure 24: (a) VPVS vs DTCO (b) RHOZ v/s TNPHI (c) RHOZ v/s PEFZ.

Gas if present in the formation slows down the compressional wave, while it has no effect on the shear wave propagation. So, if the compressional wave (DTCO) becomes slower while shear wave stays constant (a lower VPVS), then this phenomenon can be interpreted as a qualitative indication of the presence of gas.

The occurrence of gas can be identified in Fig. 24(a) as sonic logs are sensitive to light fluids.

The three lines in the neutron density cross-plot represent sandstone, limestone, and dolomite lines. The distance between the plotted point and the matrix lines determines the percentage of the lithology (Kiakojury, et al., 2018). Thus, the Main Buntsandstein deposits in NLW-GT-01 comprise of sandstones, dolomites and limestones, see Fig. 24(b).

The tool used for the measurement of the photoelectric factor is sensitive to the mean atomic number of the formation (Glover, n.d.). However it is unaffected by the variations in porosity and fluid saturation. This makes it one of the most reliable lithology indicators. As seen in Fig. 24(c), the lithologies are primarily concentrated between the quartz sandstones and dolomite line.This is in agreement of the cored interval which comprises of sandstones cemented by dolomite.

A good correlation can be established between the cross-plots obtained by plotting VPVS against sonic, density against neutron and density against the photo-electric factor.

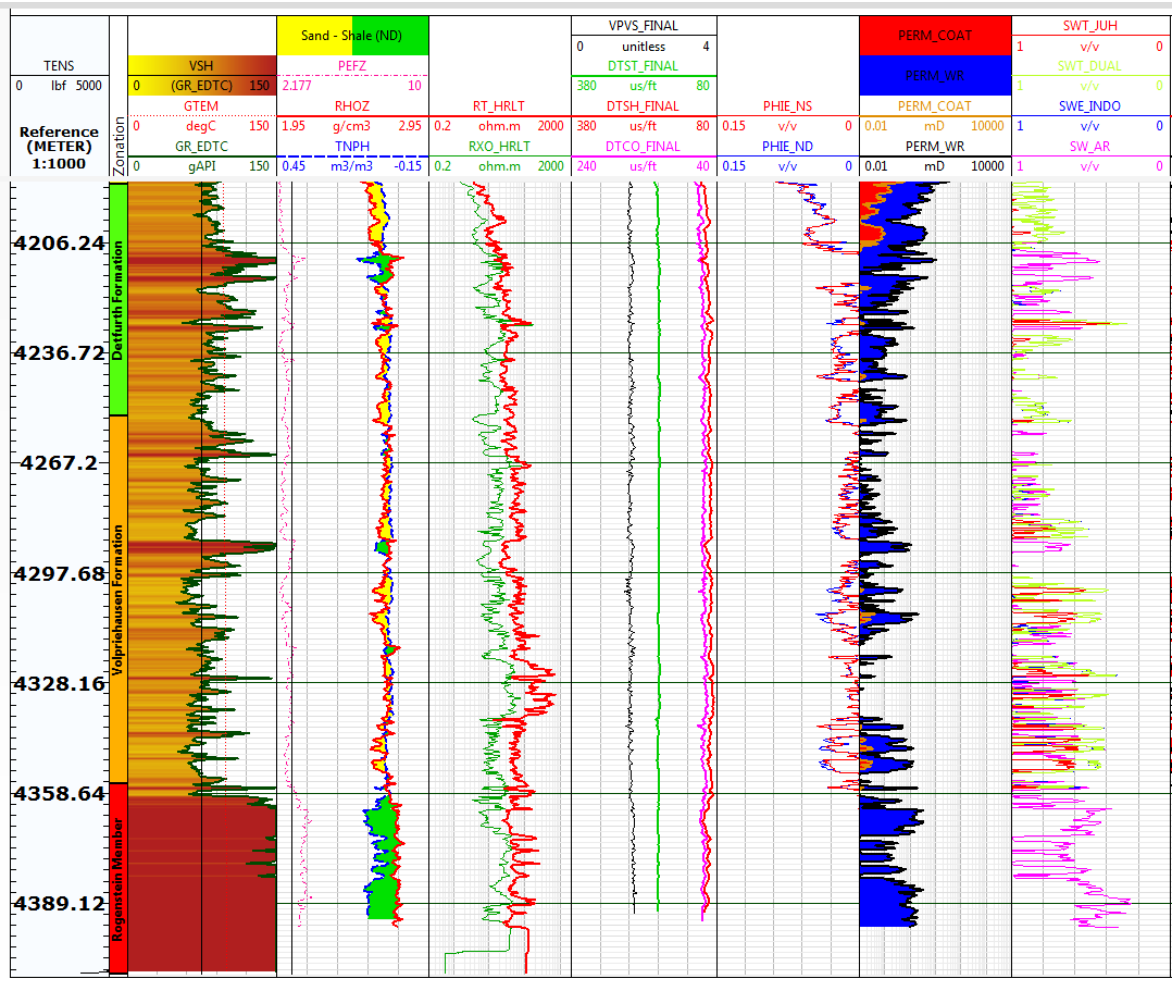

Figure 25: Petrophysical Logs for NLW-GT-01.

The cross-over between neutron and density logs also indicates gas infill (see Fig. 25). Gas occurs between the intervals of 4150-4210m.

The resistivity logs were measured in two different penetration depths, shallow (RXO_HRLT) and deep resistivity (RT_HRLT). The difference in the readings between the two resistivity logs could indicate that the mud filtrate has penetrated the formation. This could be due to the higher permeability of this portion (see Fig. 25).

5.2.2. Porosity

The porosity has been determined using the combinations of neutron-density and neutron-sonic logs. The first calculation using density and neutron logs is a reasonable estimate of the porosity for especially complex lithologies like shaly sandstones.

The porosity values obtained from both the log combinations agree with each other (see Fig. 25). Porosity ranges between 0-11.8% for the entire stratigraphical interval of the Main Buntsandstein Subgroup. The average porosity values for the Volpriehausen, Detfurth, Hardegsen Formations are 1.4%, 2.6% and 5.1% respectively.

In order to check the reliability of the porosity readings, log porosity values were plotted against those derived from the core. The comparison of these porosities can be found in Fig. 26. The correlation between them is poor. This may be due to the limited number of core plug samples used to measure porosity.

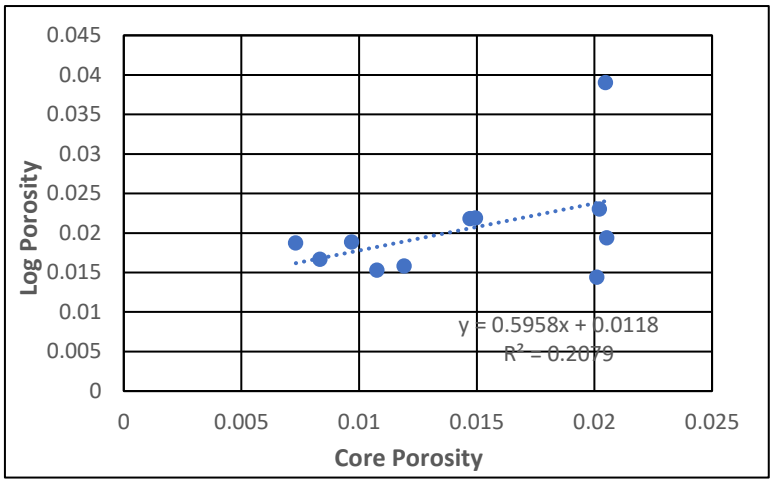

Figure 26: Core porosity plotted against log porosity.

5.2.3. Permeability

The permeability data from the cores was obtained by using air injection, which gives higher permeabilities than when the pores are filled with liquids. This effect is due to three main factors: the Klinkenberg effect, absence of confining stresses, and the dryness of the sample used for the measurements. The two methods used for log permeability estimation are Wyllie- Rose and Coates approaches. Wyllie and Rose formula makes use of porosity from the density log and empirical coefficients while Coates formula considers the values of the porosity from the neutron-density logs, total and the effective porosities along with the irreducible water saturation.

As seen in the Fig. 25, Wyllie and Rose approach overestimates the permeability values of the cored interval (0-53.67mD, average=1.95mD) while the permeabilities obtained through Coates method (0-0.9mD, average=0.04mD) are in much closer agreement with the permeabilities measured from the core plugs (0-0.02mD).

The average permeability values (Wyllie-Rose and Coates) for the Volpriehausen, Detfurth, Hardegsen Formations are 0.06mD, 0.56mD and 3.97mD respectively.

To determine the porosity permeability relation from the core data, the data is plotted in a scatter plot, and a conventional regression is made. The relationship of the Klinkenberg horizontal permeability with the helium porosity is good as indicated by Fig. 27 (Panterra,2018).

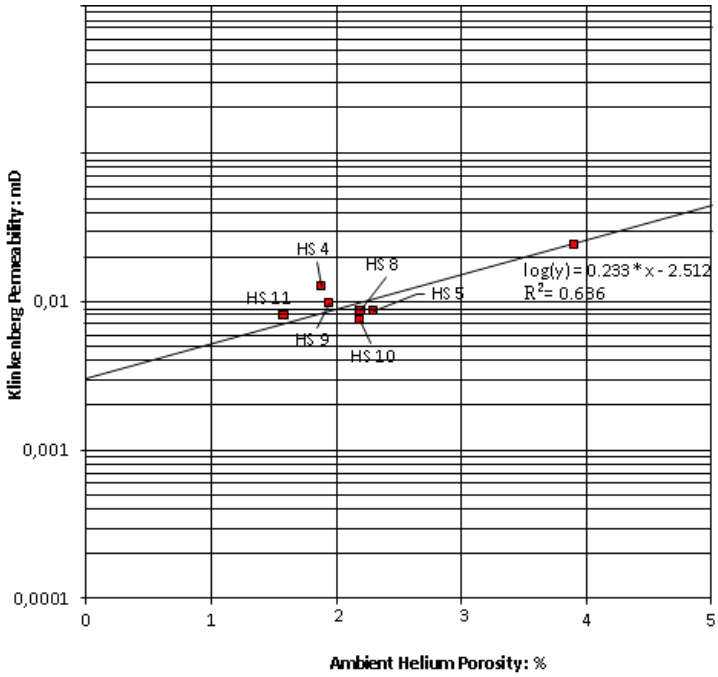

Figure 27: Klinkenberg permeability versus Helium porosity measured for the 11 core plugs (Panterra,2018).

5.2.4. Water Saturation

Several methods can be implemented to determine water saturation from log data. Most commonly used is Archie if the formation is relatively clean. For shaly formations, the most common methods are Indonesian and Waxman-Smith. Waxman-Smith approach has proved to be more accurate in predicting the water saturation in a wide range of shale conditions. It is good to mention that Archie's equation accounts for the electrical conductivity behaviours of shale-free rocks. The Waxman-Smith equation, on the other hand, accounts for the dual conductivity pathways which are formed by brine in pores and clay minerals exchanging cations in shaly sands.

5.2.5. Well-log Correlations

Stratigraphic correlations between wells help in understanding the spatial distribution and extent of sand bodies. It also helps in creation of thickness maps of sandstone units.

The wells used for establishing the correlations include the wells present in the vicinity of NLW-GT-01 and the wells in the Drechtsteden area as HVC wanted to determine the spatial reservoir quality variations of the Main Buntsandstein between the Naaldwijk and Drechtsteden areas. Three NW-SE and one W-E cross sections have been made. The sand-body distribution is obtained by connecting the strata chronostratigraphically.

Since this study mainly deals with the evaluation of the Volpriehausen Formation of the Triassic, only this formation distribution has been further described below.

The Lower and Upper Volpriehausen Sandstone Members have been encountered in all the wells with appreciable thickness distribution. Thus, the deposition of Volpriehausen sediments is laterally extensive in the West Netherlands Basin and the Roer Valley Graben.

The Upper Volpriehausen Sandstone Member generally follows the same thickness trend as the Lower Volpriehausen Sandstone Member. Along the NW-SE sections, the Upper Volpriehausen sands exhibit an increased number of gamma-ray peaks reflecting increase in the shale-content. This increase is exceptionally well marked at the basal portion of the Upper Volpriehausen Sandstone Member.

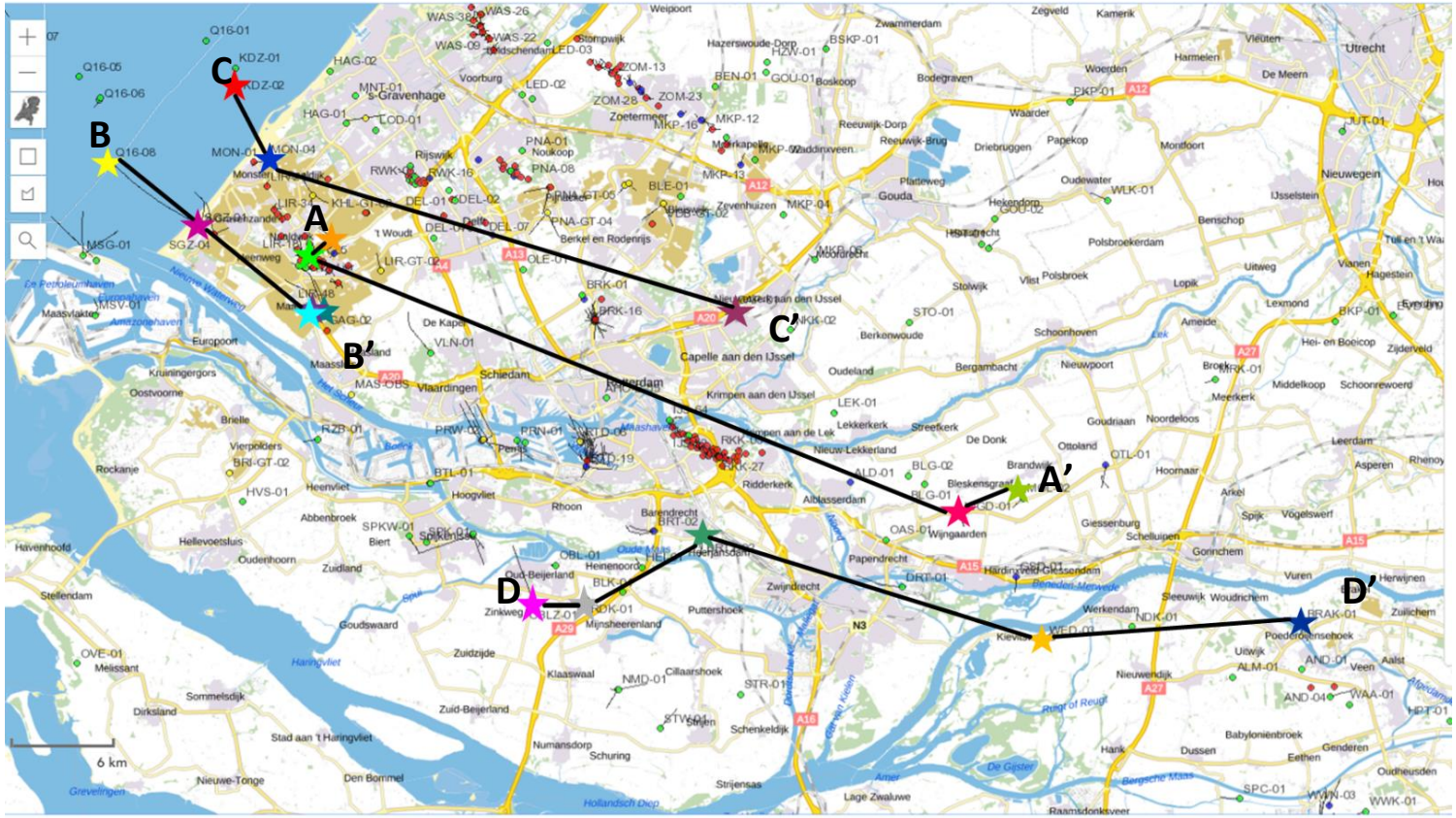

	Lower Volpriehausen Sandstone Member	(RBMVL)
	Upper Volpriehausen Sandstone Member	(RBMVU)
	Lower Detfurth Sandstone Member	(RBMDL)
	Detfurth Claystone Member	(RBMDC)
	Upper Detfurth Sandstone Member	(RBMDU)
	Hardegsen Formation	(RBMH)
	Basal Solling Sandstone Member	(RNSOB)

Figure 28: Overview of the 4 cross-sections used for the correlation of well-logs.

Gamma-ray Scale:

0-200 API

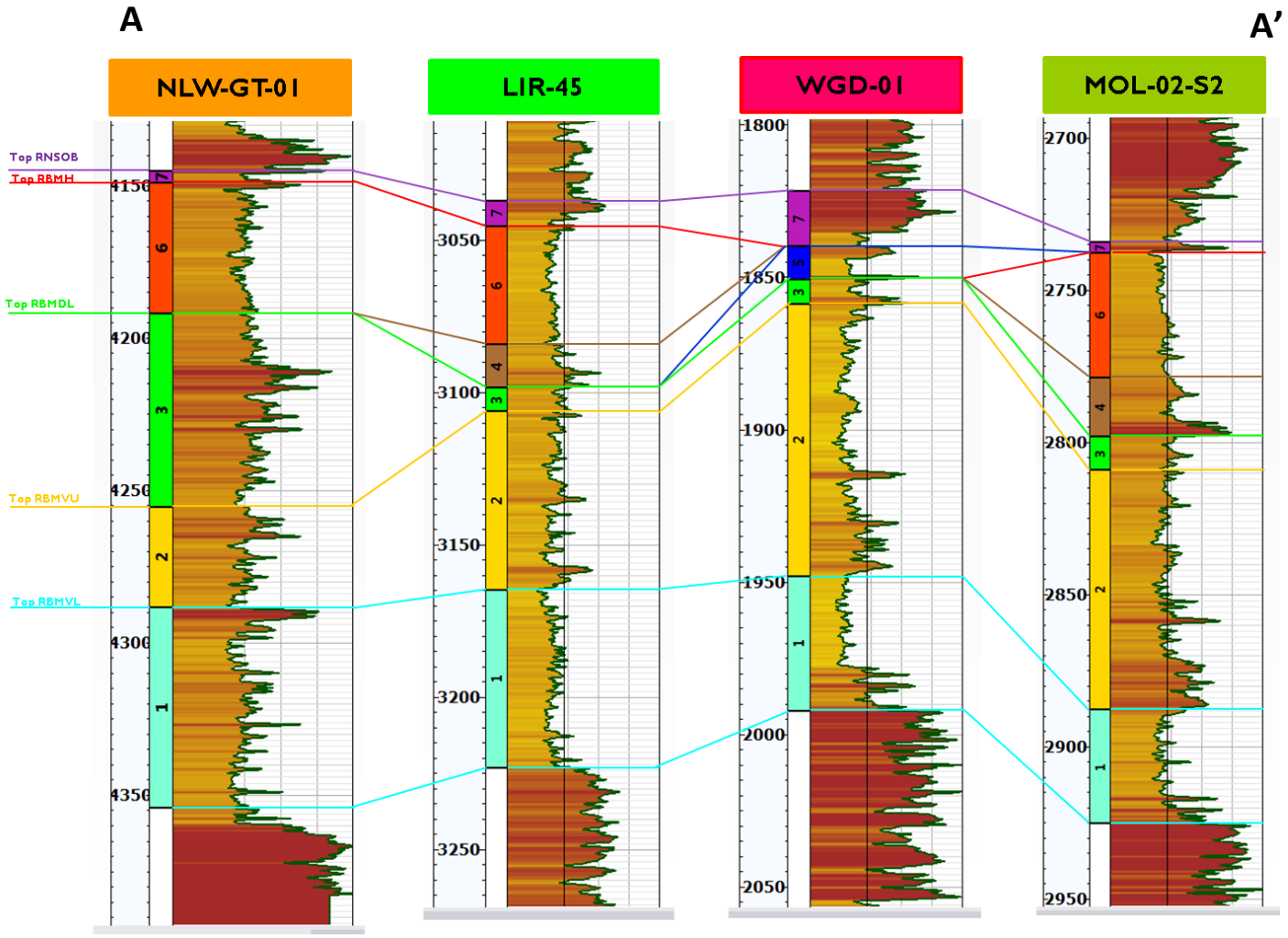
A
A'
NLW-GT-01
LIR-45
WGD-01
MOL-02-S2
Top RNSOB
Top RBMH
Top RBMDL
Top RBMVU
Top RBMVL
4150
4200
4250
4300
4350
3050
3100
3150
3200
3250
1800
1850
1900
1950
2000
2050
2700
2750
2800
2850
2900
2950

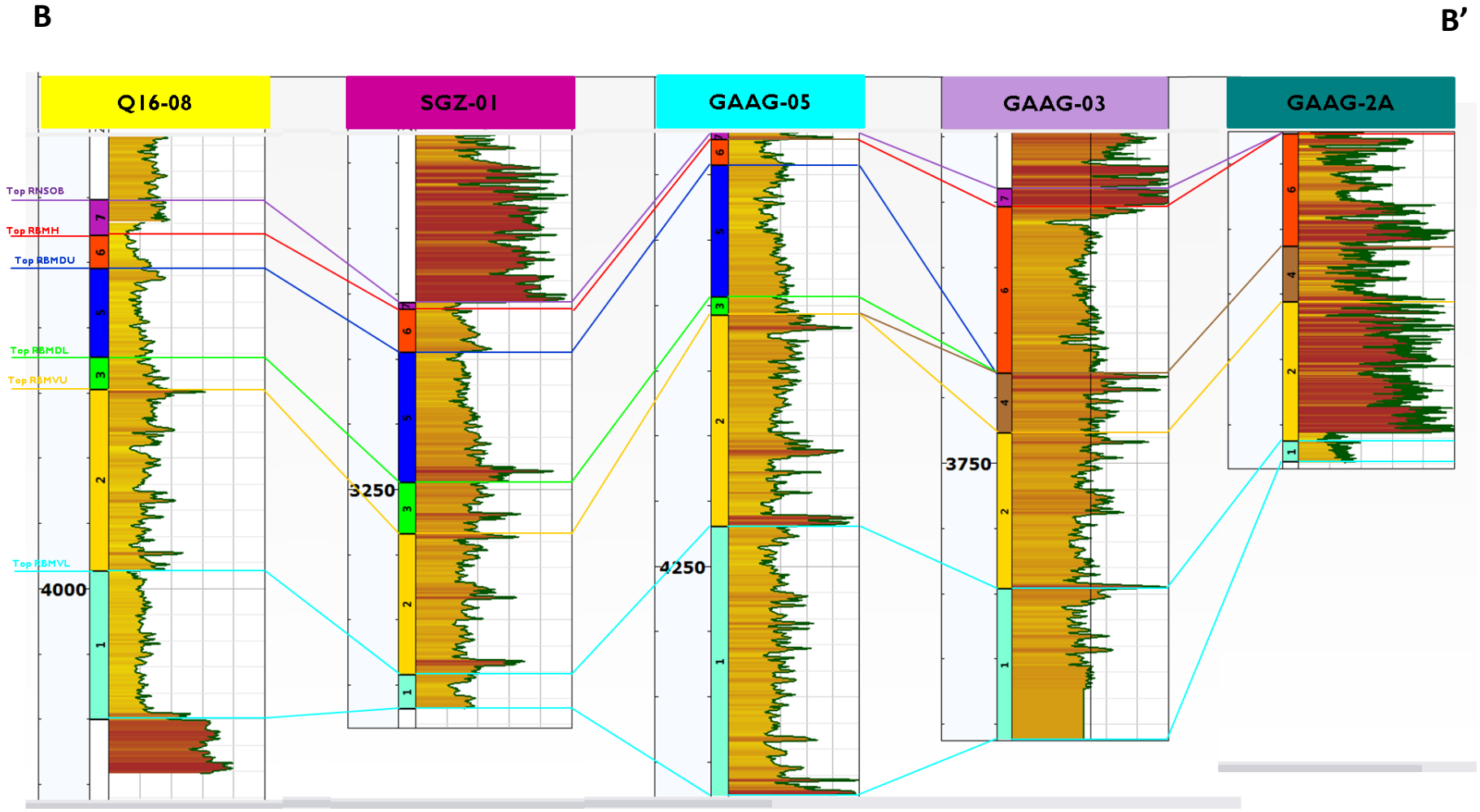
B
B'
Q16-08
SGZ-01
GAAG-05
GAAG-03
GAAG-2A
Top RNSOB
Top RBMH
Top RBMDU
Top RBMDL
Top RBMVU
Top RBMVL
4000
3250
4250
3750

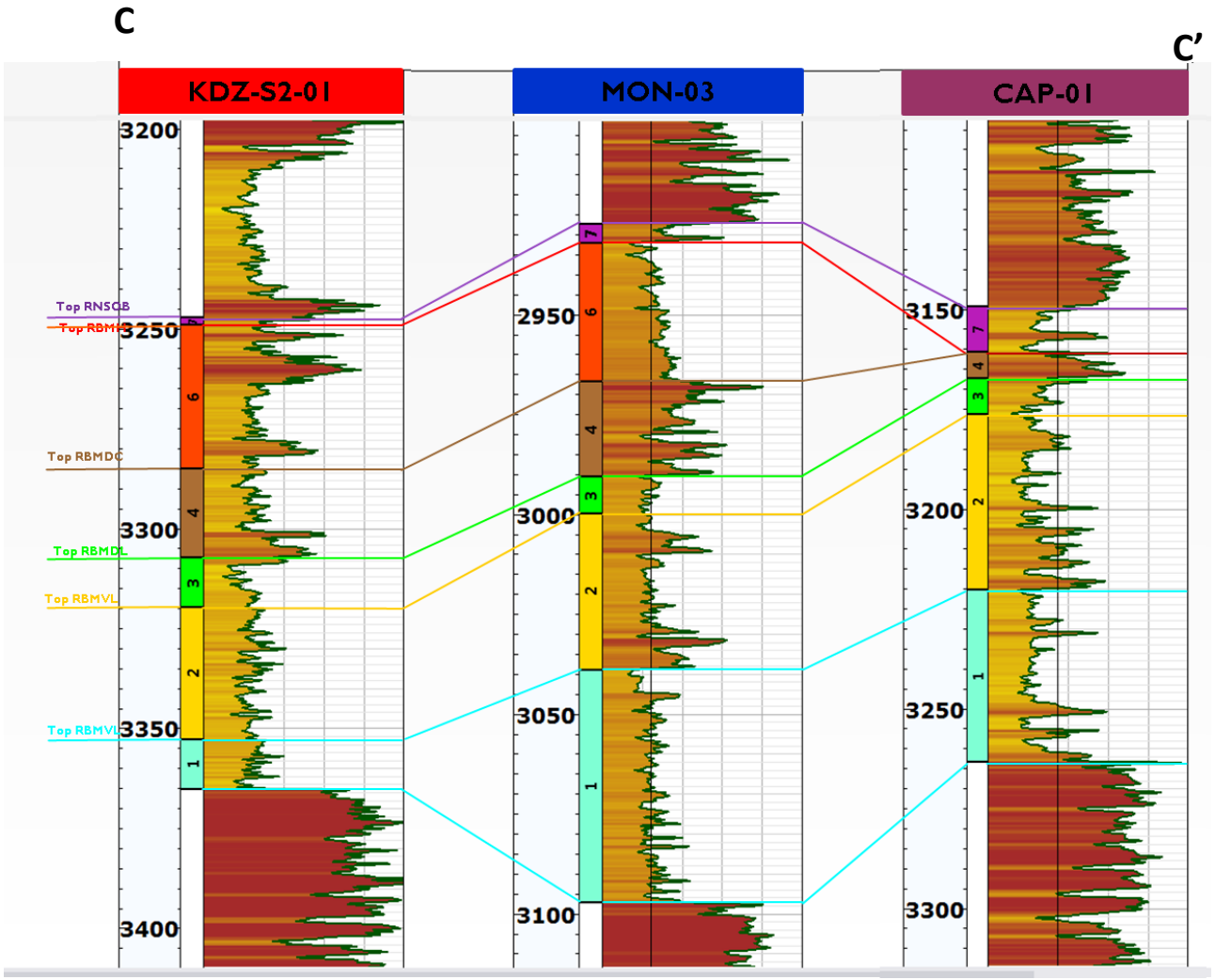
C
C'
KDZ-S2-01
MON-03
CAP-01
3200
3250
3300
3350
3400
2950
3000
3050
3100
3150
3200
3250
3300
Top RNSCB
Top RBMDC
Top RBMDL
Top RBMVL
Top RBMVL

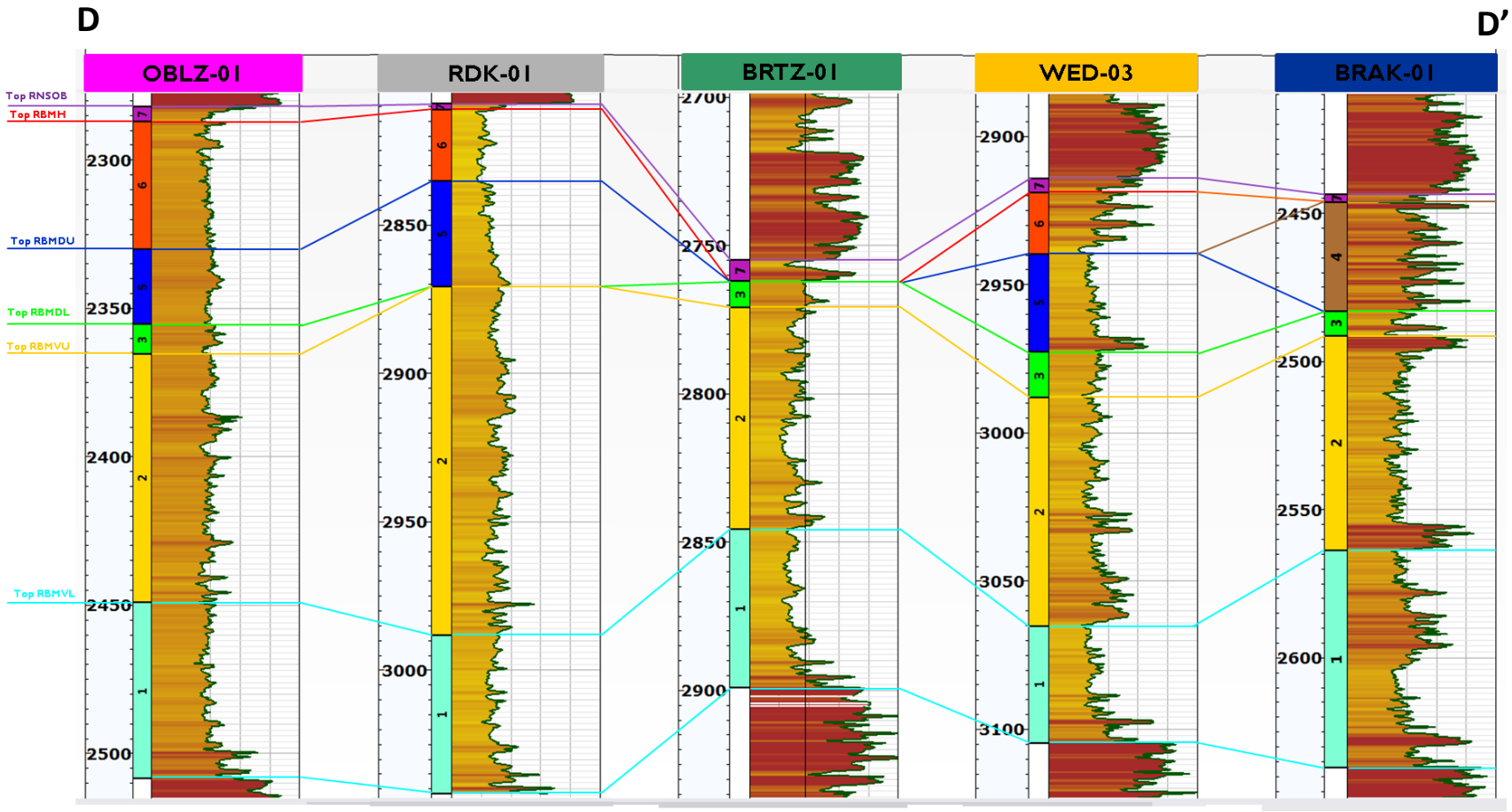

Figure 29: All the four cross-sections above display the overall upward wetting/drying trend observed in a particular Member/Formation of the Buntsandstein.

5.3. Grain Size Analysis

The study of grain textures aids the interpretation of depositional setting of clastic deposits. Studies conducted by Beard & Weyl (1973) have shown that five characteristic parameters govern the texture of clastics namely the grain-size, sorting, grain-shape or sphericity, grain roundness or angularity and finally the packing. This chapter aims at determining the grain-size distribution and degree of sorting for the core plugs samples.

Methodology:

For grain-size measurements, the trimmed ends of the core plugs were observed under a digital microscope and photographed by using LAS EZ Leica software. A square grid comprising of 49 squares (7x7 grid) was placed on each photograph. This was done to obtain a statistically sound dataset of grain-size measurements. 50-grain diameters were measured for every sample. These grains consisted of those that were located at the corners and nodes of the square blocks of the grid. However, in case of absence of a conspicuous grain at these positions, the diameter of grains lying on the edges of the square was measured. These readings were taken using the software ImageJ.

After obtaining the grain-size measurements and sorting them into 13 grain-size classes ranging from pebble to silt. The data was graphically represented in a frequency curve which was further used to derive the cumulative frequency distribution as shown in the following Fig. 30 (a, b, c, d). These curves (Fig. 30 (c, d)) make use of the grain-size depicted in the phi (φ) scale given by Udden-Wentworth where $\varphi = -log_2 d$ (d is the grain-diameter in millimetres). The phi scale makes the mathematical calculations related to the grain-size of the sediments easier (Tucker, 2001). Later, the data was used for the determination of initial (at deposition) values of porosity and permeability through empirical relationships, which will be explained in the following chapter.

From the cumulative frequency distribution curves, the grain-size parameters such as mean grain diameter (φ) and sorting (σ) were calculated using formulae given by Folk & Ward (1957) which are as follows:

$$\varphi = \frac{(\varphi_{16} + \varphi_{50} + \varphi_{84})}{3}$$

$$\sigma = \frac{(\varphi_{84} + \varphi_{16})}{4} + \frac{(\varphi_{95} + \varphi_{5})}{6.6}$$

The percentile measure φ_n is the grain-size in phi units at the *n*th percentile frequency (Tucker, 2001).

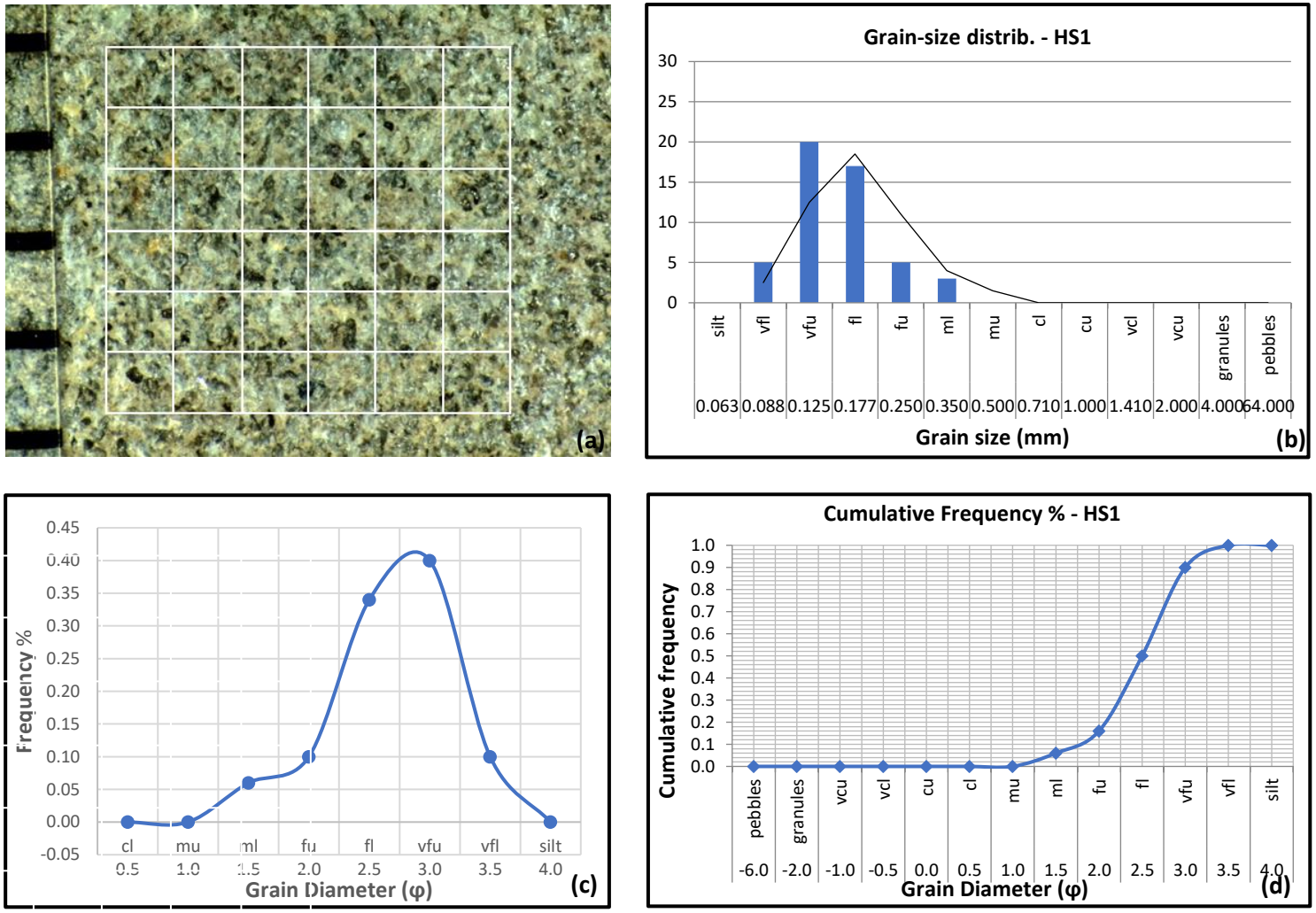

Figure 30: (a) A digital microscope image of Hot Shot number 1 of NLW-GT-01 core taken as an example (b) A distribution of the measured grain-diameters divided into grain-size classes ranging from extremely fine-grained silt to coarser grained pebbles. (c)Frequency distribution curve of the diameter lengths in decreasing order of grain-sizes (d) A cumulative distribution curve generated from the frequency distribution curve also in decreasing order of grain-diameter.

NDW-01

The statistical distribution of 50 grain-diameters measured for NDW-01 are plotted in the Fig.31 below.

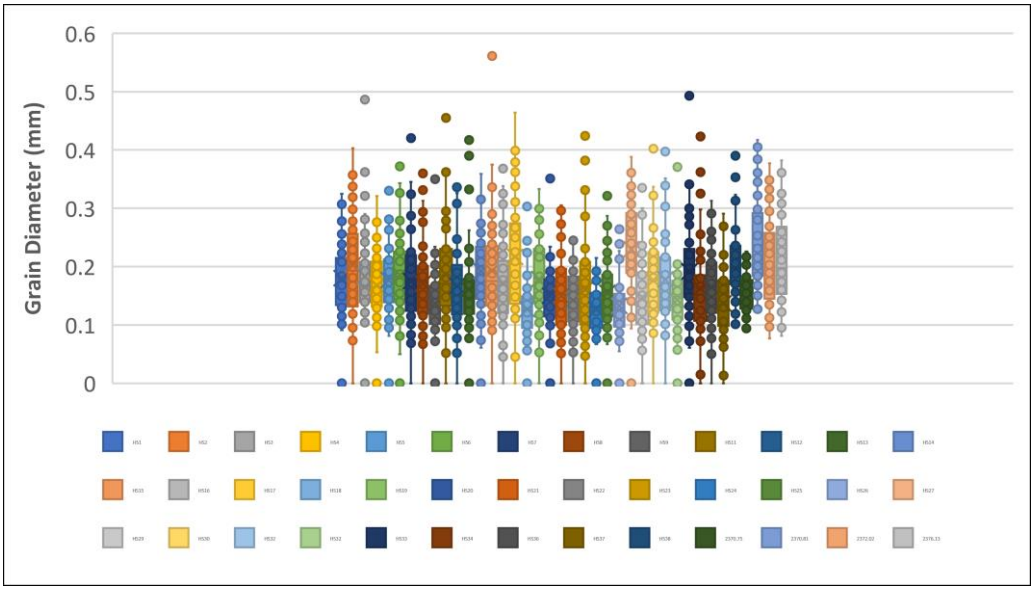

Figure 31: Box-plot for 50 grain-size measurements for the 39 core plugs of NDW-01.

The mean grain-size lies between 0.1-0.3mm (medium-lower to very fine-upper) (see Fig. 31 above).

Table 3: Mean Grain-Diameter and Sorting values for the core plug samples of NDW-01

Sample Number	Core Depth (m)	φ (ϕ)	σ (ϕ)
1	2368.51	2.445	0.450
2	2368.75	2.273	0.576
3	2369.01	2.418	0.463
4	2369.23	2.551	0.473
5	2369.44	2.472	0.476
6	2369.69	2.400	0.542
7	2369.92	2.484	0.576
8	2370.17	2.519	0.561
9	2370.22	2.848	0.495
11	2370.73	2.397	0.547
12	2370.99	2.555	0.623
13	2371.47	2.609	0.525
14	2371.64	2.352	0.540
15	2371.88	2.344	0.573
16	2372.13	2.513	0.628
17	2372.3	2.179	0.654
18	2372.48	2.950	0.543
19	2372.76	2.455	0.572
20	2372.94	2.707	0.433
21	2373.19	2.708	0.644
22	2373.39	2.786	0.498
23	2373.66	2.608	0.700
24	2373.88	2.957	0.432
25	2374.02	2.664	0.508
26	2374.27	2.883	0.490
27	2374.54	2.093	0.490
29	2375.13	2.737	0.588
30	2375.37	2.475	0.556
32	2375.67	2.460	0.542
33	2375.89	2.782	0.529
34	2376.11	2.354	0.570
36	2376.68	2.590	**0.778**
37	2376.83	2.573	0.547
38	2377.04	2.843	0.723
2370.75	2370.75	2.276	0.477
2370.81	2370.81	2.713	**0.332**
2372.02	2372.02	2.040	0.448
2374.85	2374.85	2.288	0.538
2376.13	2376.13	2.186	0.567

*The five core plug samples mentioned at the bottom in Table 3 were picked while conducting the core description study and have not been officially numbered yet.

For core-plugs obtained from NDW-01, the grain-size ranges from coarse lower to silt, with an average grain-size of 2.525ϕ ranging between fine-lower and very fine-upper.

Sorting is a measure of the spread of the grain-size distribution and hence can be related to the standard deviation. According to Folk & Ward (1957), sorting values can be defined as below:

φ less than 0.35	very well sorted
0.35-0.50	well sorted
0.50-0.71	moderately well sorted
0.71-1.00	moderately sorted
1.00-2.00	poorly sorted
greater than 2.00	very poorly sorted

From Table 3 and Fig. 32 below, the core plug sample lying at a depth of 2370.81m is the most sorted out of the 39 core plugs with a sorting value of 0.331 (ϕ) and core plug number 36 can be seen to have a much wider range of grain-size distribution from medium-upper to silt with a sorting of 0.778 (ϕ), see Fig. 32. Thus, in terms of sorting of grains, the Nederweert Sandstone Member is analysed to be moderately to bimodally sorted (see Table 3 and Fig. 34).

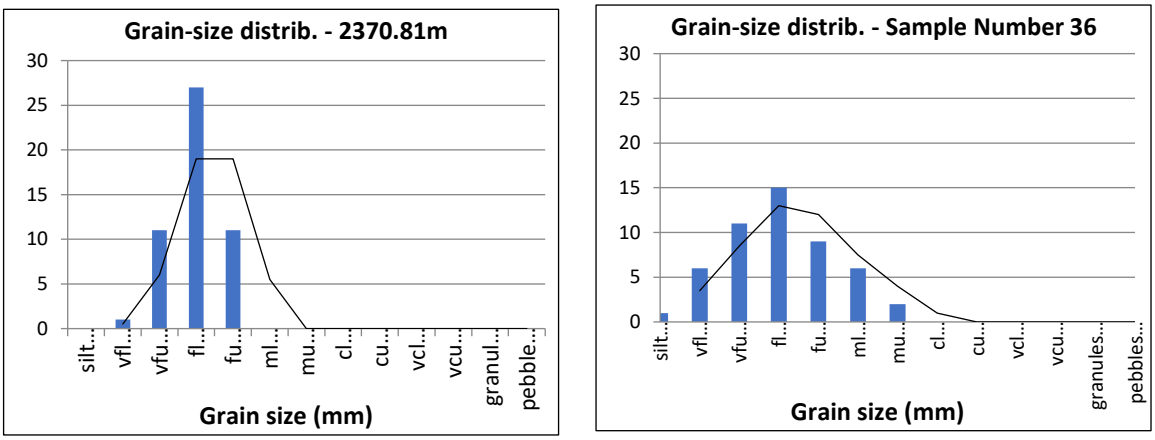

Figure 32: Comparison of the grain-size distribution between the most well sorted sample at a depth of 2370.81m and the least sorted sample number 36 amongst all of the 39 core plugs of NDW-01.

The correlation between standard deviation and grain-diameter is good (see Fig. 33), Overall, the standard deviation (in mm) shows an increasing trend with the progressively larger grain-diameters. Thus, the sorting improves with the decrease in the mean grain-diameter.

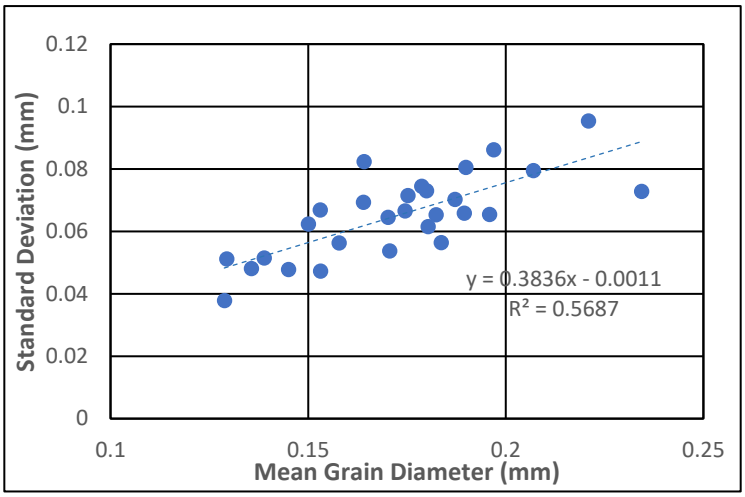

Figure 33: Plot of standard deviation/sorting against the mean grain-diameter.

The plot of frequency distribution against the grain-diameter, as shown in Fig. 34 indicates that most of the NDW-01 core plug samples exhibit a bimodal grain-size distribution. Majority of the distribution curves do not have any distortion and thus no skewness.

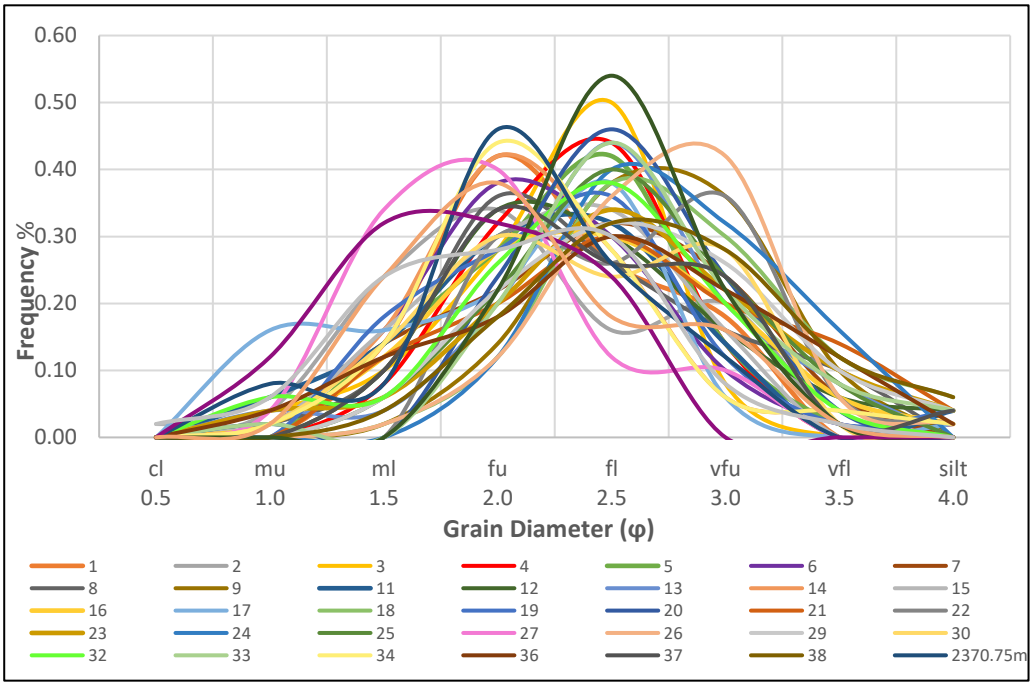

Figure 34: Smoothed frequency distribution curves showing sorting and skewness for the NDW-01 core plugs.

The bimodal nature of the samples can be explained by the fine-grained bottomsets grading upwards to coarser-grained foresets which are cemented at the top (refer Chapter 5). The finer-grained deposit in the bottom part of a cross strata forms a distinct textural contact with the overlying foresets and an underlying coarser fraction of the adjacent cross-bed. The sharp set boundaries observed in the core suggests that the larger sand flows reached the bottom partially comprising of sediments from smaller sand flows and redepositing sediments of different grain-sizes. The bottomsets, as observed in the core description study, are lined by dark-coloured heavy minerals. In that case, due to the difference in the grain density, the

lighter sediments were carried forward while, the finer heavier grains were left behind enclosed between larger grains resulting in a less sorted clastic deposit.

The absence of skewness suggests that the core plug samples consist of almost equal amounts of coarse-grained material as much as finer-grained sediments.

NLW-GT-01

The same workflow is adopted for the calculation of the grain-size parameters, as stated for NDW-01 previously.

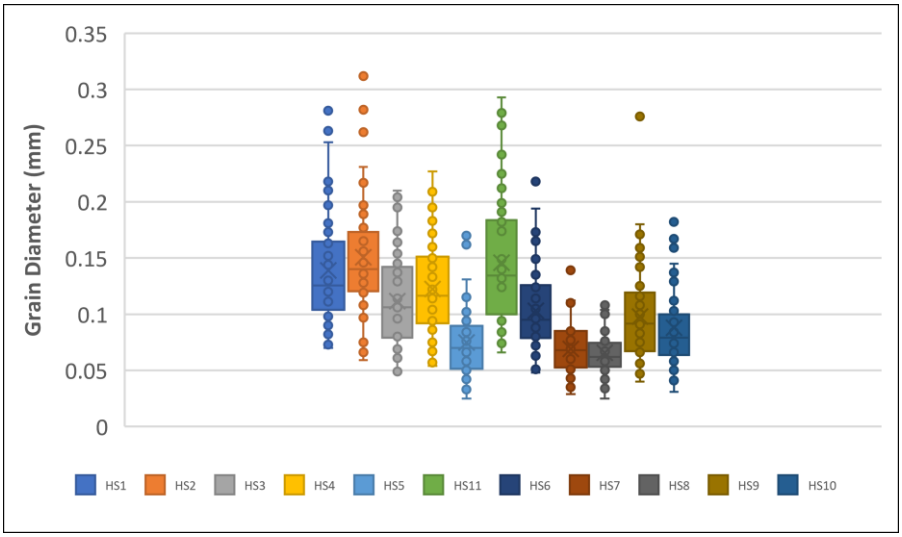

Figure 35: Box-plot for 50 grain-size measurements for the 39 core plugs of NLW-GT-01.

The mean grain-size lies between 0.05-0.15mm (silt to fine-lower) (see Fig. 35).

Table 4: Mean grain-diameter and sorting values for the 11 core plugs of NLW-GT-01.

Sample Number	Core Depth (m)	φ (ϕ)	σ (ϕ)
HS 1	4251.26	2.847	0.470
HS 2	4254.25	2.731	0.499
HS 3	4258.25	3.166	0.569
HS 4	4262.26	3.030	0.508
HS 5	4265.25	3.744	**0.575**
HS 11	4266.62	2.779	0.533
HS 6	4267.24	3.280	0.475
HS 7	4270.23	3.857	0.474
HS 8	4274.01	3.930	**0.415**
HS 9	4276.25	3.352	0.561
HS 10	4278.25	3.507	0.563

The grain-size of the NLW-GT-01 core ranges from medium-lower sand to silt with an average grain-diameter of 3.292 (ϕ) lying between very fine upper and very fine lower-grained sand.

Table 4 and the sorting value classification given by Folk & Ward (1957) suggest that the core plugs of NLW-GT-01 are moderately well to bimodally sorted (see Fig. 38).HS5 is the least sorted (0.575 φ) while HS8 (0.415 φ) is the most sorted sample (Table 4).

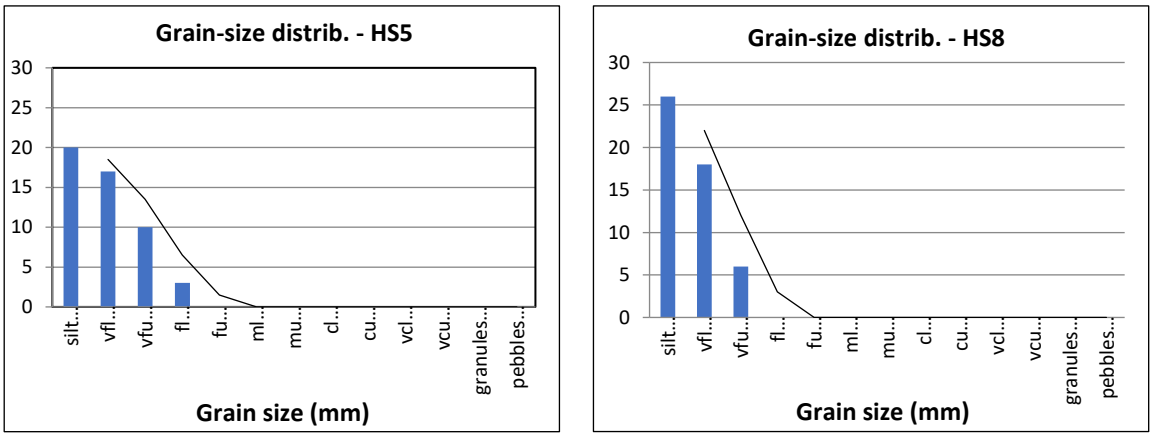

Figure 36: Comparison of the grain-size distribution between the most well sorted sample HS5 and the least sorted sample HS8 out of all the 11 core plugs.

The range of grain-size variation between the two samples above is not large indicating that the depositional medium was very effective in sorting the two sandstones samples (see Fig. 36).

A strong relationship exists between the degree of sorting (standard deviation) and the grain-diameter (see Fig. 37). Thus, the sorting decreases with the increase in the mean grain-diameter similar to the trend derived from the core plug samples of NDW-01.

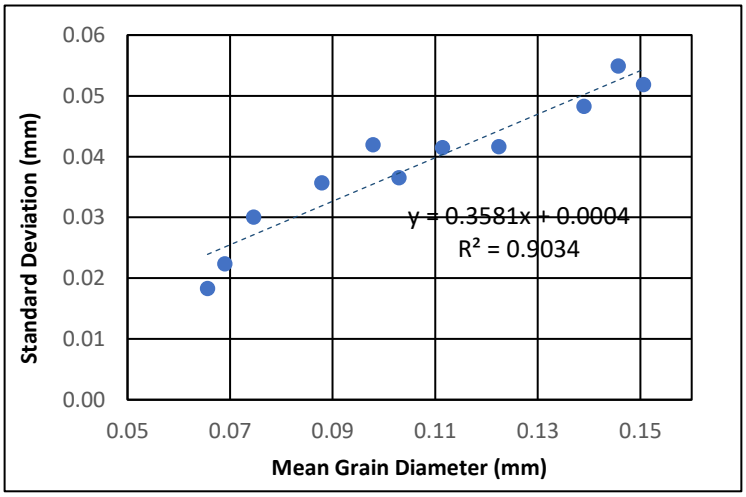

Figure 37: Plot of standard deviation/sorting against the mean grain-diameter.

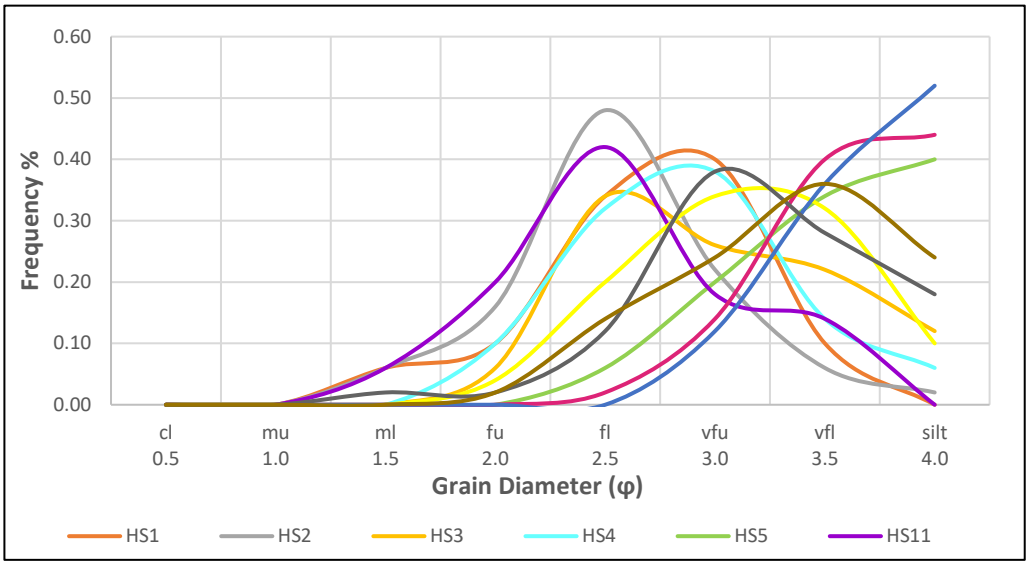

Figure 38: Smoothed frequency distribution curves showing sorting and skewness for all the hotshots of NLW-GT-01.

The bell-shaped frequency distribution curves (see Fig. 38) of the core plugs imply a unimodal grain-size distribution. However, Hotshots 3 and 11 demonstrate a bimodal distribution.

A more coarse-grained sediment (fine-tail) is said to be positively skewed, and fine-grain rich sediment (coarse-tail) is said to be negatively skewed (Tucker, 2001).The curves above appear to be negatively skewed where a majority of the grains are fine in size. As the sediments become finer, the frequency distribution curve becomes more negatively skewed.

For a well sorted sample, the bell curve has a narrow range suggesting that the constituent grains are of a similar size. Particle sorting is a typical expression of selective processes of transport. With increase in the travel distance, the degree of sediment reworking increases. The larger grains may become fragmented into smaller sized grains. However, in Fig. 38, the bimodal distribution observed in HS3 and HS11 is attributed to the presence of a considerable amount of matrix present in these samples. The negative skewness observed in the samples mentioned above may result from the inability of the fluvial system to carry away the fine sands and silt, which later get trapped between the larger sand-sized particles.

The cross-beds in NDW-01 exhibit a more pronounced grain-size variation due to considerably different grain-sizes occurring in adjacent laminae while this variation is not as common in NLW-GT-01.

5.4. Porosity and Permeability Model

Porosity and permeability are strongly affected by grain-size and the extent of grain sorting (Beard & Weyl, 1973). Other grain properties such as sphericity and roundness only have a minor secondary influence on the flow properties (Beard & Weyl, 1973). Studies conducted by Beard & Weyl (1973) and Freytag & Roque (2013) have led to the finding that grain packing also strongly impacts porosity. According to Schenk (1987), loosely packed sands can have a porosity of up to 50% while in tightly packed sands it can be as low as 25%. However, packing density is not one of the easily measurable textural parameters. A direct technique to measure the elementary virtual packing density is not available yet (Lecomte, 2006).

Previous research (Fraser, 1935; Rogers & Head, 1961; Beard & Weyl, 1973) have concluded that with the improvement in sorting, porosity increases. In this chapter, the porosity and permeability values during sediment deposition are calculated to determine the porosity loss after deep burial.

5.4.1. Porosity Calculations

Several mathematical relationships have been formulated that establish a link between the grain-size, sorting and the initial porosity and permeabilities (Fraser, 1935; Rogers & Head, 1961; Beard & Weyl, 1973; Yu & Standish, 1991). Beard & Weyl (1973) found that under wet surface conditions, the calculated porosity for unconsolidated sediments does not vary much with the change in the grain-size but is strongly dependent on the sorting. However, these empirical relations do not consider packing of grains while calculating porosity and assume fixed structural assemblages.

Yu & Standish (1991) developed a statistical geometrical model that predicts the contact points of packing of spheres to mathematically characterize the microstructure of particles. They designed this model to depend on the packing of the controlling mixture by depending on the size-ratio of the constituent grains. It is important to note that this model is limited to spherical particles and cannot be applied to all non-spherical particle mixtures (Yu & Standish, 1993).

Yu, et al. (2003) established a relationship between porosity and interparticle forces applicable only to a porosity fraction less than 0.6.

The relationship between porosity and capillary forces is given by the equation:

$$\varepsilon = \varepsilon_o + 0.0283 R_F^{0.295} \quad \text{.....(i)} \qquad R_F = F_c / F_g$$

where ε_o is the porosity of coarse dry spheres which is equal to 0.4 if the packing is loose.

R_F is the ratio between the the magnitude of the capillary force (F_c) and the

gravitational force (F_g) acting on the particle.

Due to their cohesive nature, both capillary and van der Waals forces have equivalent effects on the packing of particles giving rise to the assumption that wet coarse particles are also applicable to the packing of fine dry particles (Yu, et al., 2003). Thus, van der Waals force can be determined from porosity using equation(i). The integration of the calculated interparticle forces with measured porosity data led to the development of the following empirical equation.

$$\varepsilon = \varepsilon_o + (1 - \varepsilon_o)\exp\left(-mR_F^{-n}\right) \text{.....(ii)}$$

where ε_o is the porosity without any interparticle force other than gravity

R_F is the ratio between the magnitudes of the total interparticle force and gravity.

m and n are constants. (Yu, et al., 2003)

On similar terms, Yu, et al., (1997) established a relationship between porosity ε and the grain-diameter d is experimentally, and it is given by:

$$\varepsilon = \varepsilon_o + (1 - \varepsilon_o)\exp\left(-\alpha \times d^{\beta}\right) \text{.....(iii)}$$

where ε	Initial Porosity
ε_o=0.394	Porosity without any interparticle force for loose random packing
d	Mean grain diameter(μm)
α = 0.4	constant
β = 0.468	constant

NDW-01

Previously mentioned equation (iii) was used for the determination of the initial porosity values for the 39 core plug samples of the Nederweert core. The results are as follows:

Table 5: Calculated values of the porosity at the time of deposition.

Sample Number	Core Depth (m)	φ (mm)	σ(mm)	Initial ϕ
1	2368.51	0.1837	0.0564	0.4002
2	2368.75	0.2069	0.0795	0.3987
3	2369.01	0.1871	0.0703	0.3999
4	2369.23	0.1706	0.0537	0.4012
5	2369.44	0.1803	0.0615	0.4004
6	2369.69	0.1895	0.0659	0.3998
7	2369.92	0.1787	0.0744	0.4005
8	2370.17	0.1745	0.0665	0.4009
9	2370.22	0.1389	0.0515	0.4048
11	2370.73	0.1898	0.0805	0.3997
12	2370.99	0.1702	0.0645	0.4012

13	2371.47	0.1640	0.0693	0.4018
14	2371.64	0.1959	0.0654	0.3994
15	2371.88	0.1969	0.0862	0.3993
16	2372.13	0.1752	0.0715	0.4008
17	2372.3	0.2209	0.0954	0.3981
18	2372.48	0.1294	0.0512	0.4063
19	2372.76	0.1824	0.0654	0.4003
20	2372.94	0.1531	0.0472	0.4030
21	2373.19	0.1530	0.0669	0.4030
22	2373.39	0.1450	0.0478	0.4040
23	2373.66	0.1641	0.0823	0.4018
24	2373.88	0.1288	0.0378	0.4064
25	2374.02	0.1578	0.0563	0.4024
26	2374.27	0.1356	0.0481	0.4053
27	2374.54	0.2343	0.0728	0.3975
29	2375.13	0.1500	0.0624	0.4033
30	2375.37	0.1799	0.0730	0.4004
32	2375.67	0.1818	0.0741	0.4003
33	2375.89	0.1454	0.0530	0.4039
34	2376.11	0.1956	0.0757	0.3994
36	2376.68	0.1660	0.0813	0.4016
37	2376.83	0.1680	0.0581	0.4014
38	2377.04	0.1394	0.0566	0.4048
2370.75	2370.75	0.2064	0.0687	0.3988
2370.81	2370.81	0.1525	0.0347	0.4030
2372.02	2372.02	0.2432	0.0752	0.3972
2374.85	2374.85	0.2048	0.0726	0.3989
2376.13	2376.13	0.2197	0.0979	0.3981

Table 6: Final Porosity and grain density measurements of lost core plugs acquired from nlog.

Sample Number	Depth	Final Porosity	Grain Density	Hor.perm
	(m)	Fraction	(g/ml)	(mD)
31	2368.5	0.091	2.68	0.4 mD
32	2369.5	0.089	2.69	< 0.2 mD
33	2370.5	0.069	2.69	< 0.2 mD
34	2371.5	0.047	2.69	< 0.2 mD
35	2372.5	0.056	2.68	< 0.2 mD
36	2373.5	0.048	2.67	< 0.2 mD
37	2374.5	0.065	2.68	< 0.2 mD
38	2375.5	0.073	2.69	< 0.2 mD
39	2376.5	0.106	2.68	2 mD

The initial porosity values range between 39.72% and 40.64% with an average initial porosity of 40.12%, see Table 5. The final porosity measured from the core plugs varies between the values of 4.7% to about 10.6%, with an average porosity of 7.15%. The difference between the average porosities is about 32.97% (see Fig.39).

As observed from Table 6 above the grain density ranges between 2.67 g/ml and 2.69 g/ml with an average of 2.68 g/ml.

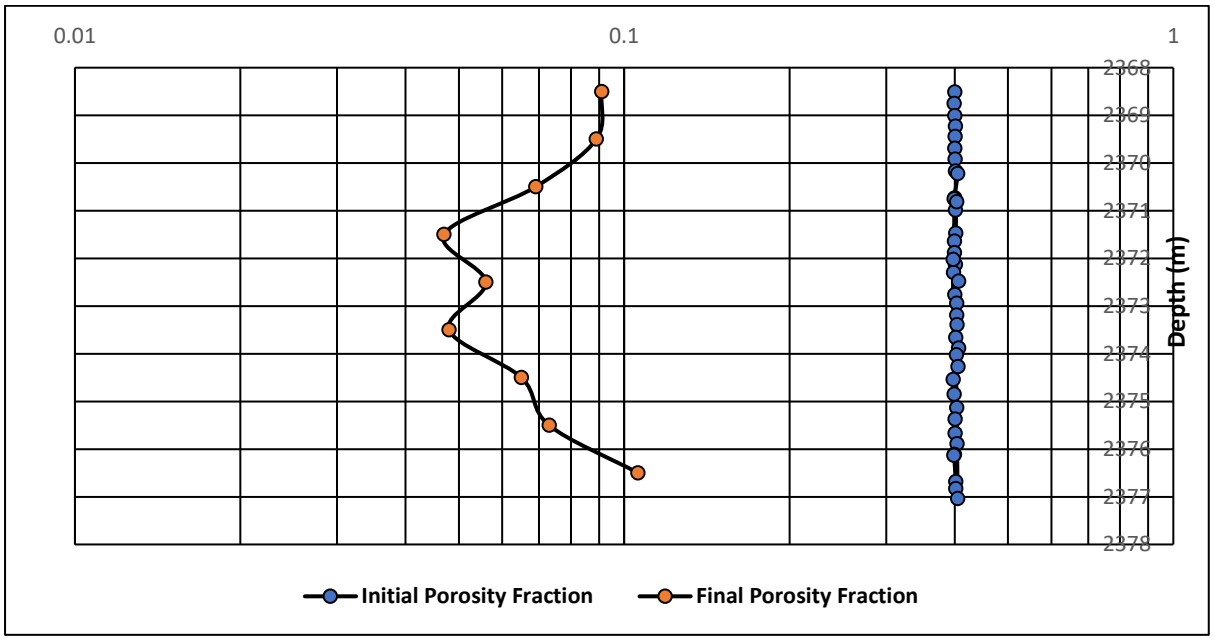

Figure 39: Graphical representation of the porosity of the newly deposited poorly consolidated NDW-01 sandstones and the compacted sandstones that underwent burial enduring mechanical and chemical compaction.

The loss in porosity with depth is mainly due to the weight of the overlying rock strata. Due to unavailability of thin sections, much cannot be said about the relation between the porosity loss and the diagenetic history of the Nederweert Sandstone Member in the well NDW-01.

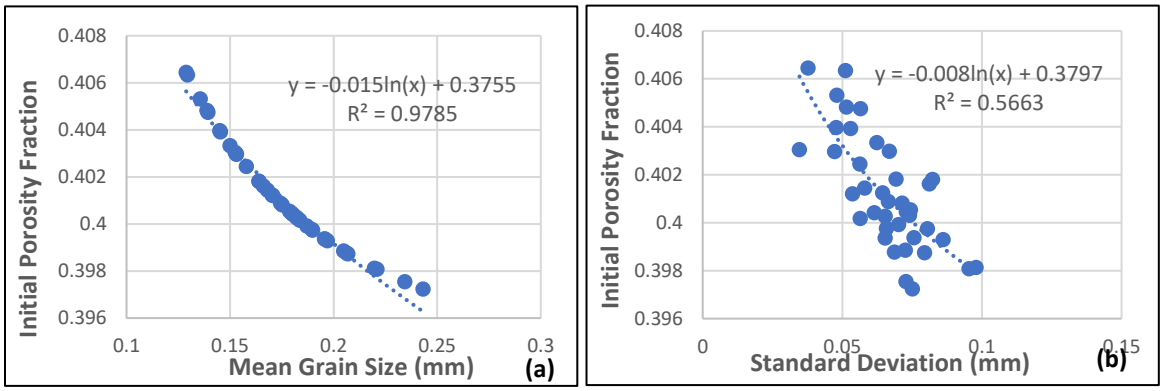

Figure 40: Graphical comparison between the initial and final porosity values against grain parameters, namely mean grain diameter and sorting.

The porosity of poorly consolidated sands decreases with the increase in the grain-size due to the action of interparticle forces (see Fig 40a). Overall as the sediments become less sorted which implies a higher standard deviation, the porosity progressively reduces (see Fig. 40b).

NLW-GT-01

By adopting the same workflow as NDW-01, the initial porosity values of NLW-GT-01 are calculated (see Table 7 below).

Table 7: Calculated values of the porosity at the time of deposition and the porosity loss upon burial.

Sample Number	Core Depth (m)	φ (mm)	σ (mm)	Initial Porosity Fraction	Final Porosity Fraction	Porosity Loss
HS 1	4251.26	0.1390	0.0482	0.4048	0.0390	0.3658
HS 2	4254.25	0.1506	0.0518	0.4033	0.0144	0.3889
HS 3	4258.25	0.1114	0.0415	0.4100	0.0167	0.3934
HS 4	4262.26	0.1224	0.0416	0.4076	0.0187	0.3889
HS 5	4265.25	0.0746	0.0300	0.4239	0.0230	0.4008
HS 11	4266.62	0.1457	0.0549	0.4039	0.0158	0.3881
HS 6	4267.24	0.1030	0.0365	0.4123	0.0153	0.3970
HS 7	4270.23	0.0690	0.0223	0.4273	0.0189	0.4084
HS 8	4274.01	0.0656	0.0183	0.4296	0.0219	0.4077
HS 9	4276.25	0.0979	0.0419	0.4139	0.0194	0.3945
HS 10	4278.25	0.0879	0.0357	0.4175	0.0218	0.3957

The final porosity data calculated by PanTerra Geoconsultants was used to determine the reduction in porosity from the time when the sediments were recently deposited to when they were subjected to deep burial (see Table 8).

The final porosity of the sample was calculated by the direct measurement of the grain volume and the bulk volume. Boyle's Law Porosimeter that makes use of the function of pressure drop due to volume expansion was used to measure the grain volume. The reference cell was charged with helium at 100 psig and this gas was then allowed to expand into the chamber with the core sample (Felder & Fernandez, 2018). The bulk volume was measured by submerging the core sample in mercury. This is based on the Archimedes' Principle.

Table 8: Laboratory calculated measurements of the core plug parameters.

Sample Number	Core Depth (m)	Dry weight (g)	Bulk Volume (ml)	Grain Density (g/ml)	Grain Volume (ml)	Pore Volume (ml)	Final Porosity Fraction
HS 1	4251.26	145.13	56.29	2.683	54.09	2.2	0.0391
HS 2	4254.25	150.66	56.29	2.716	55.48	0.81	0.0144
HS 3	4258.25	149.9	56.39	2.703	55.45	0.94	0.0167

HS 4	4262.26	147.85	56.16	2.683	55.11	1.05	0.0187
HS 5	4265.25	147.55	56.67	2.665	55.36	1.3	0.0229
HS 11	4266.62	149.32	56.51	2.685	55.62	0.89	0.0157
HS 6	4267.24	148.8	56.52	2.674	55.65	0.86	0.0152
HS 7	4270.23	147.71	56.38	2.670	55.32	1.06	0.0188
HS 8	4274.01	148.19	56.52	2.681	55.28	1.24	0.0219
HS 9	4276.25	148.09	56.2	2.687	55.11	1.09	0.0194
HS 10	4278.25	146.95	56.4	2.664	55.17	1.23	0.0218

The grain density is calculated as the ratio of the dry weight to the bulk volume. The values range from 2.66 to 2.72 g/ml, with an average of 2.68 g/ml.

As a reference, the grain density of pure sand is 2.65 g/ml. This means that the sands constituting the core plugs are not entirely clean but also consist of cement and clay.

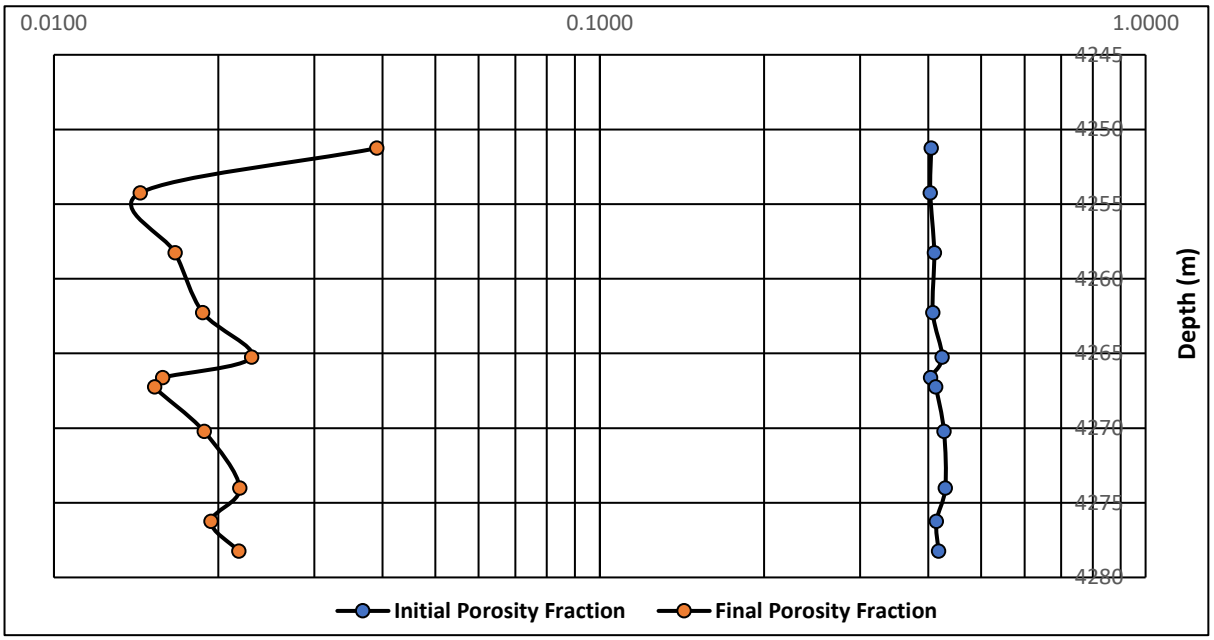

Figure 41: Graphical representation of the porosity of the newly deposited poorly consolidated NLW-GT-01 sandstones and the compacted sandstones that underwent burial enduring mechanical and chemical compaction.

The final porosity values range between 1.4% to 3.9% with an average value of 2% while the porosity of these sands when newly deposited ranges between 43% and 40.5% with an average value of 41.4%. Thus, the average loss in the porosity after deep burial is about 39.36% (see Fig.41 above).

The extent of this porosity loss depends upon the local geology and the depth under consideration (Glassey, 2015).With the increase in the burial depth, the overlying burden increases and results in greater lithostatic pressure. In response, the rocks compress and expel fluids out thereby becoming more densely packed. For mechanically resistant rocks

higher pressure is needed to reduce the porosity and permeability to the same value as that for poorly unconsolidated mechanically weak rock.

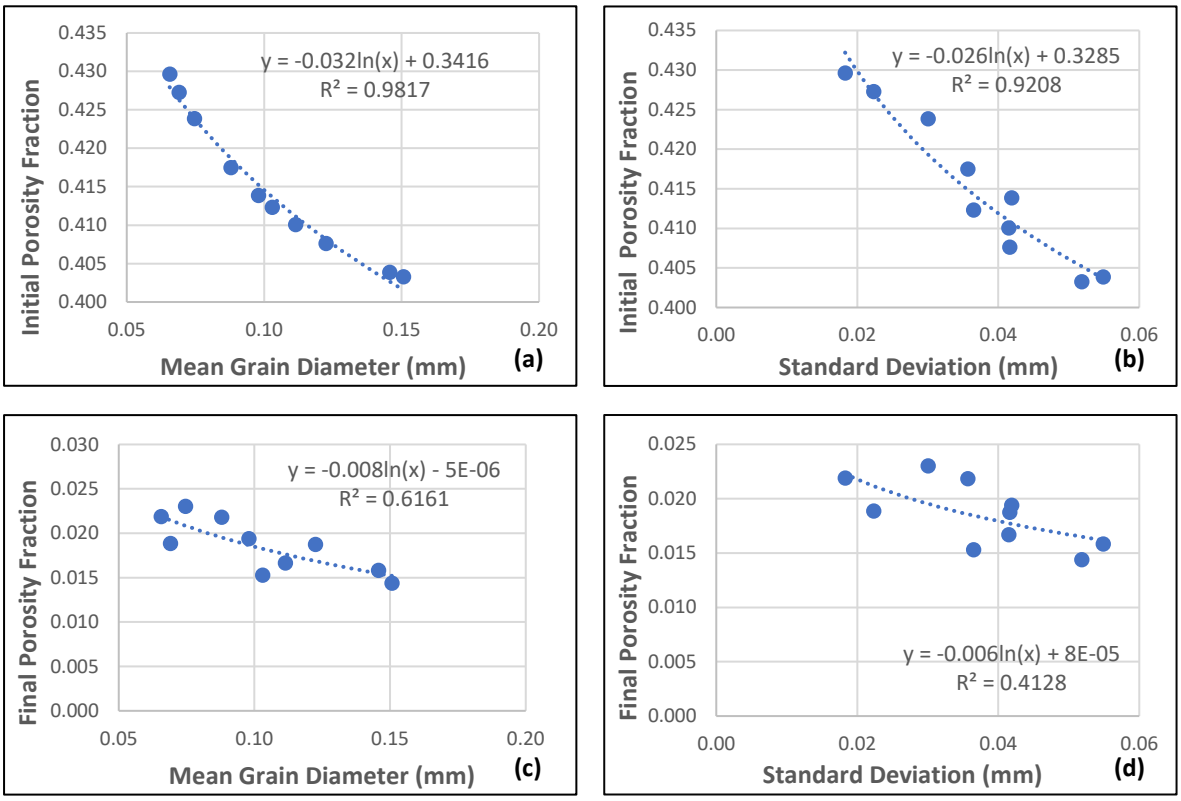

Figure 42: Graphical comparison between the initial and final porosity values against grain parameters namely mean grain-diameter and standard deviation.

Both the initial and final porosities increase with the decrease in the grain-size see Fig. 42 (a, c). Overall the porosities increase with the improvement in the sorting see Fig. 42 (b, d).

In weakly consolidated sandstones, the grain-size correlates well with the pore size and acts as the primary control on permeability (Beard & Weyl, 1973; Smith, 2013). Yu, et al. (1997) observed that the porosity increases with decreasing grain-size. This takes place due to the weak forces such as van der Waals that restrict the relative movement of the particles and thus the sample exhibits a high porosity (Yu, et al., 1997). This is only applicable to particles with a diameter less than 0.5mm.

5.4.2. Permeability Calculations

Many equations relating permeability to fractional porosity have been formulated. Krumbein & Monk (1943) analysed sand packs with a constant porosity of 40% and measured their permeabilities. Their work led to an empirical equation where permeability was a function of geometric mean grain-diameter and the standard deviation of the grain-diameter independent of porosity. Their experimental procedures where later adopted by Beard &

Weyl (1973). They found that in spite of their measured porosity values ranging between 23% and 43%, it matched their data reasonably well (Smith, 2013). On the other hand, Berg (1970) and van Baaren (1979) used grain-based models, Timur (1968) carried out studies on surface-area models and many others such as Kozeny (1927); Carman (1937); Carman (1956); Winland(1980); Katz & Thompson (1986) worked on pore-size models.

Carman-Kozeny equation for calculating permeability in a bundle-of-tubes is given by

$$k = \frac{\phi^3}{2\zeta(1-\phi)^2 * a_v^2} \quad \text{.....(iv)}$$

where k is the permeability in mm^2

ϕ is the fractional porosity

ζ is the dimensionless tortuosity which accounts for the irregular pore networks and not perfectly cylindrical bundle of tubes and

a_v is the specific surface area of the medium or the ratio of the internal area to the bulk volume in mm^{-1}

Dullien (1979) established a relation between the specific surface area and the diameter of spherical particle diameter(d), and it is given by $a_v = 6(1-\phi)/d$.When an assembly of single -size spheres of diameter d is considered, $a_v = 6/d$. (Panda & Lake, 1994).

By using the above relation in a combination of Carman-Kozeny equation derived for a bundle-of-tubes model, which is based on laminar flow inside straight tubes (Poiseuille flow), we obtain the following:

$$k = (d^2/72)(\phi^3/(1-\phi))^2 \quad \text{.....(v)}$$

However, empirically factor 180 fits the data better than 72, mainly due to tortuosity. Hence, the equation becomes:

$$k = (d^2/180)(\phi^3/(1-\phi))^2 \quad \text{.....(vi)}$$

Panda & Lake (1994) modified the equation above by expressing the particle diameter (d) as a function of the second (E_2) and third moment (E_3) of the particle size distribution $(d = E_3/E_2)$ which is as follows:

$$E_2 = e^{[-2\varphi lm(2)+4\sigma^2 ln(2)^2]} \quad \text{..... (vii)}$$

$$E_3 = e^{[-3\varphi lm(2)+4.5\sigma^2 ln(2)^2]} \quad \text{.....(viii)}$$

The permeability equation can now be expressed as:

$$k = \frac{\phi^3}{180(1-\phi)^2} e^{-[2\varphi \ln(2)+(\sigma \ln(2))^2]} \quad \text{..... (ix)}$$

where φ and σ are in phi units.

NDW-01

The initial permeability calculations are carried out using equation (ix).

Table 9: Calculated initial permeability by the using mathematical relationship between mean grain-diameter, standard deviation and the initial porosity.

Sample Number	Core Depth (m)	φ (mm)	φ (ϕ)	σ(ϕ)	Initial ϕ	Initial k (mm)2	k (D)
1	2368.51	0.184	2.445	0.450	0.400	0.0000334	33.82
2	2368.75	0.207	2.273	0.576	0.399	0.0000417	42.27
3	2369.01	0.187	2.418	0.463	0.400	0.0000346	35.02
4	2369.23	0.171	2.551	0.473	0.401	0.0000291	29.51
5	2369.44	0.180	2.472	0.476	0.400	0.0000322	32.67
6	2369.69	0.190	2.400	0.542	0.400	0.0000354	35.84
7	2369.92	0.179	2.484	0.576	0.401	0.0000317	32.15
8	2370.17	0.174	2.519	0.561	0.401	0.0000303	30.75
9	2370.22	0.139	2.848	0.495	0.405	0.0000201	20.33
11	2370.73	0.190	2.397	0.547	0.400	0.0000355	35.96
12	2370.99	0.170	2.555	0.623	0.401	0.0000290	29.39
13	2371.47	0.164	2.609	0.525	0.402	0.0000271	27.44
14	2371.64	0.196	2.352	0.540	0.399	0.0000376	38.13
15	2371.88	0.197	2.344	0.573	0.399	0.0000380	38.51
16	2372.13	0.175	2.513	0.628	0.401	0.0000306	30.98
17	2372.3	0.221	2.179	0.654	0.398	0.0000472	47.82
18	2372.48	0.129	2.950	0.543	0.406	0.0000177	17.94
19	2372.76	0.182	2.455	0.572	0.400	0.0000329	33.38
20	2372.94	0.153	2.707	0.433	0.403	0.0000239	24.22
21	2373.19	0.153	2.708	0.644	0.403	0.0000239	24.19
22	2373.39	0.145	2.786	0.498	0.404	0.0000217	21.96
23	2373.66	0.164	2.608	0.700	0.402	0.0000271	27.47
24	2373.88	0.129	2.957	0.432	0.406	0.0000176	17.79
25	2374.02	0.158	2.664	0.508	0.402	0.0000253	25.59
26	2374.27	0.136	2.883	0.490	0.405	0.0000192	19.49
27	2374.54	0.234	2.093	0.490	0.398	0.0000528	53.51
29	2375.13	0.150	2.737	0.588	0.403	0.0000230	23.35
30	2375.37	0.180	2.475	0.556	0.400	0.0000321	32.54
32	2375.67	0.182	2.460	0.542	0.400	0.0000327	33.18
33	2375.89	0.145	2.782	0.529	0.404	0.0000218	22.07
34	2376.11	0.196	2.354	0.570	0.399	0.0000375	38.02
36	2376.68	0.166	2.590	0.778	0.402	0.0000277	28.08
37	2376.83	0.168	2.573	0.547	0.401	0.0000283	28.69
38	2377.04	0.139	2.843	0.723	0.405	0.0000202	20.46
2370.75	2370.75	0.206	2.276	0.477	0.399	0.0000415	42.07
2370.81	2370.81	0.152	2.713	0.332	0.403	0.0000237	24.04
2372.02	2372.02	0.243	2.040	0.448	0.397	0.0000567	57.43
2374.85	2374.85	0.205	2.288	0.538	0.399	0.0000409	41.45

2376.13	2376.13	0.220	2.186	0.567	0.398	0.0000467	47.35

The depositional permeability value ranges between 17.79-57.43D with an average of 31.92D (see Table 9)

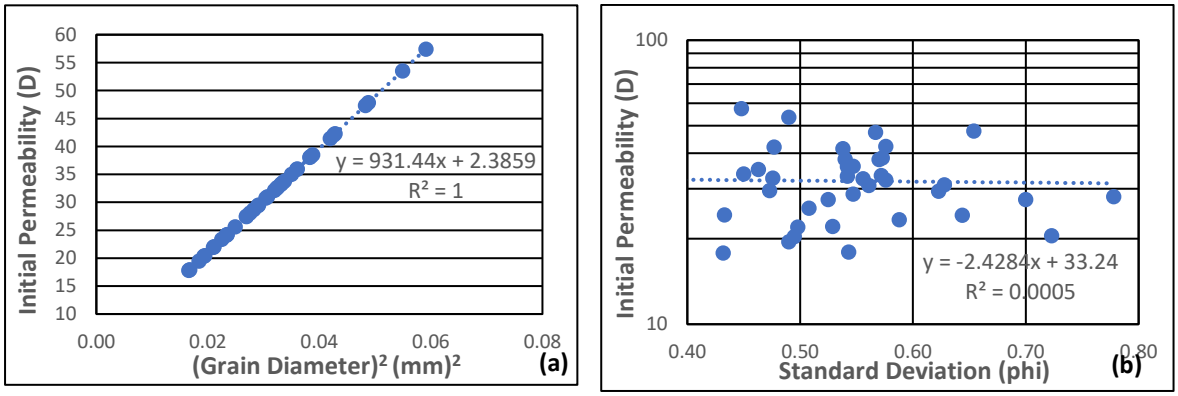

Figure43: Plot of initial permeability against square of grain-diameter and standard deviation. for NDW-01.

The theoretical models suggest that the flow through a porous medium is proportional to the square of the radius of the pore opening (Smith, 2013). Thus, from Fig. 43 (a) it can be concluded that the grain-diameter is proportional to the pore-diameter. The relationship between the initial permeability and sorting is unclear.

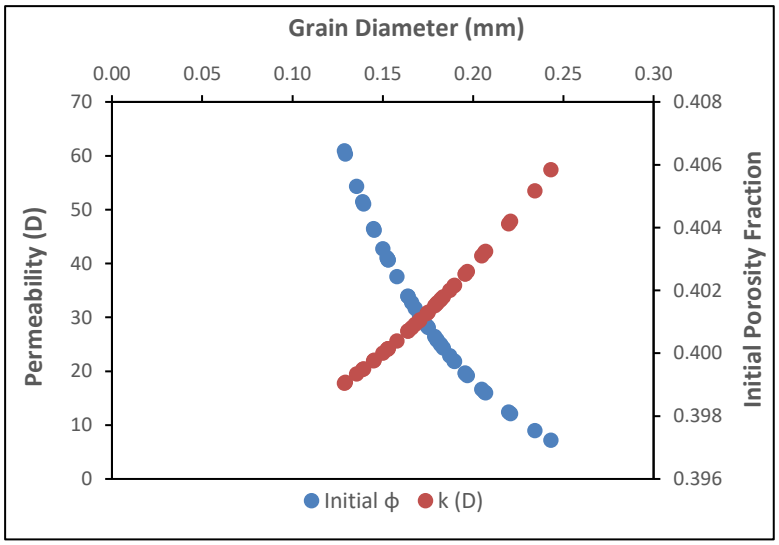

Figure 44: Plot of porosity versus permeability versus the grain diameter of NDW-01.

In Fig. 44 above the porosity decreases exponentially with the increase in permeability. This may be due to the fact the equation (iii) is limited to spherical grains which is not the case when the sandstones in NDW-01. Also, the formula does not include sorting parameter for the calculation of porosity.

On the other hand, the initial permeability increases exponentially with the grain-diameter which should be the case (see equation (ix)).

NLW-GT-01

A nitrogen permeameter was used to deduce the gas permeability of the hotshots. After mounting the core plug in a “Hassler” type core holder, a steady state was established at a confining pressure of 400 psig (Felder & Fernandez, 2018). The parameters such as the flow rate, gas temperature, pressure differential, horizontal permeabilities, and ambient pressures were noted and used in the Darcy equation to calculate the permeabilities (Felder & Fernandez, 2018).

Table 10: Final porosity and Horizontal Permeability values as calculated through laboratory experiments.

Sample Number	Core Depth	Ambient He Porosity	Gas Horizontal Permeability	Emp. Klink. Hor. Perm.
	(m)	(% of Vb)	(mD)	(mD)
HS 1	4251.26	3.9	0.04	0.02
HS 2	4254.25	1.4	<0.01	<0.01
HS 3	4258.25	1.7	<0.01	<0.01
HS 4	4262.26	1.9	0.02	0.01
HS 5	4265.25	2.3	0.02	0.01
HS 11	4266.62	1.6	0.02	0.01
HS 6	4267.24	1.5	<0.01	<0.01
HS 7	4270.23	1.9	<0.01	<0.01
HS 8	4274.01	2.2	0.02	0.01
HS 9	4276.25	1.9	0.02	0.01
HS 10	4278.25	2.2	0.01	0.01

Table 11: Initial permeability values calculated using the equation(ix).

Core Depth (m)	φ (mm)	φ (phi)	σ(phi)	Initial ϕ	k at surface(mm)2	k (D)
4251.26	0.139	2.847	0.470	0.405	0.0000201	20.37
4254.25	0.151	2.731	0.499	0.403	0.0000232	23.52
4258.25	0.111	3.166	0.569	0.410	0.0000137	13.85
4262.26	0.122	3.030	0.508	0.408	0.0000161	16.29
4265.25	0.075	3.744	0.575	0.424	0.0000071	7.19
4266.62	0.146	2.779	0.533	0.404	0.0000219	22.15
4267.24	0.103	3.280	0.475	0.412	0.0000120	12.11
4270.23	0.069	3.857	0.474	0.427	0.0000063	6.38
4274.01	0.066	3.930	0.415	0.430	0.0000058	5.90
4276.25	0.098	3.352	0.561	0.414	0.0000110	11.14
4278.25	0.088	3.507	0.563	0.417	0.0000092	9.34

The initial permeability values range between a minimum of 6D and a maximum of 24D (see Table 11). The average permeability is around 13D. Table 10 indicates that the final permeability measured in the laboratory is less than 0.01mD

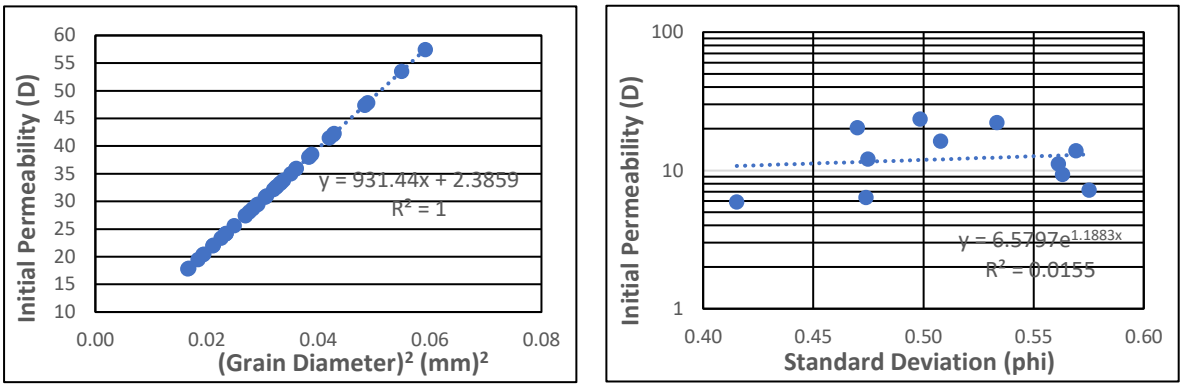

Figure 45: Permeability against the square of the (a) grain-size and (b) standard deviation.

From equation (vi) it is experimentally proven that permeability correlates perfectly well with the square of the particle diameter. The calculated permeability values become progressively lower with the decrease in the mean grain-size. However, it cannot be well-correlated with the sorting parameter (see Fig. 45(a, b)).

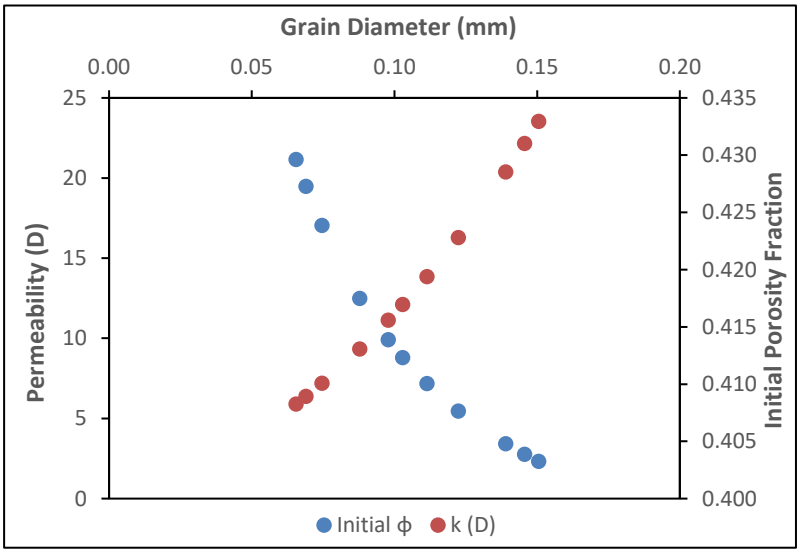

Figure 46: Plot of porosity versus permeability versus the grain diameter of NLW-GT-01.

The relation between the parameters (see Fig. 46) is similar to that observed in the case of NDW-01.

5.5. Diagenesis

Three thin-section samples namely HS1, HS2, and HS11 were obtained from the NLW-T-01 core. They were analysed for the interpretation of diagenetic history of the Triassic sandstones. These samples lie at depths of 4251.26m, 4254.25m and 4266.62m respectively. The destruction of the original porosity of the Triassic sandstones in the Naaldwijk field from 41% to a mere 3.9%(maximum) can be explained by the diagenetic events that affected these siliciclastic sediments with their progressive burial.

The percentages of the different sandstone constituents (displayed below) are taken from the XRD results and signify the quantitative abundance of each mineral in the whole rock composition.

5.5.1. Textures

The sandstone samples appear nearly structureless when observed under a digital microscope, except for HS2 which contains elongated rip-up clasts. Maximum grain-size ranges from silt to medium-lower grained sandstone. The dominant average grain-size is that of fine-lower grained sandstone. In all of the samples, patchy cement fills the pore space leaving no visual porosity. Samples HS1 and HS2 appear well-sorted while HS11 shows a bimodal grain-size distribution. Grain shapes vary mostly between sub-angular to sub-rounded. Grain contacts are point to straight indicating moderate compaction.

5.5.2. Detrital Mineralogy

The studied samples fall under the category of arkosic arenites (Nagtegaal, 1978). This classification makes use of the XRD data since a petrographic point-count data was not available. As a distinction between the feldspars and quartz that form parts of the lithic fragments was not made from individual quartz and feldspar grains, the quantitative abundance data is not precise.

The detrital components comprise of quartz, feldspar, lithic fragments and trace amounts of illite and mica.

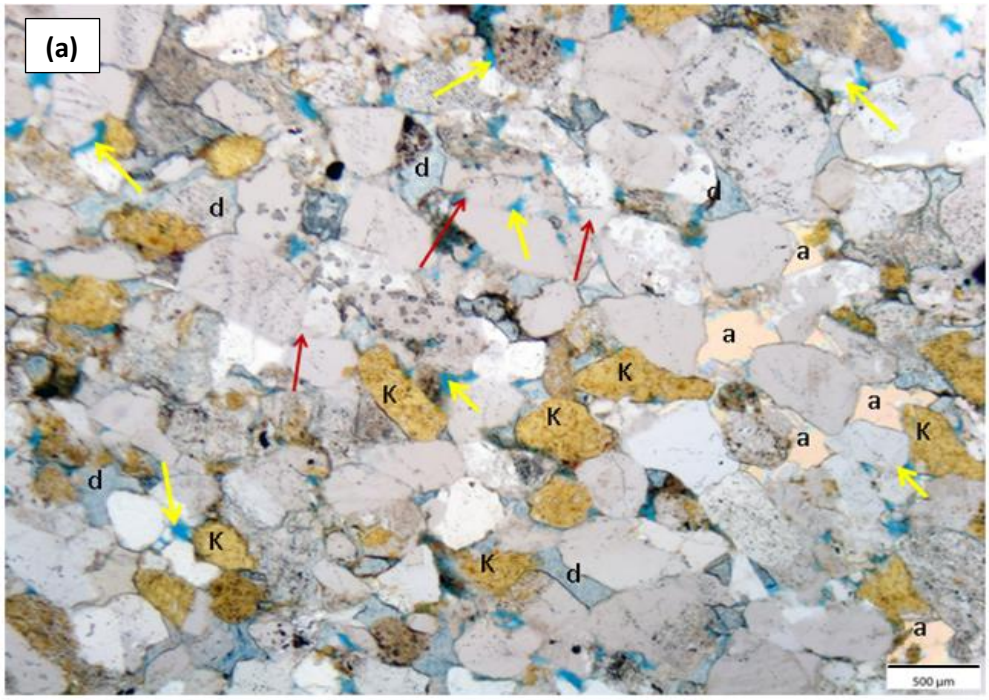

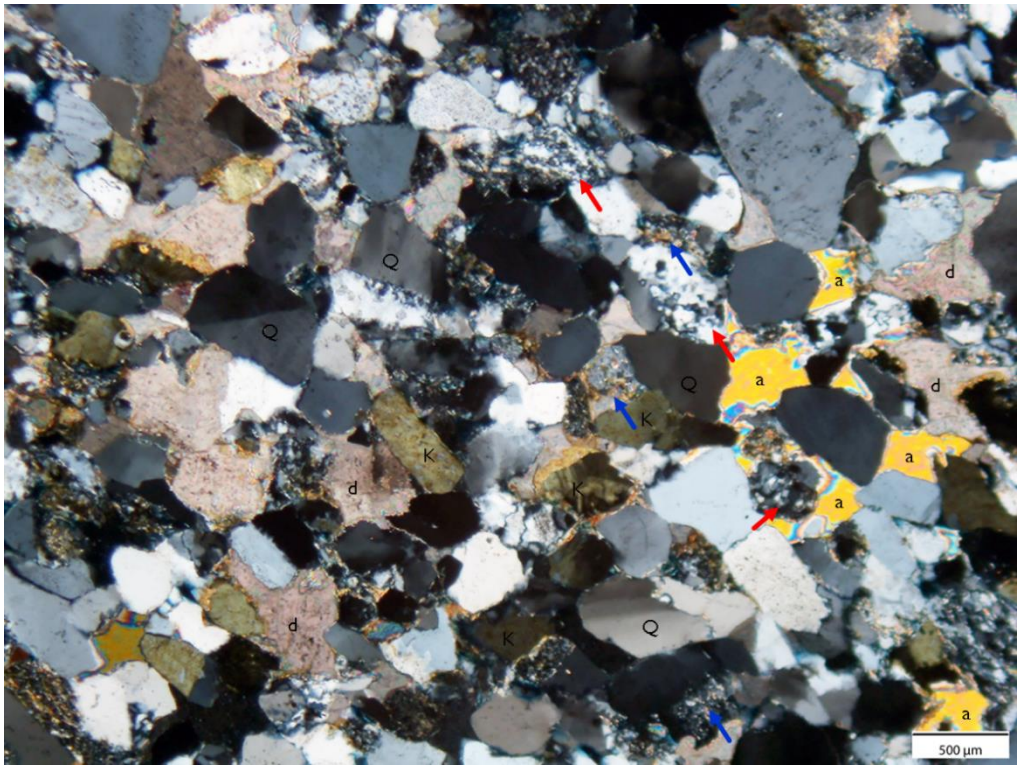

Figure 47: (a) Plane Polarised Light: The thin section has been dyed. Pores appear blue (yellow arrows), K-feldspar s(K) are dyed yellow, dolomite (d) and anhydrite (a) cements are present along with quartz cement (red arrows.) (b) Crossed polar: Monocrystalline zoned quartz grains(Q), polycrystalline quartz (red arrows), K-feldspars (K) along with the lithic fragments (blue arrows) comprise the detrital mineralogy. Patchy dolomite (d) and anhydrite cement are also present.

Quartz (63-68%)

Quartz is the most dominant mineral in the thin-sections (see Fig. 47). Monocrystalline quartz grains are more abundant than polycrystalline quartz.Monocrystalline quartz displays straight to undulose (strained) extinction. Polycrystalline quartz grains are characterized by moderate to strong undulose extinction with irregular/equant crystal units having straight or wavy boundaries. Quartz grains contain dust-like inclusions. Strained quartz grains with abundant inclusions suggest a plutonic/metamorphic origin.

Feldspar (Microcline 4-6% and Albite 5-6%)

The yellow K-feldspar grains appear to have a distinct boundary with insignificant dissolution. The plagioclase feldspars, however, appear to be partially leached.

Lithic Fragments:

The lithic rock fragments are composed mainly of quartz, feldspar and mica minerals. Some fragments have aligned mica minerals giving rise to a schistose texture and indicating a metamorphic origin. Metamorphic clasts mainly include phyllite, schist and quartzite. Sedimemtary clasts comprise of claystone, sketetal carbonate clasts, dolomitic rip-up clasts (HS2) and chert.

5.5.3. Authigenic Mineralogy

Dolomite (14-21%)

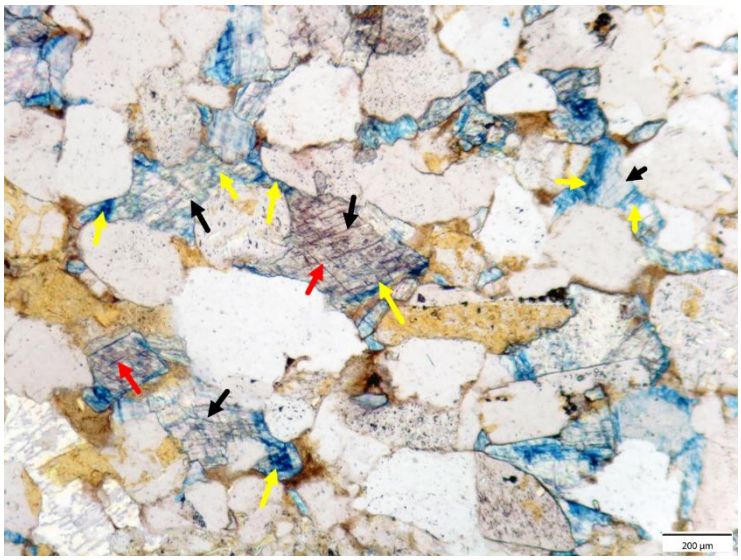

Figure 48: Brownish-red carbonate remnant (black arrows) overgrown by non-ferroan (red arrows) and blue-stained ferroan (yellow arrows).

Iron-rich (ferroan dolomite/ ankerite) and iron-deficient dolomite (non-ferroan dolomite) both varieties are present (see Fig. 48). The thin sections are stained to help distinguish ferroan dolomite (stained blue) from the unstained non-ferroan dolomite. In HS2 and HS11, the calcite cement is preserved as cores in the ferroan dolomite cement. The calcite cores have a dusty brownish appearance due to inclusions. The ferroan dolomite is seen surrounding the previously precipitated non-ferroan dolomite. However, the boundaries between them are not distinct. Ferroan dolomite mainly fills the primary macropores but it is rarely observed projecting into secondary pores. Dolomite also occurs as patchy cement and in the form of euhedral rhombic crystals embedded in a clayey matrix in rip-up clasts (detrital) observed in HS2.

Quartz

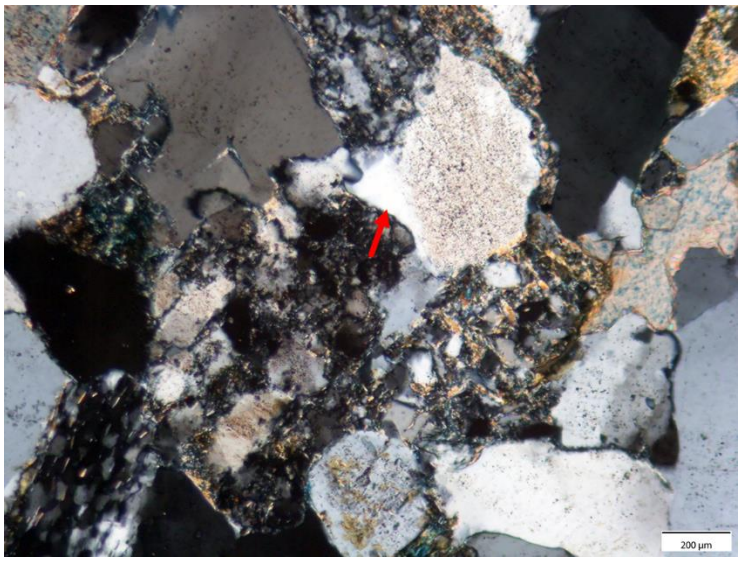

Quartz overgrowth rarely occurs; however, quartz cement is more abundant (see Fig. 49).

Figure 49: Clear quartz overgrowth (red arrow) distinguishing itself from the dusty detrital quartz grain.

Anhydrite (0-1%)

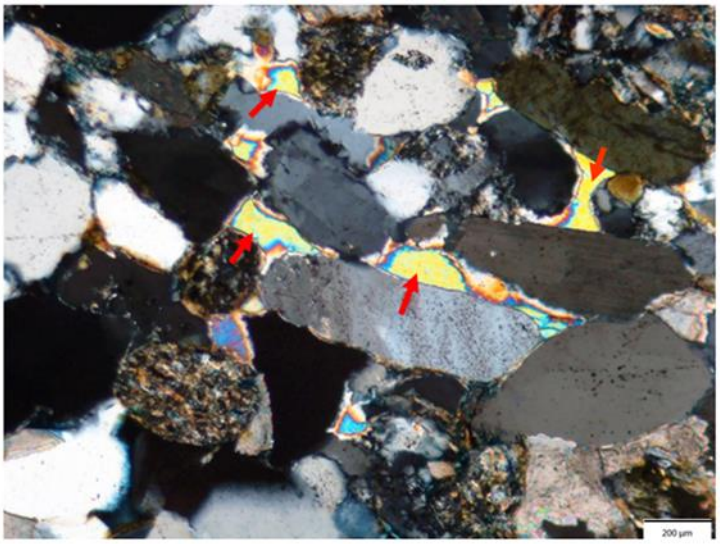

Patchy and localized anhydrite cement can be seen only in sample HS1 (4251.26m) (see Fig. 50).

Figure 50: Highly birefringent anhydrite grains cementing grain-size pores. The boundaries of the anhydrite grains appear to be leached.

Porosity

Over-sized pores and macropores are nearly absent. Macroporosity is restricted to very few spots due to limited grain dissolution. Apparent porosity is almost negligible. HS1 is the most porous thin section sample with a porosity of 3.9% while HS2 and HS11 have porosities of about 1.4% and 1.6% respectively.

5.5.4. Diagenetic sequence and porosity evolution

The progressive burial of sediments and the introduction of chemically different solutions alters the mineralogy and pore-system of the sandstones. The paragenetic sequence of cement emplacement and pore evolution is presented as follows (see Fig.55):

Subsurface- Shallow Burial Diagenesis:

During subsurface-shallow burial diagenesis, labile grains such as feldspars, mica and lithic rock fragments were degraded by meteoric pore fluids. An early carbonate cement may have formed locally preserving uncompacted grain fabric and inhibiting compaction during the early stages of burial. The presence of crinoidal fossil remains and calcretes can be explained by the Dinantian biohermal build-ups (Van Hulten & Poty, 2008) and the onlap of Devonian and Carboniferous siliciclastic and carbonate deposits on the northern side of London Brabant Massif (Rijkers, et al., 1993) which served as the source for these siliciclastic sediments. Throughout the shallow burial phase, sediments underwent relatively rapid compaction due to the lack of abundant cementation, resulting in the loss of significant primary intergranular porosity. It is essential to note that the calcrete content is important for its control on subsequent diagenesis. The zones with sparsely early cementation allow more easy penetration of sulphate solutions and dolomitising solutions (Bath, et al., 1987).

Deep Burial Diagenesis:

The framework grains become more tightly packed due to mechanical compaction with continued burial. Increasing pressure due to the increased effective stress is locally concentrated at the grain contacts and leads to mineral dissolution. The studied samples show point to point and elongate grain contacts with the absence of grain rimming clay coats making them more prone to compaction. However, the samples exhibit insignificant pressure dissolution and lack sutured and concavo-convex grain contacts, which suggests that the degree of chemical compaction due to mechanical compaction was rather weak to moderate. The dominance of short to long grain-to-grain contacts in all cemented patches indicates that the main cements quartz, dolomite, and anhydrite formed after significant compaction had already occurred (Paxton, et al., 2002). The labile rip-up clasts seen in HS2 and the mechanically weak lithic fragments have undergone a partial deformation evidenced by their elongated shape (see Fig. 51). Ductile illite grains appear to be crushed between more resistant quartz grains due to mechanical compaction.

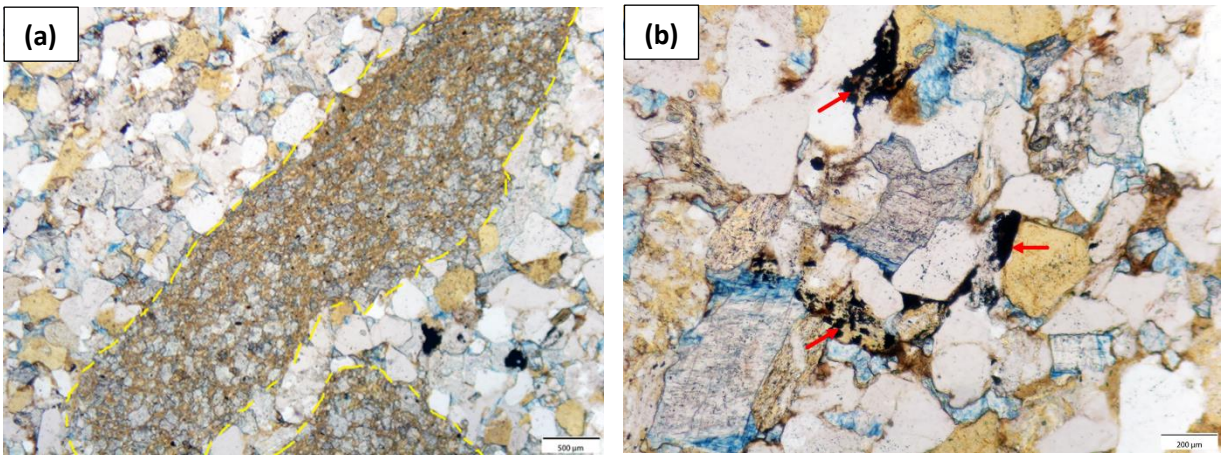

Figure 51:(a) Elongated rip-up clasts in HS2 comprising of rhombic dolomite grains of varying sizes enclosed in a clayey matrix (b) Deformed clay clasts (red arrows) forming pseudomatrix after mechanical compaction.

The dolomite is compositionally zoned, with ferroan dolomite typically occurring as overgrowths on the previously precipitated non-ferroan dolomite. Slight variations in the chemical composition of dolomite grains (non-ferroan and ferroan) suggest that the dolomite does not result from the dolomitization processes of previous calcite minerals (Hardie, 1987). The calcitic cores in ferroan dolomite may represent remnants of an early cement surviving dissolution (see Fig. 52).

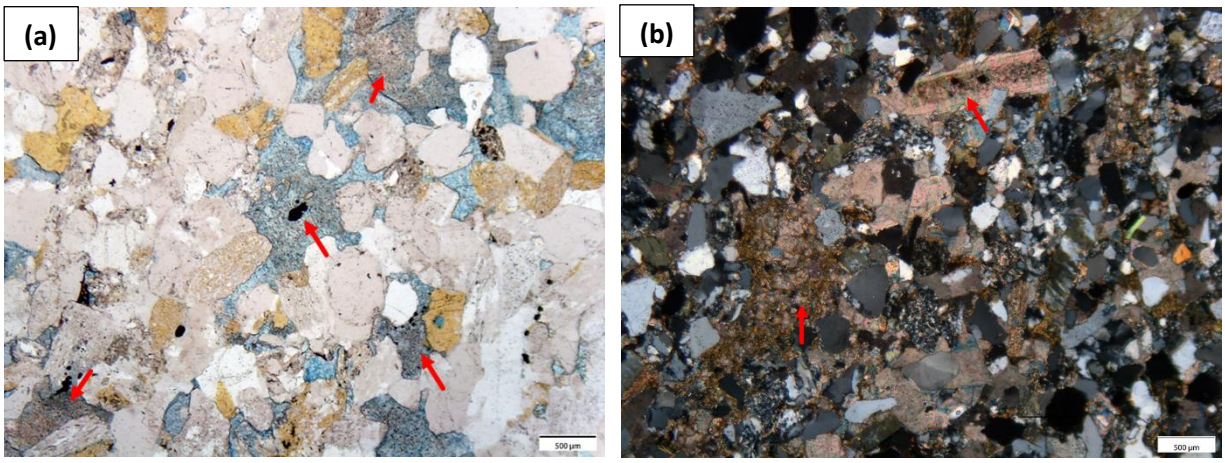

Figure 52 (a) Ferroan dolomite overgrowing early formed calcite cement (red arrows)/ calcitic fossil remain (centre of the image indicated by a red arrow pointing towards a clayey core. (b) Dolomite clasts (red arrows).

The compositional zonation suggests that dolomite precipitation is multiphase with an early finely crystalline predominantly non-ferroan dolomite possibly precipitating from hypersaline groundwaters and later more ferroan dolomite precipitating during burial. Brine influx from the Upper Germanic Trias Group (Röt, Muschelkalk and Keuper Formations) and/or reflux of connate waters from Zechstein Formation led to the development of alkaline conditions during later stages of burial causing the precipitation of ferroan dolomite. Another possible dolomite source can be the dolomite intraclasts seen in HS2, however they appear to be well-preserved with no pressure solution that might be responsible for redistributing dolomite.

The apparent difference in timing of quartz and ferroan dolomite cements although they have the same origin may have been caused by the fractionation of these phases due to differences in solubility trends. Worden & Burley (2003) found that carbonate cementation during late burial diagenesis is dominated by ferroan dolomite, which precipitates at similar or slightly higher temperatures than illite and quartz cements. Their finding suggests that the dolomite cementation can occur simultaneously with quartz precipitation(quartz and dolomite growing around two different grain boundaries and then meeting at a common interface) or after it (dolomite overlying quartz cement). Both of these cases are possibilities and coincide with the observations of the NLW-GT-01 thin sections.

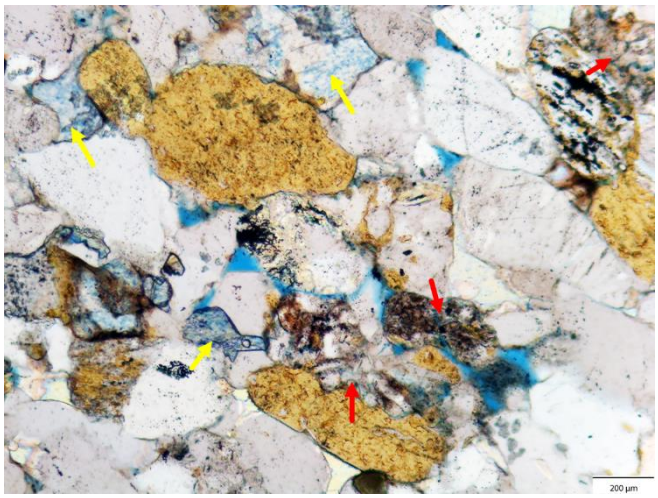

The remnants of dissolved grains showing limited pore-lining and pore-filling clays and often lacking dolomite cement within an otherwise pervasively dolomite sample likely implies that a second mineral dissolution/sample flushing phase took place during a late stage of diagenesis (see Fig.53).

Figure 53: Partially dissolved lithic fragments producing secondary porosity. Dolomite cement (yellow arrows) predominantly present in the primary pore space (dyed blue).

Calcium and sulphate bearing fluids percolating down from the overlying Triassic evaporites or the entry of Zechstein formation fluids were responsible for the localized anhydrite precipitation due to extremely poor permeability as a result of the cumulative effect of the previous diagenetic activities.

The calcium sulphate cement has locally been leached possibly by meteoric waters during uplift evidenced by the dissolution at the boundaries of the anhydrite grains.

The deeply buried sandstones (>4000mMD) in NLW-GT-01 have well-preserved detrital K-feldspar grains. The shorter distance of transport from the provenance (London- Brabant Massif) to the basin (West Netherlands Basin) explains the resistant to weathering during transport. In addition, the salt beds of the underlying Zechstein and the overlying Röt Formations bathed these cored Triassic sandstones with Na^+ and K^+ rich pore waters stabilizing the K-feldspars.

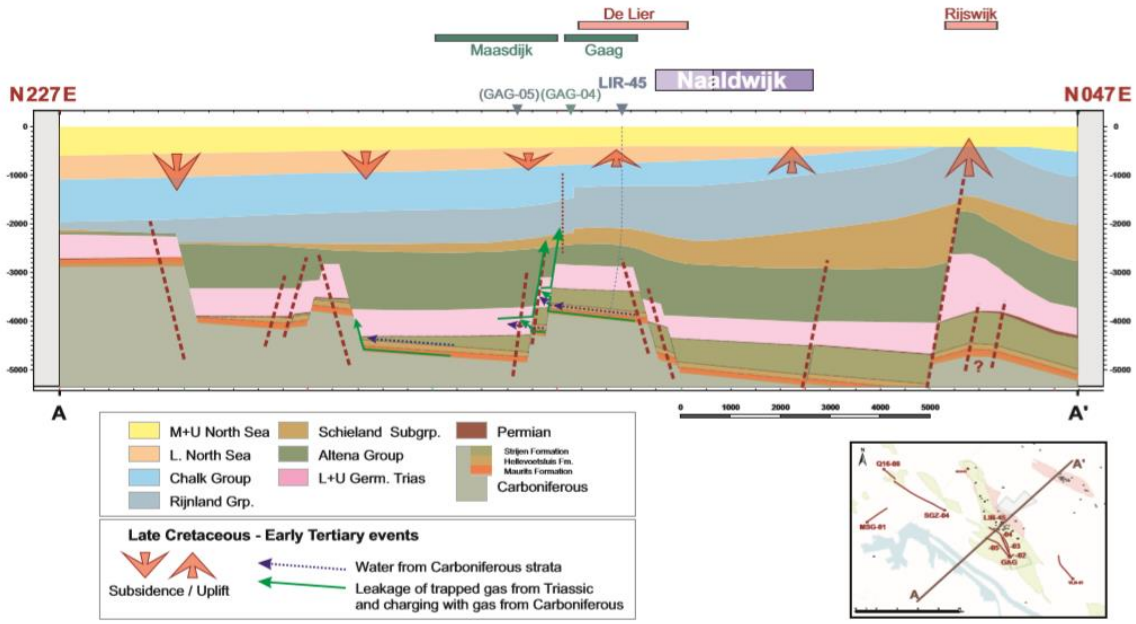

Figure 54: SW-NE cross-section through the Gaag/De Lier High and the Naaldwijk field (T&A Survey, 2013).

During the Late Cretaceous and Early Tertiary period, the structural unit south of the Gaag/De Lier unit underwent subsidence while the structural unit to the north experienced an uplift. However, the contact of the Triassic layers with the Carboniferous in the Naaldwijk area is normal (see Fig. 54). Due to no juxtaposition, the acidic Carboniferous waters were unable to enter the Triassic strata in the Naaldwijk leading to no creation of secondary porosity by K-feldspar dissolution. These reasons caused the K-feldspars to have a higher preservation potential.

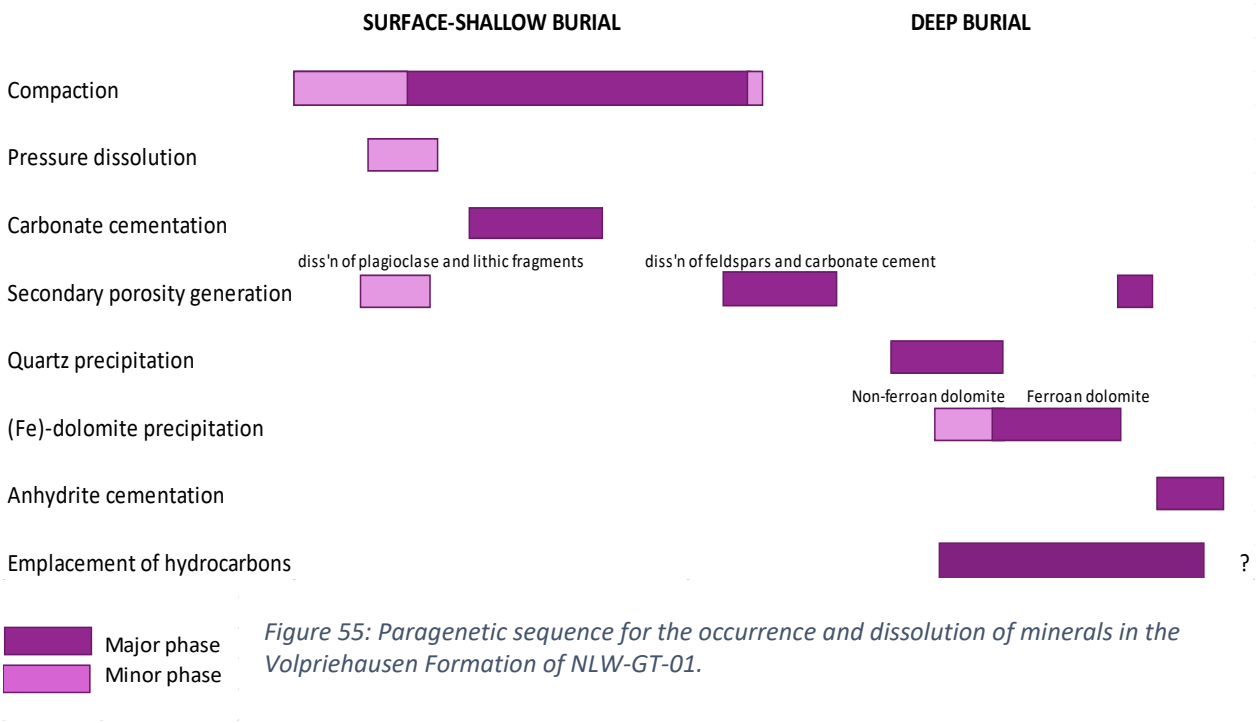

Figure 55: Paragenetic sequence for the occurrence and dissolution of minerals in the Volpriehausen Formation of NLW-GT-01.

5.6. FMI Analysis and Interpretation of Geological Features:

The Formation Micro-Imager data was acquired from the NLW-GT-01 well in the Naaldwijk field over an 8.5 in. section. This FMI data was procured on the 14th of February 2018 and covered an interval between 4110-4395m MD.

The fast formations of NLW-GT-01 were drilled with a water-based mud having a density of 1.19 g/cm^3 and a sonic velocity of 182µs/ft which is close to the optimal value for strong competent formations. The FMI images were acquired in high-resolution mode (spatial resolution of 0.51cm) in the 8.5-inch section.

5.6.1. Data quality

The acquired FMI data is of very good quality with well-expressed waveforms. The major conductive features with large apertures can be precisely correlated with the sonic reflections in most cases. Appreciable pad contact quality and continuity over the full trace of the features with absence of stick and pull events or borehole breakouts have resulted in good quality image data.

5.6.2. Data Interpretation:

The sedimentary and structural features between the depths of 4250-4280m MD were classified into three categories namely cross-beds represented in red, continuous and discontinuous conductive fractures indicated in blue and the continuous major conductive fractures with greater widths (Schlumberger, 2018) represented in green (see Schimdt projection below in Fig. 56a).

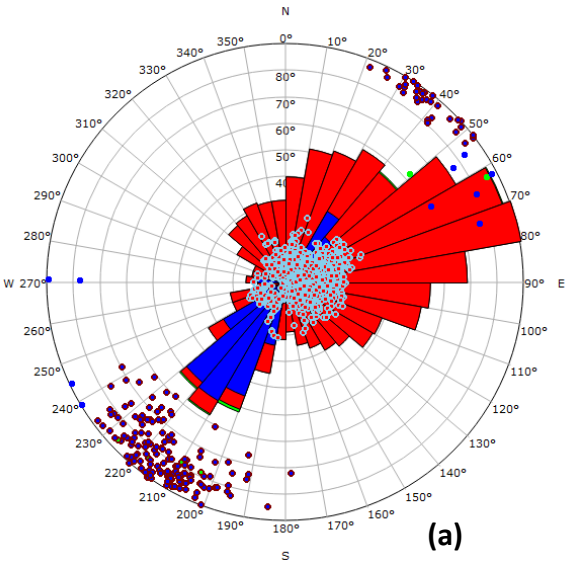

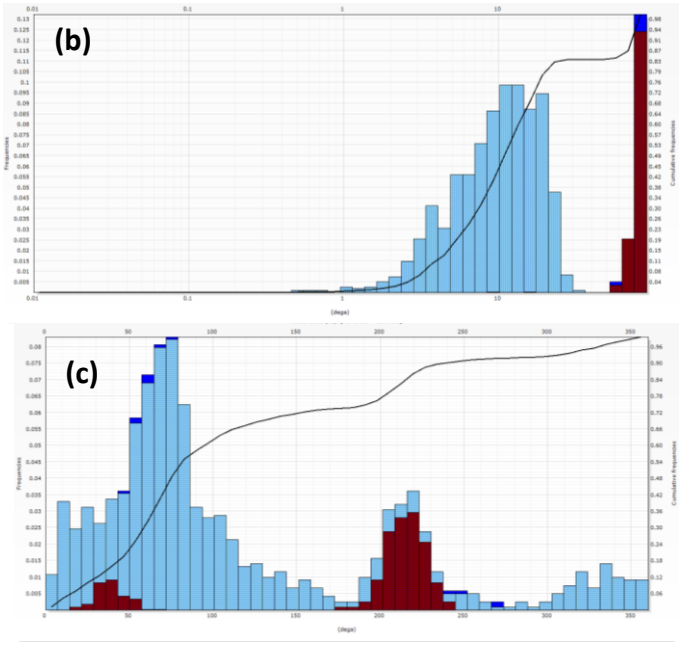

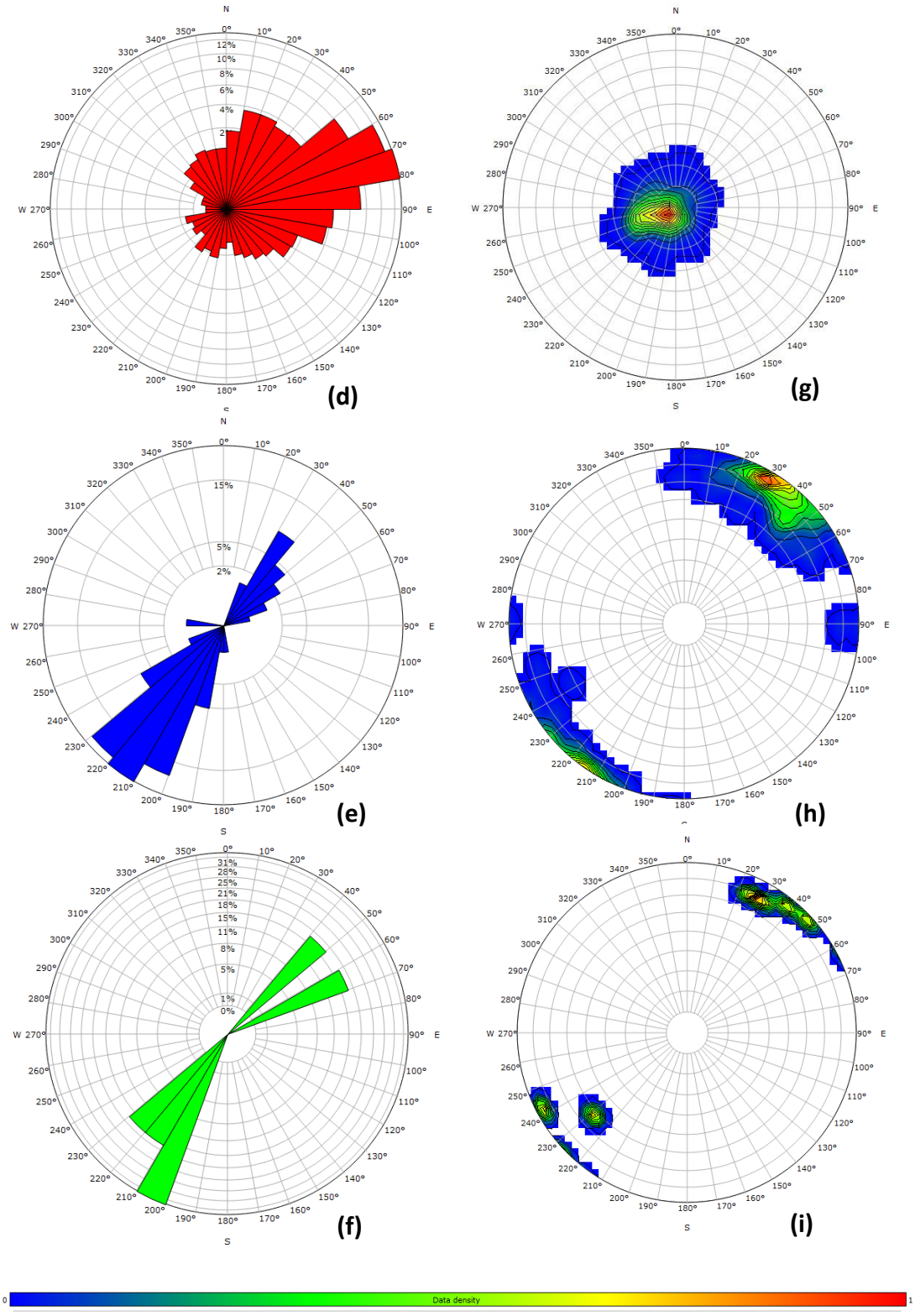

Figure 56: (a) Schmidt stereonet plot for all the interpreted features.(b) Dip histogram (c) Azimuth histogram (d)Rose diagram for the dip of the cross beds (e)Rose diagram for the conductive fractures striking NW-SE. (f)Rose diagram for major conductive fractures striking NW-SE. (g,(h),(i)) Data density for the cross-beddings, conductive fractures and the major conductive fractures respectively.

Fig.57 below is a broad overview of the interpreted geological features, their orientations, and distribution over the studied interval. The track adjacent to the reference is the Static FMI Log where sandy resistive units are displayed as white-yellow coloured intervals. These units become progressively darker in shade (brown) with increasing conductivity associated with the increase in the amount of shale. The fourth track represents the Dynamic Image Log which displays the depositional features in greater detail. The red, blue and green dip traces on the dynamic image log below signify the cross-beds, conductive fractures and major conductive fractures respectively. The first and second group stereoplot tracks reflect the true dip direction of the cross-beds and fractures respectively.

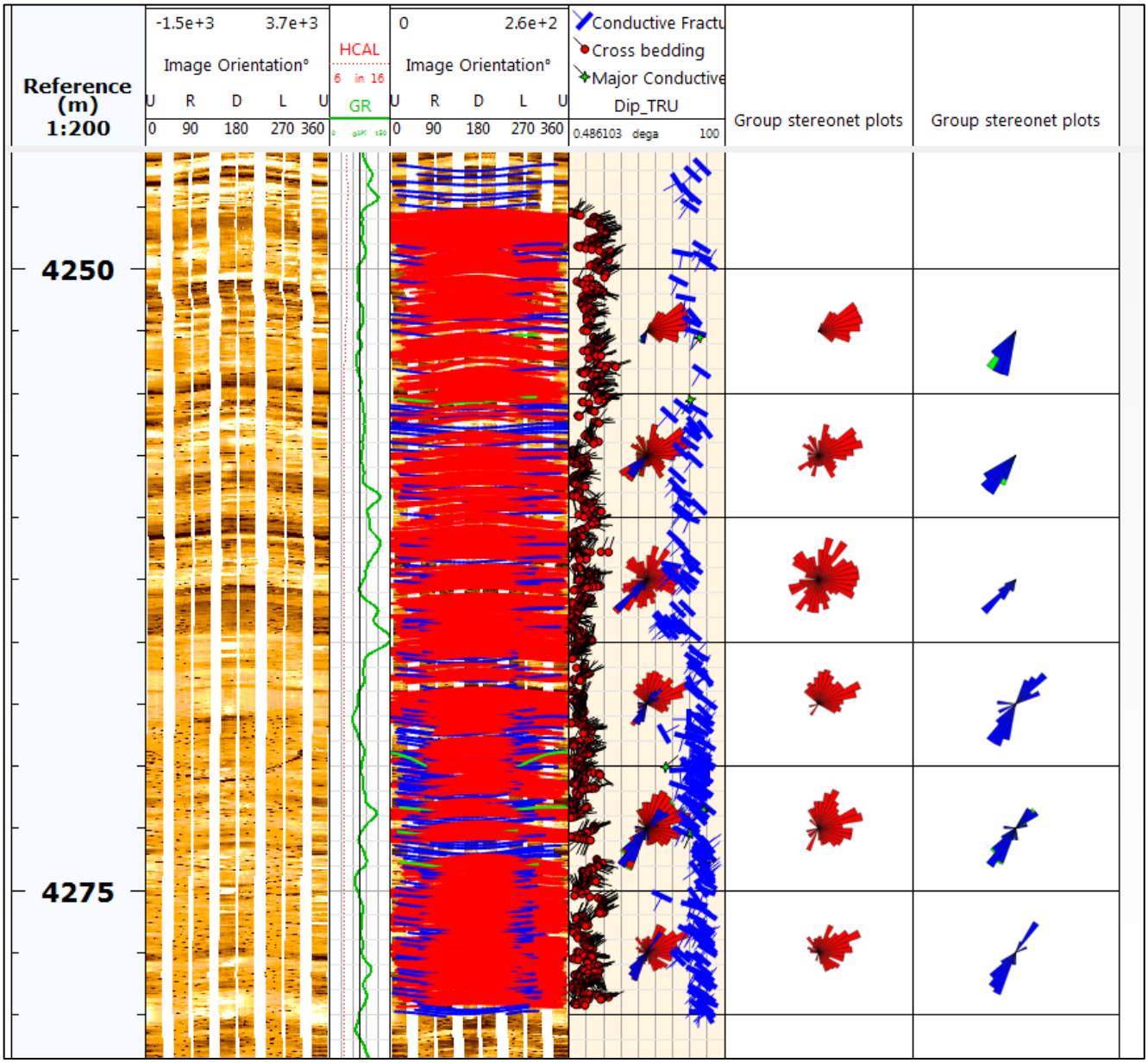

Figure 57: Dip picking carried out in the interval between 4250-4280m MD. The high gamma-ray (track 3) values can be correlated with intervals containing clay clasts and siltstone pebbles.

5.6.3. Stereonet Analysis

5.6.3.1. Sedimentary Structures

A total of 1217 features comprising of cross-beds and fractures were picked on the 8.5 in. section.

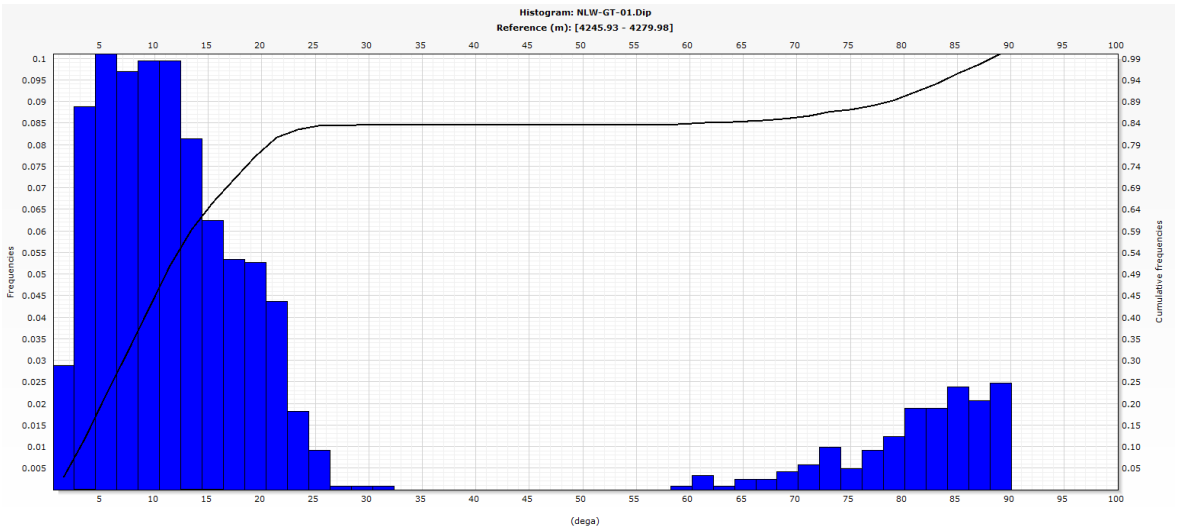

Figure 58: The cross-beds can be seen dipping between 0° -33° while the steeply dipping fractures have dip angles ranging between 58° and 90°.

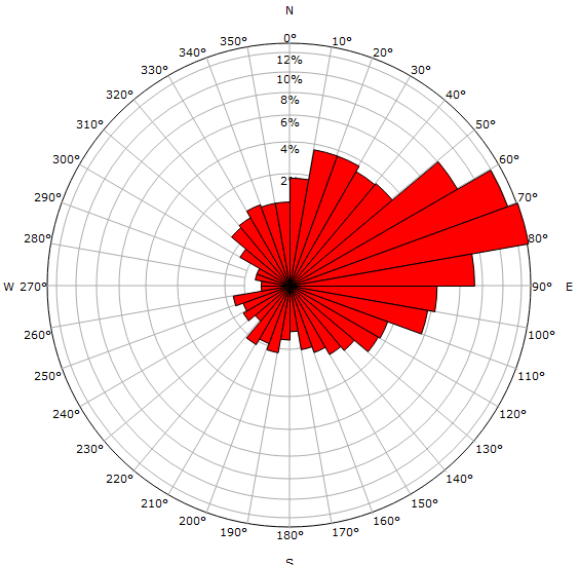

Figure 59: Stereoplot for the cross-beddings that show a dominant ENE paleodepositional direction.

The true dips of the cross-beds show quite a spread in their values with dominant paleocurrent trends towards NE, ENE, and ESE (see Fig. 59). Dip magnitudes show more consistent and less scattered values generally less than 35 degrees. However, majority of the cross-bed population have dip angles less than 15 degrees, see Fig. 58.

The recovered core and the FMI logs can be correlated in the following manner.

Box 2 Top: 4250.60m Bottom: 4251.60m

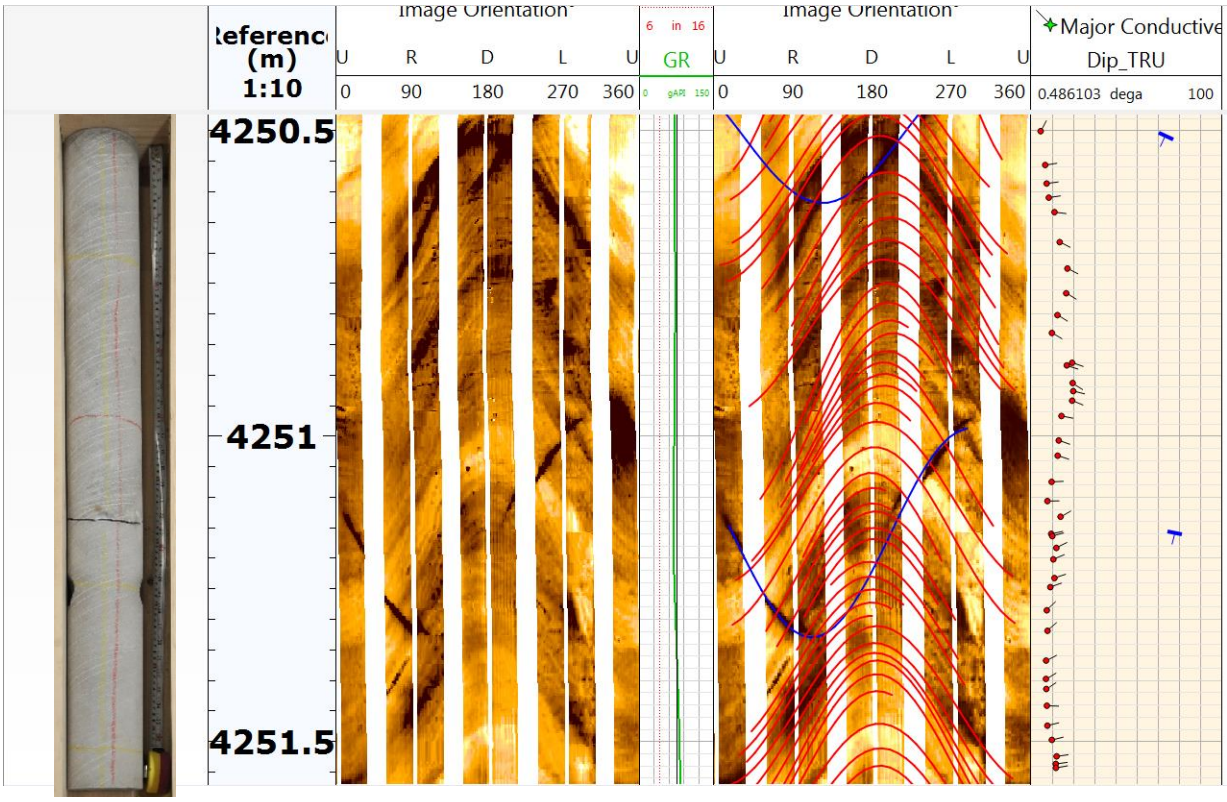

Figure 60: Resistive sand-rich (yellow) intervals and more conductive shale-rich intervals (brown) observed on the static (left) and dynamic (right) FMI logs. The blue fractures expressed as dark sinusoids on the dynamically processed FMI image exhibit high conductivity and dip 180° opposite to the beds.

In Fig. 60, the dip angles can be seen to vary between 5 and 25 degrees. There appears to be an increasing followed by a decreasing dip angle pattern as we move upwards. This trend is the expression of the transition from low angle bottomsets to the high angle foresets of one set followed by another. There is no preferential fining upwards sequence.

Box 4 Top: 4252.60m Bottom: 4253.60m

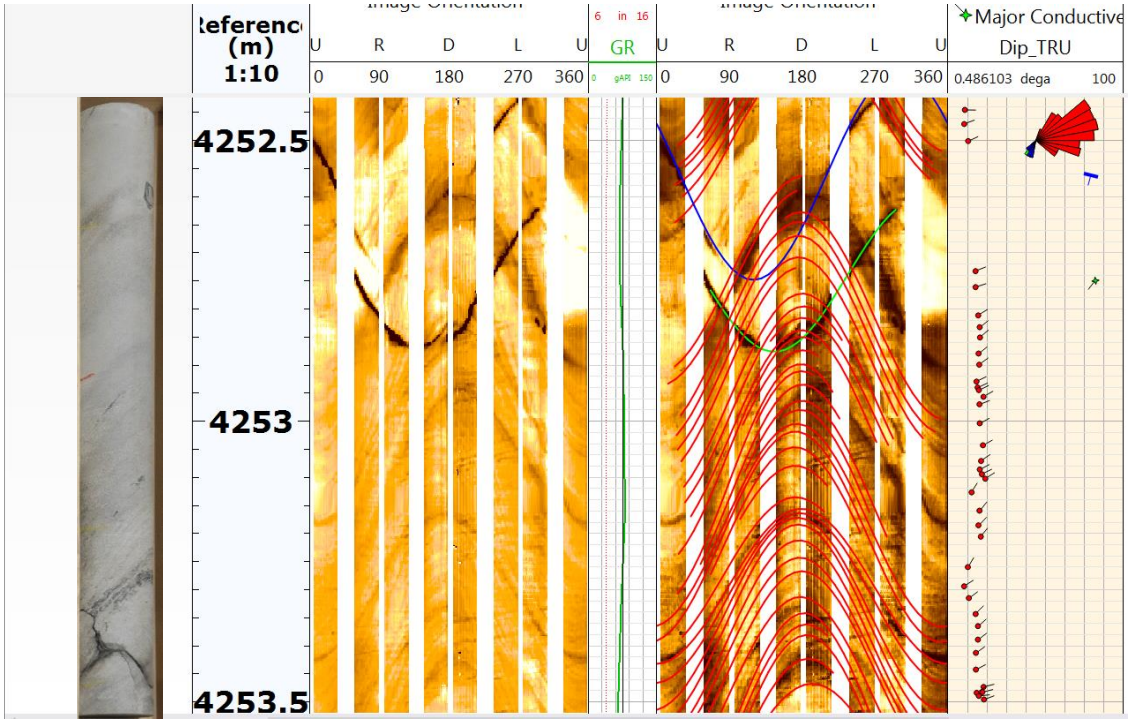

Figure 61: The dip plot indicates a unidirectional dip with a very low scatter over an interval of 1 m of sandy sediments symbolizing a low-sinuous system.

Box 10 Top: 4258.50m Bottom: 4259.50m

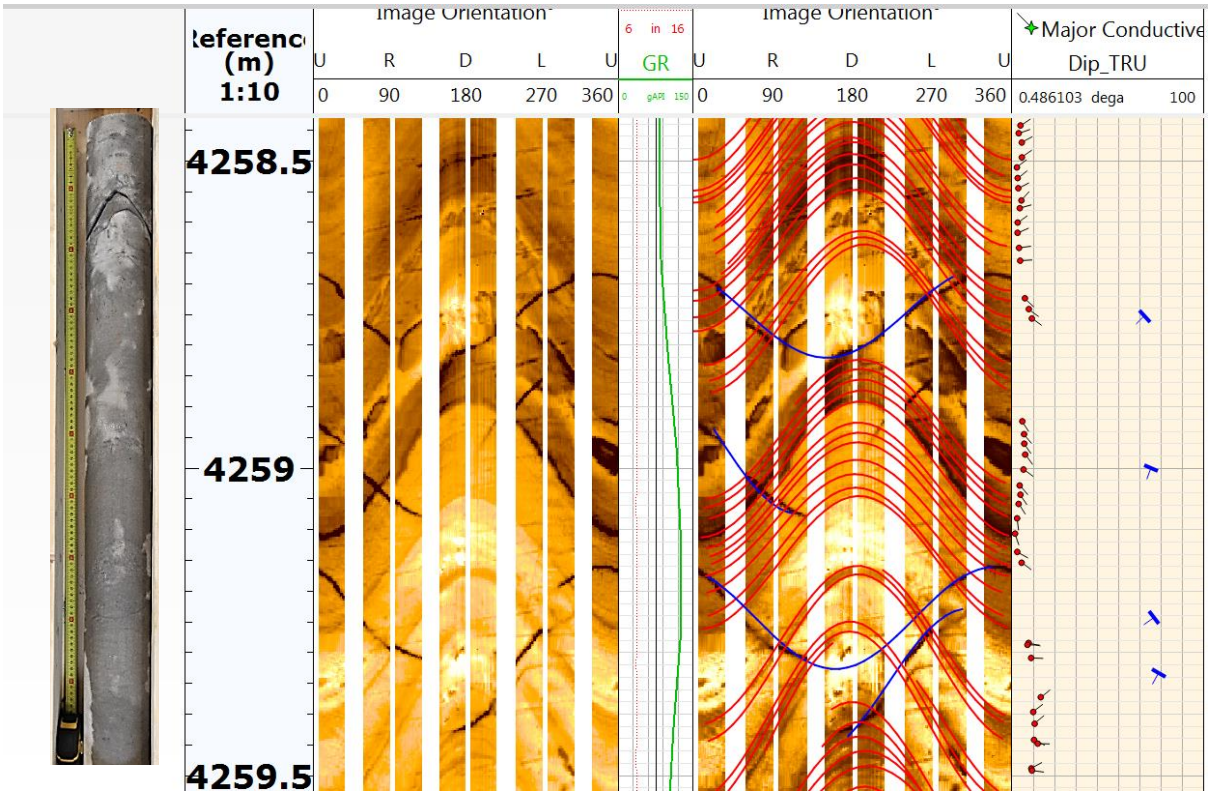

Figure 62: The intraformational siltstone clasts are well-imaged in the FMI log. The coarsening upwards trend associated with pebbles in the basal portion indicates the erosive nature of the channel causing a facies shift from floodplain to a fluvial channel.

Box 19 Top: 4266.70m Bottom: 4267.80m

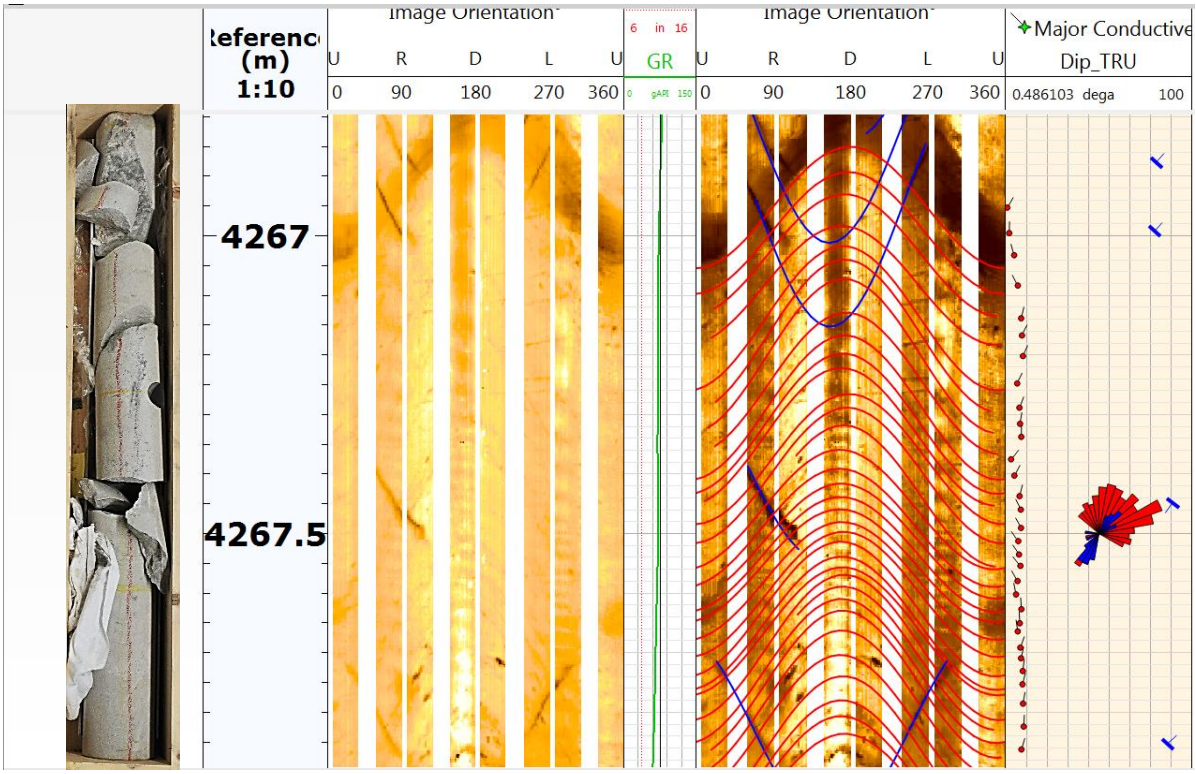

Figure 63: The light-yellow interval representing sand-rich facies shows a rather consistent dip magnitude with gradual changes in the dip direction represented by the rotation of the tadpole tails.

Box 22 Top: 4269.80m Bottom: 4270.80m

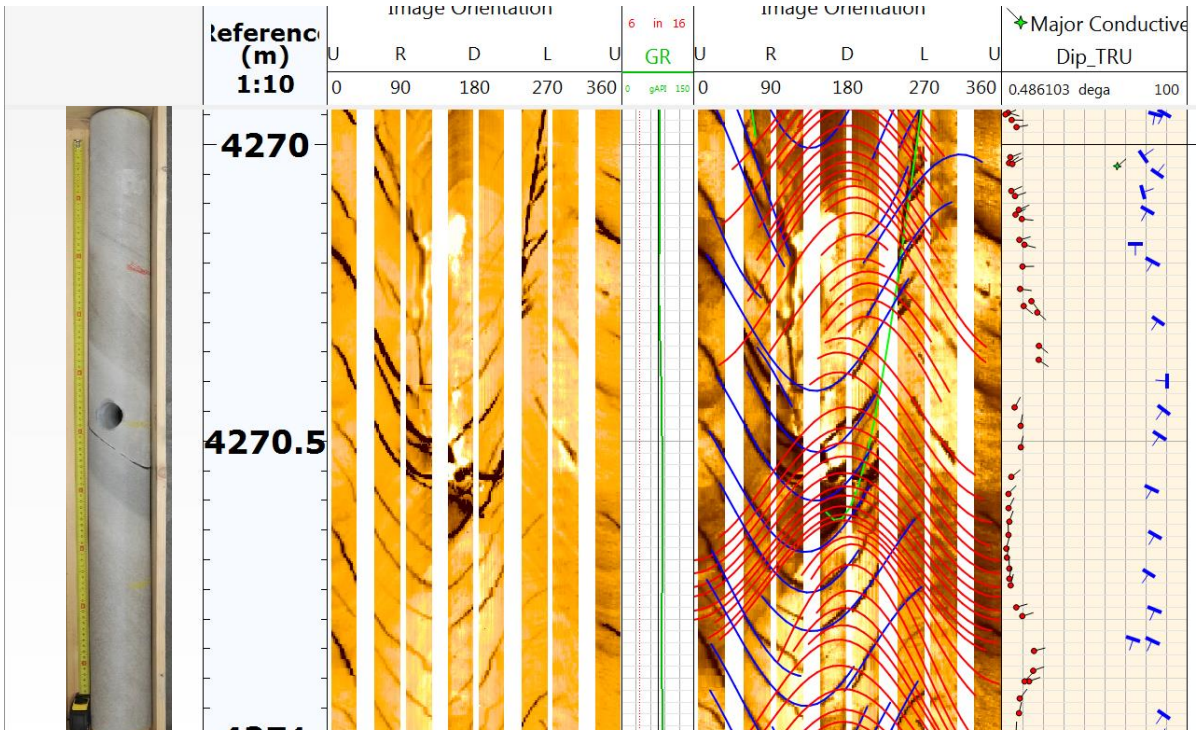

Figure 64: The dark-coloured, conductive fractures are distinctly visible, the transition from cleaner steeply dipping foreset sands to gently dipping shaly bottomsets of the next cross-bed set can be seen in the lower part. Abrupt dip angle changes occur due to the fractures.

Box 27 Top: 4274.90m Bottom: 4275.90m

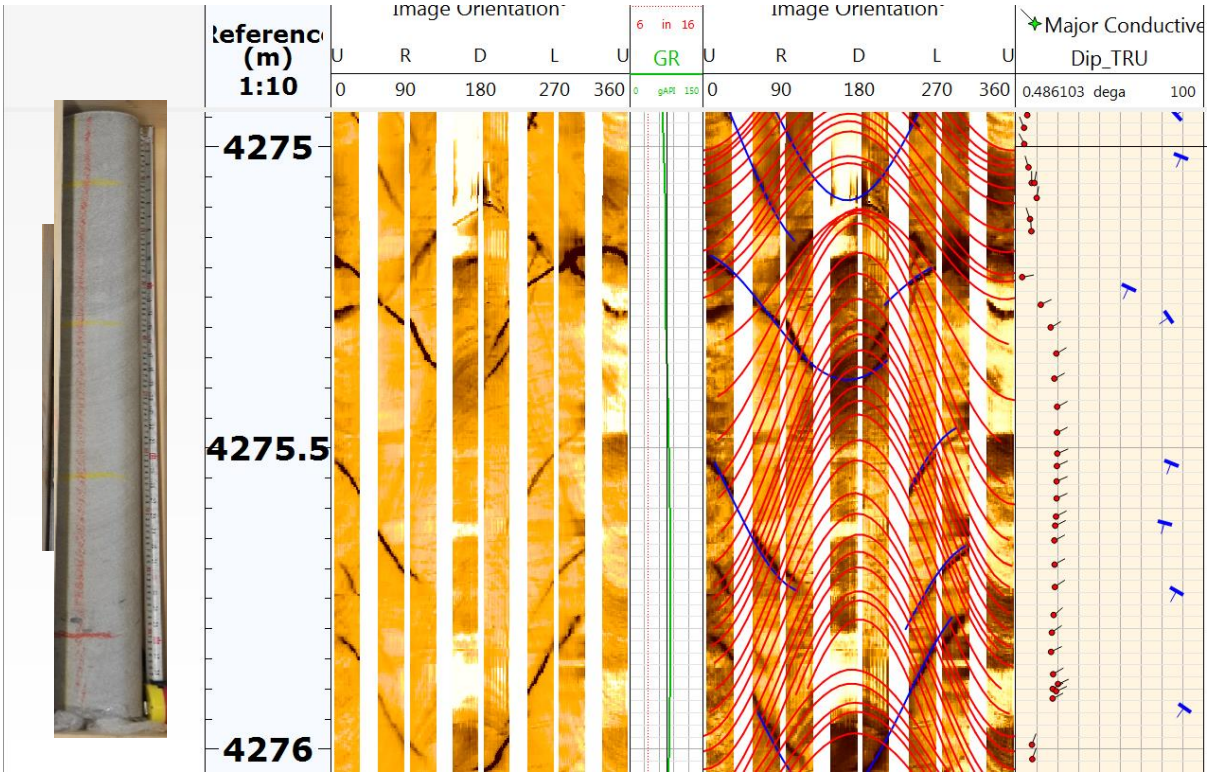

Figure 65: A fairly consistent dip magnitude and unidirectional dip distribution.

Box 29 Top: 4276.90m Bottom: 4277.90m

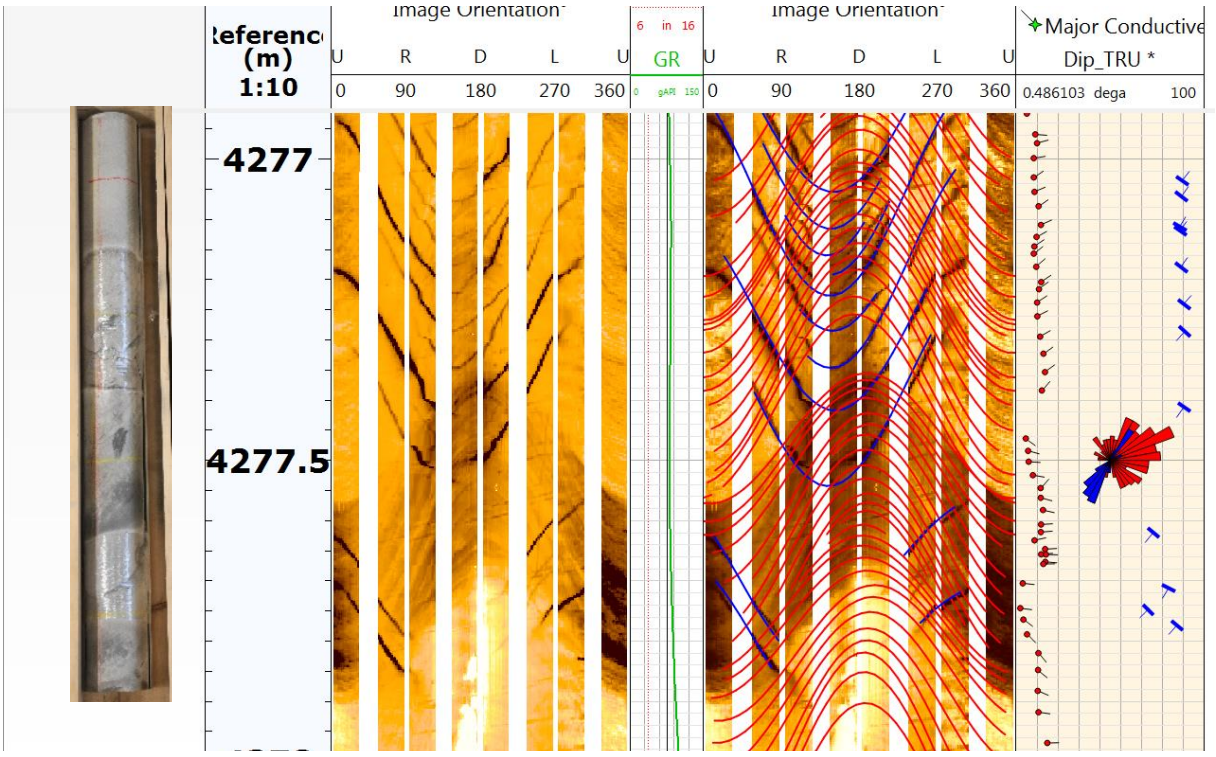

Figure 66: The pattern of progressively decreasing and gradually increasing dip angles due to the interval containing stacked bottomsets and foresets.

A stereoplot for the cross-stratified beds in the FMI images indicates ENE to be the dominant paleodepositional direction. Dips are organized in 0.1-1.0m thick packages with uniform dip direction (Fig. 61-66). The thickness variations depend on an axial or lateral cut through the stacked section. Each package constitutes of a set of trough cross-beddings. The stacking of these packages gives rise to a zig-zag true-dip pattern (low-angle bottomsets overlain by high-angle foresets) visible in the entire interpreted interval. The subtle clockwise or counter clockwise rotation (bimodality) of the tadpole plot can be explained by taking a vertical section of stacked cross-beds, See Fig. 67 (c).

The absence of appreciable fining upward successions rules out the possibility of coarse-grained high-energy meandering river systems (Donselaar & Schmidt, 2005). Also, facies corresponding to accretionary point-bar or braid bar deposits were not observed in the core. Studies in the past have concluded that the Triassic sediments in the West Netherlands Basin were deposited by a low sinuous fluvial system. However, the distribution of the foreset dip directions is not entirely unimodal but shows a large scatter.

Donselaar & Schmidt (2005) conducted a research using the geometric model of Luthi, et al. (1990). This model establishes a relationship between the ellipticity (ratio of the axis along the transport direction (d) over the axis perpendicular to transport (b1) in a semi-ellipse) of the trough cross-beds and the dip distribution pattern (see Fig. 67(d); Donselaar & Schmidt, 2005). It was found that the frequency distribution becomes bimodal if ellipticity of the trough cross-bedding is greater than 1 due to the over-representation of the two sides of the semi-ellipse. Also, the frequency distribution becomes significantly more bimodal with the increase in the ellipticity (Donselaar & Schmidt, 2005). Thus, with the decrease in the curvature of the spoon-shaped trough cross beds, a unimodal azimuth distribution is reached. Thus, the bimodality of trough cross-beds seen in NLW-GT-01 may be attributed to their possible elongate shape where ellipticity is greater than 1.

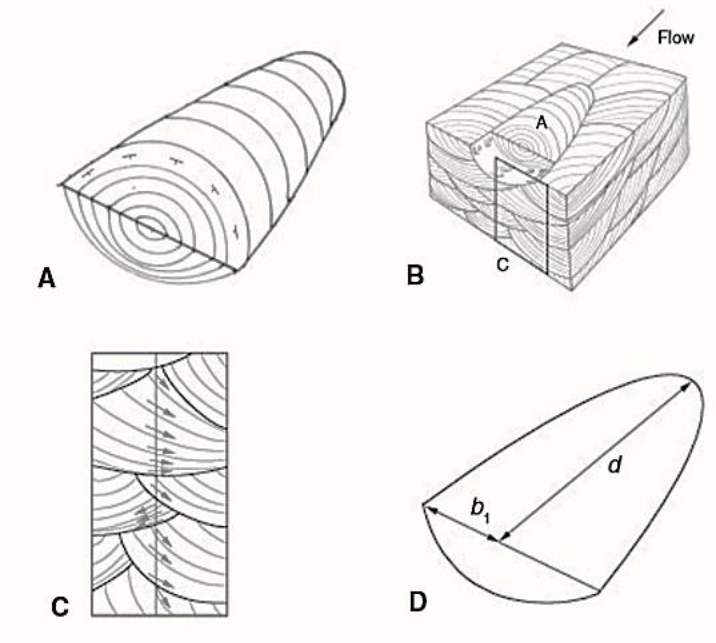

Figure 67: (a) Dip variation in the fill of the cross-bedding. (b) Stacked sets of trough cross-beds. (c) Dip variation in a vertical section (d) Ellipticity of the trough cross bed expressed as the ratio (d/b1) between the axis parallel to flow (d) and the axis of the semi-ellipse normal to the flow b1. (Donselaar & Schmidt, 2005)

5.6.3.2. Fractures

The fractures correspond to high-angle dark sinusoids on the FMI amplitude image. They show a dominant NW-SE strike trend. Their dip magnitudes range between 58° and 90°. The strike orientation of these fractures lies parallel to the present-day maximum horizontal compressional stress (S_{Hmax}), which also strikes NW-SE (Heidbach, et al., 2018),see Fig. 68(a, b). This gives rise to the possibility that these fractures might be open and hydraulically conductive. However, on examination of the core, open fractures were not found. Fractures are maximally visible when oriented perpendicular to the wellbore and minimally visible when oriented (close to) parallel to the wellbore. The intensity of the fractures observed on the FMI does not show any relatable correlation with the frequency of fractures observed in the cylindrical core. This might be due to the rupturing of the core along the weak fracture planes during the acquisition of the core from the subsurface and/or filling of open fractures by mud filtrate. Slabbing of the core would provide insight about the nature of the fractures which can then be distinguished as open or closed (infiltration of the mud filtrate).

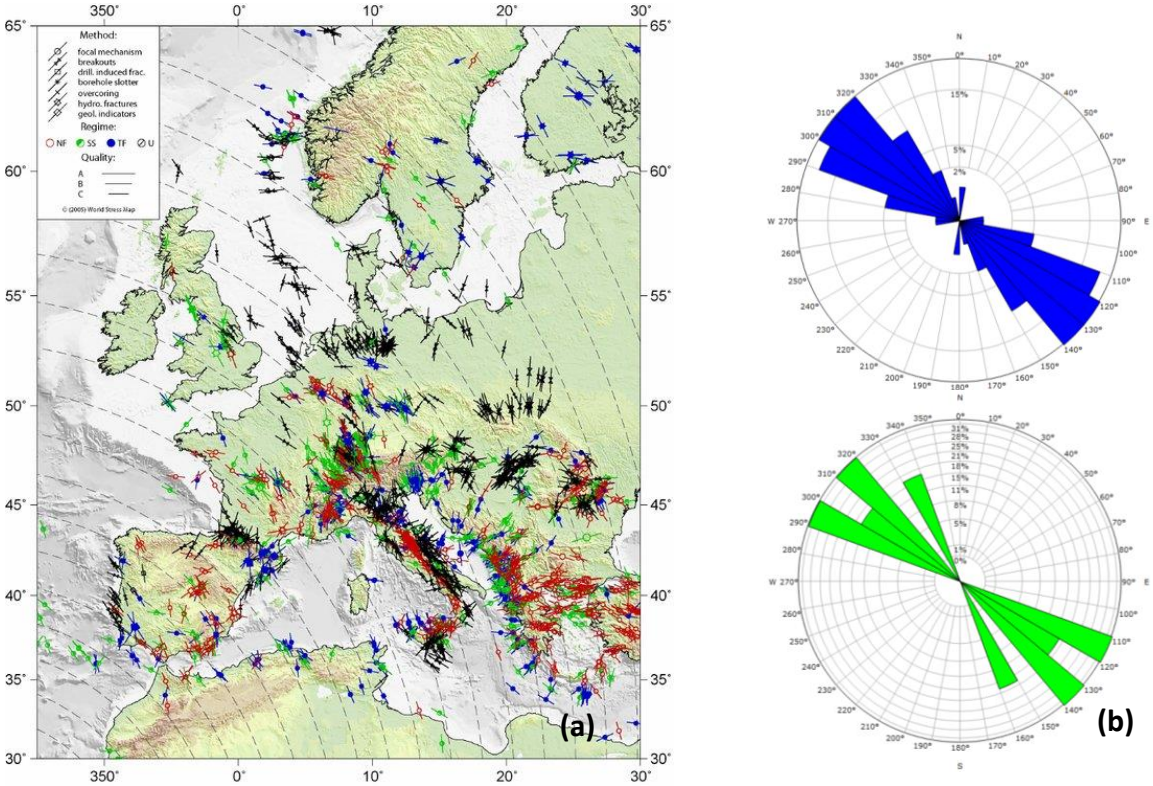

Figure 68 :(a) The European stress map. Red- Normal faults (NF), Green-Strike-slip faults (SS), Blue-Thrust faults (TF) and Black-Unknown regime(U). The orientation of the largest horizontal principal stress (S_{Hmax}) is represented by a line and the length of the line is proportional to the quality. (Heidbach, et al., 2019) (b) The orientation of the fractures observed in the Naaldwijk well NLW-GT-01.

Worum et al. (2005) characterized six regional domains based on significant changes in the fault pattern in the West Netherlands Basin and the Roer Valley Graben (see Fig. 69). Domains C and F consist of the northern part of the Roer Valley Rift System and the West Netherlands Basin respectively as well as the Zandvoort Ridge, Maasbommel High, and the Peel Block. The dominant direction in domains C, F, D, and E are N148°, N130°, N162°, and N154°. The fault patterns in domains C and F are unidirectional, which means that the pre-existing lineaments were so weak that they were always reactivated before differently oriented faults could develop during the Mesozoic deformation. An N146°-148° peak present in domain C also occurs in domain D but is absent in domain E. Thus, domain C and D have inherited the direction of the pre-existing weak lineaments. Different crustal domains occur in the northern and the southern parts of the investigated area. The Mid-Netherlands Weakness Zone located in the middle of the Roer Valley Graben and slightly north of the center of the West Netherlands Basin manifested itself and controlled the crustal domains (Worum, et al., 2005).

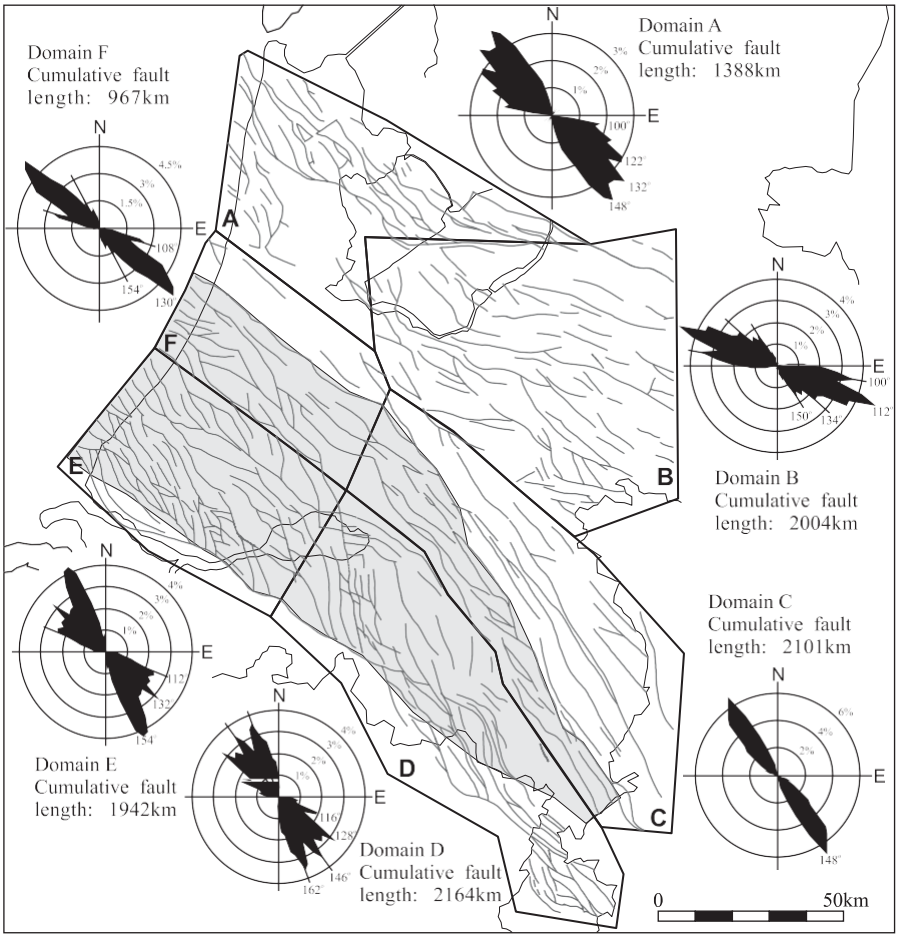

Figure 69: Map illustrating the Early-Middle Mesozoic fault patterns. The rose diagrams represent the percentage of cumulative fault length/orientation for different domains. The study area comprises of domains C to F (Worum, et al., 2005)

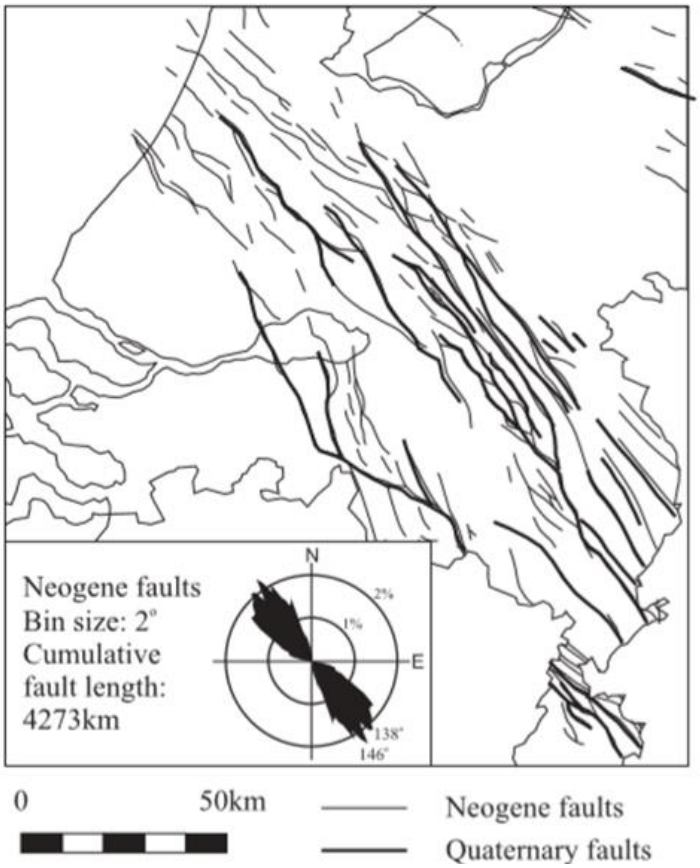

Figure 70: Map illustrating the Neogene and Quaternary fault patterns observed in the area of study. (Worum, et al., 2005)

As seen in Fig. 69 (Worum, et al., 2005) above, NW-oriented faults can also be observed in the Neogene indicated in the rose diagram (see Fig. 70; Worum, et al (2005)). The primary fault orientation direction is N148° which reflects the stable Neogene stress pattern while a new peak is observed at N138° (Worum, et al., 2005). The upward rotation of the reactivated N132° and N148° Mesozoic faults can explain this new fault peak at N138° (Worum, et al., 2005). The fracture pattern observed in NLW-GT-01 shows a dominant peak between N120°-140°. This could mean that these fractures are fault-related and not diagenetic, formed in an association with the Mesozoic and Neogene fault patterns. In addition to this, the alignment of the stress orientation of the NLW-GT-01 fractures with the present-day maximum horizontal stress could also mean that these fractures are not local but occur at a regional scale.

With the determination of major sediment transport direction and the orientation of the fractures through FMI analysis, it is now important to look at the possible sediment suppliers during the Triassic. This will be discussed in much greater detail in the following chapter.

5.7. Paleogeography

Widespread playa dominated the South Permian Basin during the Early Triassic with development of large lakes which left a limited record of the oolitic Rogenstein shoreline deposits (Geluk & Rohling, 1997; Bachmann, et al., 2010) .The Bunter sandstone terminal fluvial systems prograded towards the centre playa region. During the Early Triassic rifting phase, the Bohemian and the London-Brabant massifs (see Fig 71(a); Bachmann, et al., 2010) remained essential sources of clastic detritus, whereas the Rhenish Massif gradually subsided beneath the erosional base level due to thermal re-equilibration of the asthenosphere-lithosphere system shedding detritus in the surrounding areas (Bachmann, et al., 2010).

Compared to the Lower Buntsandstein, syn-sedimentary faulting resulted in a highly differentiated thickness pattern of the Main Buntsandstein. Fluvial systems from the Variscan hinterland built out northwards over the Southern Permian Basin during base-level fall that accompanied rifting (see Fig. 71(b); Bachmann, et al., 2010). Building out of the fluvial systems throughout the Southern Permian Basin occurred in a cyclic, contemporaneous way which strongly suggests a climatic control on sediment dispersal (Bourquin, et al., 2009; Mckie & Williams, 2009; Bachmann, et al., 2010). Tethyan monsoonal seasonal precipitation over the Variscan Mountains which were active during the Early Triassic weakened during the Middle-Late Triassic limiting the areal extent of the sand-rich fluvial flows draining the Variscan Mountains (Mckie & Williams, 2009) . This led to increased aridity in the basin. The fluvial channels supplied limited sediments and later became seasonal to dormant during the aeolian deposition of the Hardegsen which caused the transition of the areas without desert lakes into desert sandflats at the basin centre.

The Variscan Hinterland was a barrier for humid air as it separated the South Permian Basin from the Tethys. The air loses its moisture content as it rises over the mountains and as a result, dry air would descend onto the basin. The denudation of the Variscan Mountains and the connection to the Tethys during the Middle Triassic resulted in a humid climate which manifested itself by the formation of coaly material in the Lower Keuper. Before the marine transgression of the Lower Muschelkalk Sea, the Variscan remnants ceased to be the major contributor of the clastic influx (Geluk, 2005).

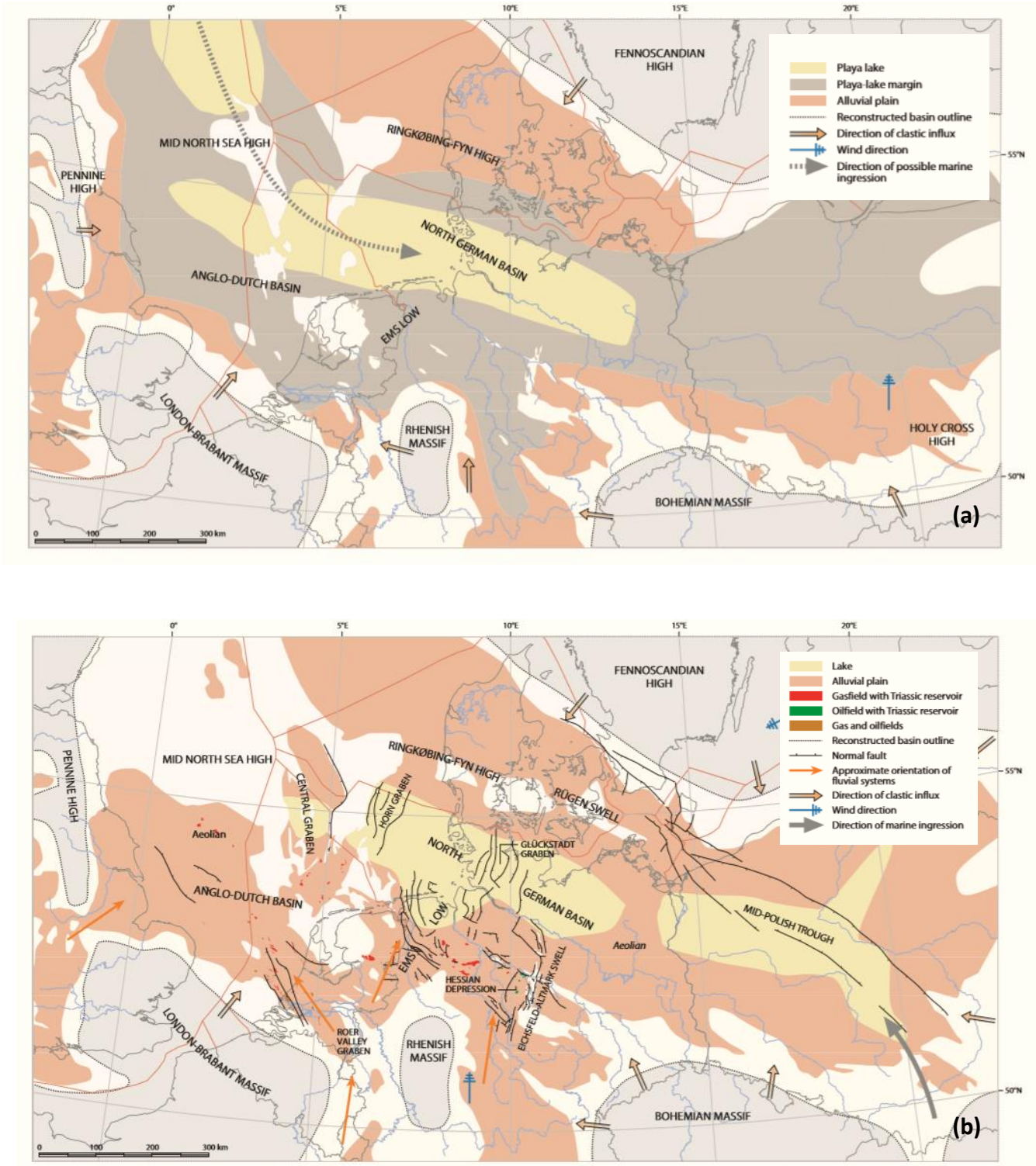

Figure 71: Present-day distribution and the facies map of the (a) Lower Buntsandstein Subgroup (Late Permian-Early Triassic) (b) Middle Buntsandstein Subgroup (Olenekian to Early Anisian) and their equivalents. (Bachmann, et al., 2010)

The cross-beddings within a sand-prone channel-fill association are indicative of the direction of the paleoflow. The paleocurrent data was obtained from the dip interpretation performed on FMI log of NLW-GT-01 while for NDW-01, the data was acquired from nlog site. The Nederweert Sandstone Member (NDW-01) forms a part of the Lower Buntsandstein deposited in the Early Triassic. It shows a bulk sediment transport direction towards the NNW which suggests the influx of sediments from the Rhenish Massif (denudated during Early Triassic Bachmann, et al., 2010) carried by a low sinuous river system (see Fig. 72). The intricate architecture of the fluvial bar forms causes the large scatter in the dip data as seen in Fig. 72,73 (a, b). The proximal position of the source to the location of NDW-01 is explained by fine to medium grain-size and the poor-moderate sorting of the Nederweert sands (Britton, 1979).

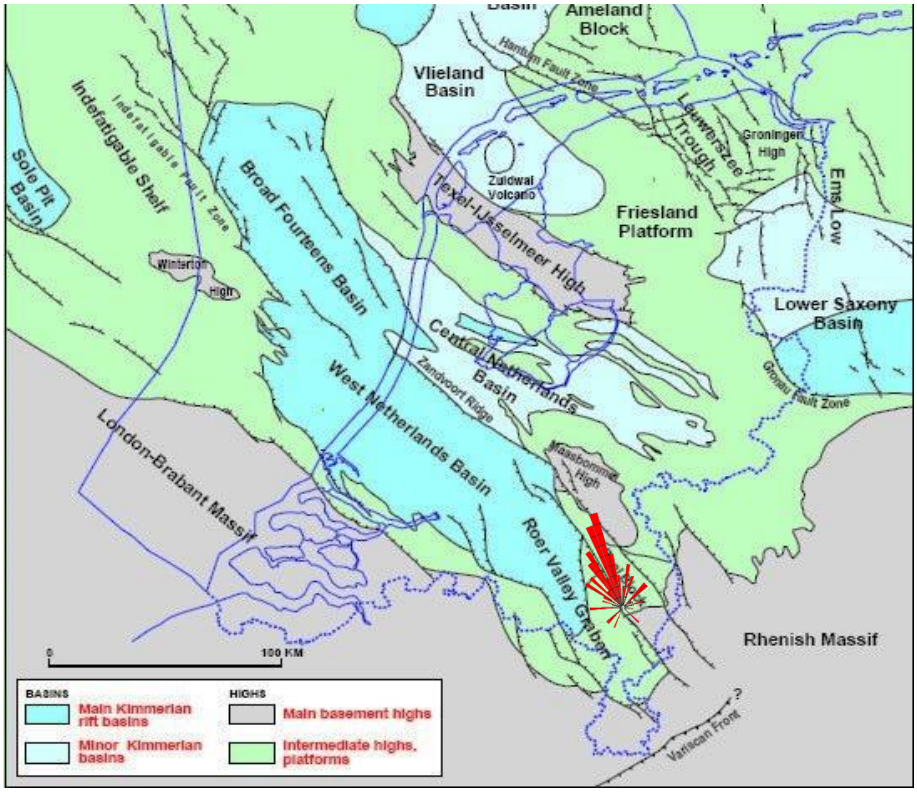

Figure 72: Paleoflow direction that lead to the deposition of Nederweert Sandstone Member in the Roer Valley Graben.

The dominant paleoflow direction for the lower parts of the Detfurth Formation and the upper parts of the Volpriehausen Formation is towards ENE (see Fig. 73). This signifies that the clastic influx came from the London-Brabant Massif. The sediments were transported by means of confined fluvial channels resulting in the stacked cross-beds. The Volpriehausen Formation comprises of sand-rich facies which becomes more dominated by shale-rich intervals along a NW-SE cross-section of the West Netherlands Basin (see section 5.2.5). The Volpriehausen Claystone Member is undeveloped in the West Netherlands Basin as compared to the Roer Valley Graben (Matev, 2011).This implies a primary fluvial channel closer to the south-western part of the basin whose transport energy decreases as it travelled to the distal end in the south-east.

`

This complements the possibility of a braided system originating from the London-Brabant Massif flowing onto south-western part of the West Netherlands Basin where it deposits sandy sediments and then flowing into the Roer Valley Graben where it deposits the finer clayey material. Due to the shorter transport direction, the feldspars observed in the thin-sections of NLW-GT-01 appear to be well preserved, making the sediments mineralogically immature. During the Dinantian times, the sea transgressed onto the peneplain of the London-Brabant Massif (DINOloket, n.d.; Rijkers, et al., 1993). This resulted in the development of a vast carbonate platform on and around the massif. During the Late Permian times, fine-grained clastics, carbonates, and anhydrite were deposited on this platform. The possibility of the London-Brabant acting as a sediment source for the Volpriehausen Formation in the well NLW-GT-01, explains the occurrence of skeletal carbonate material within the Triassic sands.

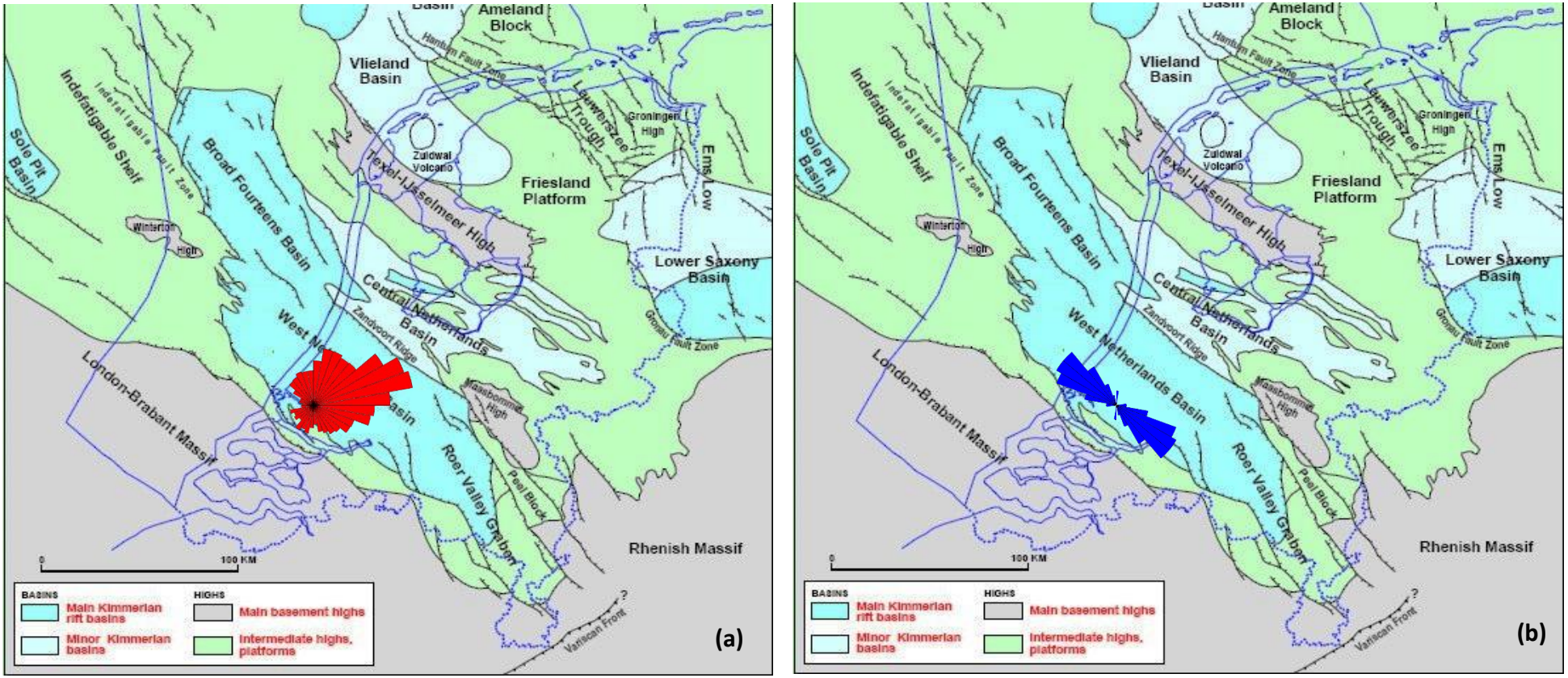

Figure 73: (a) Paleoflow direction that lead to the deposition of the cored Vopriehausen sandstones in the Naaldwijk field. (b)Strike orientation of the fractures in NLW-GT-01

5.8. Depositional Environment

The reddish pink-coloured NDW-01 core is severely trough cross-bedded. Trough cross-beddings present in the core indicate that deposition took place, at least part of the time in confined channels. During the deposition of the Nederweert Sandstone Member, confined braided fluvial systems carried sediment northwards from the Variscan hinterland onto arid dune fields and playa (see Fig. 74).

High-angle and horizontal to sub-horizontal cross-beddings characterize the NLW-GT-01 core. The presence of clayey intraclasts reflects the fluvial origin of the NLW-GT-01 sandstones. The lack of vertical grain-size trends and the organized successions of lithofacies suggests that these channels were rapidly shifting. The siltstone-claystone alternation observed in the interval of 4260.6-4261.6m indicates that the periods of sand deposition were alternating with periods of restricted sand influx, during which lacustrine conditions prevailed within depressions. This alternation may be ascribed to intermittent tectonic activity or alternatively to autocyclic mechanisms such as channel shift. Thinner claystone intervals may represent deposition in inactive or abandoned channels or suspension settling after flooding stages. Absence of bioturbation in these beds indicates that the damp conditions did not last long enough to allow burrowing organisms to establish. The depositional setting of NLW-GT-01 is characterised by a braided fluvial system (see Fig. 75).

The wireline log expression of the Upper Volpriehausen Sandstone Member is similar to the that of the Lower Volpriehausen Sandstone Member. However, the main difference is the increase in the lateral variation of these deposits. The Volpriehausen Formation shows characteristic differences in the south-western and south-eastern part of the West Netherlands Basin. In the southwestern region, the formation is more sand-rich implying a proximal position to the major fluvial channel while towards the south-eastern area massive shales define the Volpriehausen Formation indicating a more distal location from the main channel. The transition between the sand-rich to shale-rich facies along NW-SE strike occurs at different points for the Upper Volpriehausen and the Lower Volpriehausen Sandstone Members characterizing a lateral channel shift of the fluvial body, see section 5.2.5. The Detfurth Formation marks a transition period between the fluvial dominated deposits of the Volpriehausen Formation and the aeolian deposits of the Hardegsen Formation.

The Tethyan monsoons which were active during the Early Triassic became weaker during the Mid-Late Triassic limiting the extent of the sandy fluvial systems draining off the Variscan Mountains. The lack of water supply resulted in fluctuations of the groundwater and the playa-lake level. This led to an increase in the accommodation space and/or decrease in fluvial sediment supply resulting in a facies shift from fluvial to floodplain or playa lake settings (Mckie & Williams, 2009). Thus, the preservation of alternating fluvial and aeolian sediments characterize an alternating wet and dry climatic period (Bourquin, et al., 2009).

The extensive lateral distribution of cyclic sedimentation patterns of the Buntsandstein from the basin centre to basin margin and their independence of lithofacies signifies that these

patterns represent sequences of an extrabasinal origin (Geluk & Rohling, 1997). The cyclicity is hierarchical and this rule out the possibility of tectonics (Geluk & Rohling, 1999). At this point, it is not possible to distinguish the depositional cyclicity due to climatic from autocyclic controls such as channel migration or fan-lobe shift.

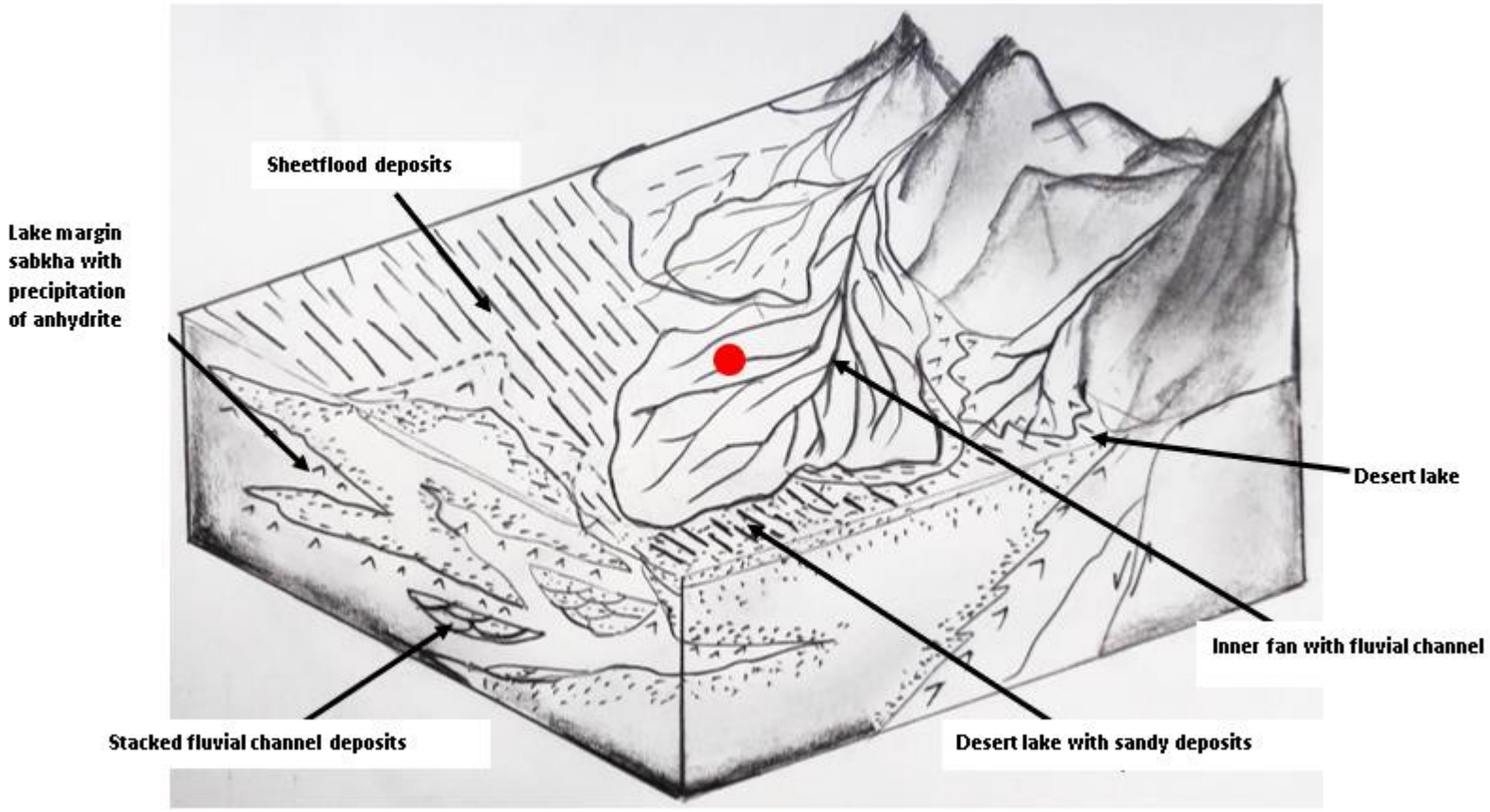

Figure 74: Conceptual depositional model for NDW-01, the red dot indicates the possible well location.

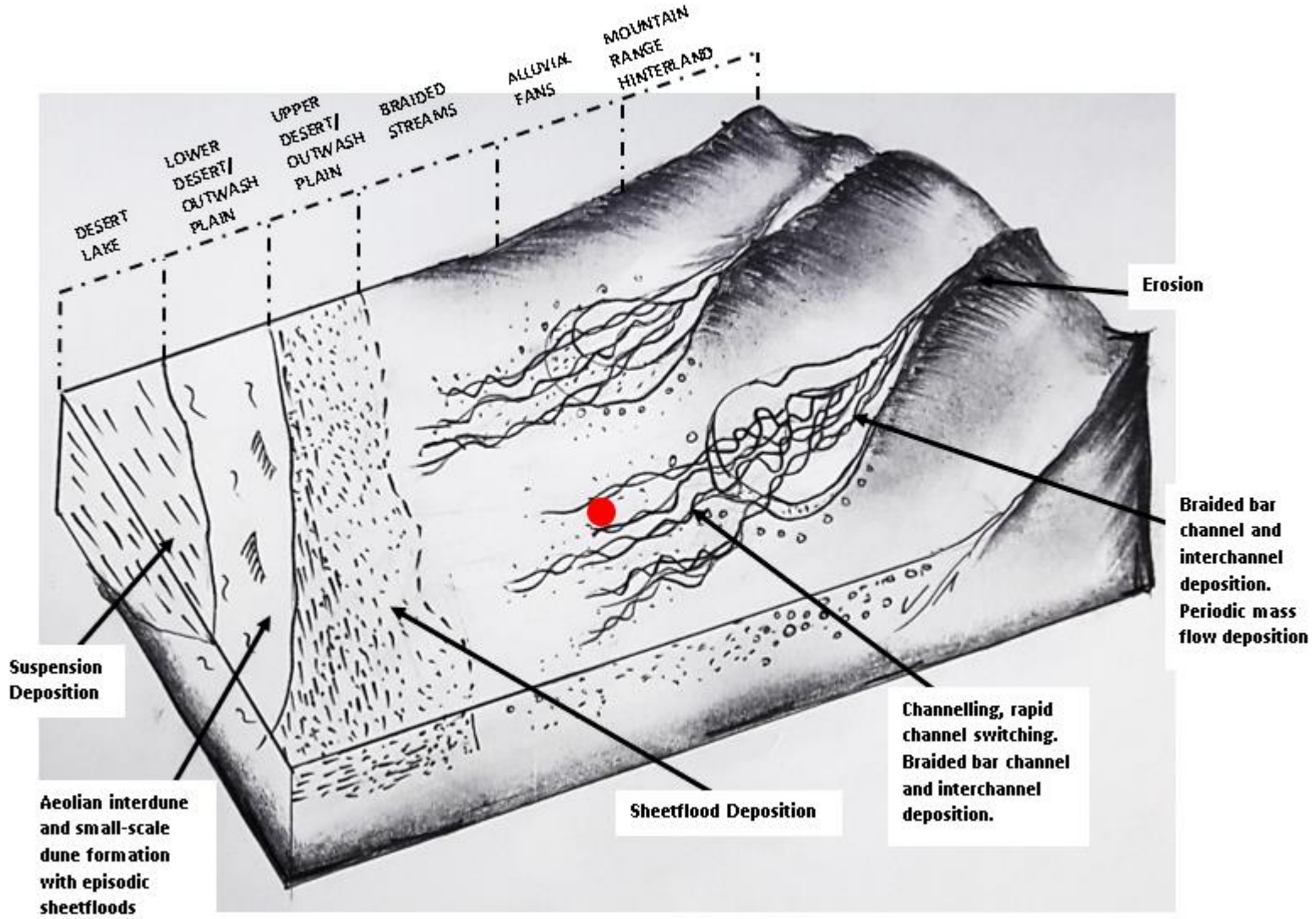

Figure 75: Conceptual depositional model for NLW-GT-01, the red dot indicates the possible well location.

5.9. Comparison with pre-drill estimates and reports

T&A Survey and TNO both conducted the pre-drill evaluations of NLW-GT-01 and held opposing views on the expected permeability values. On one hand where T&A predicted permeability range between 10-500mD with a median of 100mD, TNO stated the possible range would be between 10-15mD with a maximum value of 350mD. T&A backed their claim by the similarities in the depositional environment of the Main Buntsandstein Subgroup and the mineralogical and diagenetic resemblance despite their current depths. However, TNO concluded that the porosities are only dependent on the maximum burial depths.

The main focus of this chapter is to put the post-drill reservoir quality results into perspective with the pre-drill estimations.

The wells used for the comparison study include the previously drilled old wells (GAAG-2A, GAAG-03, GAAG-05, SGZ-01-S1, Q16-08, KDZ-02-S1) and the wells in the Drechtsteden area (RDK-01, OBLZ-01, CAP-01, BRAK-01, BRTZ-01, MOL-02-S2, WED-03, and WGD-01) (refer Fig. 76 for well locations).The former wells were used in the pre-drill analysis while a reservoir quality comparison of NLW-GT-01 with the latter wells was requested by HVC.

Figure 76: Locations of the wells used for the comparison of reservoir quality.

Table 12: Summary of the available core data.

Well	Cored interval (m)	Stratigraphic Interval (well reports)	Stratigraphic Interval (nlog site)
GAAG-2A	3080.00-3093.00	Hardegsen-Upper Detfurth	Hardegsen
GAAG-03 (sidewall samples)	3666.65	Hardegsen	Hardegsen
	3670.1		
GAAG-05	4085.00-4107.00	Solling -Hardegsen	Basal Solling-Hardegsen-Upper Detfurth
SGZ-01-S1	3206.00-3216.53	Middle Bunter	Upper Detfurth
Q16-08	3932.50-3944.20	Lower Detfurth	Upper Volpriehausen
	3944.20-3947.28		
NLW-GT-01	4250.00-4280.00	Lower Detfurth -Upper Volpriehausen	Lower Detfurth -Upper Volpriehausen
KDZ-02-S1	3255.00-3273.40	Hardegsen -Upper Detfurth	Hardegsen
RDK-01	2816.25-2825.30	Middle Bunter	Hardegsen
OBLZ-01	2275.00-2296.58	Middle Bunter	Basal Solling-Hardegsen
CAP-01	3204.50-3223.25	Middle Bunter	Upper Volpriehausen-Lower Volpriehausen
BRAK-01	2454.00-2480.65	Middle Bunter	Detfurth Claystone

A discrepancy was identified between the stratigraphic interval of GAAG-05, Q16-08, KDZ-02-S1 as mentioned in the well reports and the nlog site (see Table 12).

However, the cored intervals in wells other than Q16-08 and a portion of CAP-01 do not contain the same stratigraphic interval as NLW-GT-01. It is therefore not possible to directly compare the proportions of lithofacies associations or depositional sub-environments in these wells with NLW-GT-01.

5.9.1. Sedimentology:

As the NLW-GT-O1 core was not slabbed, the proportion of fluvial lithofacies was not determined.

Table 13: Percentage abundance of depositional sub-environments for the cored Triassic intervals of other wells.

Depositional sub-environment	GAAG-2A	GAAG-05	SGZ-01-S1	Q16-08	KDZ-02-S1
Aeolian Dune	11.6	27.0	9.8	2.2	11.5
Dry aeolian Sandflat	24.2	17.4	38.1	12.3	41.5
Homogenised Aeolian Sandflat	1.5	0.5	1.6	2.3	
Damp Aeolian Sandflat	62.7	53.1	48.4	9.3	42.5
Fluvial Channel Lag				1.0	1.1
Wadi Deposits				24.2	3.4
Fluvial Sheetflood			2.1	39.5	
Homogenized Sheetflood				2.3	
Desert Lake				0.2	
Distal Floodplain		2.0		6.7	

RDK-01, OBLZ-01 and CAP-01 were found to be deposited in the distal reaches of an alluvial fan or on a desert plain. BRAK-01 core represents a distal inner fan setting.

The predominance of desert plain lithofacies associations within wells GAAG-2A, GAAG-05, SGZ-01-S1, KDZ-02-S1, RDK-01, OBLZ-01, and BRAK-01 indicates a position on the desert plain dominated by aeolian sedimentological processes during Upper Detfurth, Hardegsen and Solling times. However, during the Upper Volpriehausen deposition, there appears to have been more significant fluvial input as observed in the cores of Q16-08, NLW-GT-01, and CAP-01.

The variation in the proportion of the lithofacies associations is thus related to the stratigraphic position of the cored interval within the Middle Buntsandstein (see Table 12 and 13) and evolution of the depositional system with time.

5.9.2. Petrography

Overall grain size is slightly coarser within well KDZ-02-S1 while the sands are comparatively fine-grained in NLW-GT-01 (see Table 14). The dry aeolian sandstones are better sorted than the other sub-environment deposits in all the wells.

Table 14: Summary of the grain parameter for the available cores.

Well name	Grain-size	Sorting	Angularity	Rock Type
GAAG-2A	silt-cU	m-b	sa-wr	arkosic arenite- quartz-arkosic arenite
GAAG-03	silt-cU	m-b	sa-r	sublitharenite
GAAG-05	silt-cU	m-b	sa-wr	quartz arenite-arkosic arenite
SGZ-01-S1	vfU-cL	mw-b	sa-r	arkosic arenite
Q16-08	vfU-mL	m-b	sa-r	arkosic arenite-lithic arenite
NLW-GT-01	silt-mL	mw-b	sa-sr	arkosic arenite
KDZ-02-S1	fL-gran	m-b	sr-wr	arkosic arenite-quartz arenite
BRAK-01	fU-mU	p-w	a-sr	lithic arkose-lithic arenite
CAP-01	vfL-cU	p-m	sa-sr	lithic arkose-lithic arenite
RDK-01	vfU-mU	m-b	sa-sr	quartz arenite
OBLZ-01	vfU - mU	vp-m	sa-r	claystone-dolomite-lithic arenite-arkosic arenite-quartz arenite quartz psammite

Sorting	
vp	very poor
p	poor
m	moderate
mw	moderately well
w	well
b	bimodal

Angularity	
a	angular
sa	sub-angular
sr	sub-rounded
r	rounded
wr	well-rounded

5.9.3 Diagenesis

Although the wells are from different stratigraphical positions, they have broadly similar authigenic mineralogies differing principally in abundance rather than occurrence. This variation in detrital mineralogy may reflect a change of provenance with time and/or a higher degree of sediment reworking depending on the stratigraphical level of the cored succession. For instance, the sediments derived by the weathering of granite will have different mineralogical proportions (mineralogical maturity is less due to greater abundance of feldspar) as compared to the clastic deposits supplied by weathering of sandstones (mineralogically more mature due to increase in quartz percentage.

Table 15: Summary of detrital and authigenic mineralogy for the cored interval by point count except for NLW-GT-01, where only the XRD data is available.

	GAAG-2A	GAAG-03	GAAG-05	SGZ-01-S1	Q16-08	NLW-GT-01 (XRD)	KDZ-02-S1	BRAK-01	RDK-01	CAP-01	OBLZ-01
Detrital Minerals											
Quartz	51.0-69.4	51.7-53.7	68.7-80.7	51.3-63.4	62.3-82.3	63.0-73.0	33.0-87.0	36.3-49.0	62.7-70.7	35-42	14.3-67.7
Feldspar-sodium	Tr-0.7	0.3-1.3	Tr	0.3-0.5	Tr-1.0	3.0-6.0	0.0-1.0	3.7-8.7	2.0-6.0	10	
Feldspar-potassium	7.0-20	0.3-2.3	1.3-8.7	3.0-5.0	8.7-14.7	4.0-6.0	1.0-10.0				2.3-10.0
Lithic Fragments	Tr-0.7	9.7-11.1	Tr-0.7	2.0-3.7	0.3-1.0		0.3-4.0	15.0-20.3	0.7-2.0	15	0.7-11.7
Mica		Tr-0.3		0.0-0.7	0.0-Tr		0.0-0.3	0.3-3.0	Tr-0.3	Tr	Tr-1.0
Detrital clay	Tr-7.0	0.0-0.7	0-6.3				0.0-0.7		1.0-3.3		Tr-8.7
Authigenic Minerals											
Quartz	Tr-1.0	0.7-3.7	Tr-15.0	0.0-1.3	0.3-7.0		0.0 -5.0	0.7-14.3	2.7-7.3	Tr-10	Tr-0.7
Ferroan Dolomite	0.3-3.3		Tr-4.3	0.3-1.7	2.0-8.0				Tr-8.6		Tr
Non-ferroan Dolomite	0.3-5.0	2.3-4.7	Tr-5.0	2.0-7.3	1.3-14.0				Tr-11.7		0.7-64.0
Total Dolomite	0.7-7.3	2.3-4.7	0.2-8.0	2.7-8.7	4.3-20.0	14.0-21.0	0.0-13.7	0.0-20.0	Tr-20.3	10.0-20.0	Tr-64.0
Anhydrite	Tr-1.3	Tr-1.7	0.3-7.3			0-1.0	0.0-6.0		0.3-8.7		Tr
Illite	0.1-0.1	7.4-8.7	Tr-0.3	0.3-1.7	0.0-2.3	3.0-6.0	1.3-6.3	6.0-8.0	2.0-6.7	Tr-4	
Kaolinite				1.7-4.7					Tr-2.0		Tr
Chlorite					0.0-0.7					Tr-4	
Feldspar	Tr-0.1				0.0-Tr				Tr		Tr-0.7
Haematite	Tr	0.7	Tr		0.0-Tr						
Pyrite	0.0-0.7		Tr	0.7-3.0	0.0-Tr		Tr -1.0	Tr-0.7		Tr	Tr-1.3
Barite							0.0-1.3				
Siderite		0.0-2.3			0.0-Tr		0.0-0.7	Tr-0.7	0-2.7		Tr
Carbonate Clasts											
Ti-oxide											0.3-0.7

`

5.9.4. Reservoir quality

Th reservoir quality is known to depend on the nature of the lithofacies, petrography and diagenesis.

Table 16: Summary of the reservoir quality parameters.

Well name	GAAG-2A	KDZ-02-S1	GAAG-03	Q16-08	GAAG-05
Compactional Porosity Loss (COPL%)	20.70-25.65	16.70-32.10	29.79-30.96	23.70-35.20	19.30-36.20
Cementational Porosity Loss (CEPL %)	0.78-3.79	4.40-13.30	8.978-12.17	6.40-16.00	2.78-17.76
Helium Porosity (%)	14.3-20.9	7.30-16.80	14.55-19.92	2.00-14.00	5.30-14.30
Horizontal Permeability (mD)	32.3-357.2	<0.01-1027.9	Undefined	0.01-0.55	4.67-91.91

From the Table 16. above, it is clear that compaction played a more significant role than the cementation in the deterioration of porosity in the listed wells.

The following plots of the Main Buntsandstein Subgroup encompass the core plug data available for the respective wells on nlog site.

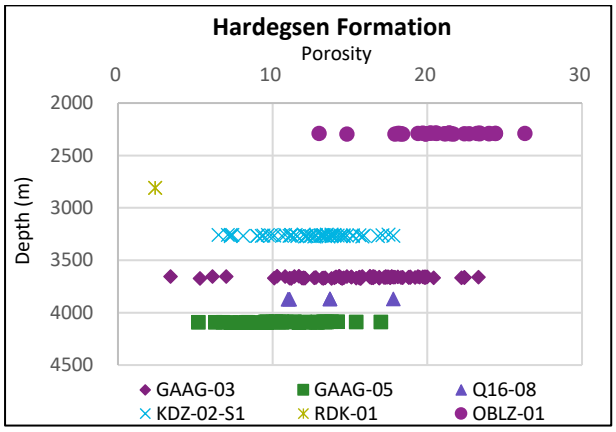

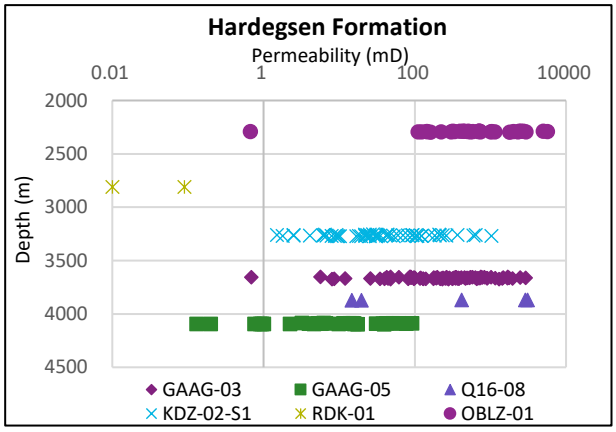

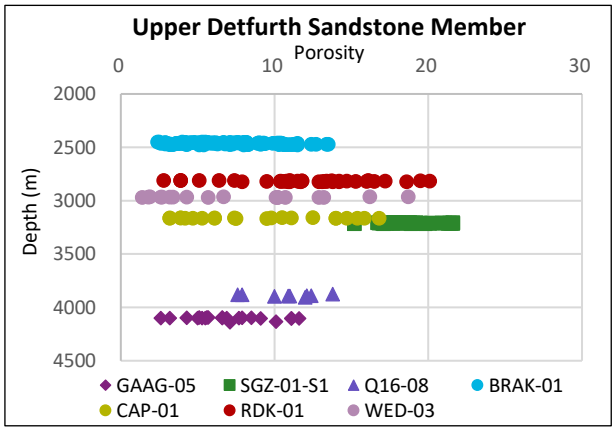

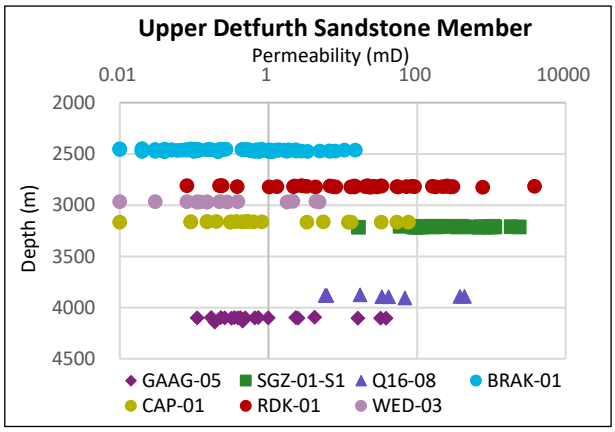

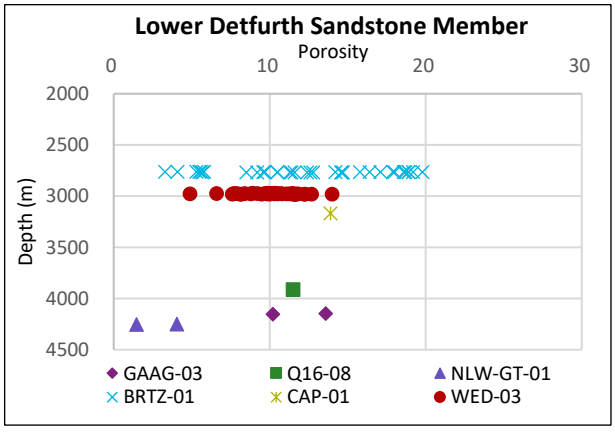

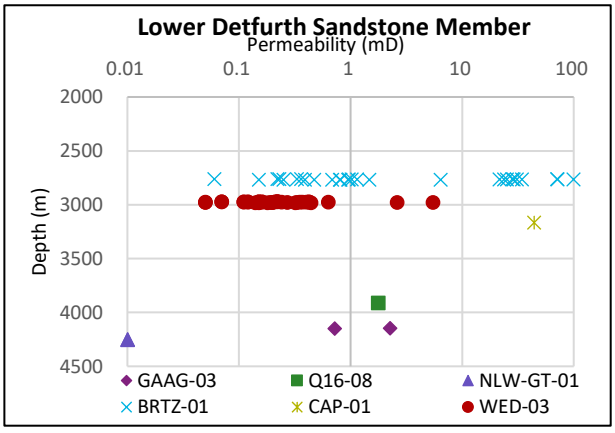

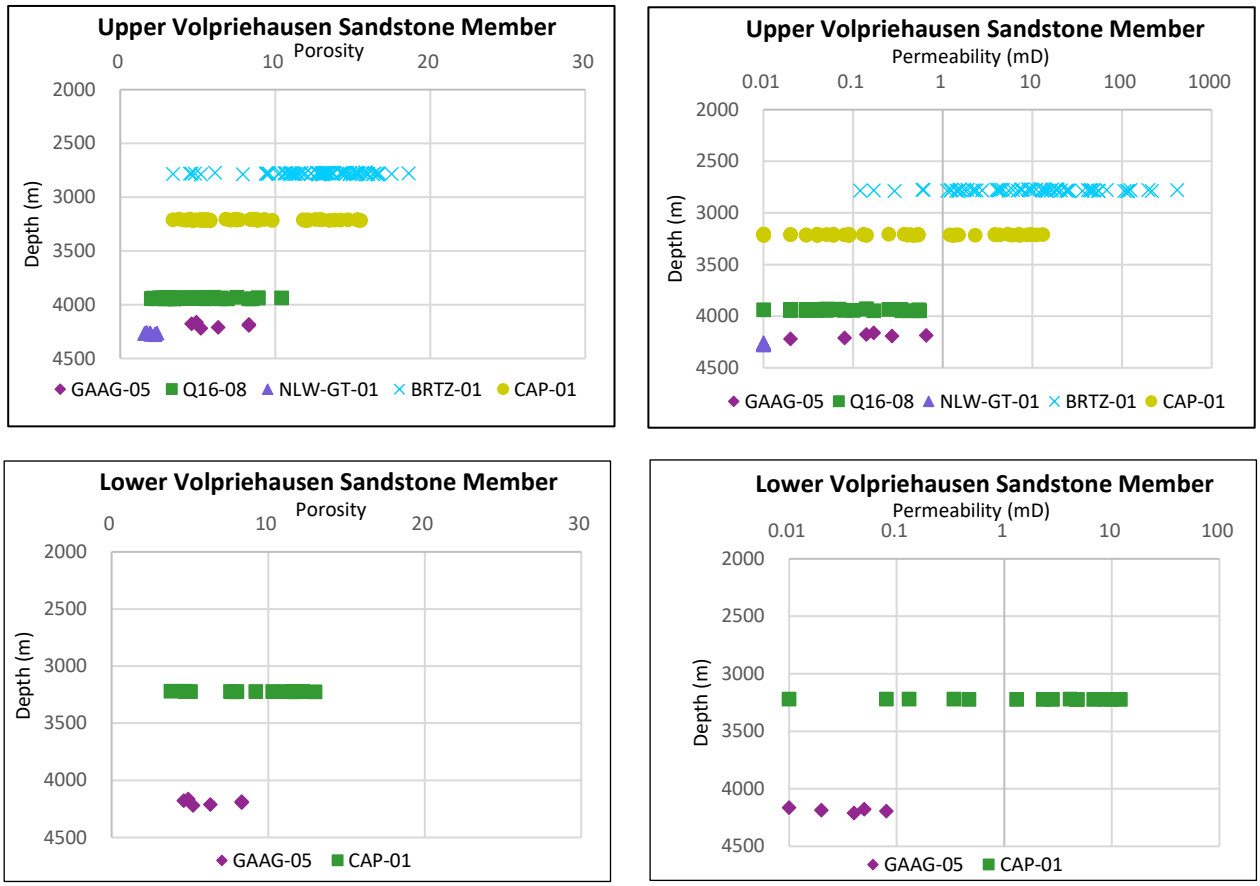

Figure 77: Plot of porosity and permeability as a function of depth for the formations of the Main Buntsandstein Subgroup.

From Fig. 77 above, the Hardegsen Formation comprise of dry and damp sandflat deposits with interbeds of aeolian dune sandstones. It exhibits the best reservoir quality amongst all the Main Buntsandstein Formations. OBLZ-01 comprises of well-stratified sandstones containing the lowest amounts of clay matrix and dolomite leading to a fairly good reservoir quality (see Table 4). The poor reservoir quality of RDK-01 is due to severe cementation by anhydrite, quartz, illite.

RDK-01, SGZ-01-S2 and Q16-08 exhibit extremely good permeabilities for the Upper Detfurth Sandstone Member reflecting the textural maturity of the sandstones (see Table 15). As shown in Table 16, the more deeply buried sediments in GAAG-05 display an overall greater compactional loss. The variable distribution of anhydrite and quartz cements within GAAG-05 results in a widespread and permeability values as they impact pore connectivity.

Lower Detfurth Sandstone Member has low values of permeability; however, BRTZ-01, CAP-01, and WED-03 show values ranging up to 100mD.

BRTZ-01 also has highest porosity and permeability values for the Upper Volpriehausen Sandstone Member, but due to unavailability of appropriate well reports the reasons for this nature cannot be deduced.

The appreciable reservoir quality of CAP-01 is attributed to the formation of smectite clay coatings which prevented later quartz overgrowths, and precipitation of an early carbonate cement, that inhibited compaction during advancing burial. Also, anhydrite cement does not occur in this cored interval. secondary porosity generation was an important process in this well. Q16-08 shows similar porosity values when compared to the other wells; however, the permeability values are extremely low. The high porosity values in Q16-08 mainly arise from the dissolution of detrital feldspar grains and the absence of calcite and anhydrite cements. Partial to complete dissolution of feldspars leads to the generation of secondary porosity. However, these poorly interconnected pores are largely ineffective. In Q16-08, illite clays occur as cement and replacement of detrital clay, while the fibrous illite bridges pore throats. Illite clays are unlikely to affect helium porosity significantly because they preserve microporosity. However, they will degrade permeability to some extent by producing tortuous flow pathways and by bridging pore throats. This is the reason for the low permeability values of the Upper Volpriehausen sandstones of Q16-08. Such pore bridging illite clays and dissolution of feldspar grains does not occur in NLW-GT-01.

Except for the wells in the Drechtsteden (BRTZ-01, CAP-01), all the other wells have a porosity range of 0-11% and a permeability range between 0.01 and 1mD. This implies that the reservoir quality of the wells located in Drechtsteden are not relatable to the values observed in NLW-GT-01. Also, instead of comparing the reservoir quality of entire Buntsandstein, it is of utmost importance to take the heterogeneity of the lithofacies into consideration and not compare formations with different depositional setting. This was overlooked by T&A Survey.

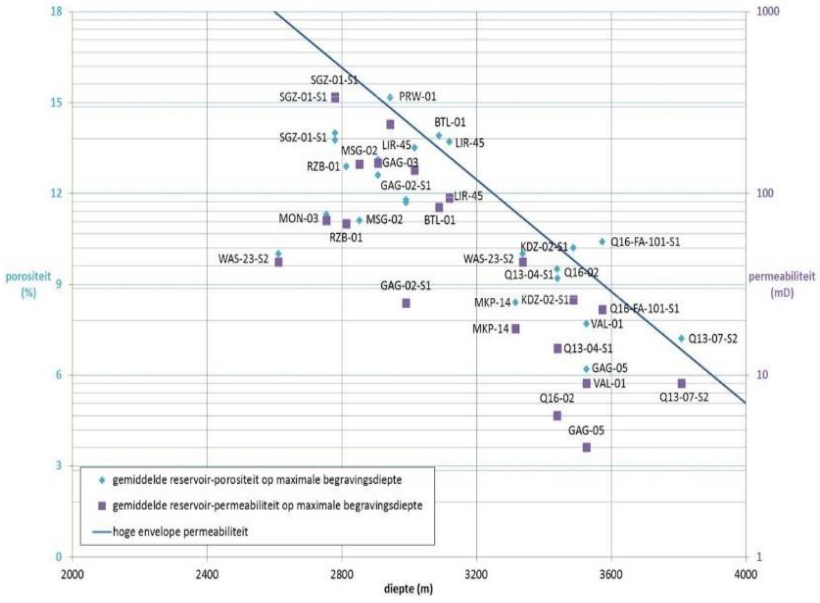

Figure 78: Plot of porosity and permeability as a function of maximum burial depth. (TNO audit Final Report, 2013)

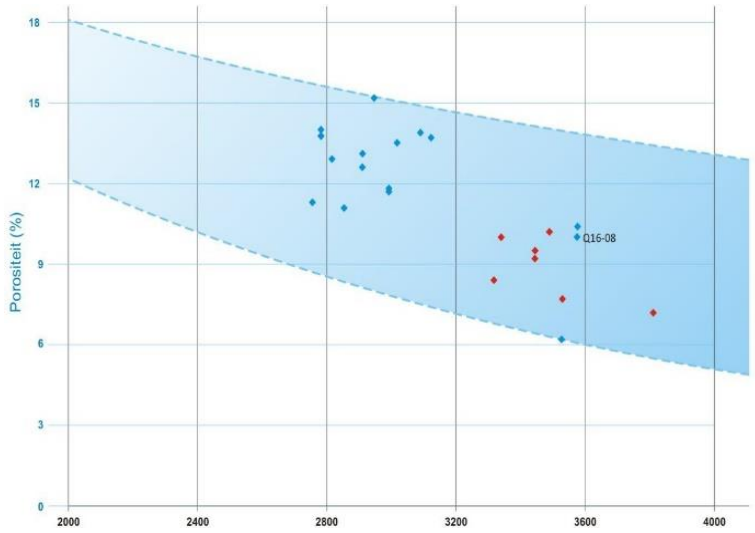

Figure 79: Porosity as a function of maximum burial depth (T&A Survey, 2013).

In Fig. 78 (TNO, 2013) above the average porosity and permeability values of the boreholes in the study area is plotted against their maximum burial depths. However, a linear relationship between them is unclear. In unlithified sandstones with minimal textural and mineralogical variations, compaction is the main reason for the porosity loss (Taylor, et al., 2010). Extrapolation of compaction trends to greater depths where cementation rates increase is prone to significant error (Taylor, et al., 2010).

In Fig.79, T&A Survey (2013) depicts that with respect to the borehole position in the West Netherlands Basin higher porosities occur in the shallow reservoirs come from drilling in the south of the WNB, the lower values relate primarily to the drilling further north.

The common factor in wells Q16-08, GAAG-05, NLW-GT-01, VAL-01, MKP-10, Q13-04-S1, and Q13-07-S2, is the abundance of cements. The latter four have dolomite and anhydrite cements ranging between 0.3-46.0 and 0.0-22.7, respectively. Porosity and permeability values observed in NLW-GT-01 are comparable to those seen in the wells VAL-01, MKP-10, Q13-04-S1, Q13-07-S2, and Q16-08(porosity values are higher). Another reason for this similarity is that all these wells are cored in the Lower Detfurth and Upper Volpriehausen interval.

The scale at which the sediments are characterized also plays an essential role as a formation may appear homogeneous on a larger scale but maybe heterogeneous on a smaller scale or vice versa. Thus, the sediments of the Volpriehausen Formation deposited by fluvial channels or the Hardegsen Formation deposited mainly by aeolian action may be heterogeneous with varied reservoir properties on a smaller scale. During the deposition of these sediments, the depositional sub-environments varied between parts of the West Netherlands Basin and changed with time. Since the depositional setting is one of the significant factors affecting diagenesis, diagenetic variations will occur at different locations of the West Netherlands Basin.

Although the formations of the Main Buntsandstein Subgroup have similar lithofacies, small-scale internal structures and initial lithological characteristics and depositional environment determine the response of sediments to diagenetic processes. T&A underestimated this impact.

NAM Well Reports used in this chapter:

Wells GAG-02 and GAG-05: Clement, S.L., Conybeare D.M., 1998. GAG-2 and GAG-5 Sedimentology, petrography and reservoir quality of the Triassic Middle Bundsandstein. Report no ZSL-98-550.

Well KDZ-02-S1: Conybeare, D. M., Dr. Aplin, G.F., and Clement, S. L. 1999. Kijkduin Zee-2A, Sedimentology, Petrography and Reservoir Quality of the Triassic Buntsandstein. Document no ZSL-99-618.

Well Q16-08: Clement, S.L., Conybeare D.M., 1998. Q16-08 Sedimentology, petrography and reservoir quality of the Triassic Bundsandstein. Report no ZSL-98-549.

Well SGZ-01-S1: Greenwood, J., 1997. A sedimentological and petrographical evaluation of the cored Middle Bunter in well SGZ-01, and a comparison with MSG-1, West Nederland basin. Nam report no 30.756

Wells RDK-01: Schobel., M., 1993. sedimentology, petrography and reservoir properties of Triassic Bunter Deposits in cores 1,2and 3 from well RDK-01 Report no G73-2

Wells OBLZ-01: G.A.P.S Nederland B.V., 1991. Sedimentology, petrography and reservoir properties of cores 1and 2 from well Oud-Beijerland Zuid-01 Report no G15-1

Wells CAP-01: G.A.P.S Nederland B.V., 1992. Sedimentology, petrography and reservoir properties of cores 1, 2 and 3 from well Capelle-01 Report no G63-2a

Wells BRAK-01: G.A.P.S Nederland B.V., 1993. Sedimentology, petrography and reservoir properties of Triassic Bunter deposits in cores 2 and 3 from well Brakel-01 Report no G15-1

Wells VAL-01, MKP-10, Q13-04-S1, and Q13-07-S2: Conybeare, D.M, MacPherson, K., 1998. Sedimentology, petrography and reservoir quality of the Carboniferous and the Triassic Bundsandstein. Report no ZSL-98-570.

6. Conclusions

i. The very fine to coarse-grained, cross-bedded sandstones of NDW-01 are moderate to bimodally sorted. The bottomsets are accentuated by dark minerals and the foresets are characterised by patchy cementation or cement laminae conforming the foresets.
The cored interval of NLW-GT-01 consists of very fine to medium-grained sandstones with subordinate siltstone-mudstone intercalations. The sandstones are organized into stacks of dm-scale cross-beddings, generally lacking clear grain-size trends. The sandstones are classified as arkosic arenite. Most of the samples exhibit a unimodal grain-size distribution and are moderately-well sorted to bimodally-sorted.

ii. The lithofacies encountered in NDW-01 are related to wadi deposits associated with changes in the flow energy. A low sinuous fluvial system led to the deposition of the sediments constituting the Nederweert Sandstone Member.
Within the context of the regional depositional model the core in NLW-GT-01 is consistent with the deposition by a shallow braided river system in a semi-arid continental basin subjected to minor flooding by unconfined flows.

iii. In NLW-GT-01, the detrital framework mineralogy is dominated by monocrystalline quartz followed by polycrystalline quartz, K-feldspar, plagioclase and lithic fragments. Authigenic minerals mainly include dolomite, quartz and anhydrite. Non-ferroan to ferroan dolomite occurs as the major pore-filling cement. Quartz cements are common but overgrowths are rare. Anhydrite distribution is localised. Illite is recorded as a minor constituent.

iv. Compaction resulted in a denser rock by crushing and reorganization of framework grains. Cementation took place in phases. Calcite cementation was followed by quartz and non-ferroan dolomite precipitation. Ferroan dolomite precipitated along previously formed non- ferroan dolomite cement. Anhydrite was the last cement to form and is highly localised. This localisation is due to the previously reduced permeable pathways for seepage calcium and sulphate rich fluids due to precipitation of earlier formed cements.

v. For NDW-01, the final porosity values range between 4.7%and 10.6% and the permeabilities vary between 0.2mD and 2mD.The difference between the initial and the final porosity and permeability values is 32.97% and 31896.98mD.
Reservoir properties are inferior throughout the cored interval in NLW-GT-01 with plug porosity values between 1.4-3.9% and permeability between 0.00-0.02mD. The porosity and permeability losses are 39.36%, and 1299.99mD, respectively.

vi. The final porosity and permeability values for the Upper Volpriehausen Sandstone Member of NLW-GT-01 are comparable with the values from same formation of the wells VAL-01, MKP-10, Q13-04-S1, and Q13-07-S2 in the northern part of the West Netherlands Basin. In all these wells, cementation is prominent and overprints the primary depositional porosity and permeability controls.

vii. The main controls on the reservoir quality are the primary depositional texture, compaction and excessive cementation by dolomite, quartz and localized precipitation of anhydrite. Closer grain packing during compaction resulted in significant porosity loss. In spite of two phases of grain dissolution reservoir properties are quite poor, as both phases were followed by significant reduction in porosity due to precipitation of cements. Secondary porosity generation as a result of K-feldspar dissolution is absent.

viii. The rose diagram of the Nederweert Sandstone Member shows a bulk transport direction towards the NNW. Hence, the Rhenish Brabant Massif is considered as a probable sediment source.
In contradiction to previous belief, the dominant paleocurrent direction of the Volpriehausen sands in the Naaldwijk area is ENE, which indicates clastic influx from the London-Brabant Massif. The strike orientation of the fractures in this core lies parallel to the present-day NW-SE striking maximum horizontal compressional stress. The development of these fractures is not diagenetic but related to the pre-existing lineaments on the basis of strike orientation.

7. Recommendations:

The NLW-GT-01 core should be slabbed in order to understand the nature of the extensively fractured interval. A fracture analysis study would provide insight to the role of the fractures in relation to the permeability of the formation. A detailed burial history study is needed to understand the evolution of the sediments. A petrographic point-count and SEM analysis needs to be conducted on the thin-sections to quantify the extent of the porosity lost by compaction and cementation respectively. It will also help in determining the nature of the pore filling cements, shape of the pore-throats and their distribution. A Cyclolog study should be carried out to understand the depositional cyclicity of the Triassic deposits.

References

Ames, R. & Farfan, P., 1996. The environment of deposition of the Triassic Main Buntsandstein Formation in the P and Q quadrants, offshore of the Netherlands. In: H. Rondeel, D. Batjes & W. Nieuwenhuis, eds. *Geology of Gas and Oil under the Netherlands..* Dordrecht: Kluwer, pp. 167-178.

Bachmann, G. H. et al., 2010. Triassic. In: J. Doornenbal & A. Stevenson, eds. *Petroleum Geological Atlas of the Southern Permian Basin Area.* Houten: EAGE Publications b.v..

Bath, A. H., Milodowski, A. E. & Spiro, B., 1987. Diagenesis of carbonate cements in Permo-Triassic sandstone sin the Wessex and East Yorkshire- Lincolnshire Basins, UK: a stable isotope study.. In: J. D. Marshall, ed. *Diagenesis of Sedimentary Sequences..* s.l.:Geological Society Special Publication No. 36, pp. 173-190.

Beard, D. & Weyl, P., 1973. Influence of texture on porosity and permeability of unconsolidated sand. *The American Association of Petroleum Geologists Bulletin,* 57(2), pp. 349-369.

Bourquin, S., Guillocheau, F. & Peron, S., 2009. Braided rivers within an arid alluvial plain (example from the Lower Triassic , western German Basin) : recognition criteria and expression of stratigraphic cycles.. *Sedimentology,* Volume 56, pp. 2235-2264.

Boxem, J. V. &. T., 2015. *Sector Outlook: Geothermal power increase in the Netherlands by enhancing the capacity,* Utrecht: TNO.

Britton, S. R., 1979. *Petrographic description of Bunter Sandstone chips from wells Nederweert-1 and St. Michielsgestel-1, South Holland,* London: s.n.

De Jager, J., 2007. Geological Development. In: T. Wong, D. Batjes & J. De Jager, eds. *Geology of the Netherlands.* Amsterdam: Royal Netherlands Academy of Arts and Sciences, pp. 5-26.

DINOloket, n.d. *www.dinoloket.nl/carboniferous.* [Online]
Available at: https://www.dinoloket.nl/carboniferous
[Accessed 18 July 2019].

Donselaar, M. & Schmidt, J., 2005. Integration of outcrop and borehole image logs for high-resolution facies interpretation:example from a fluvial fan in the Ebro Basin,Spain.. *Sediementology,* Volume 52, pp. 1021-1042.

EBN, 2018. *ebn.nl/en/energy-transition/.* [Online]
Available at: https://www.ebn.nl/en/energy-transition/
[Accessed 18 Jan 2019].

Feist-Burkhardt, S. et al., 2008. Triassic. In: T. McCann, ed. *The Geology of Central Europe..* London: Geological Society, pp. 749-821.

Felder, M. & Fernandez, S., 2018. *Core Hot Shot NLW-GT-01,* s.l.: Panterra Geoconsultants B.V..

Flemming, B., 2007. The influence of grain size analysis methods and sediment mixing on curve shapes and textural parameters: Implications for sediemnt trend analysis.. *Sedimentary Geology,* Volume 202, pp. 425-435.

Fraser, H., 1935. Experimental study of the porosity and permeability of clastic sediments.. *Journal of Geology,* Volume 43, pp. 910-1010.

Gaafar, G., Altunbay, M., Bal, A. & Anuar, N., 2014. *Ascendancy of continuous profiles of grain-size distribution for deposition environment studies..* s.l., International Petroleum Technology Conference.

Geluk, M., 2005. *Stratigraphy and tectonics of Permo-Triassic basins in the Netherlands and surrounding areas,* Utretcht: s.n.

Geluk, M. C., 2005. Permian and Triassic basins in the Netherlands.. In: T. E. Wong, D. A. J. Batjes & J. De Jager, eds. *Geology and Mineral Resources of the Netherlands..* Amsterdam: Royal Dutch Academy of Science and Arts.

Geluk, M. et al., 1994. Stratigraphy and tectonics of the Roer Valley Graben,73. *Netherlands Journal of Geosciences,* pp. 129-141.

Geluk, M. & Rohling, H.-G., 1997. High-resolution sequence stratigarphy of the Lower Triassic 'Buntsandstein' in the Netherlands and northwestern Germany. *Netherlands Journal of Geosciences,* Volume 76, pp. 227-246.

Geluk, M. & Rohling, H., 1999. High resolution sequence stratigraphy of the Lower Triassic Buntsandstein; a new tool in basin analysis. In: G. Bachmann & I. Lerche, eds. *The Epicontinental Triassic.* Halle: Zentralblatt für Geologie und Paläontology, pp. 545-570.

Glassey, W., 2015. *Geothermal Energy: Renewable Energy and the Environment.* 2nd ed. Boca Raton: Taylor & Francis Group.

Glover, P., n.d. *The Litho-density log.,* s.l.: Petrophysics MSc Course Notes.

Hardie, L. A., 1987. Perspectives on dolomitization: A critical view of some current views.. *Journal of Sedimentary Petrology.,* Volume 57, pp. 166-183.

Heidbach, O., Buchmann, T. & Muller, B., 2019. *Tectonic stress state in Europe from observation and numerical modelling.,* s.l.: s.n.

Heidbach, O. et al., 2018. The World Stress Map database release 2016: Crustal stress pattern across scales.. *Tectonophysics,* 744(July), pp. 484-498.

Kiakojury, M., Zakariaei, S. J. S. & Riahi, M. A., 2018. Investigation of Petrophysical parameters of Kangan reservoir formation in one of the Iran south hydrocarbon fields.. *Open Journal of Yangtze Gas and Oil,* Volume 3, pp. 36-56.

Kombrink, H. et al., 2012. New insights into the geological structure of the Netherlands; results of a detailed mapping project. *Netherlands Journal of Geosciences, 91(4),* pp. 419-446.

Kramers, L. et al., 2012. Direct heat resource assessment and subsurface information systems for geothermal aquifers; the Dutch perspective.. *Netherlands Jpurnal of Geosciences.,* 91(4\), pp. 637-649.

Land, L. S., 1984. Frio Sandstone Diagenesis, Texas Gulf Coast: A Regional Isotopic Study.. In: McDonald & Surdam, eds. *Clastic Diagenesis.* s.l.:American Association of Petroleum Geologists Memoir 37..

Lecomte, A., 2006. The measurement of real and virtula packing density of soft grains.. *Materials and Structures,* 39(1), pp. 63-80.

Matev, P., 2011. *Comprehensive reservoir quality assessment of Buntsandstein sandstone reservoirs in the West Netherlands Basin for geothermal applications in Zuid Holland province area.,* Delft: s.n.

Mckie, T. & Williams, B., 2009. Triassic paleogeography and fluvial dispersal across the northwest European Basins.. *Geological Journal,* Volume 44, pp. 711-741.

Michon, L., van Balen, R., Merle, O. & Pagnier, H., 2003. The Cenozoic evolution of the Roer Valley Rift System integrated at a European scale.. *Tectonophysics, 367(4),* pp. 101-126.

Nagtegaal, P. J. C., 1978. Sandstone framework instability as a function of burial diagenesis.. *Journal of the Geological Society, London,* Volume 135, pp. 101-105.

Panda, M. N. & Lake, L. W., 1994. Estimation of single-phase permeability from parameters of particle-size distribution.. *American Association of Petroleum Geologists Bulletin,* 78(7), pp. 1028-39.

Paxton, S. T., Szabo, J., Ajdukiewicz, J. M. & Klimentidis, R. E., 2002. Construction of an inter-granular volume compaction curve for evaluating and predicting compaction and porosity loss in rigid-grain sandstone reservoirs.. *American Association of Petroleum Geologists,* Volume 86, pp. 2047-2067.

Pharaoh, T. et al., 2010. Tectonic evolution. In: J. Doornenbal & A. Stevenson, eds. *Petroleum Geological Atlas of the Southern Permian Basin Area.* Houten: EAGE Publications b.v., pp. 25-57.

Pluymaekers, M. et al., 2012. Reservoir characteristaion of aquifers for diret hea production: Methodology and screening of potential reservoirs for the Netherlands. *Netherlands Journal of Geosciences,* 91(4), pp. 621-636.

Rijkers, R., Duin, E., Dusar, M. & Langenaeker, V., 1993. Crustal structure of the London-Brabant Massif , southern North Sea. *Geological Magazine,* 130(5), pp. 569-574.

Rijkers, R., Duin, E., Dusar, M. & Langenaeker, V., 1993. Crustal structure of the London-Brabant Massif, southern North Sea.. *Geological Magazine,* 130(5), pp. 569-574.

Rogers, J. & Head, W., 1961. Relationships between porosity,median size and sorting coeffcients of synthetic sands.. *Journal of Sedimentary Petrology,* Volume 31, pp. 467-470.

Smith, G., 2013. *petrowiki.org/Estimating_permeability_based_on_grain_size.* [Online]
Available at: https://petrowiki.org/Estimating_permeability_based_on_grain_size
[Accessed 27 June 2019].

T&A Survey, 2013. *Geologische studie en advies betreffende de exploitatie van geothermie uit het Trias reservoir en het Onder-Krijt/Boven Jura reservoir binnen de nieuw af te bakenen concessie Naaldwijk. Report nummber: 0913-ODE3871,* Naaldwijk: Flora Holland Naaldwijk.

T&A Survey, 2013. *Triassic Main Buntsandstein porosity and permeability with depth , and effect of gas , with special reference to the Naaldwijk 2 and Maasland concessions. Report number: 0113-OEM2372.5a,* Amsterdam: T&A Survey B.V..

T&A Survey, 2018. *ta-survey.nl/page/341/NL/geothermie/trias-westland.* [Online]
Available at: https://www.ta-survey.nl/page/341/NL/geothermie/trias-westland
[Accessed 19 January 2019].

Taylor, T. R. et al., 2010. Sandstone diagenesis and reservoir quality prediction: Models, myths, and reality.. *American Association of Petroleum Geologists,* 94(8), pp. 1093-1132.

Tucker, M., 2001. *Sedimentary Petrology: An introduction to the origin of sedimentary rocks.* 3rd ed. Oxford: Blackwell Science.

Underhill, J. & Partington, M., 1993. Jurassic thermal doming and deflation in the North Sea: implications on the sequence stratigraphic evidence. In: *Petroleum Geology of Northwest Europe: Proceedings of the 4th Conference.* London: Geological Society, pp. 337-345.

Van Hulten, F. F. N., 2008. *Rifting systems and its significance for hydrocarbon exploration in the Netherlands..* Utrecht: EBN/TNO Rifting workshop.

Van Hulten, F. F. N. & Poty, E., 2008. Geological factors controlling Early Carboniferous carbonate platform development in the Netherlands.. *Geological Journal,* Volume 43, pp. 175-196.

Van Wijhe, D., 1987a. The structural evolution of the Broad Fourteens Basin. In: *Petroleum Geology of Northwest Europe.* London: Graham and Trotman, pp. 315-323.

Worden, R. H. & Burley, S. D., 2003. *Sandstone Diagenesis: the evolution of sand to stone..* s.l.:International Association of Sedimentologists..

Worum, G. et al., 2005. Pre-Neogene controls on present-day fault activity in the West Netherlands Basin and Roer Valley Rift System (southern Netherlands): role of variations in fault orientation in a uniform low-stress regime.. *Quaternary Science Reviews,* Volume 24, pp. 475-490.

Yu, A., Bridgwater, J. & Burbidge, A., 1997. On the modelling of the packing of fine particles. *Powder Technology,* Volume 92, pp. 185-194.

Yu, A., Feng, C., Zou, R. & Yang, R., 2003. On the relationship between porosity and interparticle forces. *Powder Technology,* Volume 130, pp. 70-76.

Yu, A. & Standish, N., 1991. Estimation of the porosity of particle mixtures by a linear-mixture packing model.. *Ind. Eng. Chem. Res.,* 30(6), pp. 1372-85.

Yu, A. & Standish, N., 1993. Limitation of proposed mathematical models for the porosity estimation of non-spherical particle mixtures. *Ind. Eng. Chem. Res.,* 32(9), pp. 2179-82.

Ziegler, P., 1975. *The geological evolution of the North sea area in the tectonic framework of north-western Europe.,* The Hague, Netherlands: Shell Internationale Petroleum Maatschappij B.V..

Ziegler, P., 1990. *Geological Atlas of Western and Central Europe.* 2nd ed. London: Shell Internationale Petroleum Maatschappij B.V. and Geological Society.

Appendix

NLW-GT-01

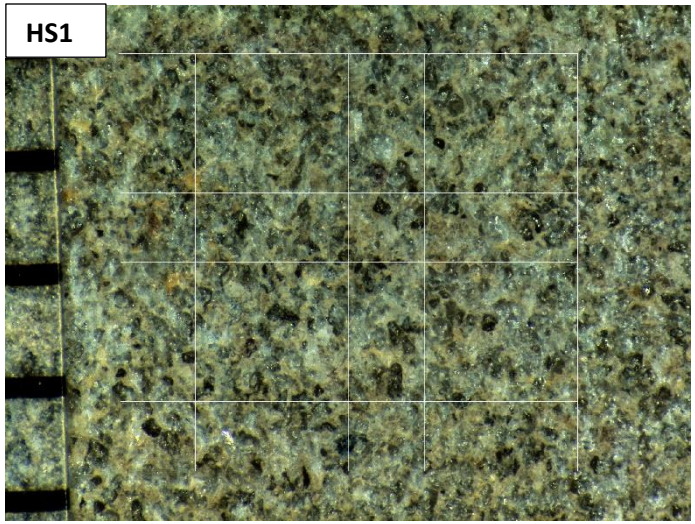

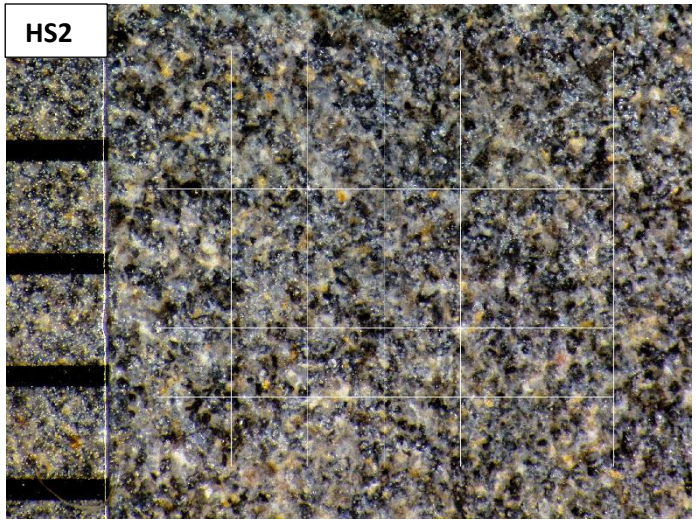

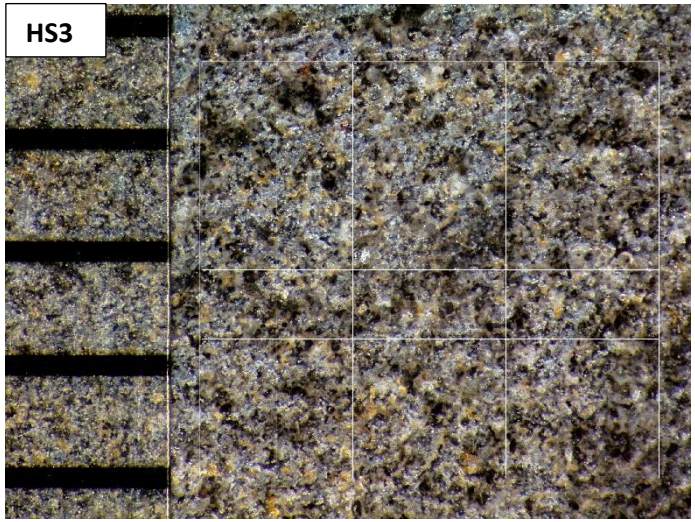

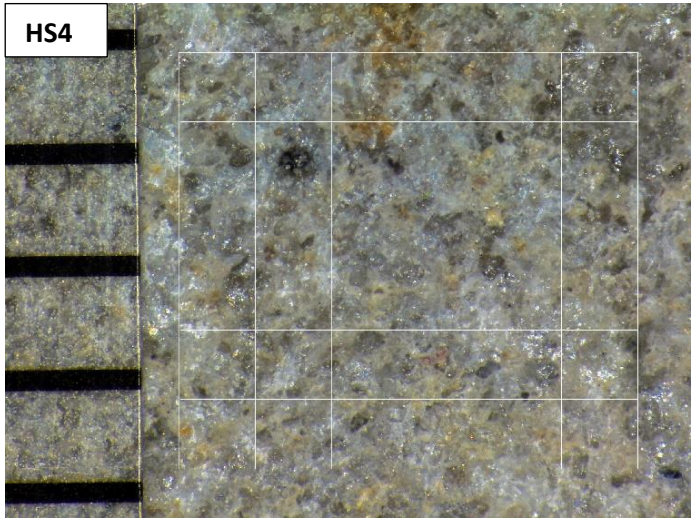

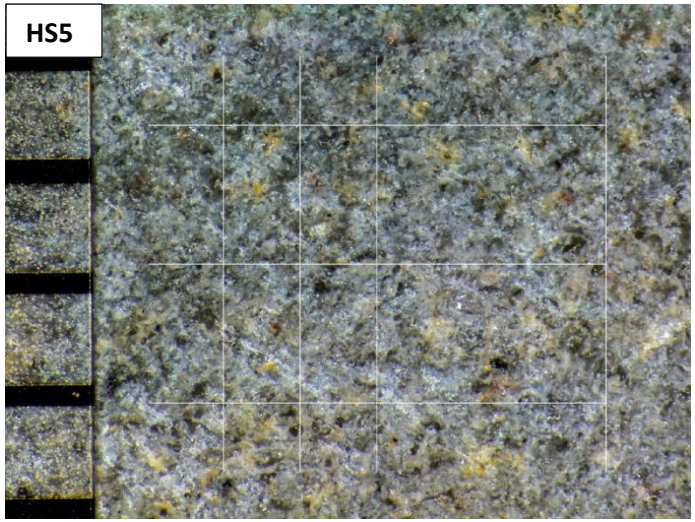
HS5

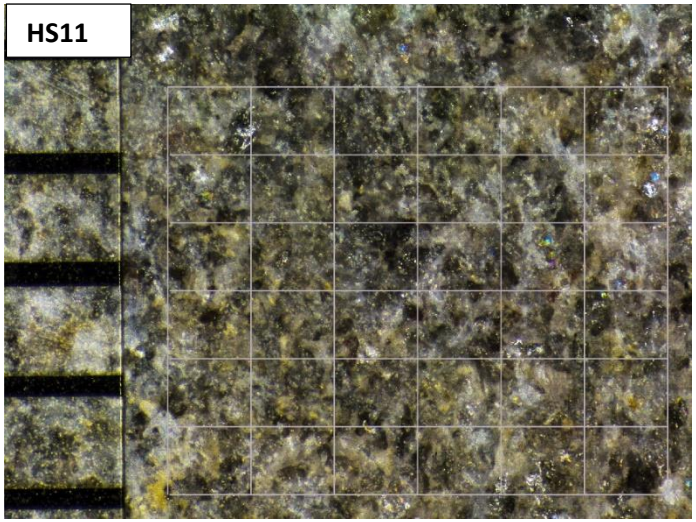
HS11

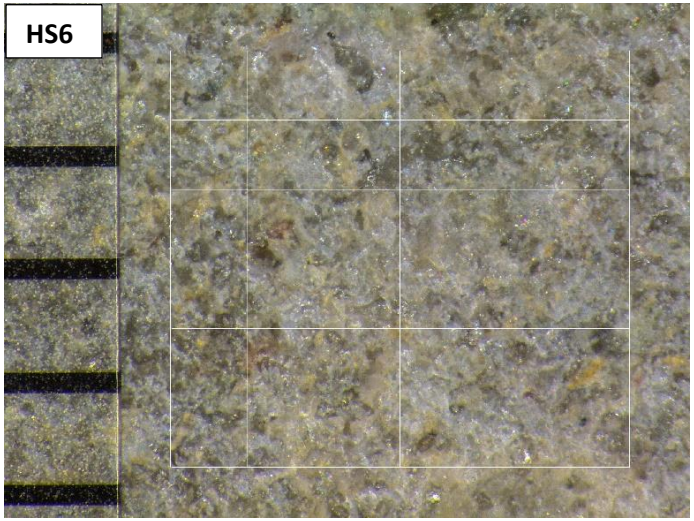
HS6

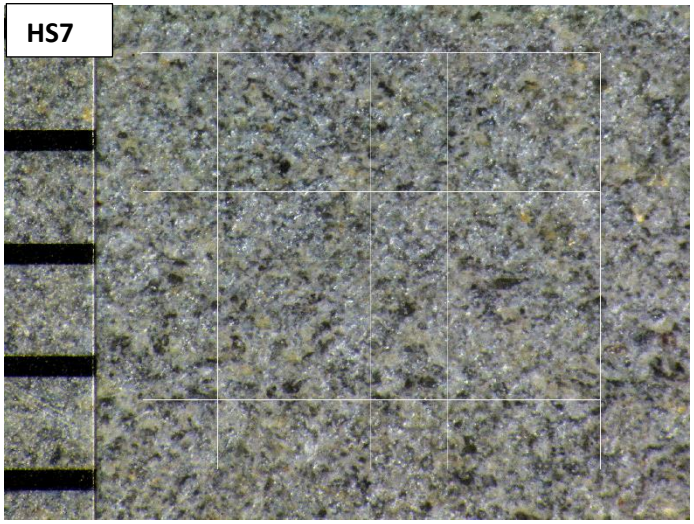
HS7

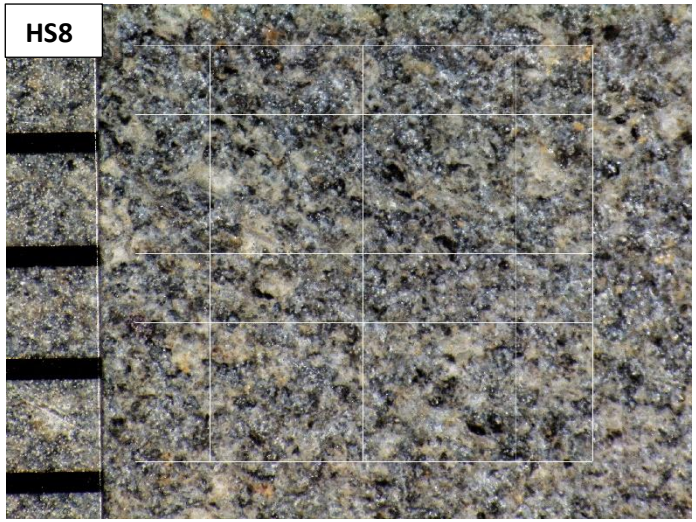
HS8

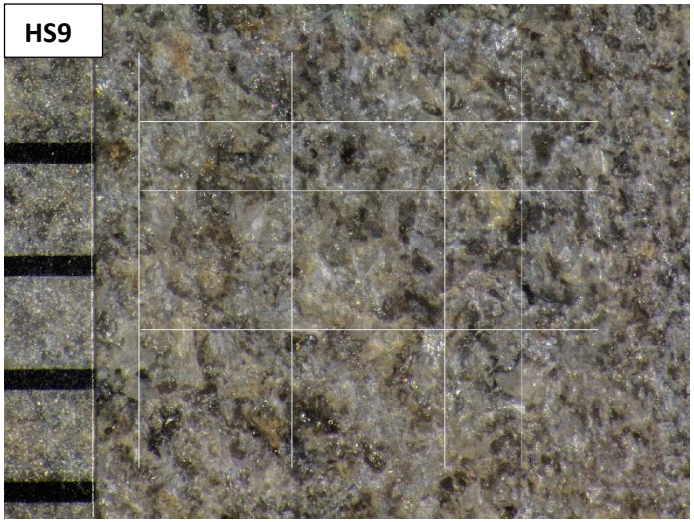
HS9

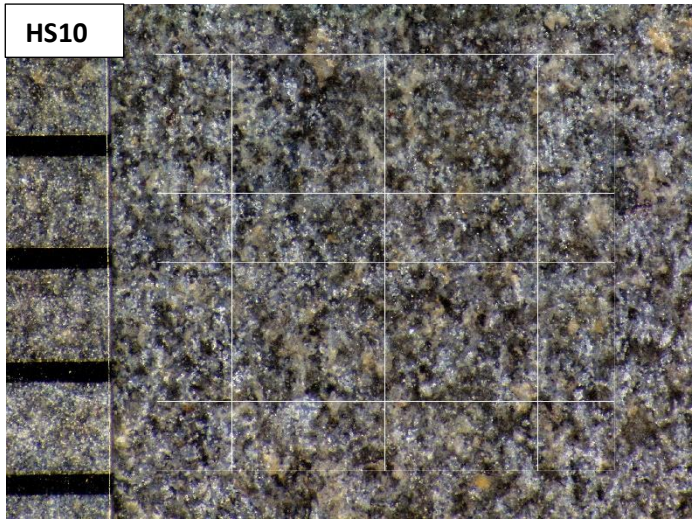
HS10

NDW-01

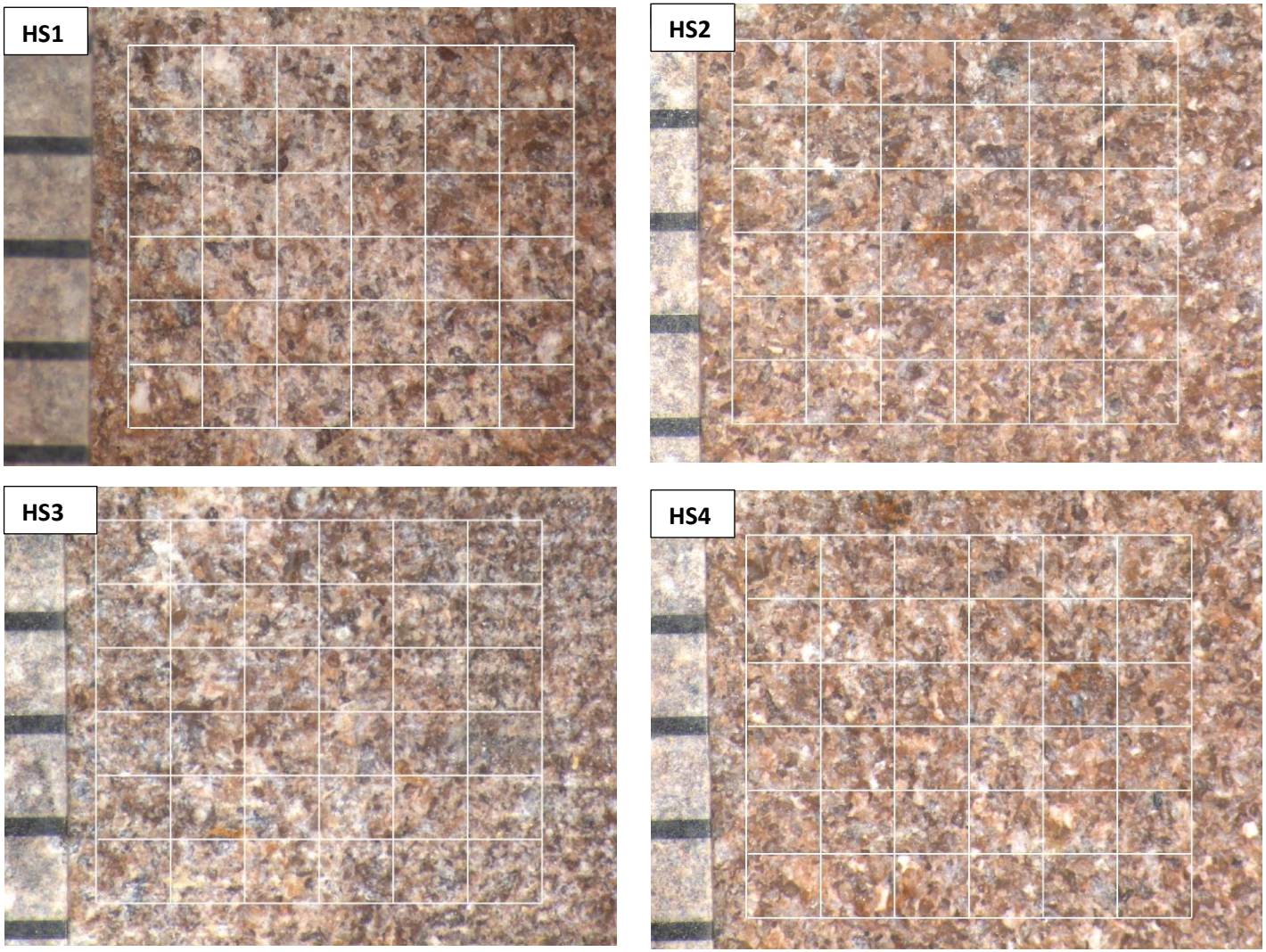

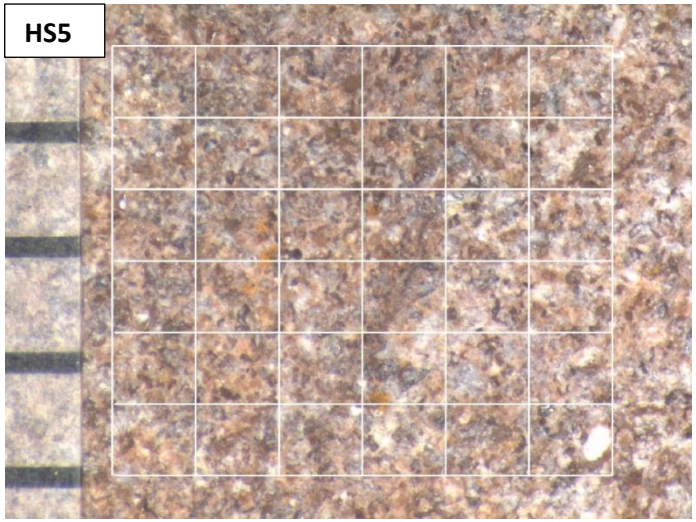
HS5

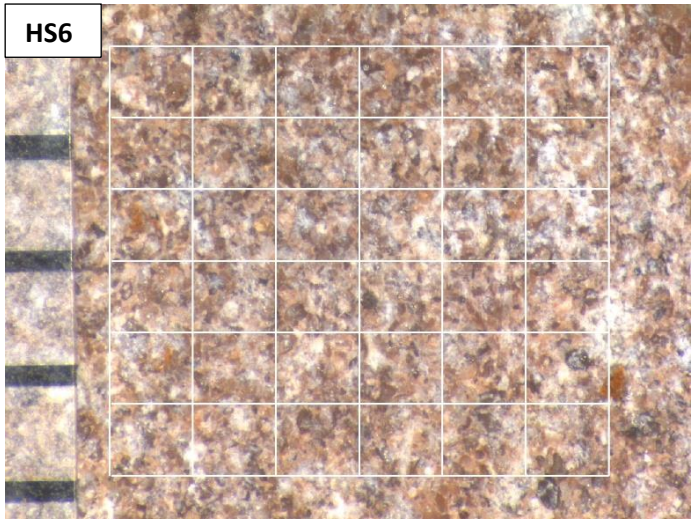
HS6

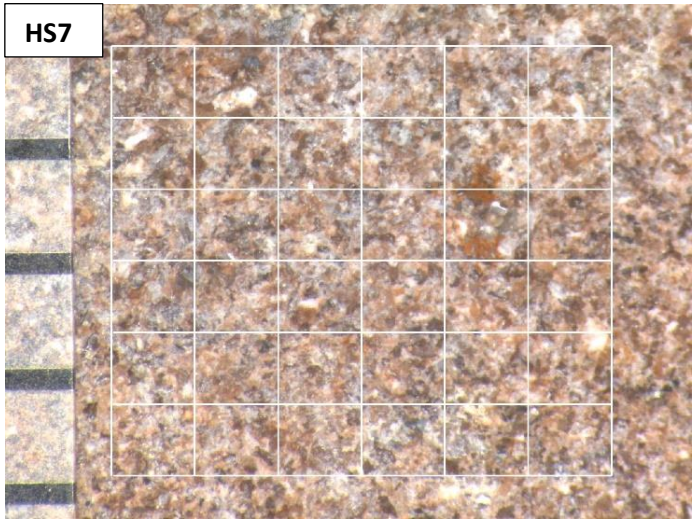
HS7

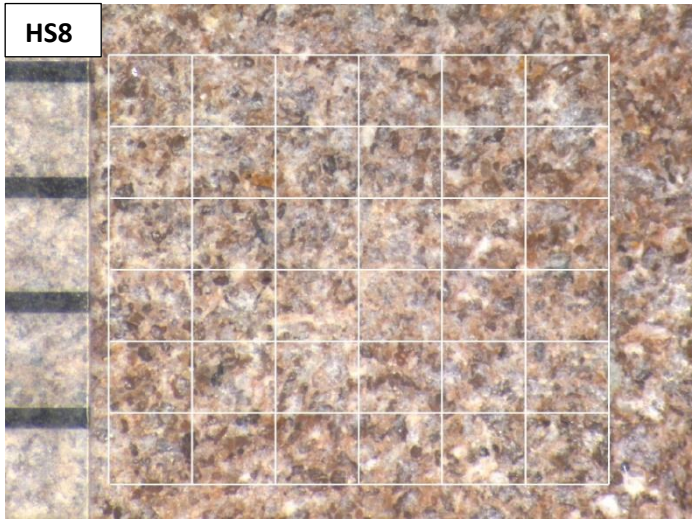
HS8

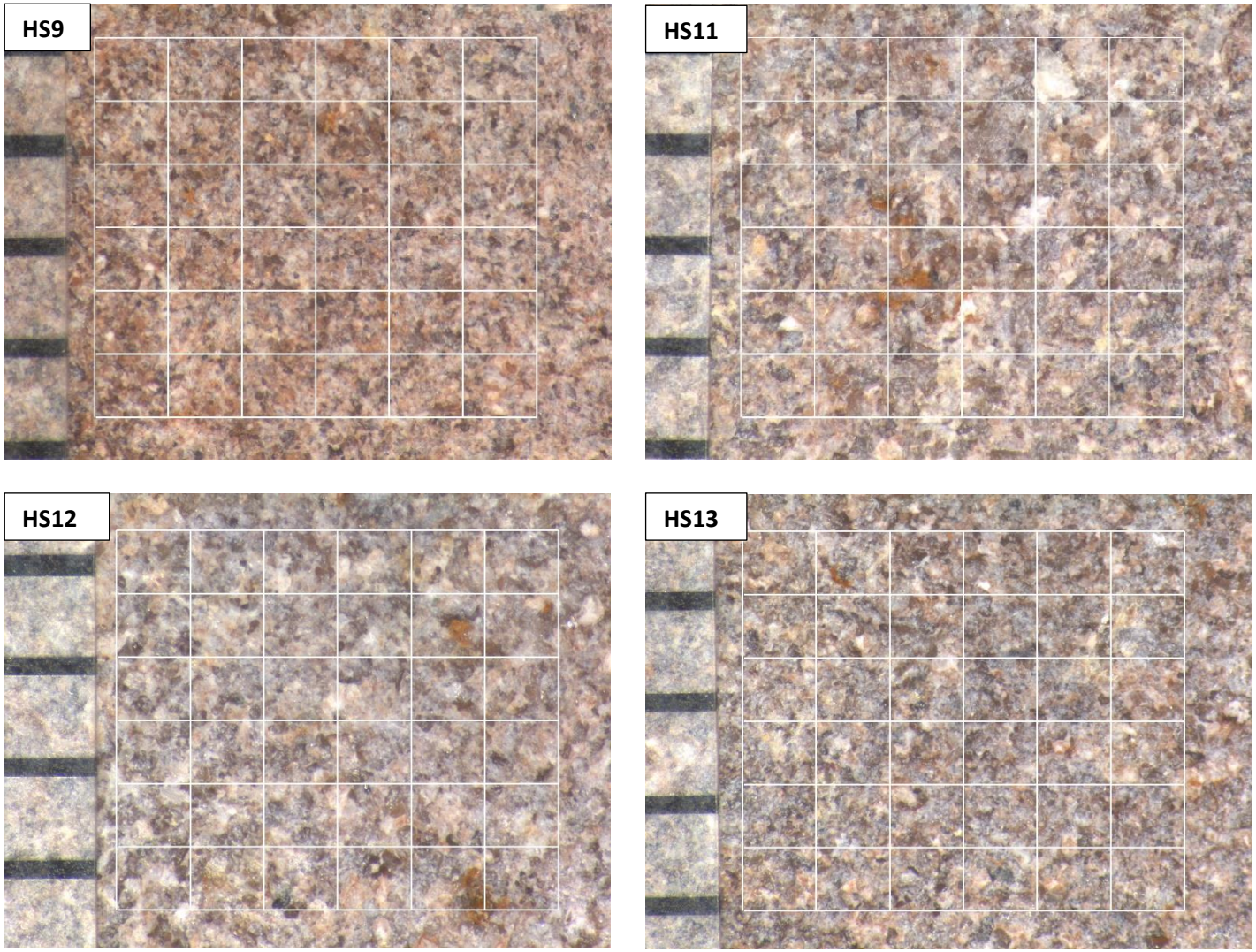
HS9
HS11
HS12
HS13

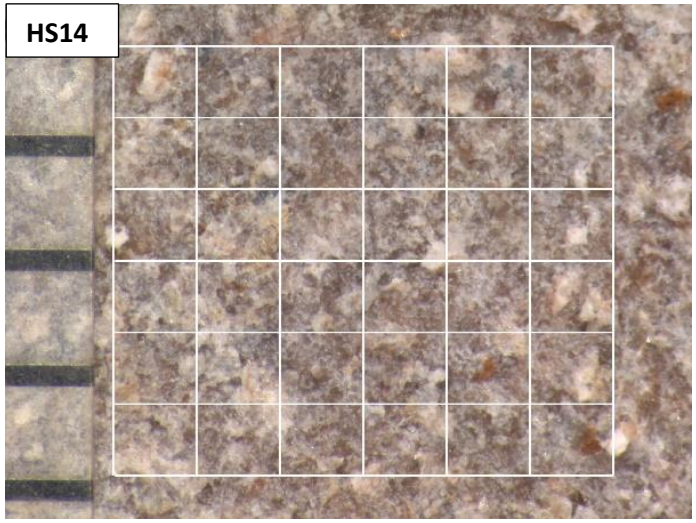
HS14

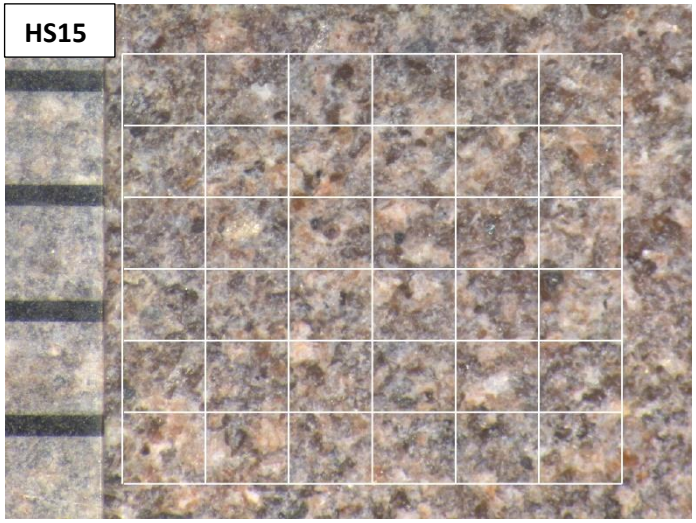
HS15

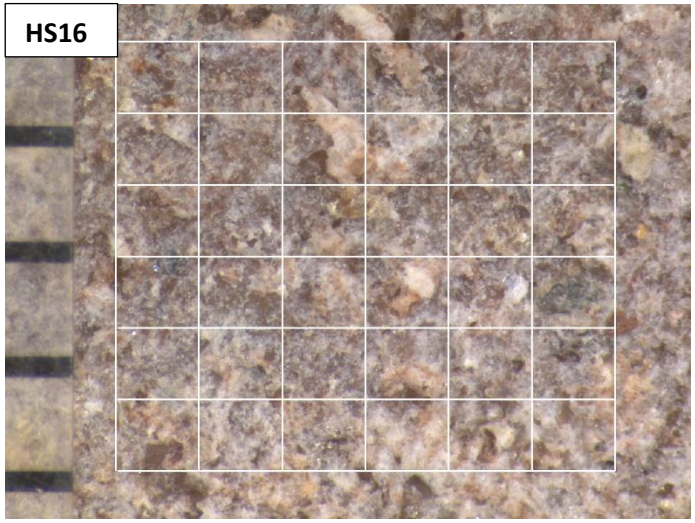
HS16

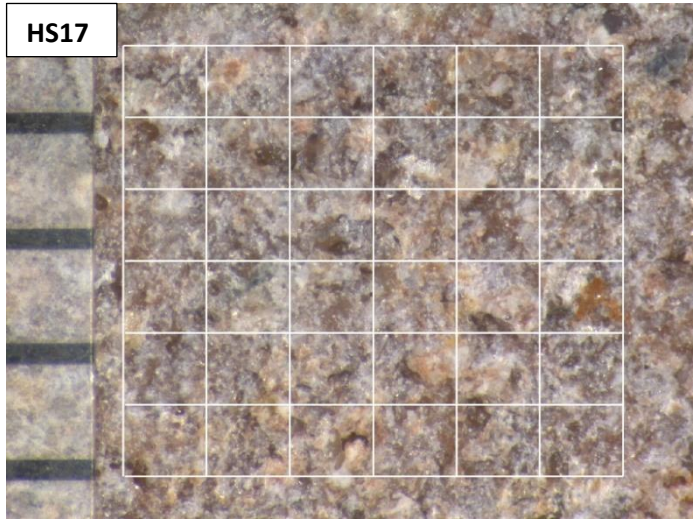
HS17

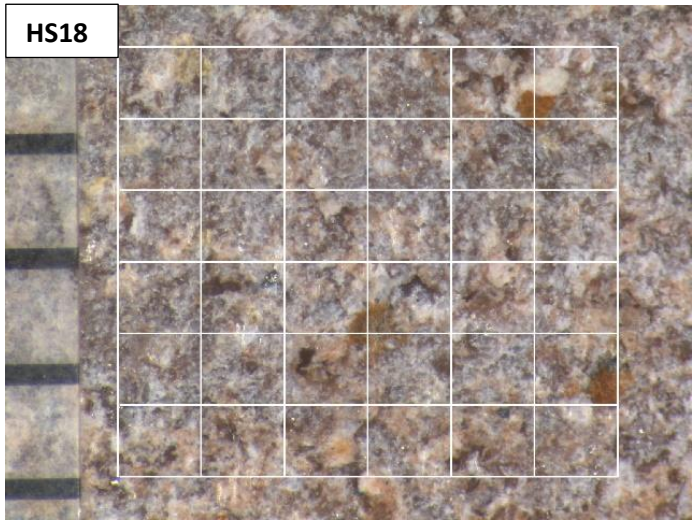
HS18

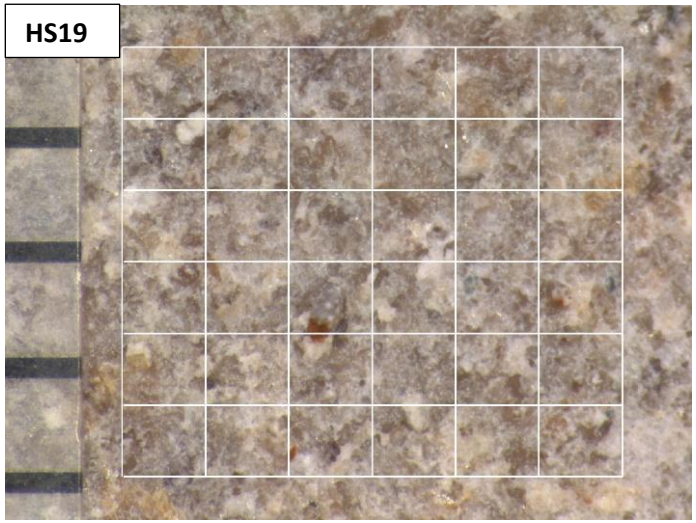
HS19

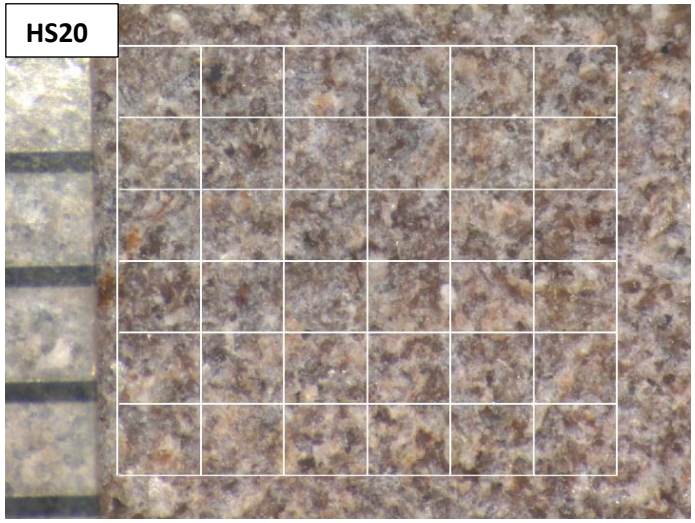
HS20

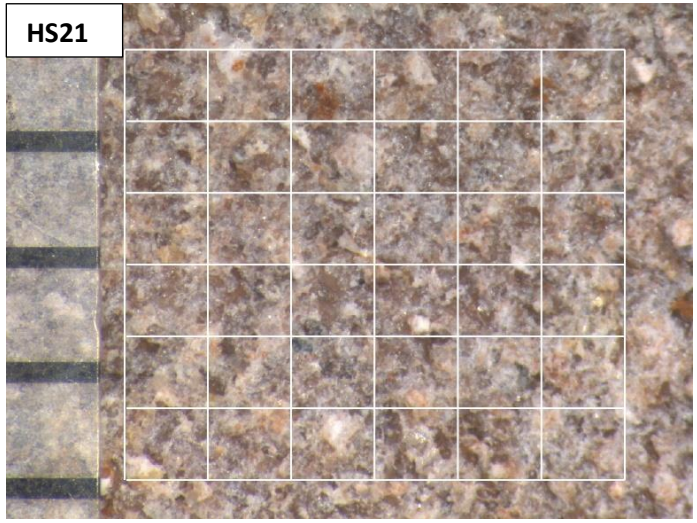
HS21

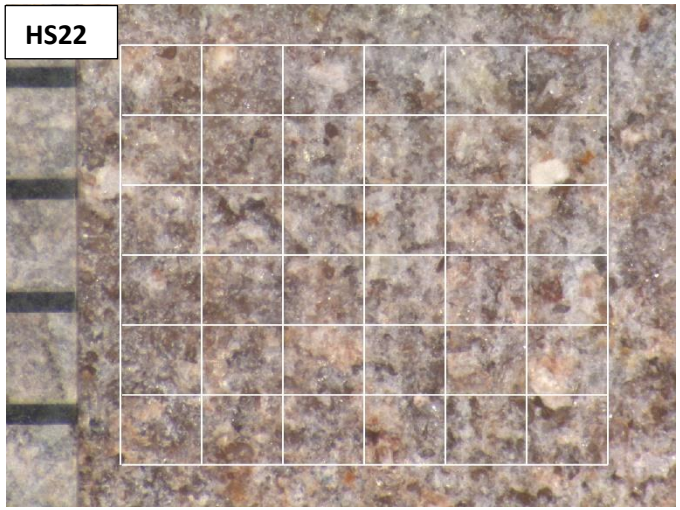
HS22

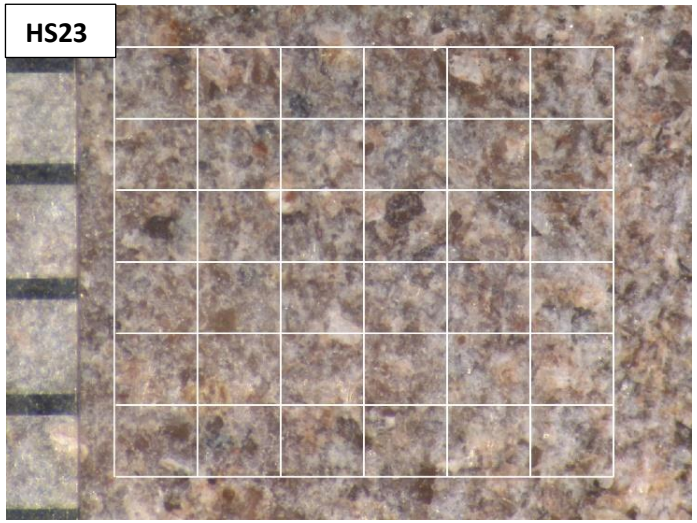
HS23

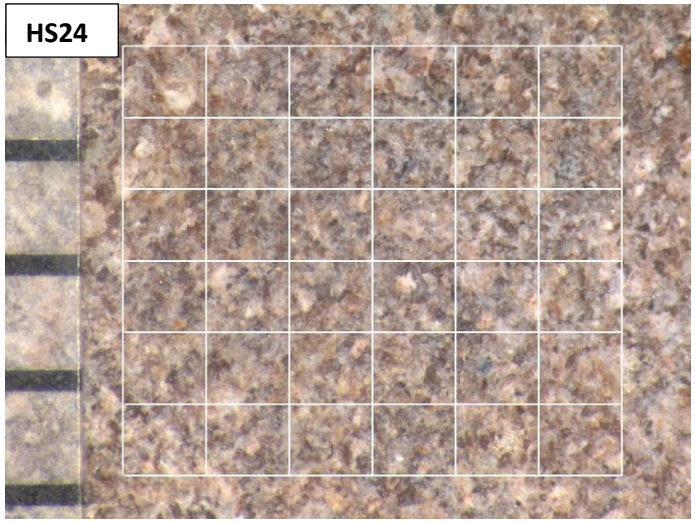
HS24

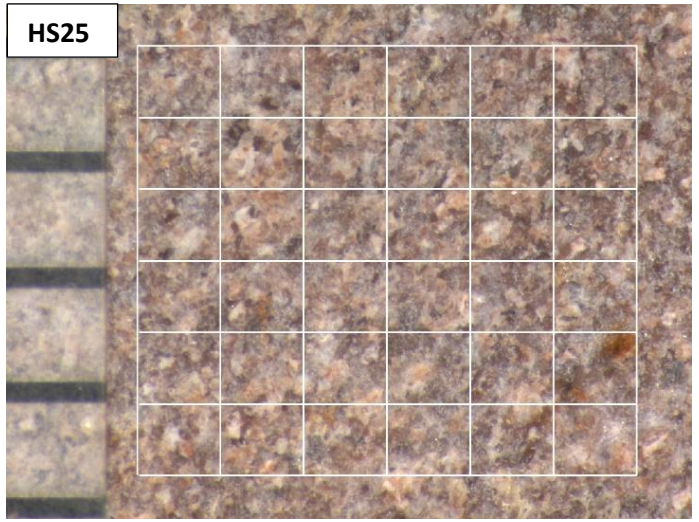
HS25

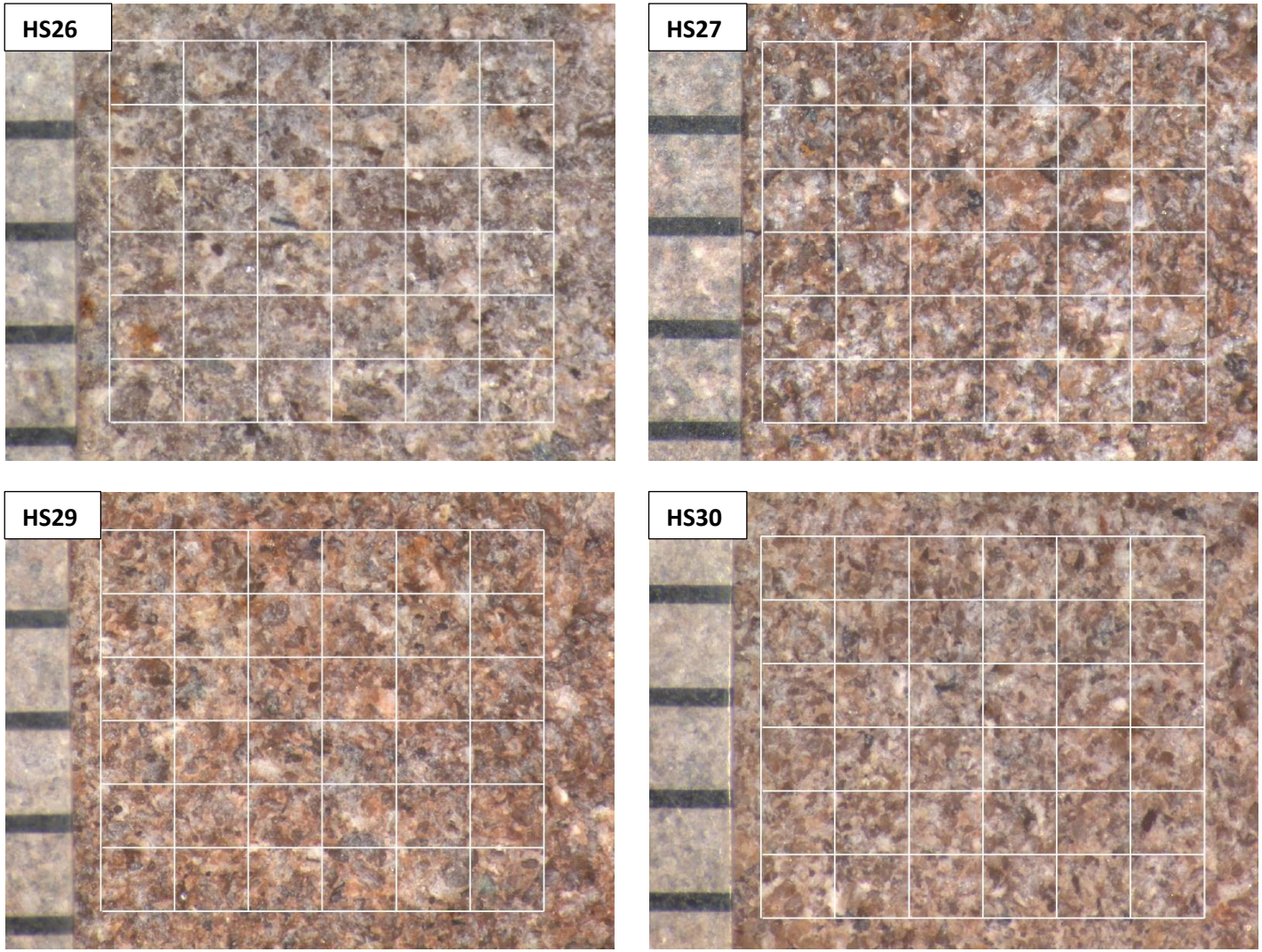
HS26
HS27
HS29
HS30

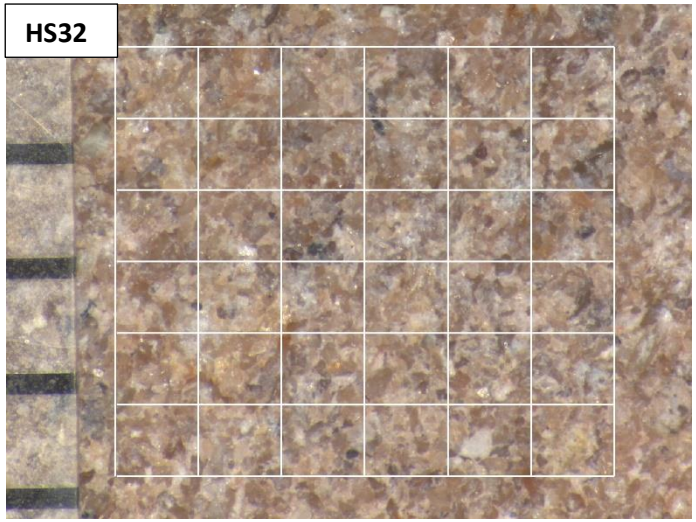
HS32

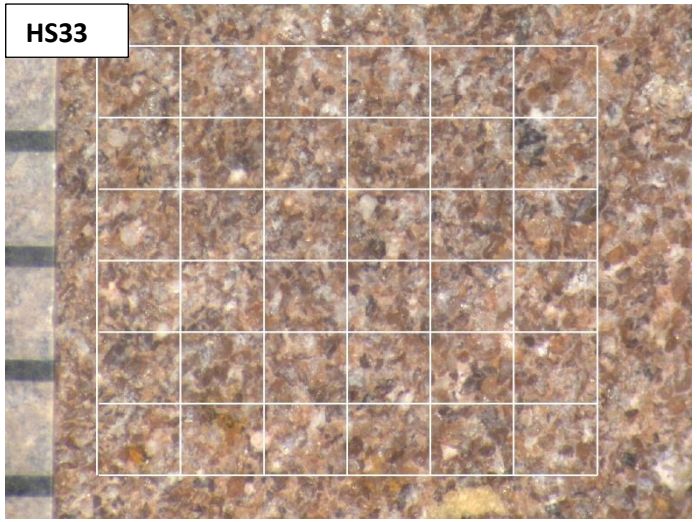
HS33

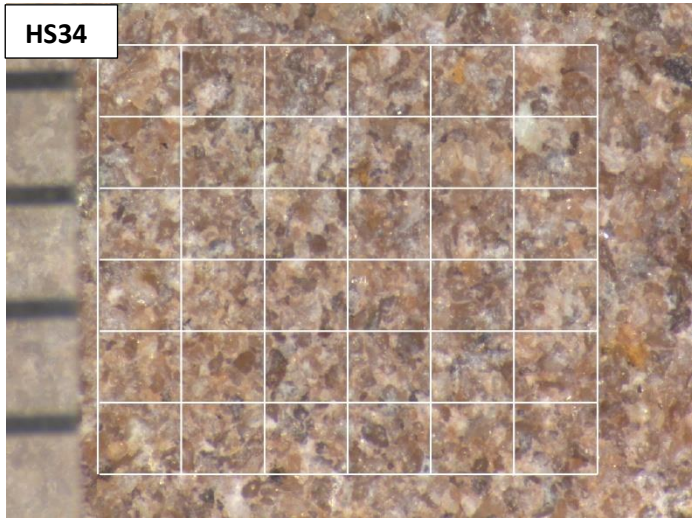
HS34

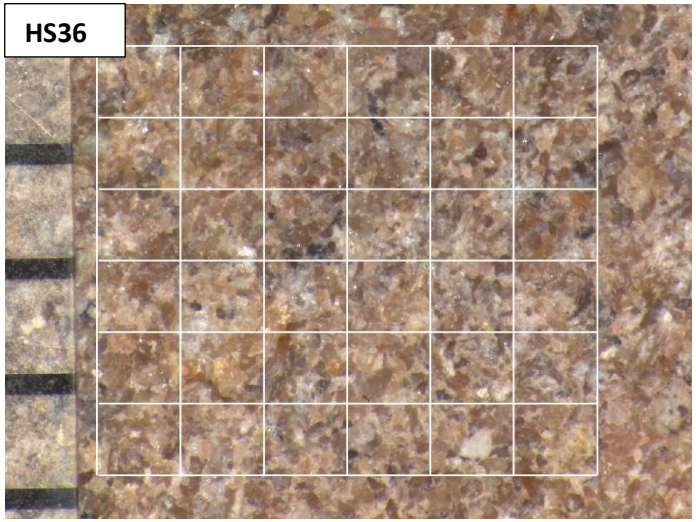
HS36

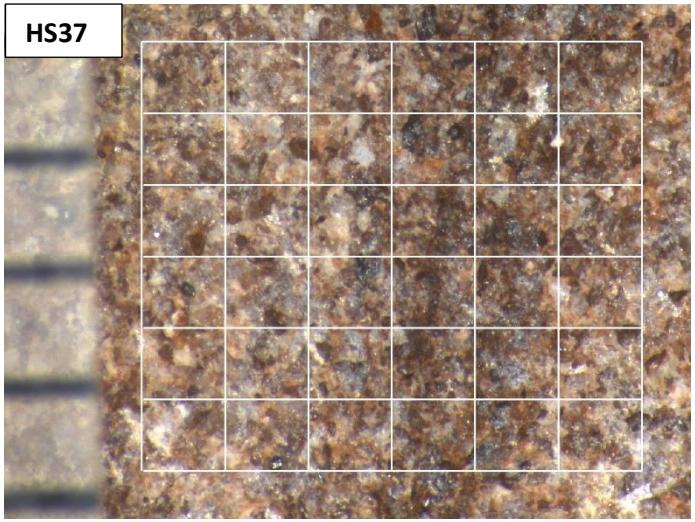
HS37

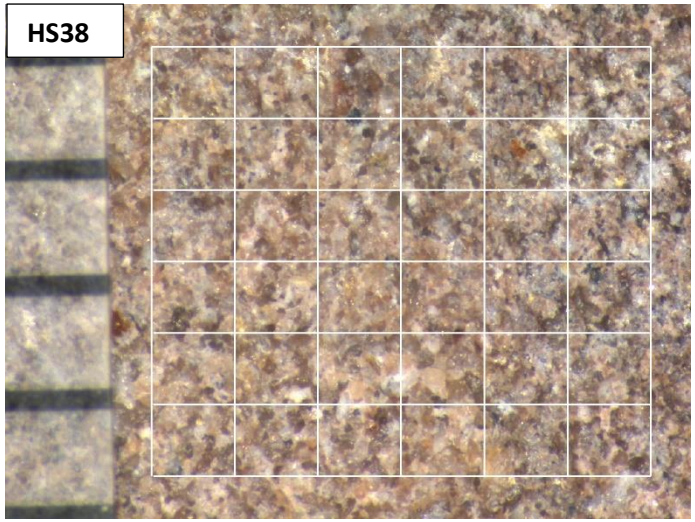
HS38

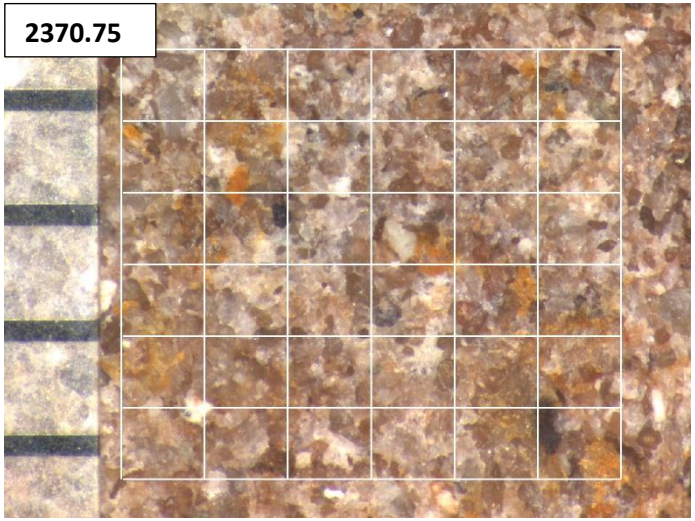
2370.75

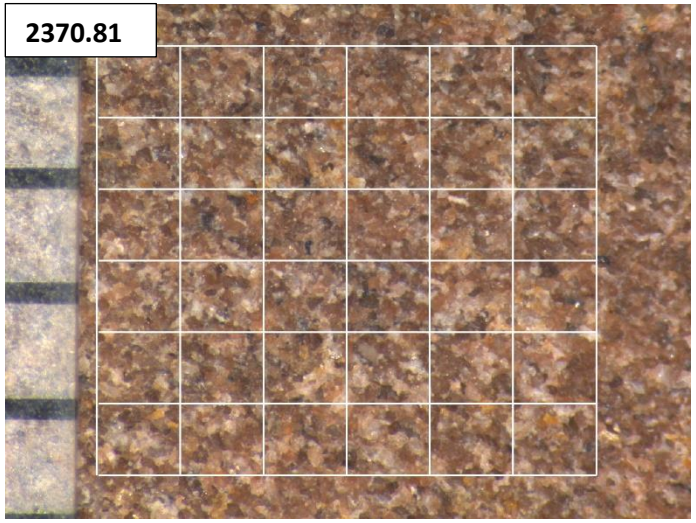
2370.81

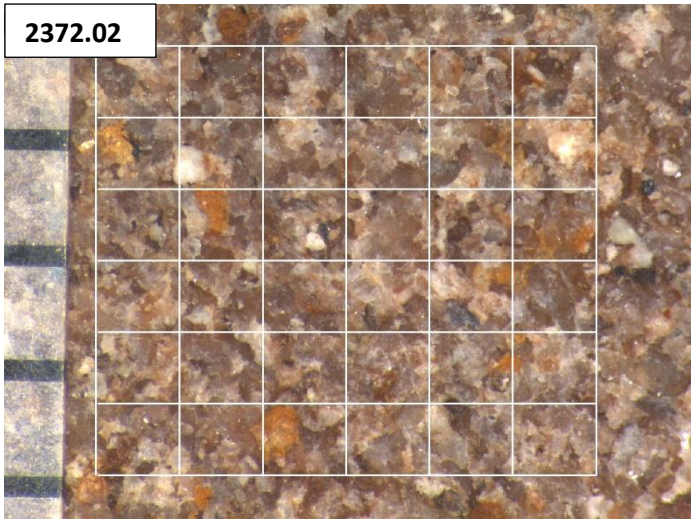
2372.02

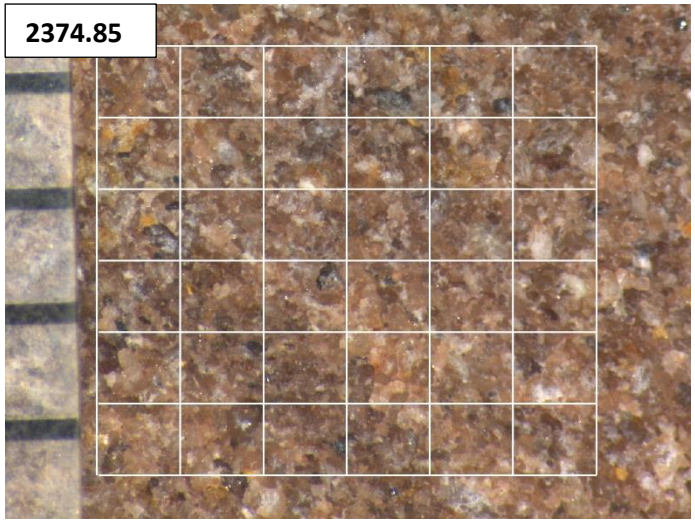
2374.85

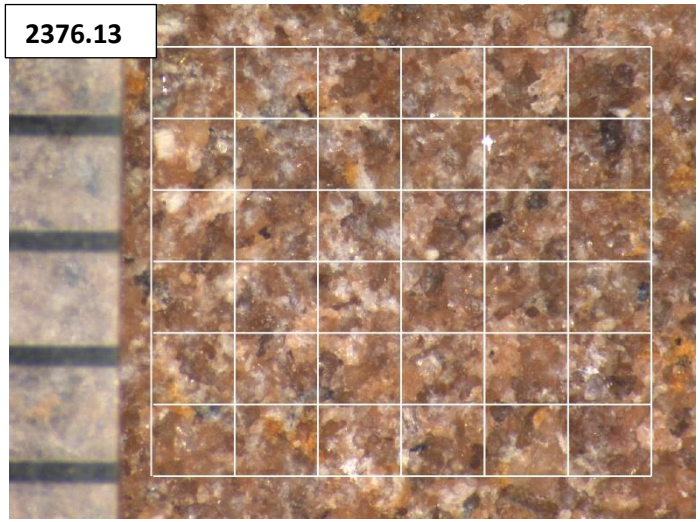
2376.13

NLW-GT-01

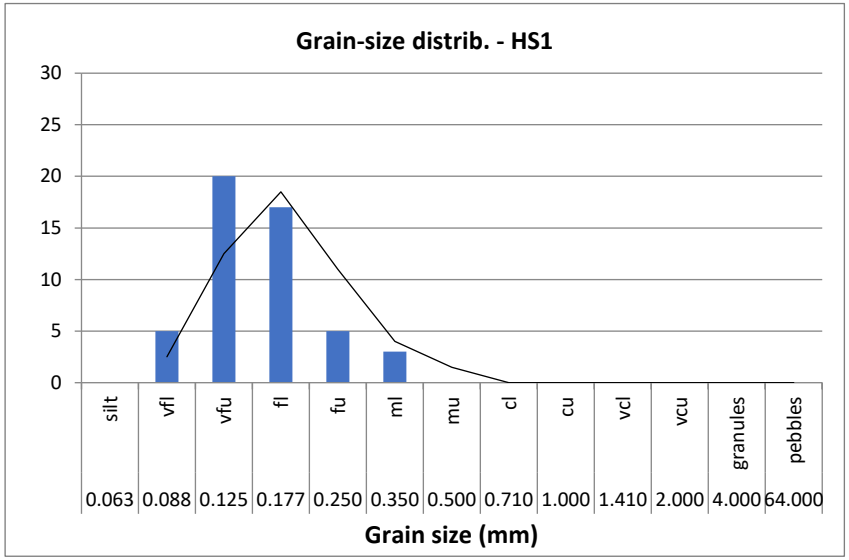
Grain-size distrib. - HS1
30
25
20
15
10
5
0
silt vfl vfu fl fu ml mu cl cu vcl vcu granules pebbles
0.063 0.088 0.125 0.177 0.250 0.350 0.500 0.710 1.000 1.410 2.000 4.000 64.000
Grain size (mm)

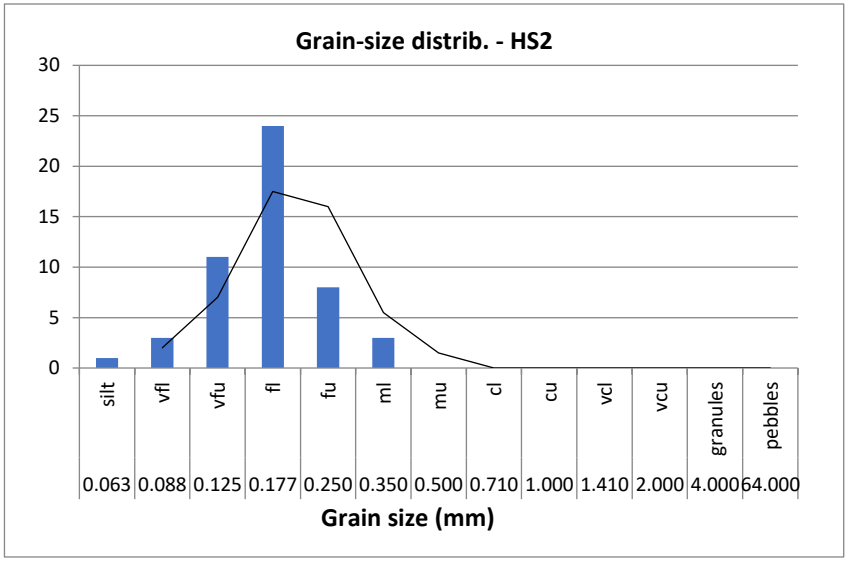
Grain-size distrib. - HS2
30
25
20
15
10
5
0
silt vfl vfu fl fu ml mu cl cu vcl vcu granules pebbles
0.063 0.088 0.125 0.177 0.250 0.350 0.500 0.710 1.000 1.410 2.000 4.000 64.000
Grain size (mm)

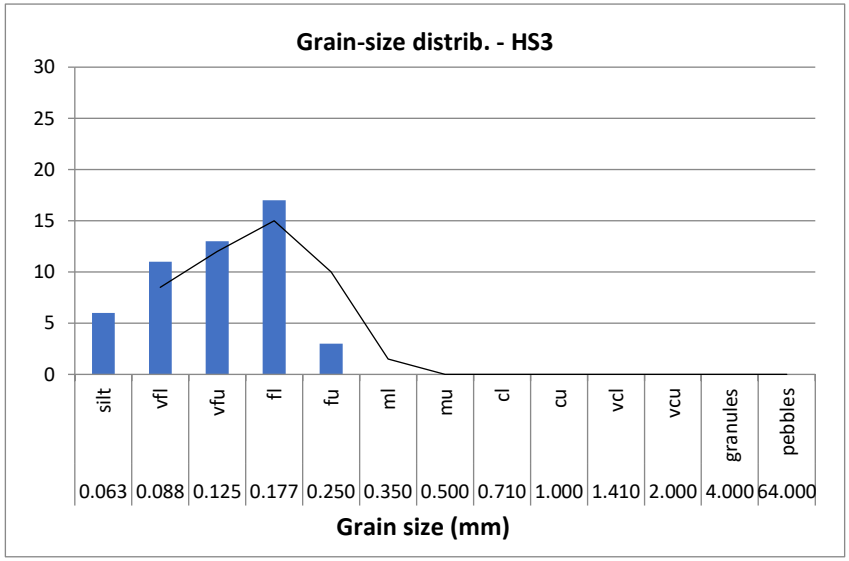
Grain-size distrib. - HS3
30
25
20
15
10
5
0
silt vfl vfu fl fu ml mu cl cu vcl vcu granules pebbles
0.063 0.088 0.125 0.177 0.250 0.350 0.500 0.710 1.000 1.410 2.000 4.000 64.000
Grain size (mm)

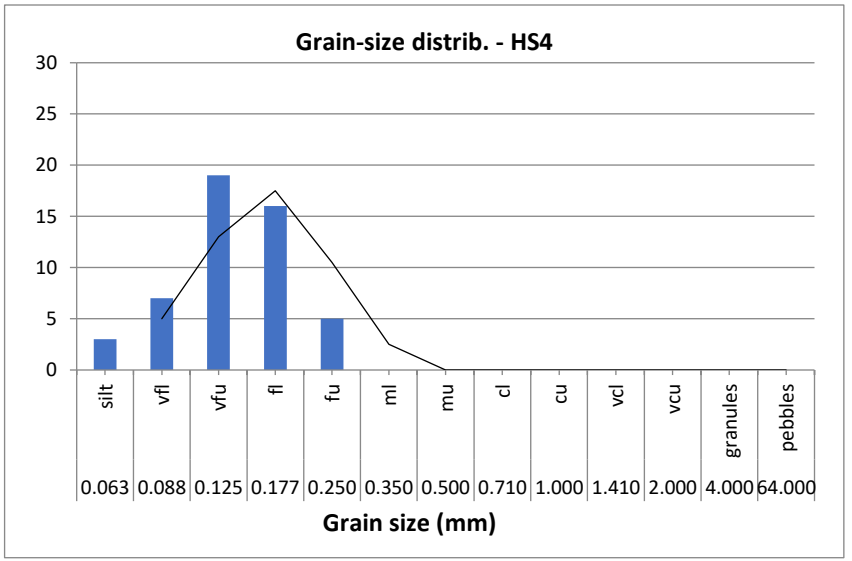
Grain-size distrib. - HS4
30
25
20
15
10
5
0
silt vfl vfu fl fu ml mu cl cu vcl vcu granules pebbles
0.063 0.088 0.125 0.177 0.250 0.350 0.500 0.710 1.000 1.410 2.000 4.000 64.000
Grain size (mm)

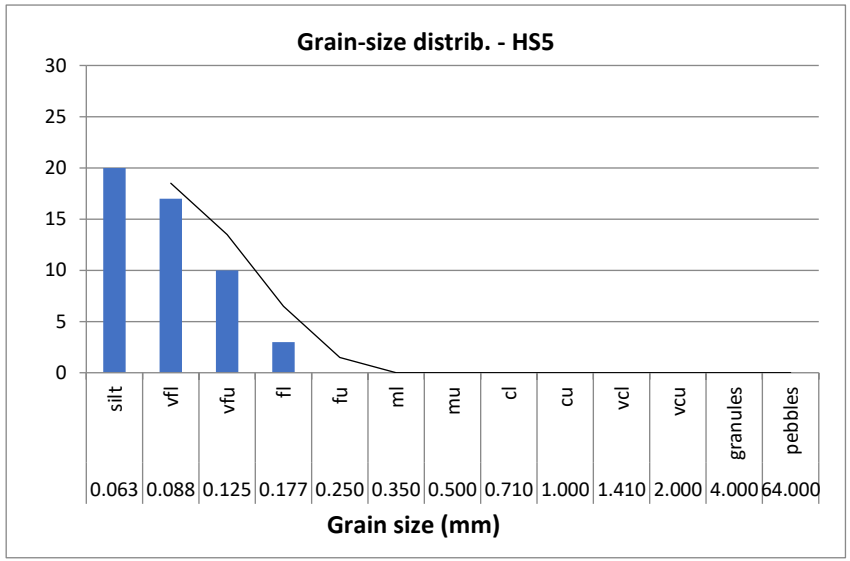
Grain-size distrib. - HS5
30
25
20
15
10
5
0
silt
vfl
vfu
fl
fu
ml
mu
cl
cu
vcl
vcu
granules
pebbles
0.063
0.088
0.125
0.177
0.250
0.350
0.500
0.710
1.000
1.410
2.000
4.000
64.000
Grain size (mm)

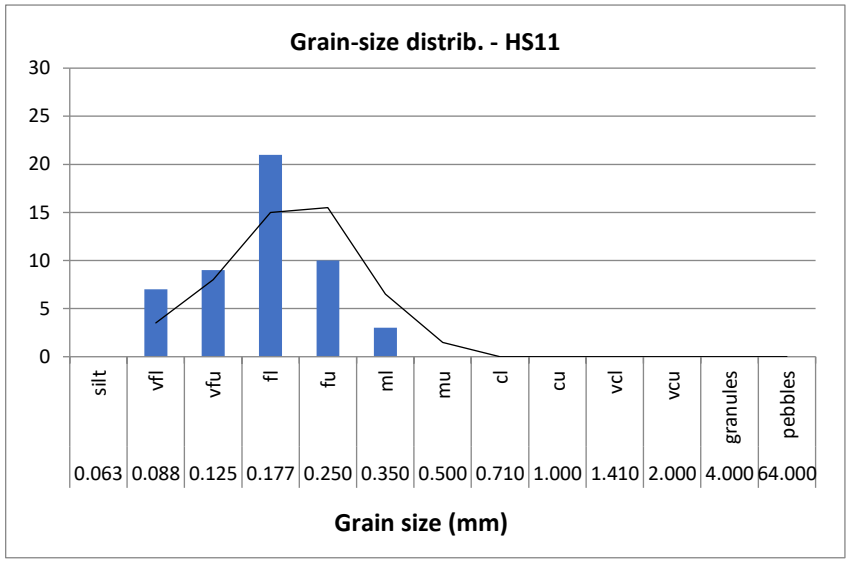
Grain-size distrib. - HS11
30
25
20
15
10
5
0
silt
vfl
vfu
fl
fu
ml
mu
cl
cu
vcl
vcu
granules
pebbles
0.063
0.088
0.125
0.177
0.250
0.350
0.500
0.710
1.000
1.410
2.000
4.000
64.000
Grain size (mm)

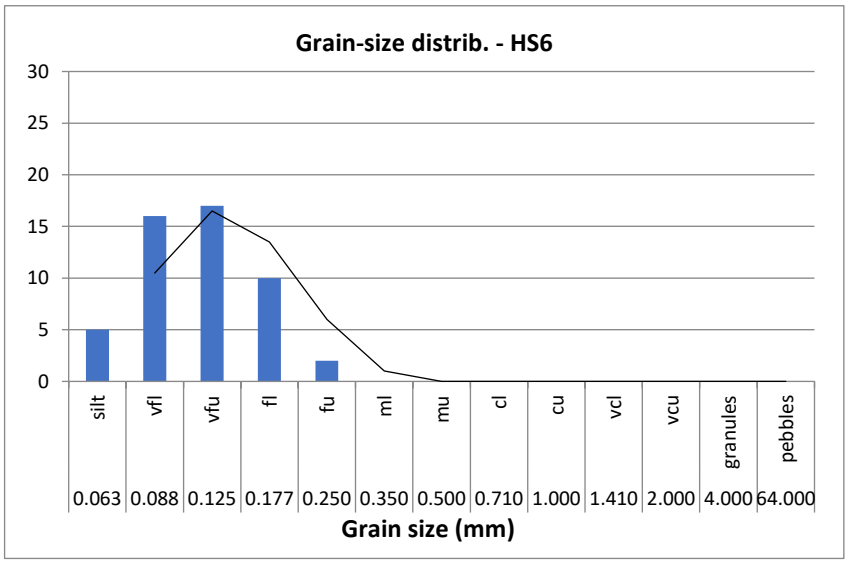
Grain-size distrib. - HS6
30
25
20
15
10
5
0
silt
vfl
vfu
fl
fu
ml
mu
cl
cu
vcl
vcu
granules
pebbles
0.063
0.088
0.125
0.177
0.250
0.350
0.500
0.710
1.000
1.410
2.000
4.000
64.000
Grain size (mm)

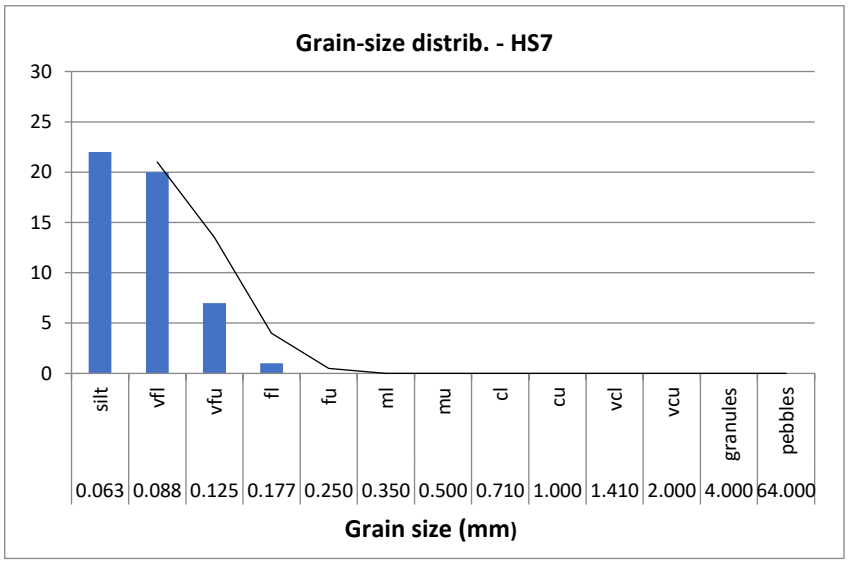
Grain-size distrib. - HS7
30
25
20
15
10
5
0
silt
vfl
vfu
fl
fu
ml
mu
cl
cu
vcl
vcu
granules
pebbles
0.063
0.088
0.125
0.177
0.250
0.350
0.500
0.710
1.000
1.410
2.000
4.000
64.000
Grain size (mm)

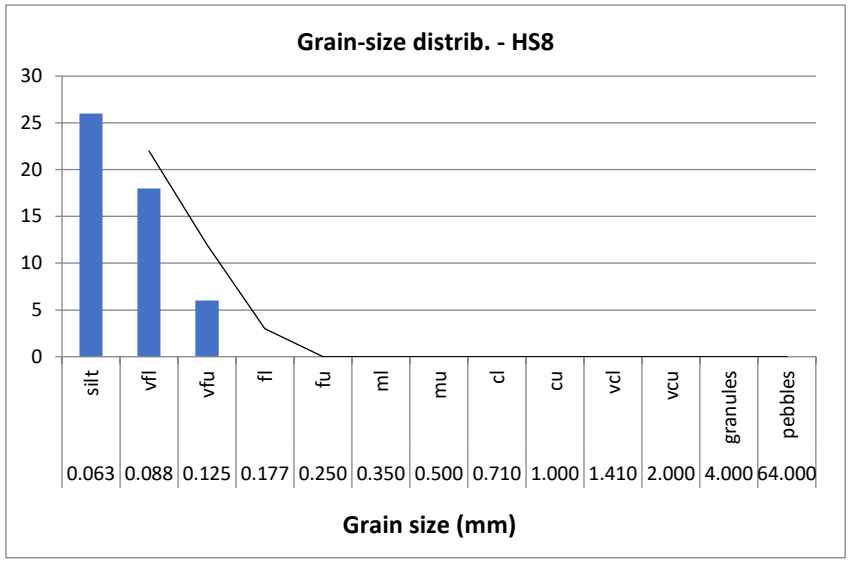
Grain-size distrib. - HS8
30
25
20
15
10
5
0
silt
vfl
vfu
fl
fu
ml
mu
cl
cu
vcl
vcu
granules
pebbles
0.063
0.088
0.125
0.177
0.250
0.350
0.500
0.710
1.000
1.410
2.000
4.000
64.000
Grain size (mm)

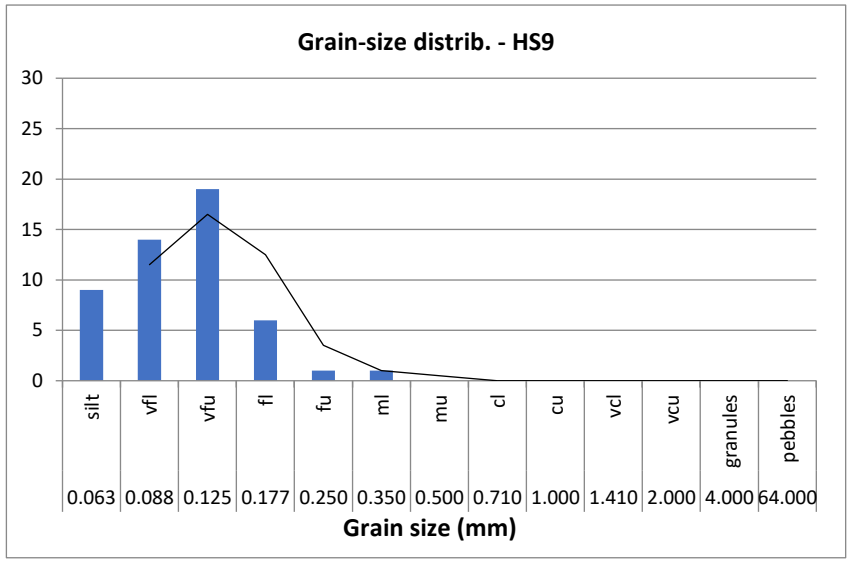
Grain-size distrib. - HS9
30
25
20
15
10
5
0
silt
vfl
vfu
fl
fu
ml
mu
cl
cu
vcl
vcu
granules
pebbles
0.063
0.088
0.125
0.177
0.250
0.350
0.500
0.710
1.000
1.410
2.000
4.000
64.000
Grain size (mm)

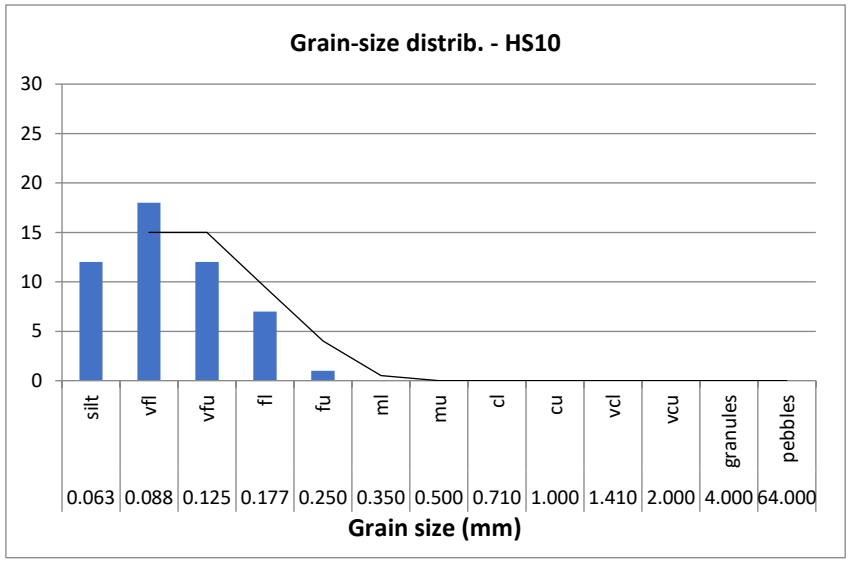
Grain-size distrib. - HS10
30
25
20
15
10
5
0
silt
vfl
vfu
fl
fu
ml
mu
cl
cu
vcl
vcu
granules
pebbles
0.063
0.088
0.125
0.177
0.250
0.350
0.500
0.710
1.000
1.410
2.000
4.000
64.000
Grain size (mm)

NDW-01

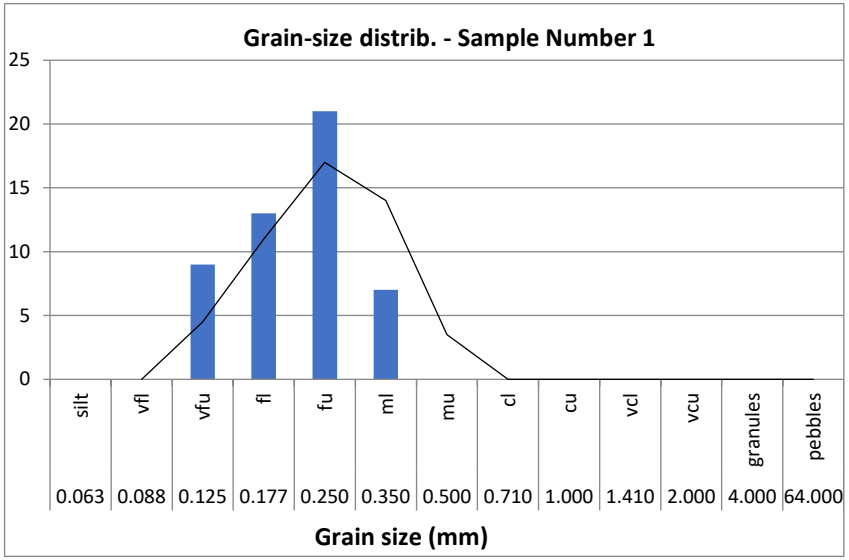
Grain-size distrib. - Sample Number 1
25
20
15
10
5
0
silt vfl vfu fl fu ml mu cl cu vcl vcu granules pebbles
0.063 0.088 0.125 0.177 0.250 0.350 0.500 0.710 1.000 1.410 2.000 4.000 64.000
Grain size (mm)

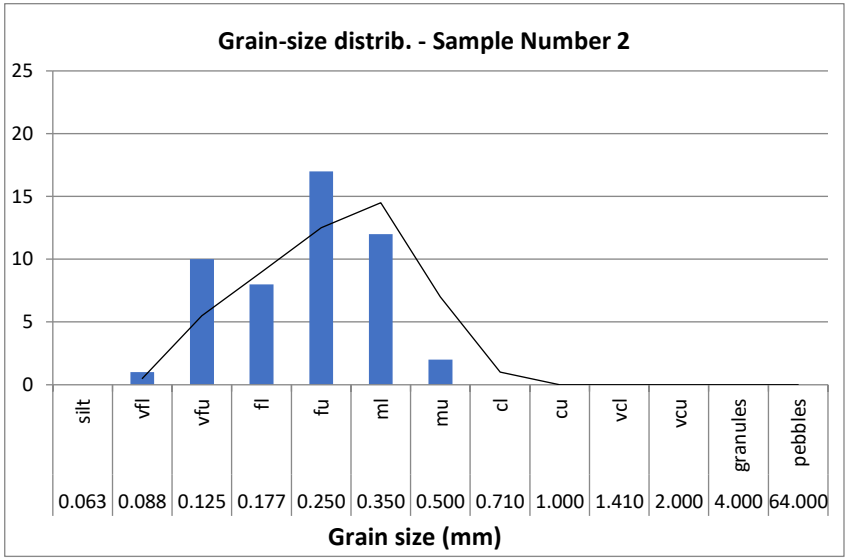
Grain-size distrib. - Sample Number 2
25
20
15
10
5
0
silt vfl vfu fl fu ml mu cl cu vcl vcu granules pebbles
0.063 0.088 0.125 0.177 0.250 0.350 0.500 0.710 1.000 1.410 2.000 4.000 64.000
Grain size (mm)

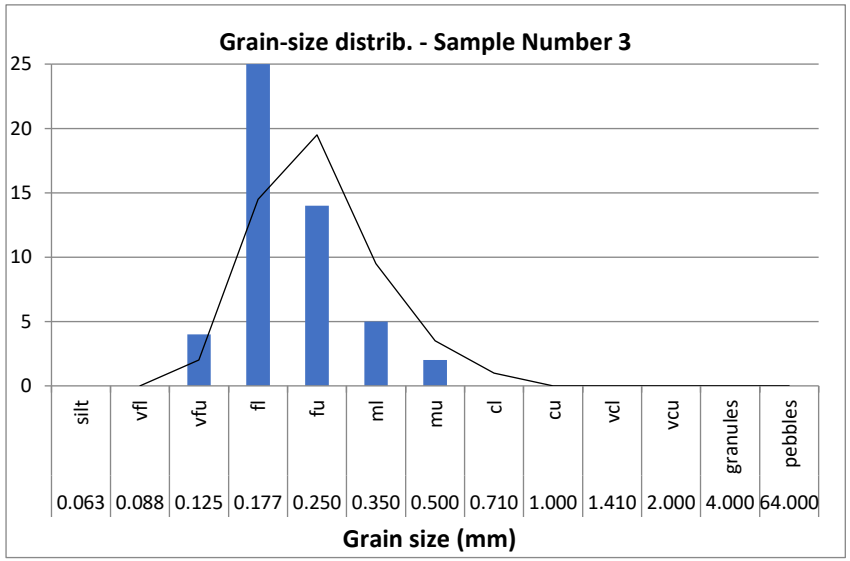
Grain-size distrib. - Sample Number 3
25
20
15
10
5
0
silt vfl vfu fl fu ml mu cl cu vcl vcu granules pebbles
0.063 0.088 0.125 0.177 0.250 0.350 0.500 0.710 1.000 1.410 2.000 4.000 64.000
Grain size (mm)

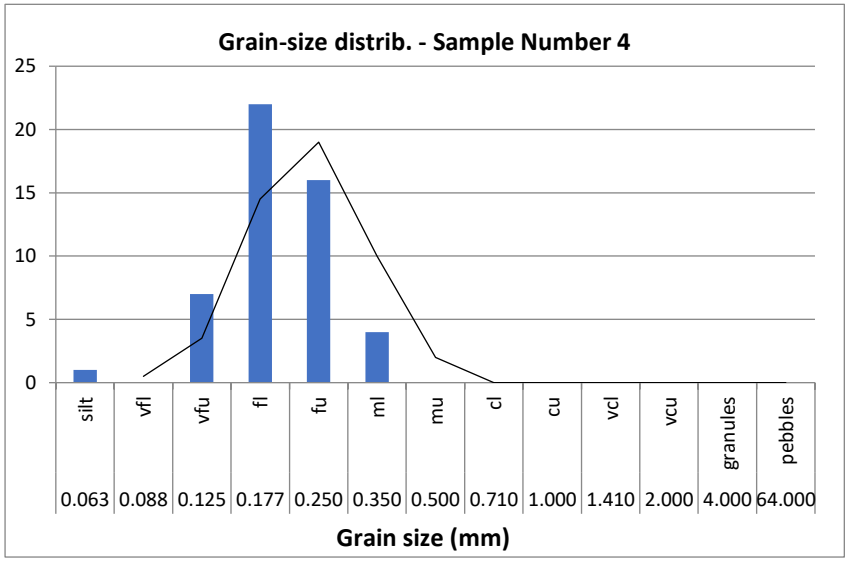
Grain-size distrib. - Sample Number 4
25
20
15
10
5
0
silt vfl vfu fl fu ml mu cl cu vcl vcu granules pebbles
0.063 0.088 0.125 0.177 0.250 0.350 0.500 0.710 1.000 1.410 2.000 4.000 64.000
Grain size (mm)

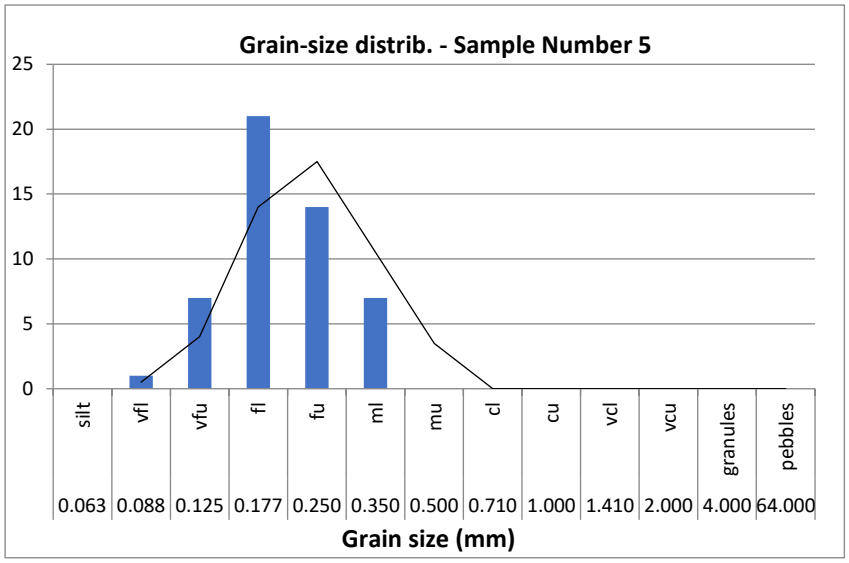
Grain-size distrib. - Sample Number 5
25
20
15
10
5
0
silt
vfl
vfu
fl
fu
ml
mu
cl
cu
vcl
vcu
granules
pebbles
0.063
0.088
0.125
0.177
0.250
0.350
0.500
0.710
1.000
1.410
2.000
4.000
64.000
Grain size (mm)

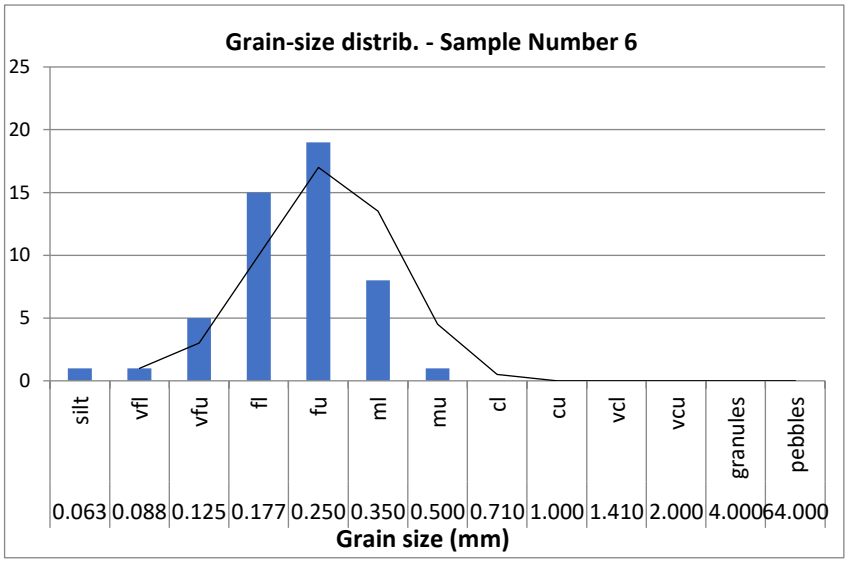
Grain-size distrib. - Sample Number 6
25
20
15
10
5
0
silt
vfl
vfu
fl
fu
ml
mu
cl
cu
vcl
vcu
granules
pebbles
0.063
0.088
0.125
0.177
0.250
0.350
0.500
0.710
1.000
1.410
2.000
4.000
64.000
Grain size (mm)

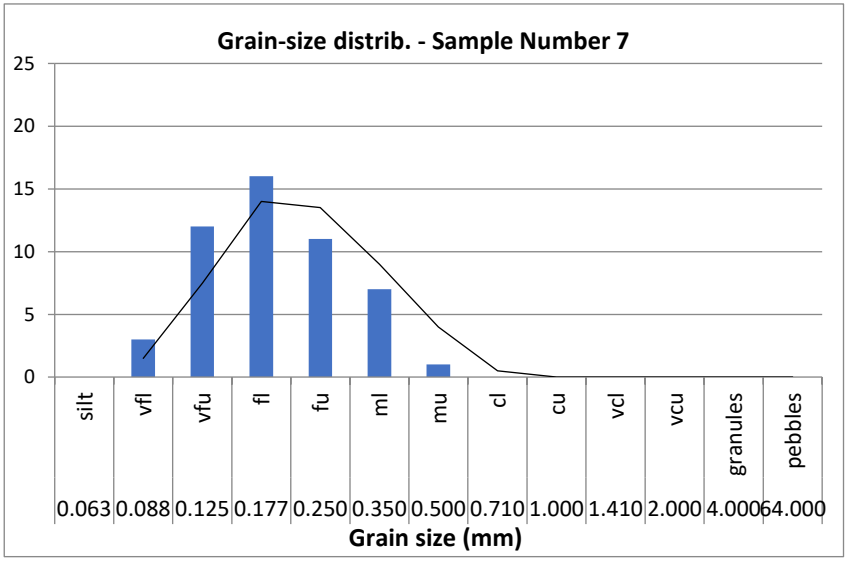
Grain-size distrib. - Sample Number 7
25
20
15
10
5
0
silt
vfl
vfu
fl
fu
ml
mu
cl
cu
vcl
vcu
granules
pebbles
0.063
0.088
0.125
0.177
0.250
0.350
0.500
0.710
1.000
1.410
2.000
4.000
64.000
Grain size (mm)

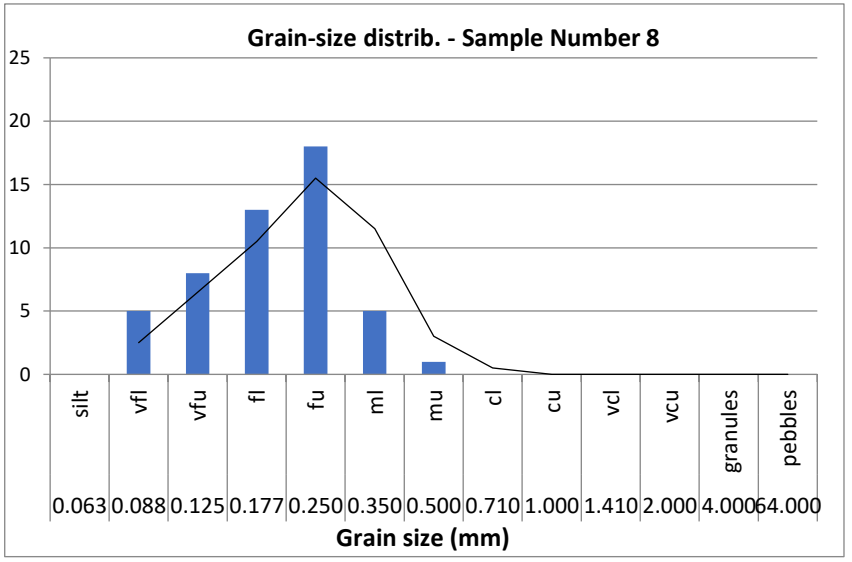
Grain-size distrib. - Sample Number 8
25
20
15
10
5
0
silt
vfl
vfu
fl
fu
ml
mu
cl
cu
vcl
vcu
granules
pebbles
0.063
0.088
0.125
0.177
0.250
0.350
0.500
0.710
1.000
1.410
2.000
4.000
64.000
Grain size (mm)

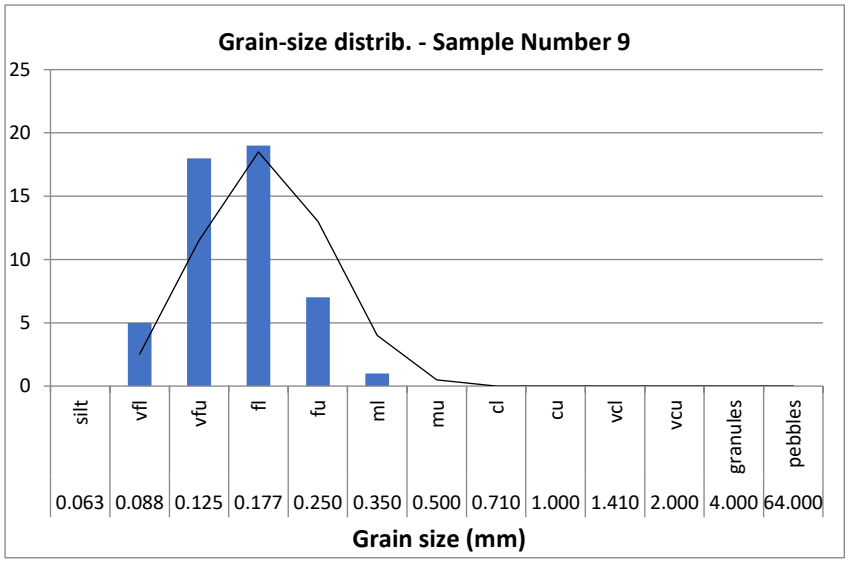
Grain-size distrib. - Sample Number 9
25
20
15
10
5
0
silt
vfl
vfu
fl
fu
ml
mu
cl
cu
vcl
vcu
granules
pebbles
0.063
0.088
0.125
0.177
0.250
0.350
0.500
0.710
1.000
1.410
2.000
4.000
64.000
Grain size (mm)

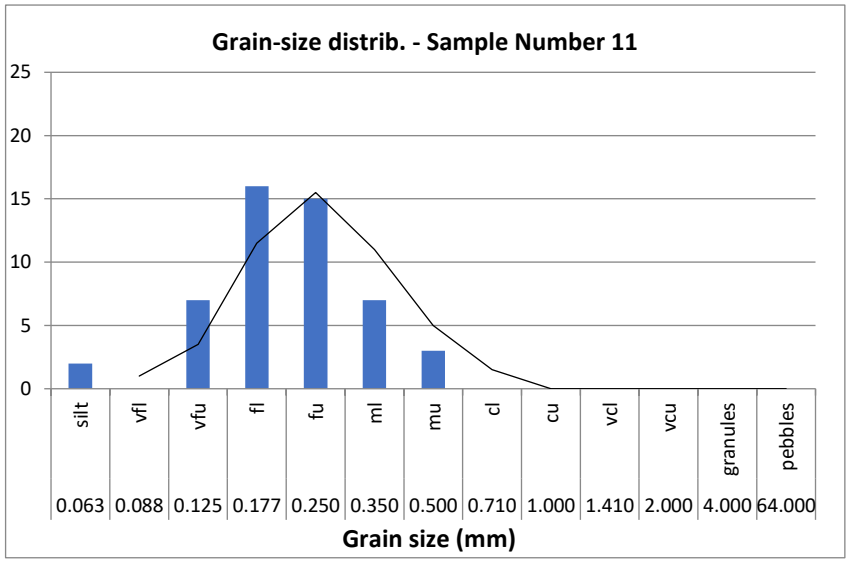
Grain-size distrib. - Sample Number 11
25
20
15
10
5
0
silt
vfl
vfu
fl
fu
ml
mu
cl
cu
vcl
vcu
granules
pebbles
0.063
0.088
0.125
0.177
0.250
0.350
0.500
0.710
1.000
1.410
2.000
4.000
64.000
Grain size (mm)

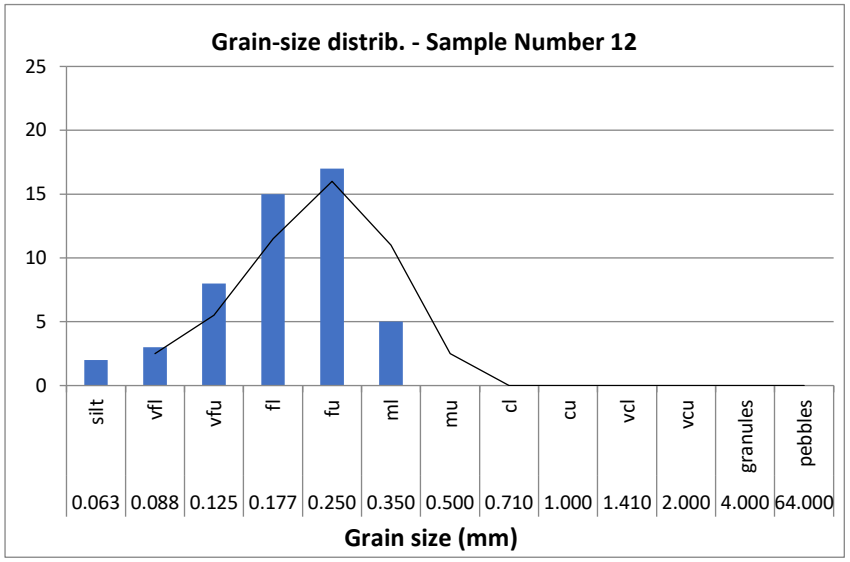
Grain-size distrib. - Sample Number 12
25
20
15
10
5
0
silt
vfl
vfu
fl
fu
ml
mu
cl
cu
vcl
vcu
granules
pebbles
0.063
0.088
0.125
0.177
0.250
0.350
0.500
0.710
1.000
1.410
2.000
4.000
64.000
Grain size (mm)

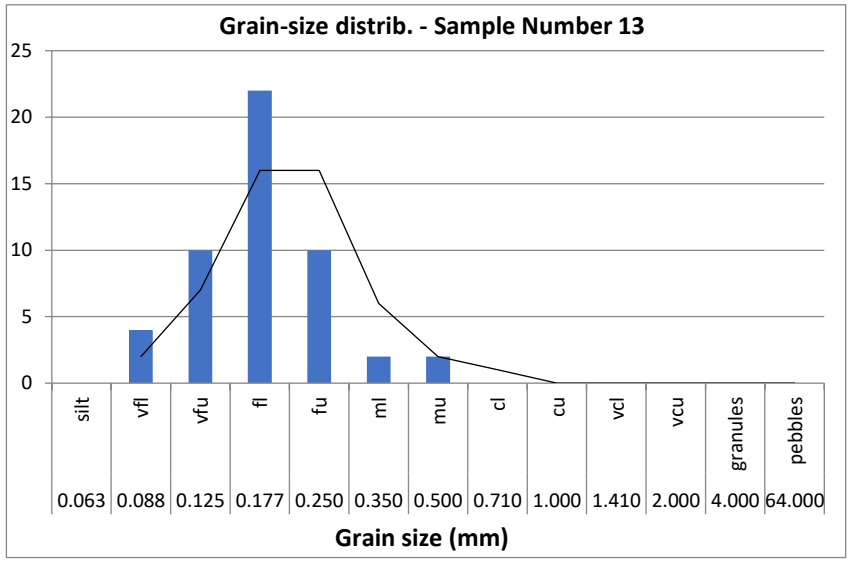
Grain-size distrib. - Sample Number 13
25
20
15
10
5
0
silt
vfl
vfu
fl
fu
ml
mu
cl
cu
vcl
vcu
granules
pebbles
0.063
0.088
0.125
0.177
0.250
0.350
0.500
0.710
1.000
1.410
2.000
4.000
64.000
Grain size (mm)

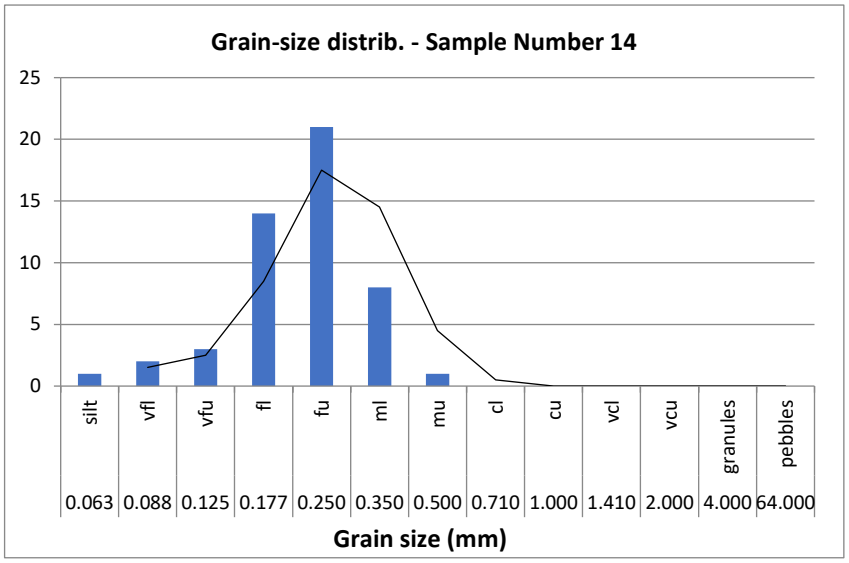
Grain-size distrib. - Sample Number 14
25
20
15
10
5
0
silt vfl vfu fl fu ml mu cl cu vcl vcu granules pebbles
0.063 0.088 0.125 0.177 0.250 0.350 0.500 0.710 1.000 1.410 2.000 4.000 64.000
Grain size (mm)

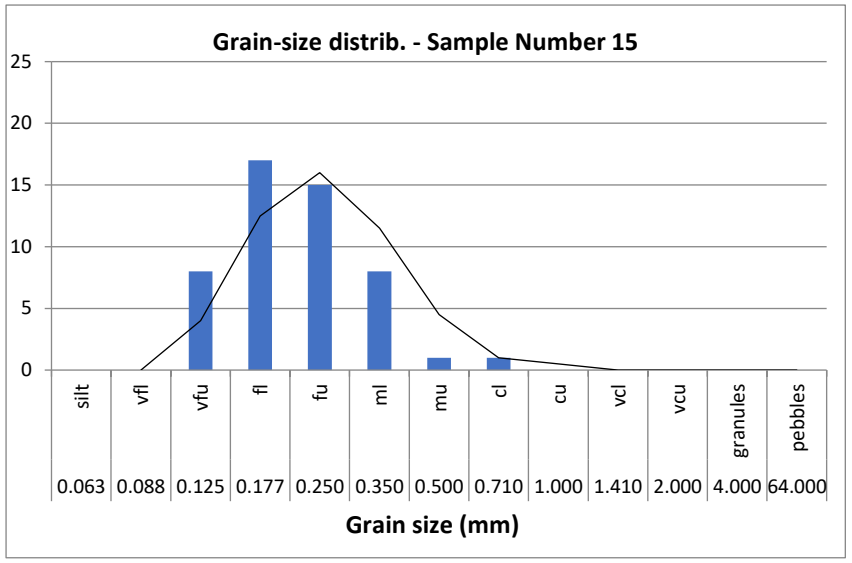
Grain-size distrib. - Sample Number 15
25
20
15
10
5
0
silt vfl vfu fl fu ml mu cl cu vcl vcu granules pebbles
0.063 0.088 0.125 0.177 0.250 0.350 0.500 0.710 1.000 1.410 2.000 4.000 64.000
Grain size (mm)

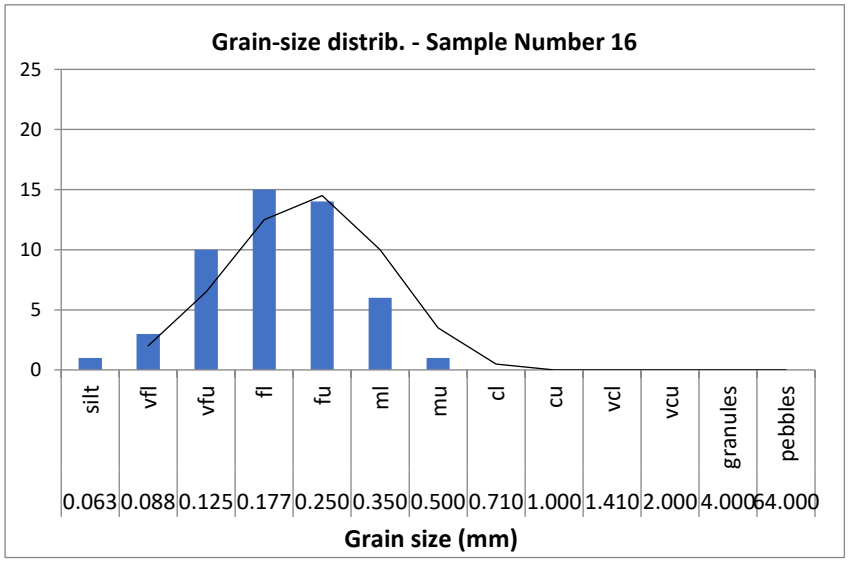
Grain-size distrib. - Sample Number 16
25
20
15
10
5
0
silt vfl vfu fl fu ml mu cl cu vcl vcu granules pebbles
0.063 0.088 0.125 0.177 0.250 0.350 0.500 0.710 1.000 1.410 2.000 4.000 64.000
Grain size (mm)

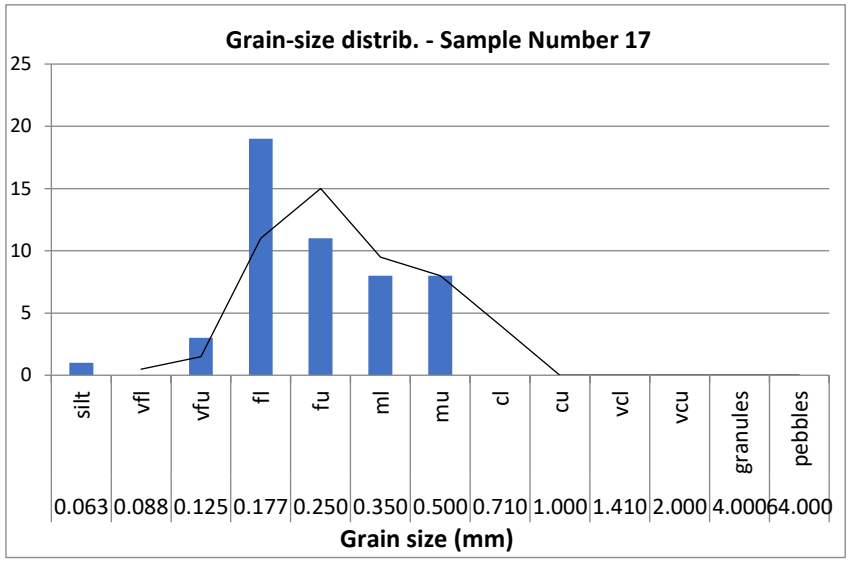
Grain-size distrib. - Sample Number 17
25
20
15
10
5
0
silt vfl vfu fl fu ml mu cl cu vcl vcu granules pebbles
0.063 0.088 0.125 0.177 0.250 0.350 0.500 0.710 1.000 1.410 2.000 4.000 64.000
Grain size (mm)

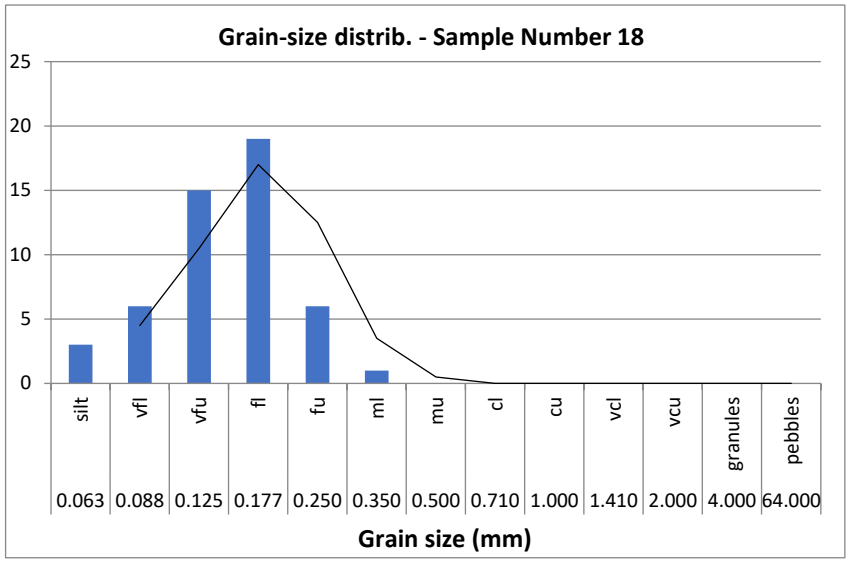
Grain-size distrib. - Sample Number 18
25
20
15
10
5
0
silt vfl vfu fl fu ml mu cl cu vcl vcu granules pebbles
0.063 0.088 0.125 0.177 0.250 0.350 0.500 0.710 1.000 1.410 2.000 4.000 64.000
Grain size (mm)

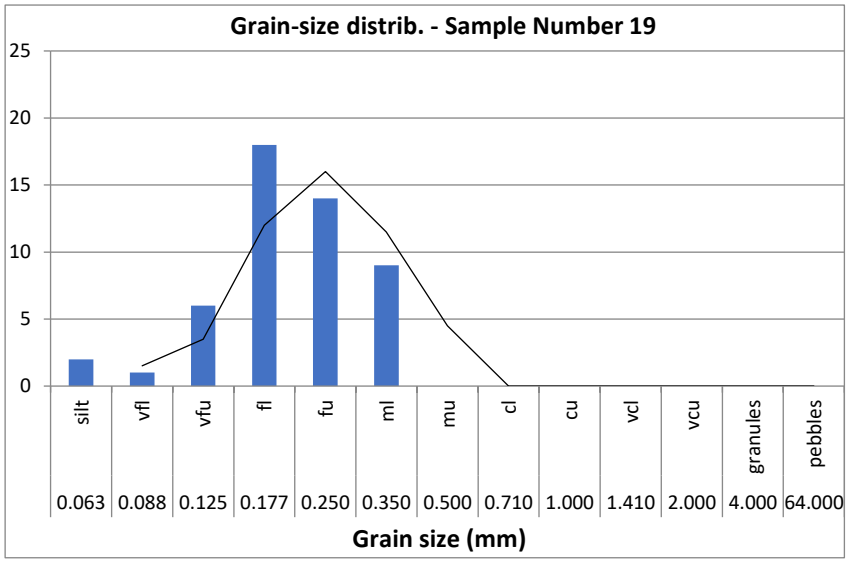
Grain-size distrib. - Sample Number 19
25
20
15
10
5
0
silt vfl vfu fl fu ml mu cl cu vcl vcu granules pebbles
0.063 0.088 0.125 0.177 0.250 0.350 0.500 0.710 1.000 1.410 2.000 4.000 64.000
Grain size (mm)

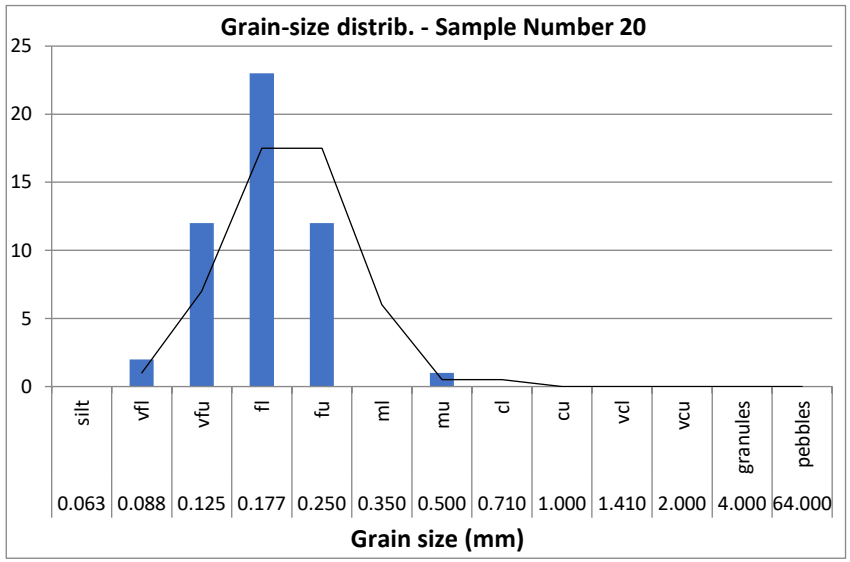
Grain-size distrib. - Sample Number 20
25
20
15
10
5
0
silt vfl vfu fl fu ml mu cl cu vcl vcu granules pebbles
0.063 0.088 0.125 0.177 0.250 0.350 0.500 0.710 1.000 1.410 2.000 4.000 64.000
Grain size (mm)

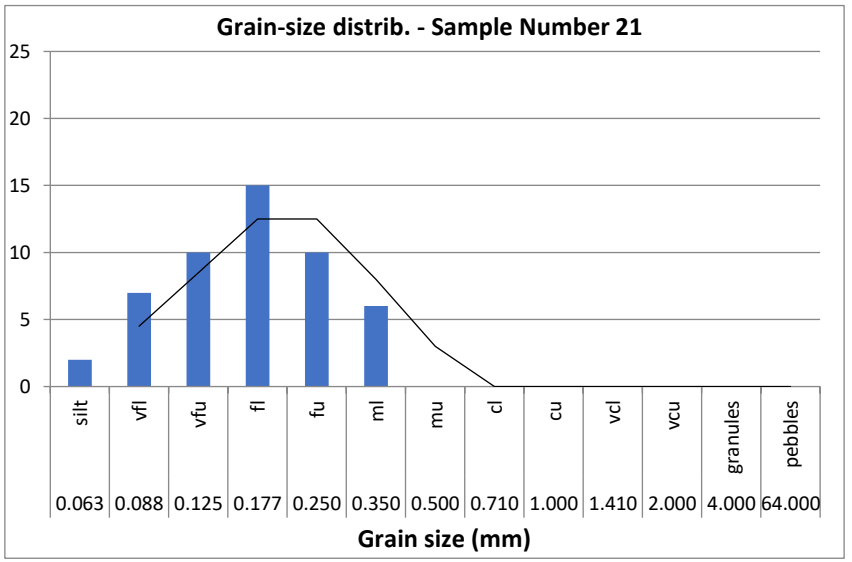
Grain-size distrib. - Sample Number 21
25
20
15
10
5
0
silt vfl vfu fl fu ml mu cl cu vcl vcu granules pebbles
0.063 0.088 0.125 0.177 0.250 0.350 0.500 0.710 1.000 1.410 2.000 4.000 64.000
Grain size (mm)

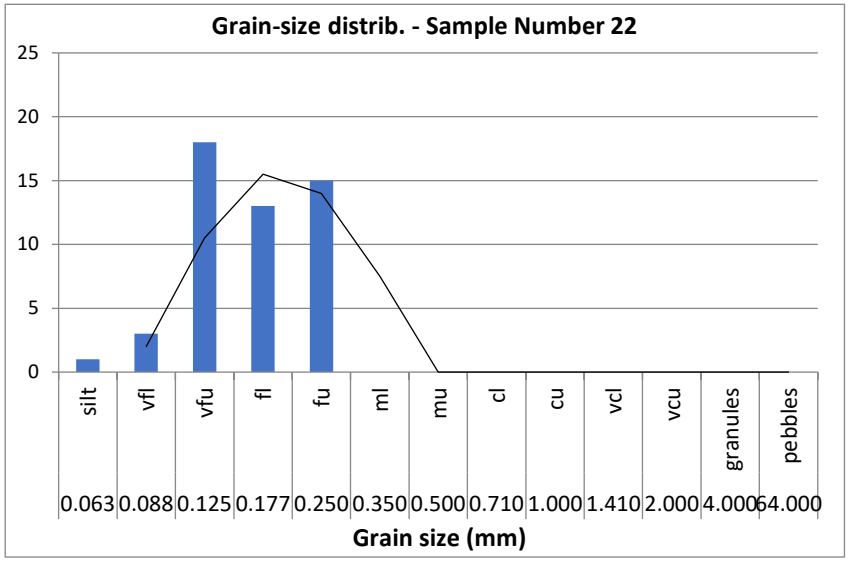
Grain-size distrib. - Sample Number 22
25
20
15
10
5
0
silt
vfl
vfu
fl
fu
ml
mu
cl
cu
vcl
vcu
granules
pebbles
0.063
0.088
0.125
0.177
0.250
0.350
0.500
0.710
1.000
1.410
2.000
4.000
64.000
Grain size (mm)

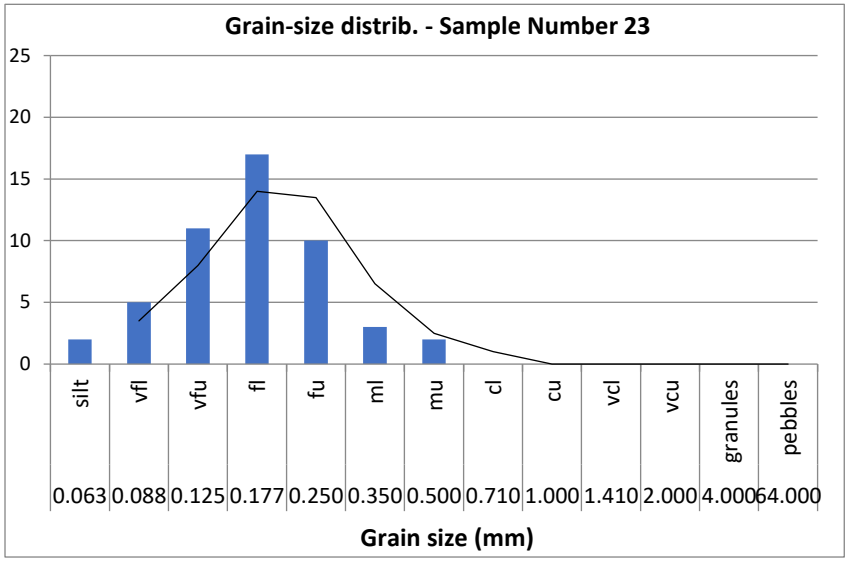
Grain-size distrib. - Sample Number 23
25
20
15
10
5
0
silt
vfl
vfu
fl
fu
ml
mu
cl
cu
vcl
vcu
granules
pebbles
0.063
0.088
0.125
0.177
0.250
0.350
0.500
0.710
1.000
1.410
2.000
4.000
64.000
Grain size (mm)

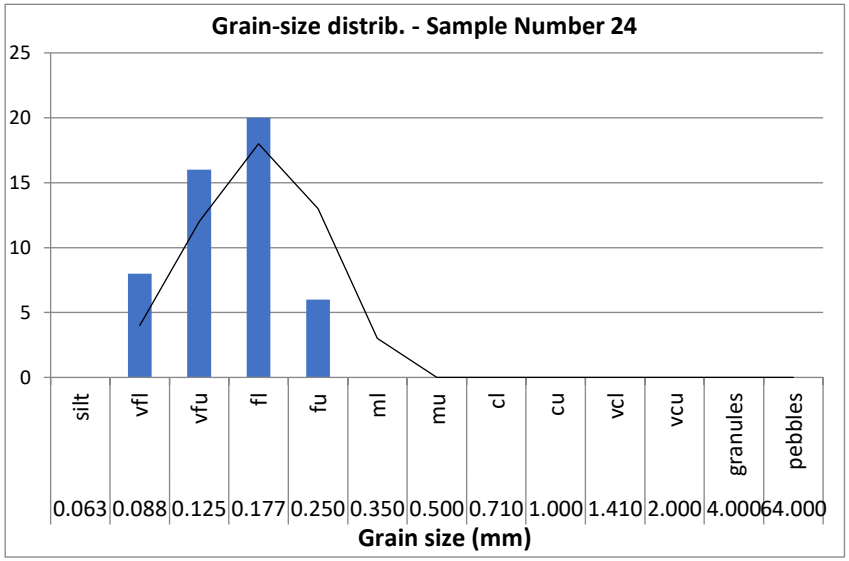
Grain-size distrib. - Sample Number 24
25
20
15
10
5
0
silt
vfl
vfu
fl
fu
ml
mu
cl
cu
vcl
vcu
granules
pebbles
0.063
0.088
0.125
0.177
0.250
0.350
0.500
0.710
1.000
1.410
2.000
4.000
64.000
Grain size (mm)

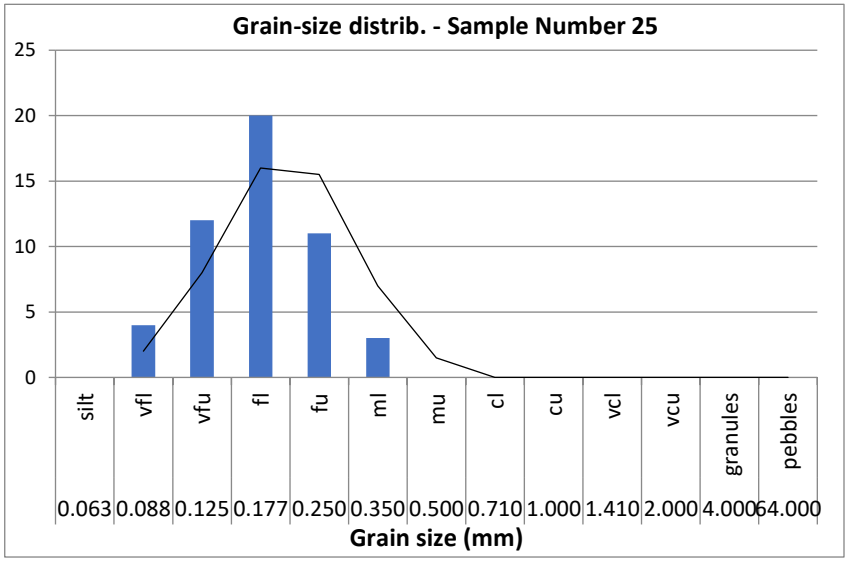
Grain-size distrib. - Sample Number 25
25
20
15
10
5
0
silt
vfl
vfu
fl
fu
ml
mu
cl
cu
vcl
vcu
granules
pebbles
0.063
0.088
0.125
0.177
0.250
0.350
0.500
0.710
1.000
1.410
2.000
4.000
64.000
Grain size (mm)

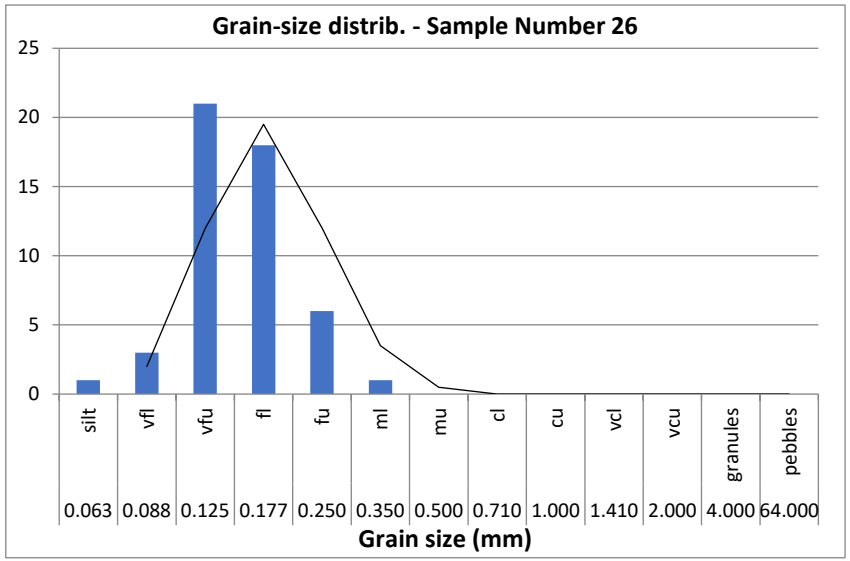
Grain-size distrib. - Sample Number 26
25
20
15
10
5
0
silt
vfl
vfu
fl
fu
ml
mu
cl
cu
vcu
granules
pebbles
0.063
0.088
0.125
0.177
0.250
0.350
0.500
0.710
1.000
1.410
2.000
4.000
64.000
Grain size (mm)

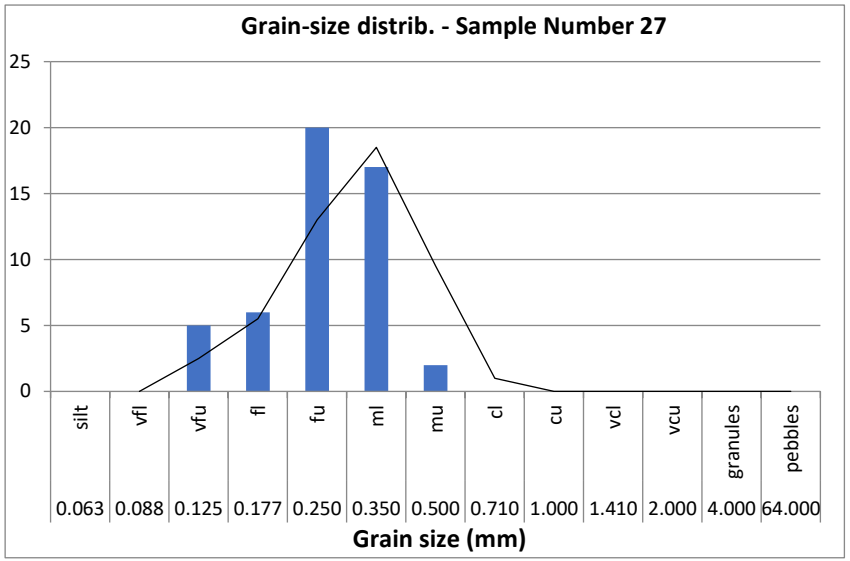
Grain-size distrib. - Sample Number 27
25
20
15
10
5
0
silt
vfl
vfu
fl
fu
ml
mu
cl
cu
vcu
granules
pebbles
0.063
0.088
0.125
0.177
0.250
0.350
0.500
0.710
1.000
1.410
2.000
4.000
64.000
Grain size (mm)

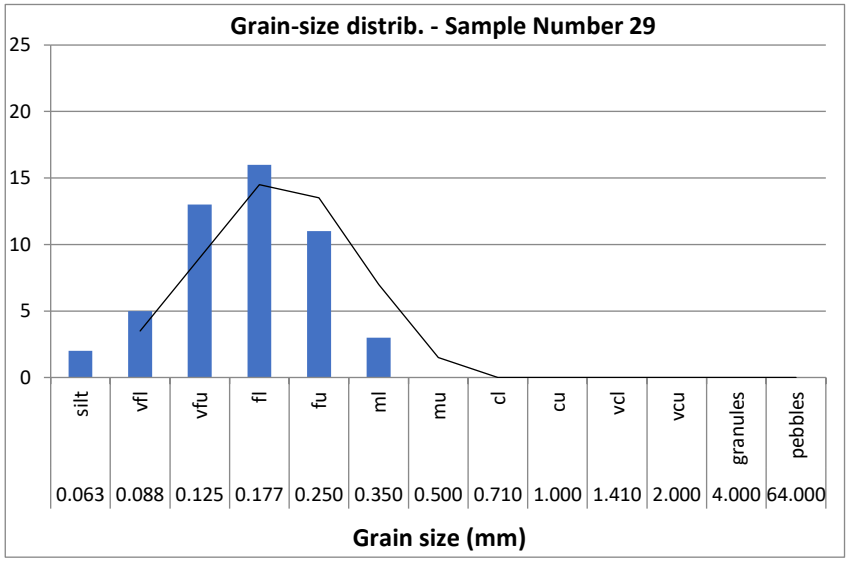
Grain-size distrib. - Sample Number 29
25
20
15
10
5
0
silt
vfl
vfu
fl
fu
ml
mu
cl
cu
vcu
granules
pebbles
0.063
0.088
0.125
0.177
0.250
0.350
0.500
0.710
1.000
1.410
2.000
4.000
64.000
Grain size (mm)

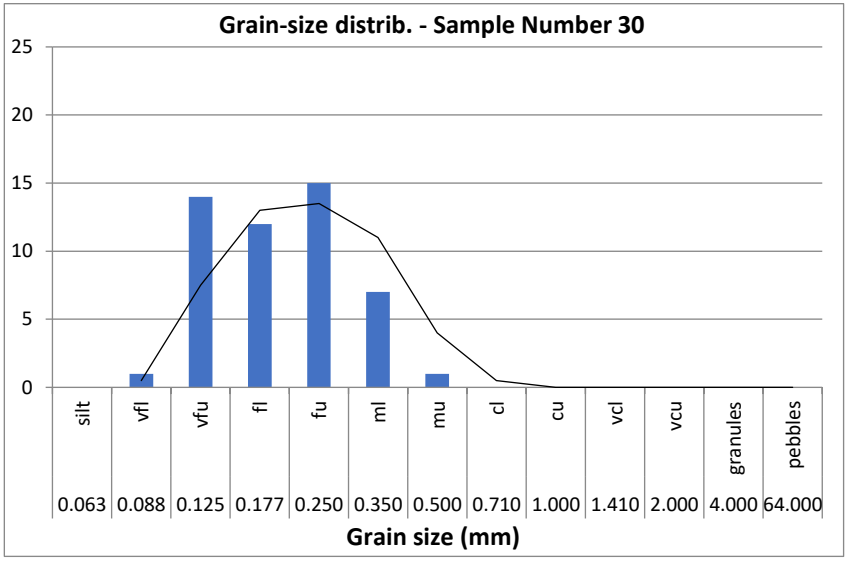
Grain-size distrib. - Sample Number 30
25
20
15
10
5
0
silt
vfl
vfu
fl
fu
ml
mu
cl
cu
vcu
granules
pebbles
0.063
0.088
0.125
0.177
0.250
0.350
0.500
0.710
1.000
1.410
2.000
4.000
64.000
Grain size (mm)

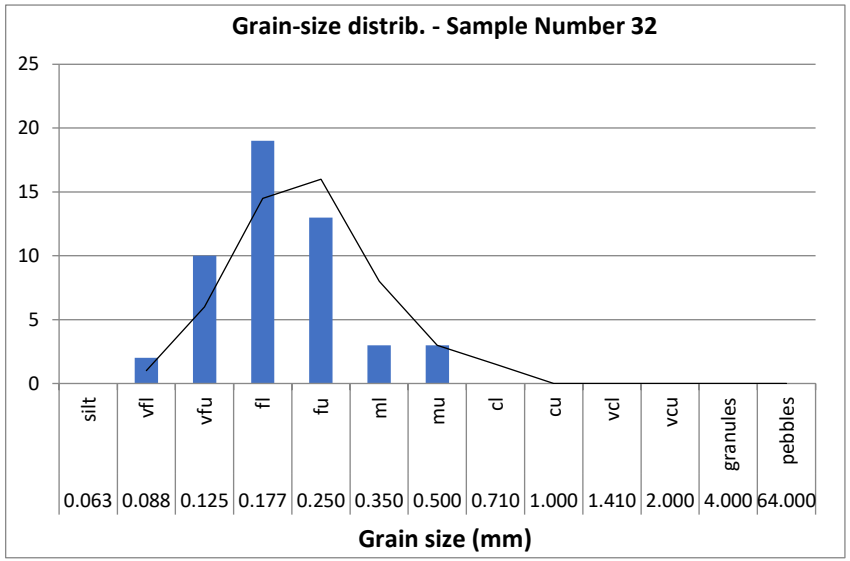
Grain-size distrib. - Sample Number 32
25
20
15
10
5
0
silt vfl vfu fl fu ml mu cl cu vcl vcu granules pebbles
0.063 0.088 0.125 0.177 0.250 0.350 0.500 0.710 1.000 1.410 2.000 4.000 64.000
Grain size (mm)

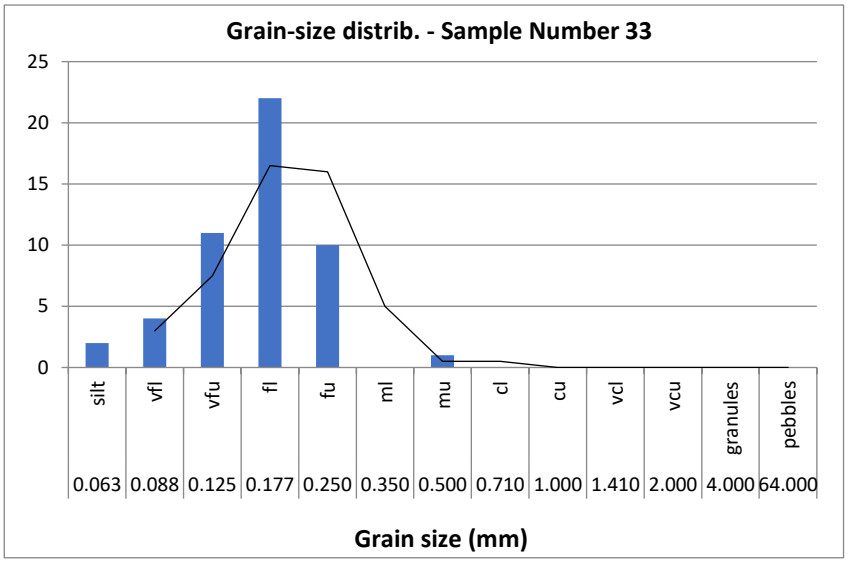
Grain-size distrib. - Sample Number 33
25
20
15
10
5
0
silt vfl vfu fl fu ml mu cl cu vcl vcu granules pebbles
0.063 0.088 0.125 0.177 0.250 0.350 0.500 0.710 1.000 1.410 2.000 4.000 64.000
Grain size (mm)

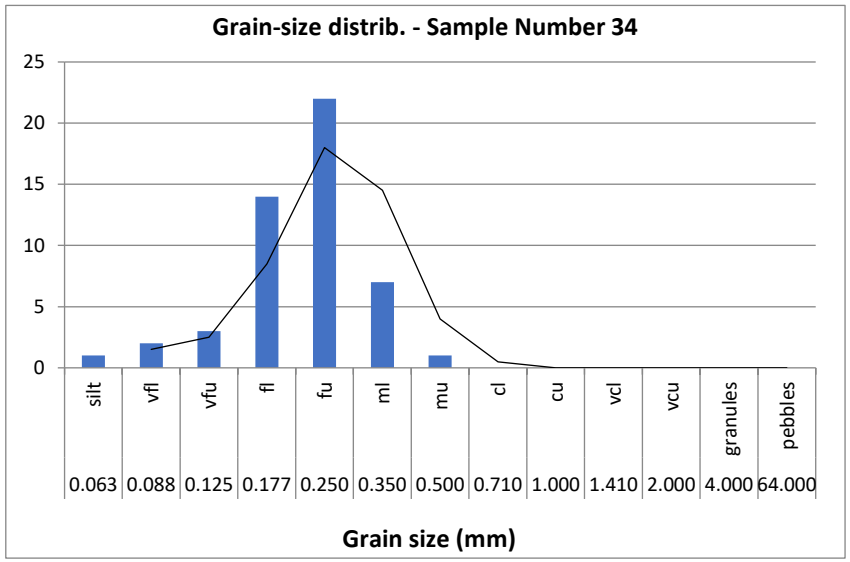
Grain-size distrib. - Sample Number 34
25
20
15
10
5
0
silt vfl vfu fl fu ml mu cl cu vcl vcu granules pebbles
0.063 0.088 0.125 0.177 0.250 0.350 0.500 0.710 1.000 1.410 2.000 4.000 64.000
Grain size (mm)

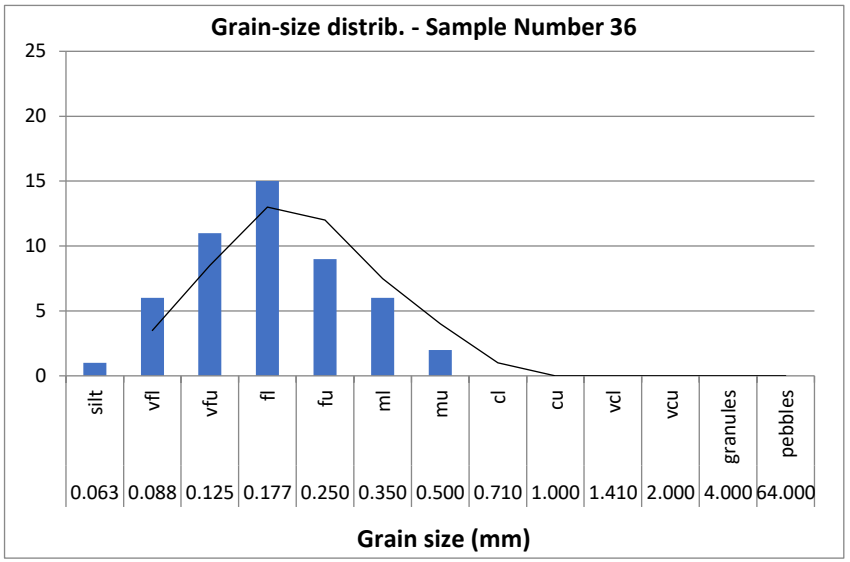
Grain-size distrib. - Sample Number 36
25
20
15
10
5
0
silt vfl vfu fl fu ml mu cl cu vcl vcu granules pebbles
0.063 0.088 0.125 0.177 0.250 0.350 0.500 0.710 1.000 1.410 2.000 4.000 64.000
Grain size (mm)

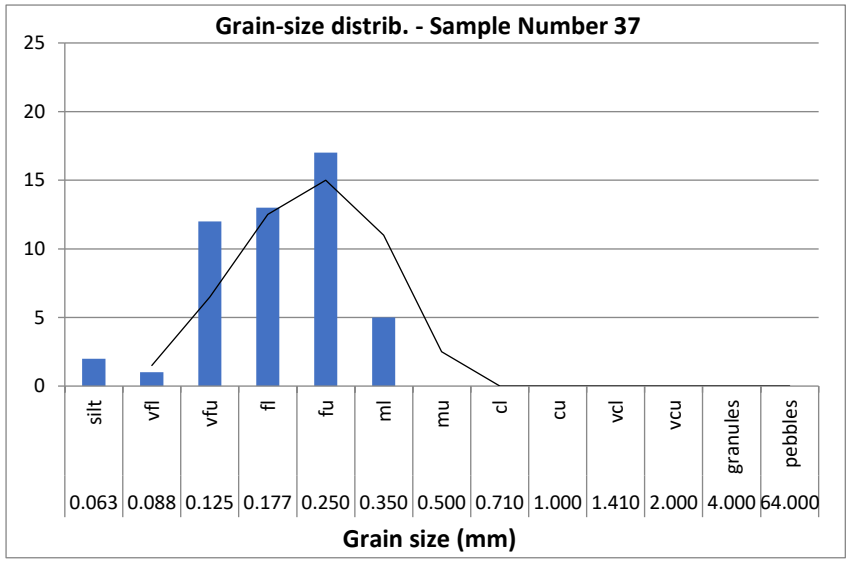
Grain-size distrib. - Sample Number 37
25
20
15
10
5
0
silt
vfl
vfu
fl
fu
ml
mu
cl
cu
vcl
vcu
granules
pebbles
0.063
0.088
0.125
0.177
0.250
0.350
0.500
0.710
1.000
1.410
2.000
4.000
64.000
Grain size (mm)

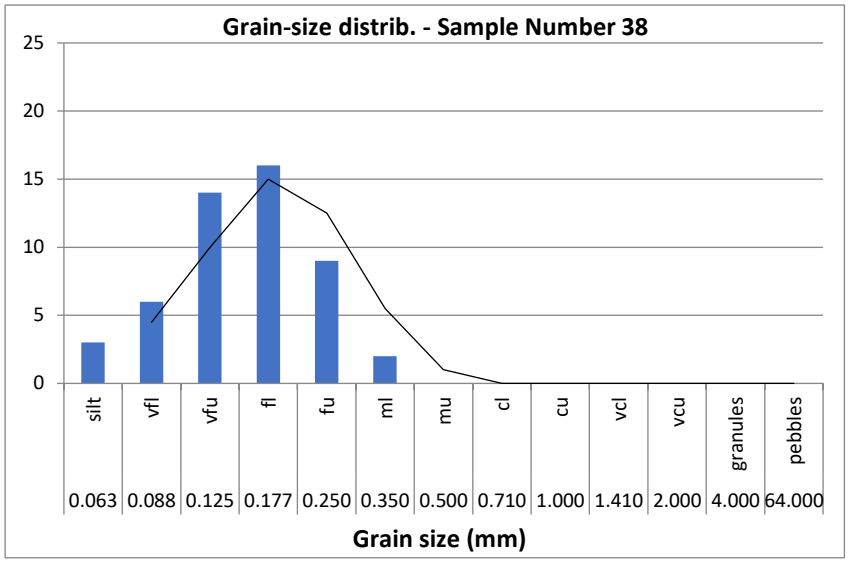
Grain-size distrib. - Sample Number 38
25
20
15
10
5
0
silt
vfl
vfu
fl
fu
ml
mu
cl
cu
vcl
vcu
granules
pebbles
0.063
0.088
0.125
0.177
0.250
0.350
0.500
0.710
1.000
1.410
2.000
4.000
64.000
Grain size (mm)

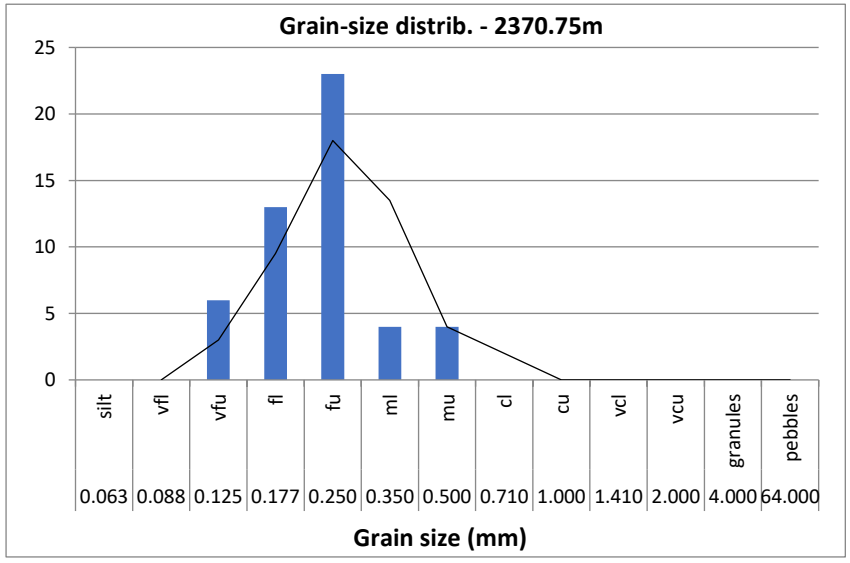
Grain-size distrib. - 2370.75m
25
20
15
10
5
0
silt
vfl
vfu
fl
fu
ml
mu
cl
cu
vcl
vcu
granules
pebbles
0.063
0.088
0.125
0.177
0.250
0.350
0.500
0.710
1.000
1.410
2.000
4.000
64.000
Grain size (mm)

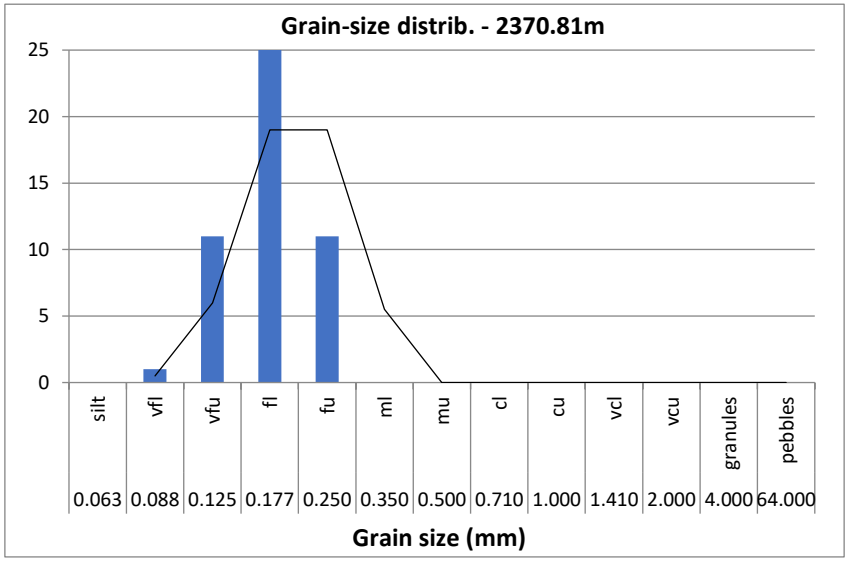
Grain-size distrib. - 2370.81m
25
20
15
10
5
0
silt
vfl
vfu
fl
fu
ml
mu
cl
cu
vcl
vcu
granules
pebbles
0.063
0.088
0.125
0.177
0.250
0.350
0.500
0.710
1.000
1.410
2.000
4.000
64.000
Grain size (mm)

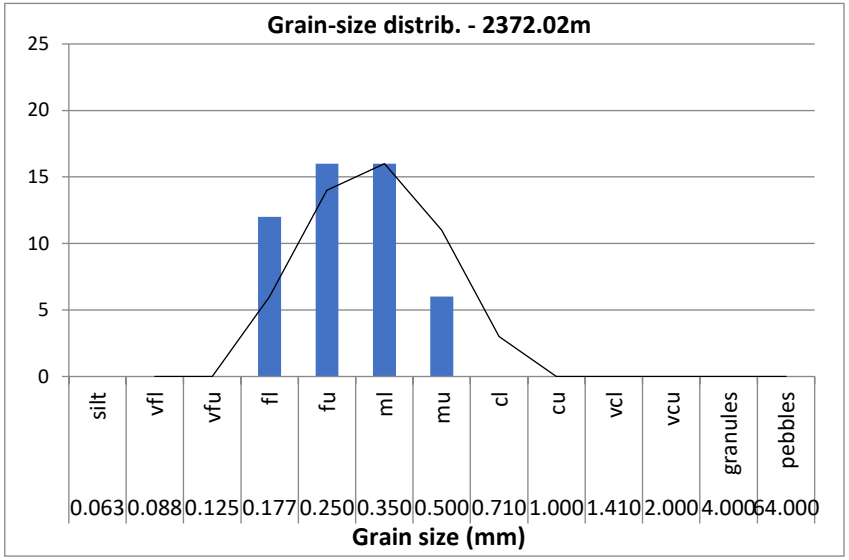
Grain-size distrib. - 2372.02m
25
20
15
10
5
0
silt
vfl
vfu
fl
fu
ml
mu
cl
cu
vcl
vcu
granules
pebbles
0.063
0.088
0.125
0.177
0.250
0.350
0.500
0.710
1.000
1.410
2.000
4.000
64.000
Grain size (mm)

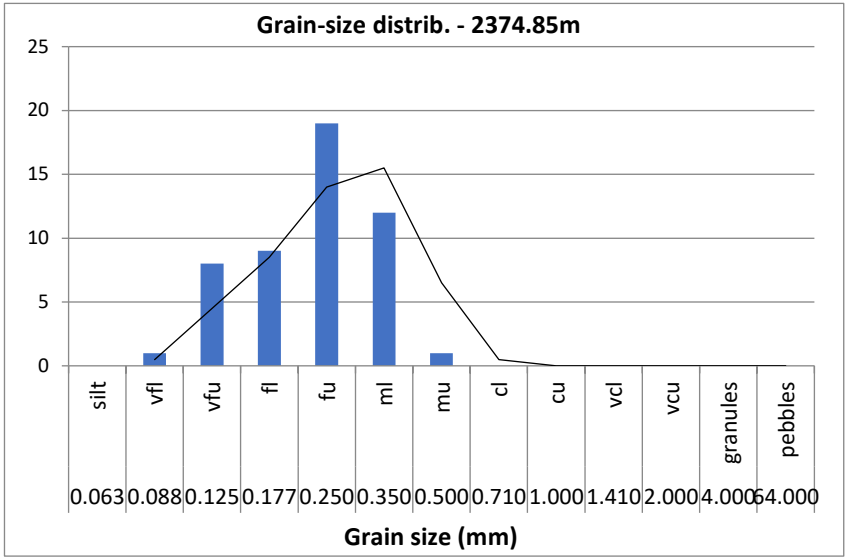
Grain-size distrib. - 2374.85m
25
20
15
10
5
0
silt
vfl
vfu
fl
fu
ml
mu
cl
cu
vcl
vcu
granules
pebbles
0.063
0.088
0.125
0.177
0.250
0.350
0.500
0.710
1.000
1.410
2.000
4.000
64.000
Grain size (mm)

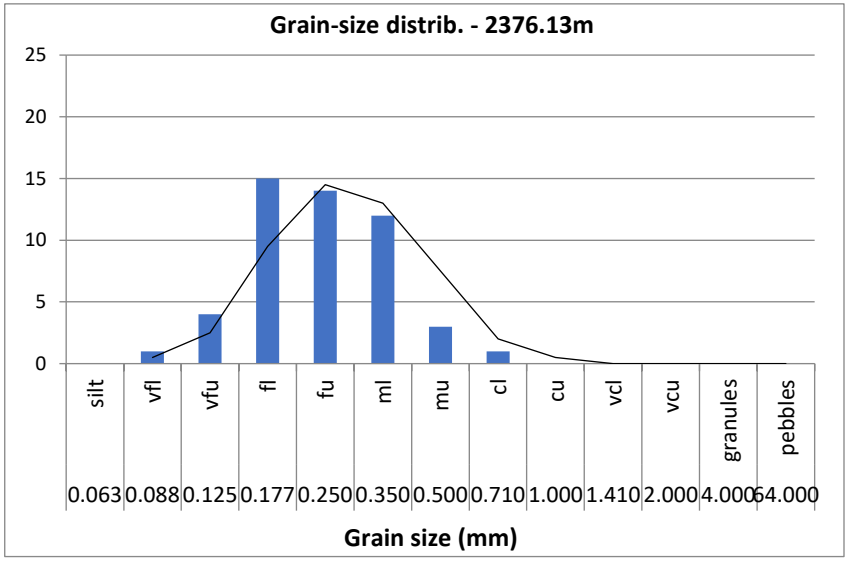
Grain-size distrib. - 2376.13m
25
20
15
10
5
0
silt
vfl
vfu
fl
fu
ml
mu
cl
cu
vcl
vcu
granules
pebbles
0.063
0.088
0.125
0.177
0.250
0.350
0.500
0.710
1.000
1.410
2.000
4.000
64.000
Grain size (mm)

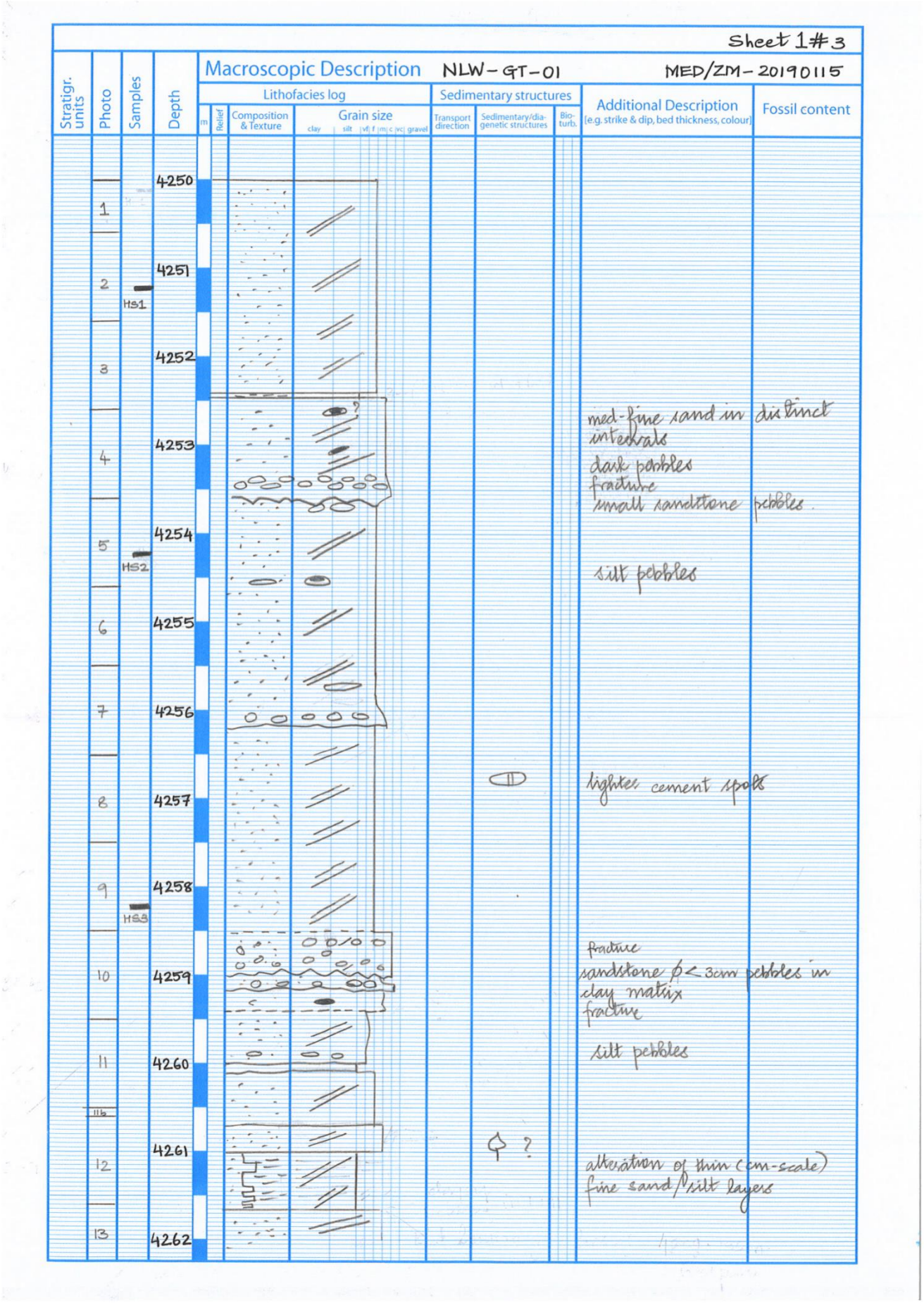
Sheet 1#3
Macroscopic Description
NLW-GT-01
MED/ZM-20190115
Lithofacies log
Sedimentary structures
Stratigr. units
Photo
Samples
Depth
Relief
Composition & Texture
Grain size
clay silt vf f m c vc gravel
Transport direction
Sedimentary/dia-genetic structures
Bio-turb.
Additional Description (e.g. strike & dip, bed thickness, colour)
Fossil content
4250
4251
4252
4253
4254
4255
4256
4257
4258
4259
4260
4261
4262
HS1
HS2
HS3
med-fine sand in interbals
distinct
dark pebbles
fracture
small sandstone pebbles
silt pebbles
lighter cement spots
fracture
sandstone ϕ < 3cm pebbles in clay matrix
fracture
silt pebbles
alteration of thin (cm-scale) fine sand/silt layers

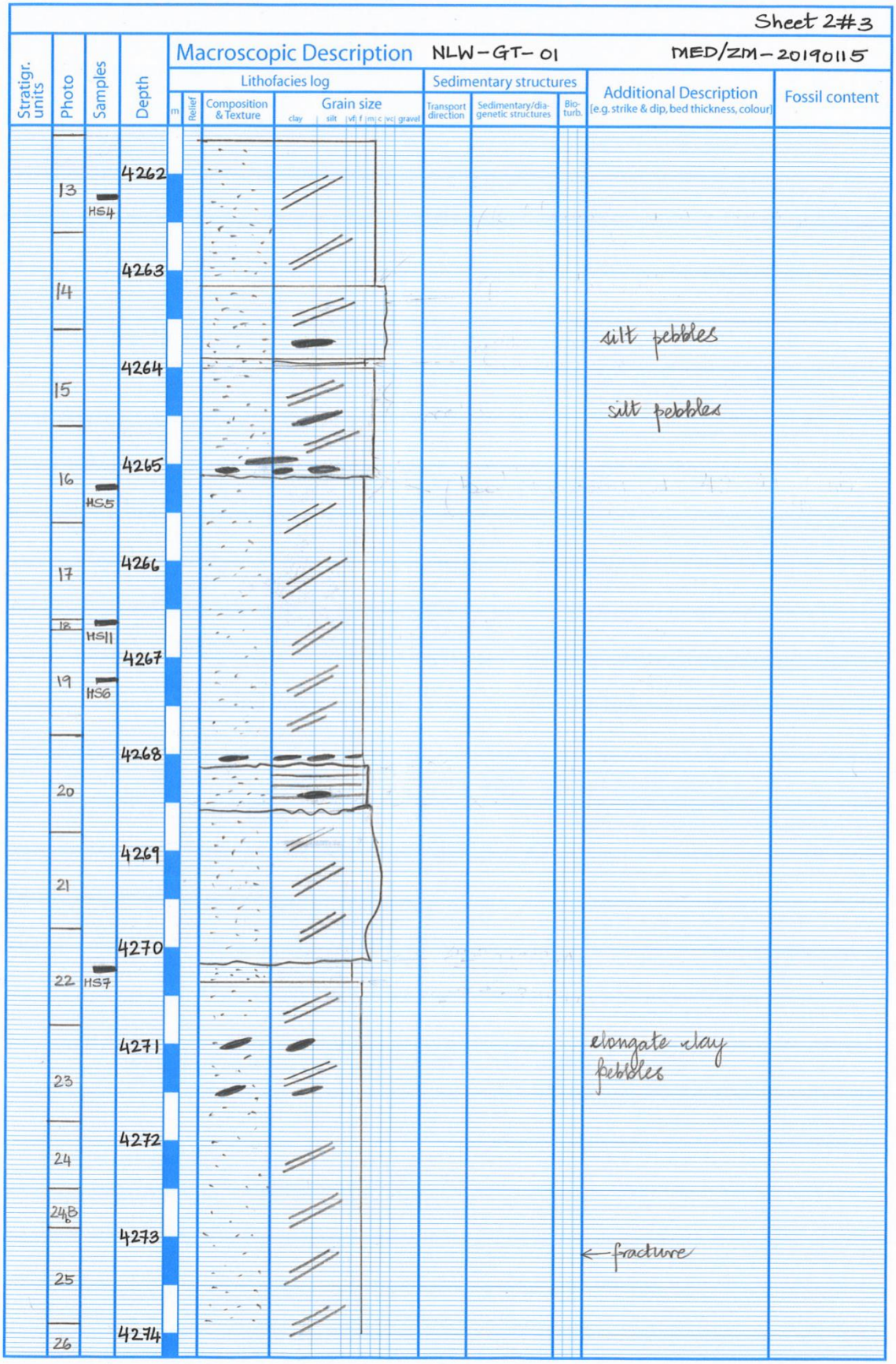
Sheet 2#3
Macroscopic Description NLW-GT-01 MED/ZM-20190115
Stratigr. units
Photo
Samples
Depth
Lithofacies log
m
Relief
Composition & Texture
Grain size
clay silt vf f m c vc gravel
Sedimentary structures
Transport direction
Sedimentary/dia-genetic structures
Bio-turb.
Additional Description [e.g. strike & dip, bed thickness, colour]
Fossil content
4262
4263
4264
4265
4266
4267
4268
4269
4270
4271
4272
4273
4274
13
14
15
16
17
18
19
20
21
22
23
24
24B
25
26
HS4
HS5
HS11
HS6
HS7
silt pebbles
silt pebbles
elongate clay pebbles
fracture

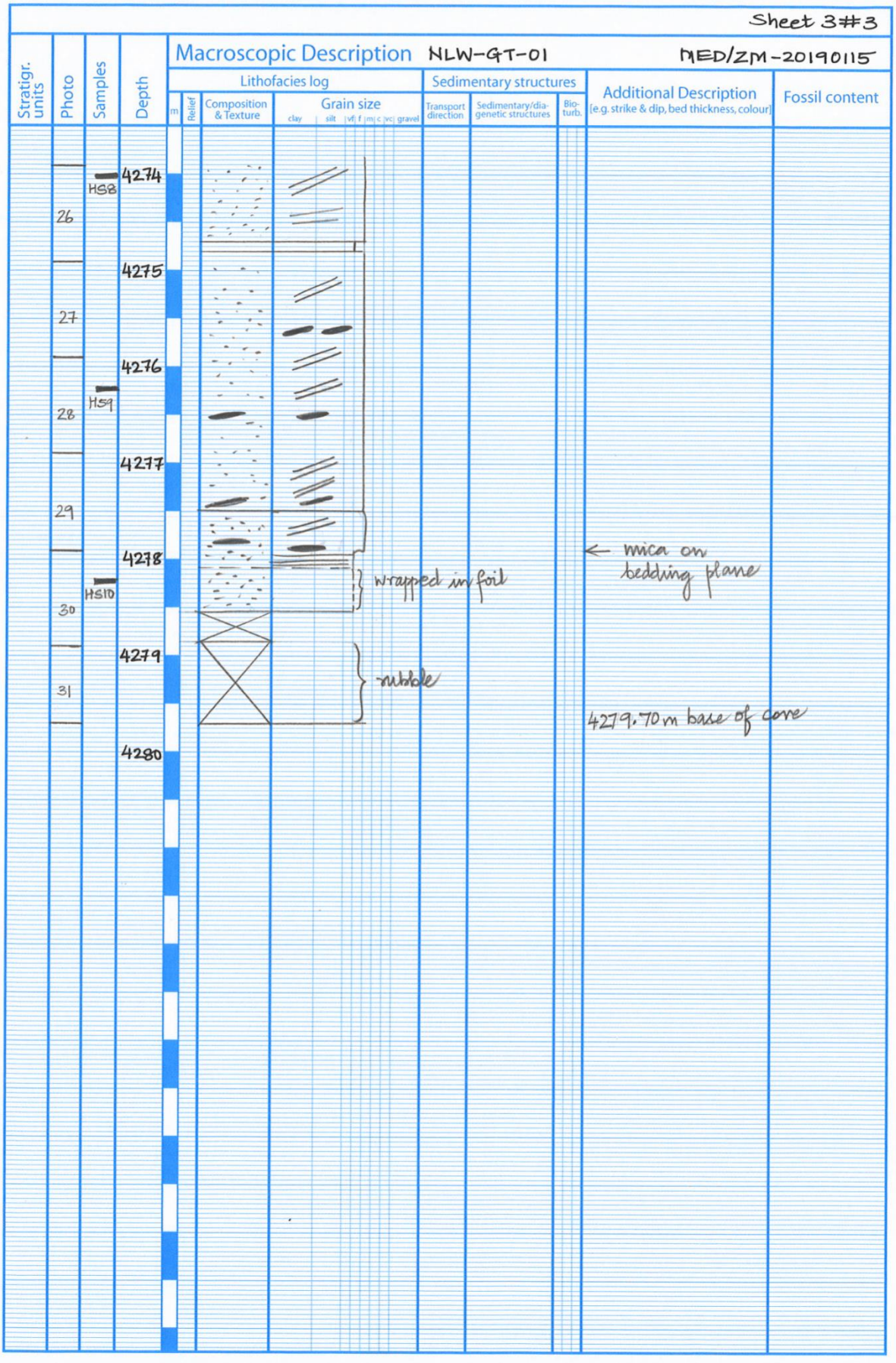

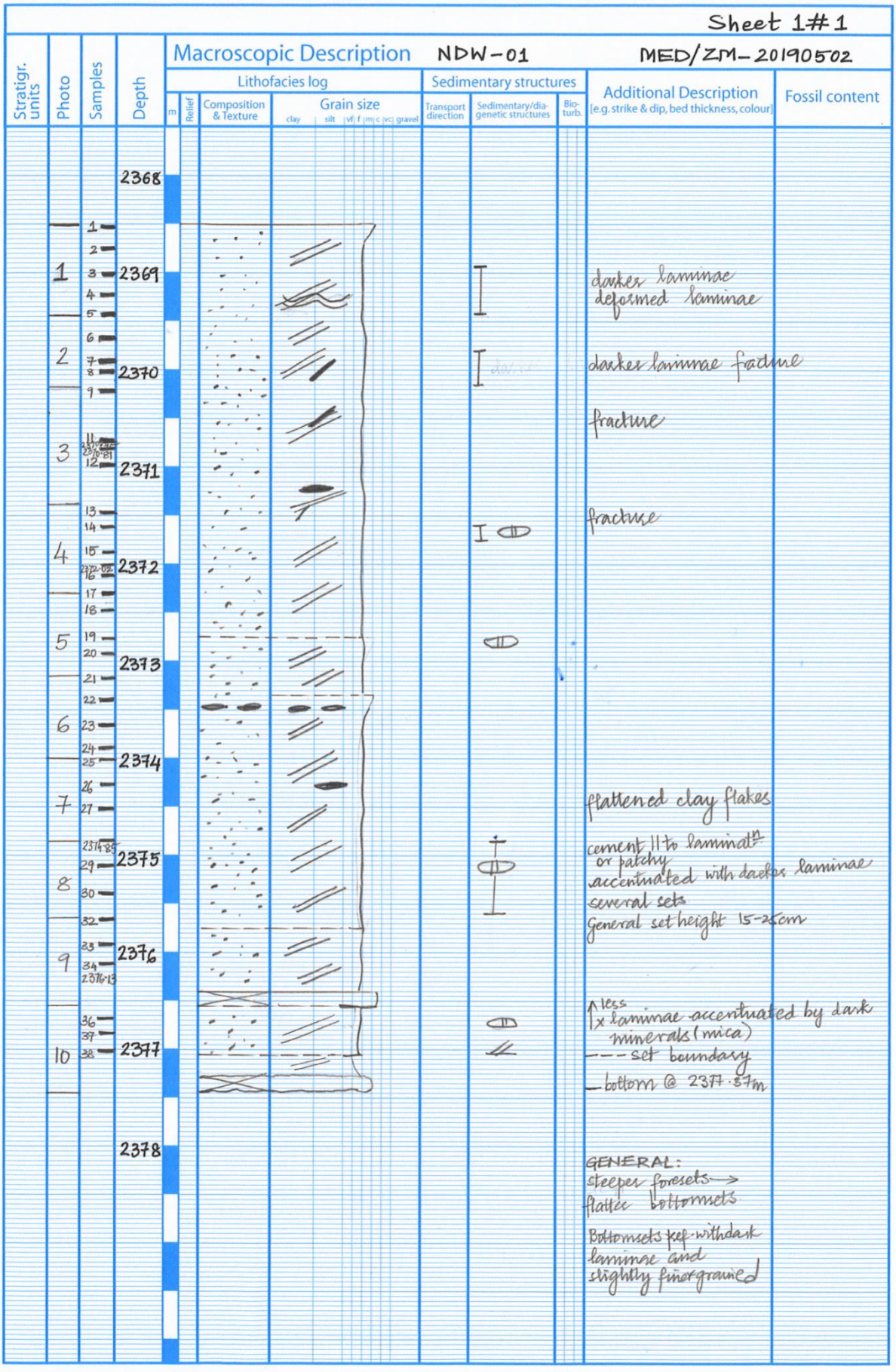

Cross Plots : Density versus Neutron Porosity Logs for the Main Buntsandstein Subgroup.

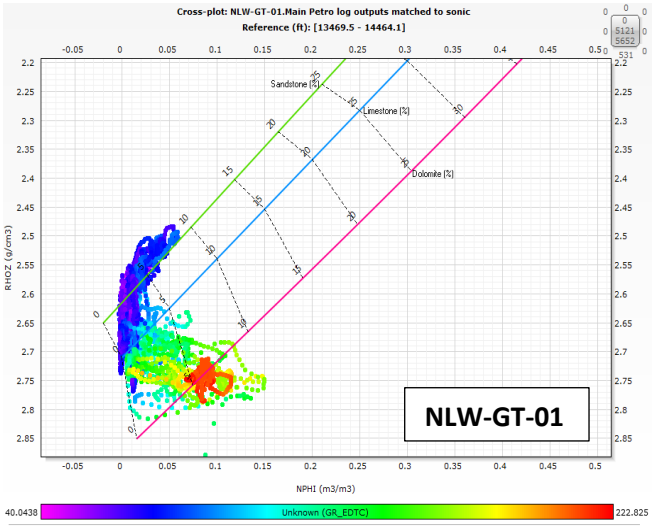

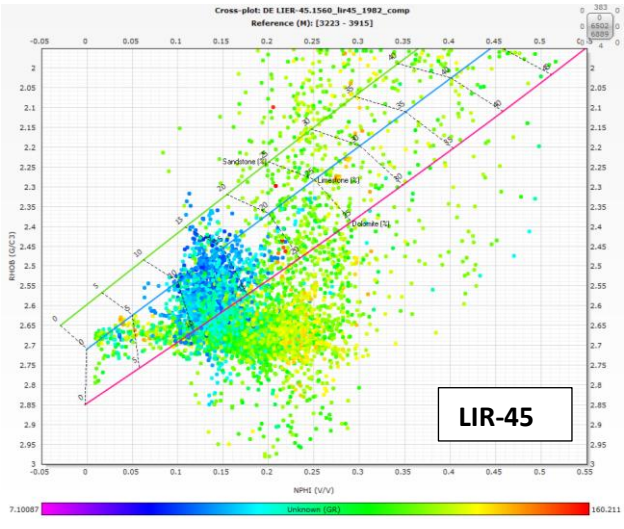

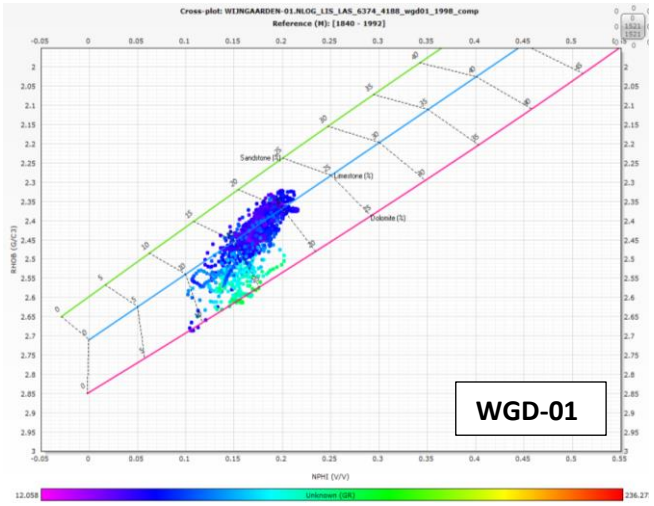

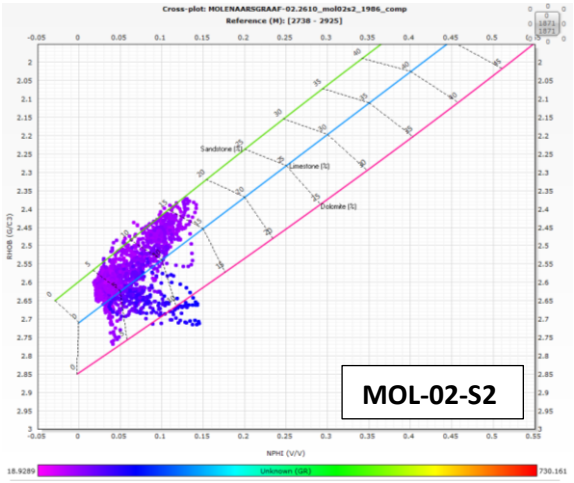

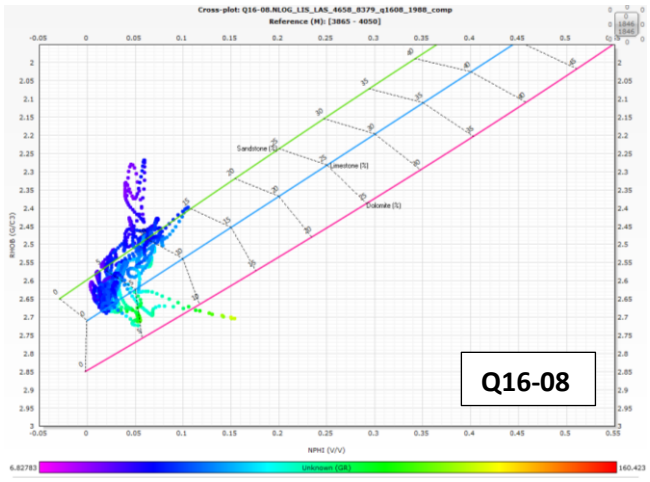

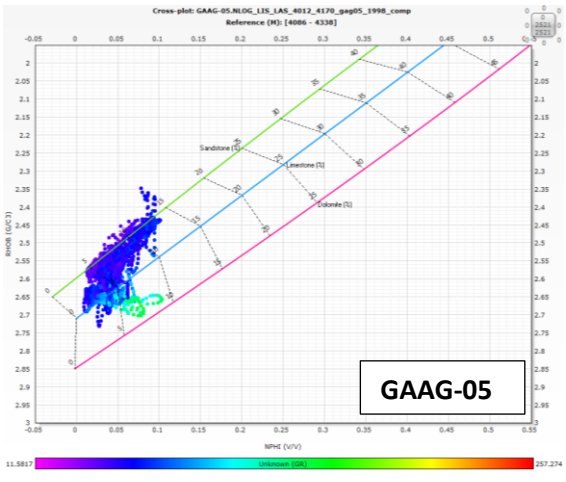

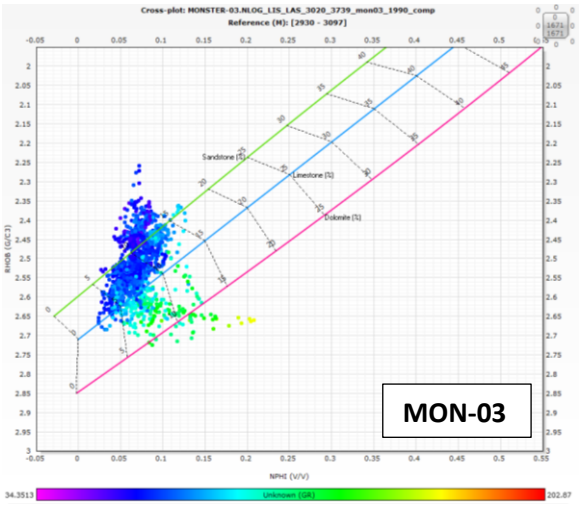
MON-03

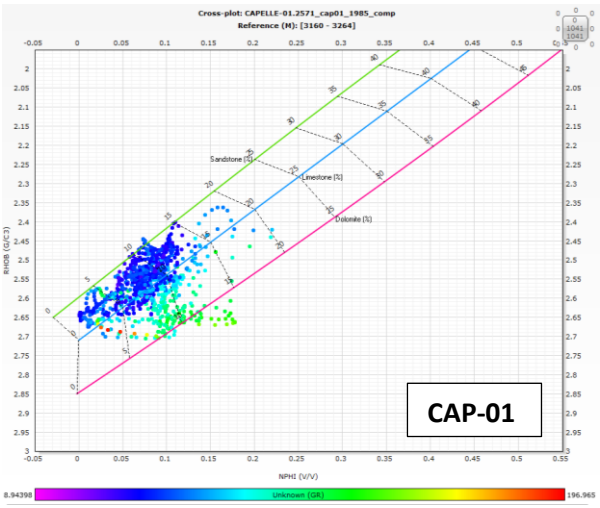
CAP-01

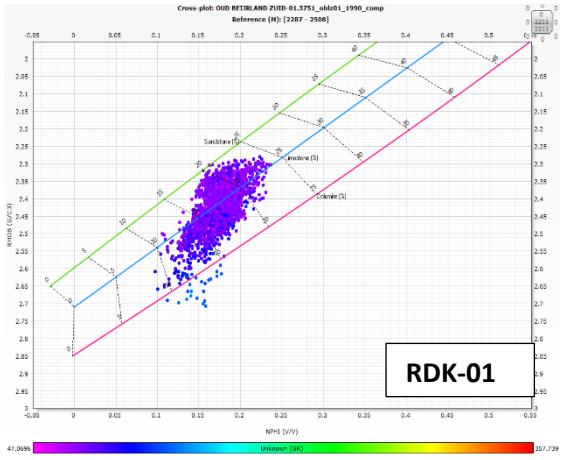
RDK-01

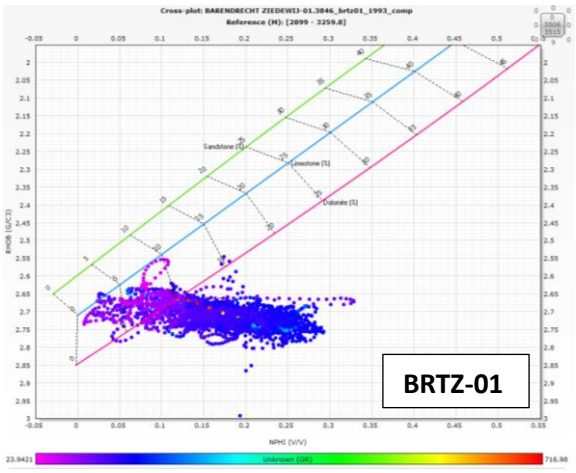
BRTZ-01

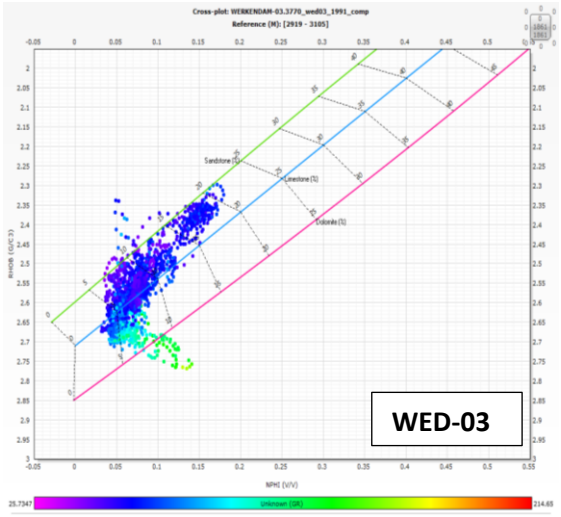
WED-03

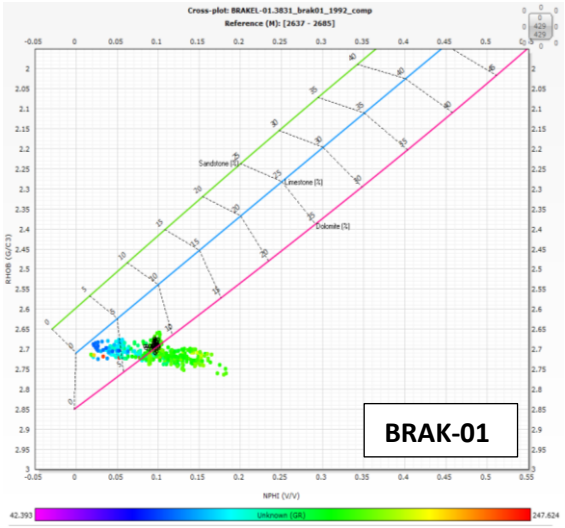
BRAK-01